Targeted Modification of Neutron Energy Spectra for National Security Applications

by

James Edward Bevins

A dissertation submitted in partial satisfaction of the
requirements for the degree of
Doctor of Philosophy

in

Engineering - Nuclear Engineering

in the

Graduate Division

of the

University of California, Berkeley

Committee in charge:

Professor Rachel Slaybaugh, Chair
Professor Lee Bernstein
Professor Jasmina Vujic
Professor Michael Nacht

Summer 2017

Targeted Modification of Neutron Energy Spectra for National Security Applications

Abstract

Targeted Modification of Neutron Energy Spectra for National Security Applications

by

James Edward Bevins

Doctor of Philosophy in Engineering - Nuclear Engineering

University of California, Berkeley

Professor Rachel Slaybaugh, Chair

A foolish consistency is the hobgoblin of little minds, adored by little statesmen and philosophers and divines.

- Ralph Waldo Emerson

At its core, research represents an attempt to break from the "this is the way we have always done it" paradigm. This idea is evidenced from the start in this research effort by the problem formulation to develop a new way to generate synthetic debris that mimics the samples that would be collected for forensics purposes following a nuclear weapon attack on the U.S. or its allies. The philosophy is also demonstrated by the design methodology used to solve the synthetic debris problem, using methods not commonly applied to nuclear engineering problems. Through this research, the bounds of what is deemed possible in neutron spectral shaping are moved ever so slightly.

A capability for the production of synthetic debris and fission products was developed for the National Ignition Facility (NIF). Synthetic debris has historically been made in a limited fashion using sample doping techniques since the cessation of nuclear weapons testing, but a more robust alternative approach using neutron spectral shaping was proposed and developed by the University of California-Berkeley and Lawrence Livermore National Laboratory (LLNL). Using NIF as a starting source spectrum, the energy tuning assembly (ETA) developed in this work can irradiate samples with a combined thermonuclear and prompt fission neutron spectrum (TN+PFNS). When used with fissile foils, this irradiation will produce a synthetic fission product distribution that is realistic across all mass chains.

To design the ETA, traditional parametric point design approaches were discarded in favor of formal optimization techniques. Finding a lack of suitable algorithms in the literature, a metaheuristic-based optimization algorithm, Gnowee, was developed for rapid convergence to nearly globally optimum solutions for complex, constrained engineering problems with mixed-integer and combinatorial design vectors and high-cost, noisy, discontinuous, black box objective function evaluations. Comparisons between Gnowee and several well-established metaheuristic algorithms are made for a set of continuous, mixed-integer, and

combinatorial benchmarks. These results demonstrated Gnoweee to have superior flexibility and convergence characteristics over a wide range of design spaces.

The Gnowee algorithm was implemented in Coeus, a new piece of software, to perform optimization of design problems requiring radiation transport for the evaluation of their objective functions. Currently, Coeus solves ETA optimization problems using hybrid radiation transport (ADVANTG and MCNP) to assess design permutations developed by Gnowee. Future enhancements of Coeus will look to expand the geometries and objective functions considered to those beyond ETA design.

Coeus was used to generate an ETA design for the TN+PFNS application on NIF. The design achieved a reasonable match with the objective TN+PFNS and associated fission product distributions within the size and weight constraints imposed by the NIF facility. The ETA design was built by American Elements, and initial validation tests were conducted at the Lawrence Berkeley National Laboratory's 88-Inch Cyclotron. These experiments used foil activation and pulse height spectroscopy to measure the ETA-modified spectrum. Additionally, pulse height spectroscopy measurements were taken as the ETA was built-up component-by-component to measure the impact of nuclear data on the ability to model the ETA performance. Some initial analysis of these results is included here.

Finally, an integral validation experiment on NIF was proposed using the Coeus generated ETA design. A scoping study conducted by LLNL determined the proposed experiment and ETA design are within NIF facility limitations and current radio-chemistry capabilities. The study found that the proposed ETA experiment was "low risk," has "no show stoppers," and has a "reasonable cost." All that is needed is a sponsor to close the last funding gap and bring the experiment to fruition.

This research broke with the current sample doping approach and applied neutron spectral shaping to design an ETA that can create realistic synthetic fission and activation products and improve technical nuclear forensics outcomes. However, the ETA presented in this research represents more than a stand alone point design with a limited scope and application. It is proof of a concept and the product of a unique capability that has a wide range of potential applications.

This research demonstrates that the concept of neutron spectral shaping can be used to engineer complex neutron spectra within the confines of physics. There are many possible applications that could benefit from the ability to generate custom energy neutron spectra that fall outside of current sources and methods. The ETA is the product of a general-purpose optimization algorithm, Gnowee, and design framework, Coeus, which enables the use of Gnowee for complex nuclear design problems. Through Gnowee and Coeus, new ETA neutronics designs can be generated in days, not months or years, with a drastic reduction in the research effort required to do so. Most importantly, the new designs could be for applications completely disconnected from the current research and do not have to even be ETA designs at all. The capability of Gnowee and Coeus have the potential to greatly improve the design process in many fields of nuclear engineering.

To Tanya,

Without whom I may have lost my sanity.

Contents

List of Figures

List of Tables

List of Acronyms

ACO - Ant Colony Optimization
ACRR - Annular Core Research Reactor
ADVANTG - AutomateD VAriaNce reducTion Generator
ASC - Advanced Simulation and Computing
BC - Boron Carbide
BCM - Beam Current Monitor
BLC - Beam Line Center
BNCT - Boron Neutron Capture Therapy
BSA - Beam Shaping Assembly
CAMS - Center for Accelerator Mass Spectrometry
CS - Cuckoo Search
DAQ - Data AcQuisition
DE - Differential Evolution
DIM - Diagnostic Instrument Manipulator
DLP - Diagnostic Load Package
DNA - Defense Nuclear Agency
DoD - Department of Defense
DOE - Department of Energy
DPP-PSD - Digital Pulse Processing - Pulse Shape Discrimination
ETA/η - Energy Tuning Assembly
ENDL - Evaluated Nuclear Data Library
FBR - Fast Burst Reactor
FOM -Figure of Merit
FP - Fission Products
FREYA - Fission Reaction Event Yield Algorithm
GA - Genetic Algorithm
GEF - GEneral description of Fission observables
HEU - Highly Enriched Uranium
HFIR - High Flux Isotope Reactor
HFNG - High Flux Neutron Generator
HPC - High-Performance Computing
HV- High Voltage
ICBM - Inter-Continental Ballistic Missile
JNFWG - Joint Nuclear Forensics Working Group

IBL - Ion Beam Lab
LBNL - Lawrence Berkeley National Laboratory
LLNL - Lawrence Livermore National Laboratory
MCNP- Monte Carlo Neutral Particle
MCS - Modified Cuckoo Search
MEIGO - MEtaheuristics for bIoinformatics Global Optimization
MINLP - Mixed-Integer Nonlinear Programming
NAS - Neutron Activation Spectrometer
NIF - National Ignition Facility
NTOF- Neutron Time of Flight
NW - Nuclear Weapon
PAT - Pulse-Amplitude-Time
PFNS - Prompt Fission Neutron Spectrum
PHS - Pulse Height Spectrum
PMT - Photo-Multiplier Tube
PSD - Pulse Shape Discrimination
PSO - Particle Swarm Optimization
PUR - Pile-up Rejection
SA - Simulated Annealing
SEU - Single Event Upset
QASPR - Qualification Alternatives to the Sandia Pulsed Reactor
SNM -Special Nuclear Material
SNOMPS - Spectral Neutron Optimization using MCNP and PyNE Simulations
SPR - Sandia Pulsed Reactor
SSP - Stockpile Stewardship Program
TC - Target Chamber
TCC - Target Chamber Center
TN - Thermonuclear
TNF - Technical Nuclear Forensics
WF - WaveForm
WSMR - White Sands Missile Range
WNR - Weapons Neutron Research Facility
WR - Weapons Related

Acknowledgments

No man is an island, entire of itself.

- John Donne

I am indebted to a great number of people who have contributed to this research significantly and of whom I can never possibly repay. The most I can hope to do is acknowledge their contributions here, the totality of which is long yet simultaneously inadequate and incomplete.

While it may take a village, I must first acknowledge those closest to home. Throughout every experience of the past 15 years, there has been only one constant, one rock which serves as my foundation. My wife Tanya, is literally the single most important reason I have attempted this journey, and the reason I made it this far. She is the best possible partner I could ever hope for in life, and she makes a great research partner, despite having no background in the subject matter. She of course had help along the way and was aided, and sometimes hindered, by my three daughters. Over the past couple of years, Alicia has grown into a beautiful young lady, and she has picked up a lot of my slack at home during "crunch times". Jaymie has a great heart and a curiosity that will take her far, and her positivity was much appreciated when the going got rough. My oldest, Mary, could always be counted upon to make life interesting.

My advisor, Dr. Rachel Slaybaugh, took a chance on me despite not being a great fit for her research given my reluctance towards heavy math. Without her and that decision, this journey would not have been possible. She has provided an immense amount of guidance and direction to my research while allowing me to maintain broad discretion and independence. Her ability to overcome a diverse array of obstacles is unmatched, and it has been a pleasure to work with someone so talented and capable. My main regret during my time at UCB is that I did not fully take advantage of all she had to offer as a mentor, but hopefully I will have the opportunity to continue to do so moving forward.

I have also been supported by a great committee, which has contributed to my development and learning in ways above and beyond what I reasonably could have expected. Dr. Lee Bernstein is a fountain of ideas and positivity, and I have greatly enjoyed and benefited from our (long) interactions. Dr. Jasmina Vujic is responsible, along with Bill Dunlop and Gene Henry, for originating the concept and allowing me the opportunity to work on this particular project, and I have appreciated her continued support and interest in my work. Dr. Michael Nacht is an incredible individual with a gift for drawing on his extensive government experience to illustrate core concepts of nuclear strategy and the policy-making process, and I was privileged to have had the opportunity to learn from him.

I also owe a debt of gratitude to Dr. Bethany Goldblum and her Bay Area Neutron Group (BANG), which allowed me to be an adopted member. Despite not being on my committee, Bethany was incredibly valuable throughout this research and a key factor to

our ability to field the 88-Inch Cyclotron experiments. I am fortunate to have had the ability to learn from and work with her during my time at UCB.

I cannot possibly thank all of the students who helped me with this research, but I will make an attempt to highlight as many as possible. Kelly Rowland is simply a great human being as well as was an invaluable resource in all things computers, and she helped me solve many Savio related difficulties. Josh Brown is brilliant, and I appreciate the time and effort he spent getting me up to speed with the systems that he and Bethany developed at the 88-Inch Cyclotron. None of the experimental validation would have been possible without leveraging their work. The interactions with Matthew Harasty were fantastic in developing ways to better utilize the existing unfolding algorithms, and I cannot wait to see the outcome of his development effort. Thibault Laplace is a selfless problem solver and can translate hex like no other. Andrew Voyles was a great friend, brewmaster, and an even better activation wizard. Although not a student, I am not sure where else to put Dr. Darren Bleuel. This is fitting given he is truly the definition of a "jack-of-all-trades", and everyone who has the privilege to work with him is better off for doing so.

I was fortunate to work with Youdong Zhang and Sandra Bogetic on improvements to Coeus, and I look forward to continuing to do so in the future. Will Kable helped develop unfolding and germanium detector models and was one of the most productive undergraduates I have ever worked with. Although the interaction with Zachary Sweger and Ninad Munshi has been brief, they are giving Will a run for his money, and I look forward to continuing to work through the foil activation analysis with them.

The 88-Inch Cyclotron staff and operators are phenomenal at what they do, and their willingness to work with pain-in-the-neck students is unmatched. Larry Phair, Ken Gregorith, and Mike Johnson were great to work with. Despite delays on our part and the cyclotron falling apart during one of the runs, they found a way to make our experiments happen through shifting the schedule and giving up valuable beam time. While all of the operators were fantastic, Brien Ninemire is a cyclotron whisper, and his ability to pull the beam that we requested and make the experiments happen was unmatched. The machine shop staff delivered quality products on often short timelines while fixing (almost) everything that we broke. Last but not least, Josh Brown, Thibault Laplace, Matthew Harasty, Keegan Harrig, Darren Bleuel, Andrew Voyles, Ethan Boado, and Jorgen Mitbo made the 88-Inch experiments possible by pulling long, and often repeated, shifts during the experiment runs.

Dr. Bethany Goldblum also provided tremendous opportunities in the nuclear policy arena though the Nuclear Policy Working Group (NPWG) and outside organizations. Her ability to perform difficult technical work and experiments while simultaneously formulating policy wonk level research is both awe-inspiring and humbling. Working and learning from her and the members of the NPWG was a unique and rewarding experience, and I will especially miss the interactions with Elie Katzenson, Sarah Laderman, James Kendrick, and Rebecca Krentz-Wee. None of these interactions and experiences will show up in this dissertation, but they will be just as valuable in my future career.

Our collaborators at Lawrence Livermore National Laboratory have been fantastic. Gene Henry and Bill Dunlop originated the idea for this research, and Bill Dunlop has been a

bulldog in chasing down the necessary funding and partners. Dawn Shaughnessy and Narek Gharibyan provided much needed insight into the radio-chemistry process and even donated some foils along the way. Brent Blue and his team have shepherded the ETA project through the NIF scoping study and design process. Specifically, Kim Christensen was key in getting the ETA order processed, Charles Yeamans provided valuable shot planning expertise and experience, and Don Jedlovec pulled together the NIF scoping study for the proposed ETA design and pushed it through the process.

Finally, all research requires sponsors, and we were fortunate to have many great sponsors contribute money and resources towards this effort. Colonel Brent Morris and Lieutenant Colonel Zickafoose of the Defense Threat Reduction Agency and Jeffrey Morrison of the National Technical Nuclear Forensics Center provided $135k in funding which enabled the building of the ETA and the NIF scoping study. The 88-Inch Cyclotron Staff, Dr. Lee Bernstein, and Dr. Ken Gregorich provided more beam time than I could have possibly imagined. Doug Mayo and Adam Parkinson arranged for Los Alamos National Laboratory to provide the highly-enriched uranium foils and saved us approximately $65k. Finally, I recieved support from the Air Force, National Science Foundation, the National Nuclear Security Administration, and the Savio cluster, all of which have official acknowledgments and disclaimers below.

This material is based upon work supported by the National Science Foundation Graduate Research Fellowship under Grant No. NSF 11-582.

This material is based on work supported by the Department of Energy National Nuclear Security Administration through the Nuclear Science and Security Consortium under Award Numbers DE-NA0000979 and DE-NA0003180.

This research used the Savio computational cluster resource provided by the Berkeley Research Computing program at the University of California, Berkeley (supported by the UC Berkeley Chancellor, Vice Chancellor for Research, and Chief Information Officer).

A portion of this work was carried out under the auspices of the US Department of Energy at the Lawrence Berkeley National Laboratory 88-Inch cyclotron under contract # DE-AC02-05CH11231.

The views expressed in this article are those of the authors and do not reflect the official policy or position of the United States Air Force, Department of Defense, or the U.S. Government.

Chapter 1

Introduction

Having stiffed Bush – and the world – in building a nuclear arsenal, testing a long-range missile, and testing a nuclear weapon, might Kim now imagine that he could also sell nuclear weapons? America's challenge is to prevent this act by convincing Kim that he will be held accountable for every nuclear weapon that originates in North Korea. This requires clarity, credibility about our capacity to identify the source of a bomb that explodes in one of our cities (however it is delivered by whomever), and a believable threat to respond. Kim must be convinced that American nuclear forensics will be able to identify the molecular fingerprint of nuclear material from his Yongbyon reactor.

- Graham Allison, "Deterring Kim Jong Il"

1.1 Motivation

September 23, 1992 marked the end of U.S. nuclear weapons (NW) testing. However, every U.S. President and Congress has reaffirmed the necessity of the U.S. nuclear arsenal, and President Obama stated in Prague in 2009, "the United States will maintain a safe, secure, and effective arsenal, both to deter potential adversaries and to assure U.S. allies" [53]. Since the Exon-Hatfield-Mitchell nine month test moratorium made Divider the last U.S. NW test in 1992, this goal of maintaining a "safe, secure, and effective arsenal" has been accomplished through the "science-based" Stockpile Stewardship Program (SSP) implemented in 1995 under President Clinton [191].

Under the SSP, annual assessments are made of the health and status of each system in the U.S. arsenal using a combination of "computer simulations, component-level experiments, subcritical experiments involving plutonium and high explosives at the Nevada Test Site, nonnuclear experiments at Livermore's remote Site 300, and analysis of historical data from past nuclear tests" [199]. This has enabled the U.S. to maintain a NW arsenal for 25 years without performing a system level test of the physics package. Tellingly, according to

William Goldstein, Director of Lawrence Livermore National Laboratory, in a statement to the Senate Committee on the Armed Services in April 2014, the SSP has not only enabled us to maintain a NW arsenal, it has enabled "confidence in the nuclear weapons stockpile without nuclear testing" [81].

However, the SSP and associated Advanced Simulation and Computing (ASC) capabilities do not address every area important to the maintenance of a NW arsenal or national security issues posed by NW. The bulk of the U.S.'s 1149 nuclear detonations, used as benchmarks for the ASC and SSP programs, were weapons related (WR) and safety tests. There were also 100 dedicated nuclear effects tests, 7 dedicated seismic sensor development tests, and numerous other tests with non-WR secondary functions such as radio-chemistry and nuclear forensics [205]. For these purposes, the nuclear weapons provided a unique source, both in intensity and scale, that ceased to exist after Divider.

The Department of Defense (DoD) and Department of Energy (DOE) have developed and maintained several facilities that cover a range of NW effects and environments in an attempt to maintain the capability to certify WR components and delivery systems to operate and survive in a nuclear environment, consistent with mission requirements. A list of the key facilities is shown in Table 1.1. However, these facilities and programs are often insufficient, overlooked, or underfunded, resulting in gaps in the ability to assess and certify systems and capabilities [51, 100]. The scope of this problem is highlighted by considering the sheer scope of the problem, as shown schematically for NW effects in Figure 1.1.

One of the more pressing gaps is in the ability to reproduce damage and nuclear reactions from the NW characteristic thermonuclear (TN)[1] and prompt fission neutron spectrum (PFNS)[2] neutrons. Figure 1.2[3] shows the energy differential neutron flux for several of the neutron sources cited in Table 1.1 in comparison with an example TN+PFNS[4]. Several sources match the spectral shape in the keV to a few MeV range well, if lacking in overall intensity. However, none of them have the high energy TN component that are significant in displacement damage and single event upsets (SEU) in electronics, and all have significant low energy components that would dominate nuclear reactions. The Rotating Target Neutron Source (RTNS) in Table 1.1 would address the TN component, but it is currently mothballed [148]. The Sandia Pulsed Reactor (SPR) has the least significant low-energy component and the most a similar time history profile, but it is also inactive, with the White Sands Missile Range (WSMR) Fast Burst Reactor (FBR) likely to follow [52].

Unfortunately, there are not any current promising alternatives. Figure 1.3 shows a brief survey of some other neutron sources that have been considered or used to study radiation effects and nuclear reactions of interest for national security applications. In addition to

[1]Due to D-T fusion.

[2]Due to fission of fissile or fissionable material such as ^{235}U, ^{238}U, or ^{239}Pu.

[3]The TN+PFNS spectra shown is derived using only the fissile mass of Godiva, thereby limiting the thermal component (see Section 2.1 for more details). The SPR-III reactor has a ^{10}B shroud and the WSMR FBR has significant stainless steel structural components that contribute to the much larger thermal component.

[4]See Section 2.1 for more details on the derivation of the TN+PFNS and method.

Nuclear Weapon Environment	Test Facilities	Comments
Prompt and modified neutron	Sandia Pulsed Reactor III (or equivalent)* Annular Core Research Reactor White Sands Missile Range Fast Burst Reactor (also combined gamma) Los Alamos Neutron Science Center, Ion Beam Laboratory, and Rotating Target Neutron Source	For nuclear warhead subsystem space simulations For nuclear warhead components For ground systems, satellites, and interceptors For component tests and model validation
Prompt cold X-rays (plasma radiation source)	Upgraded Saturn and/or Double Eagle National Ignition Facility and/or Z-Refurbished (ZR)	For space system components/optics For future re-entry vehicle/re-entry body (RV/RB) material and interceptors
Prompt warm/hot X-rays (Bremsstrahlung source)	Upgraded Saturn and/or Pithon Modular Bremsstrahlung Source	For medium-dose electronics and cables For hardness surveillance and low-dose boxes
Prompt gamma	High-Energy Radiation Megavolt Electron Source (HERMES) III Pulserad (1150 or 958)	High dose-rates for strategic systems Low dose-rates for satellites and interceptors
Electromagnetic pulse	White Sands Missile Range Horizontally Polarized Dipole (HPD) Facility (2nd generation) Naval Air Warfare Center HPD Facility, Vertically Polarized Bounded Wave	For Army systems For aircraft and missiles
Source region electromagnetic pulse	HERMES III	For Army vehicles and field command, control, and communication systems
Impulse	Light Initiated High Explosive (LIHE) at Sandia National Labs Flyer-plate (magnetic or LIHE)*	For RV/RB internal components/mounts For future RV/RB aeroshells
Blast and shock	Large Blast Thermal Simulator Sandia National Laboratory Thunder Range	For ground vehicles, structures, non-ideal air blast (NIAB) simulations For RV/RB systems
Disturbed atmospheric radio frequency/infrared/ visible	Communication Chanel Scintillation (Wide-band Channel Simulator) Optical background (Nuclear Optical Dynamic Display System)	For military satellite communications, interceptor in-flight communications, and seekers

*Not currently available.

Table 1.1: Nuclear Weapons Effects Simulator Capabilities [100].

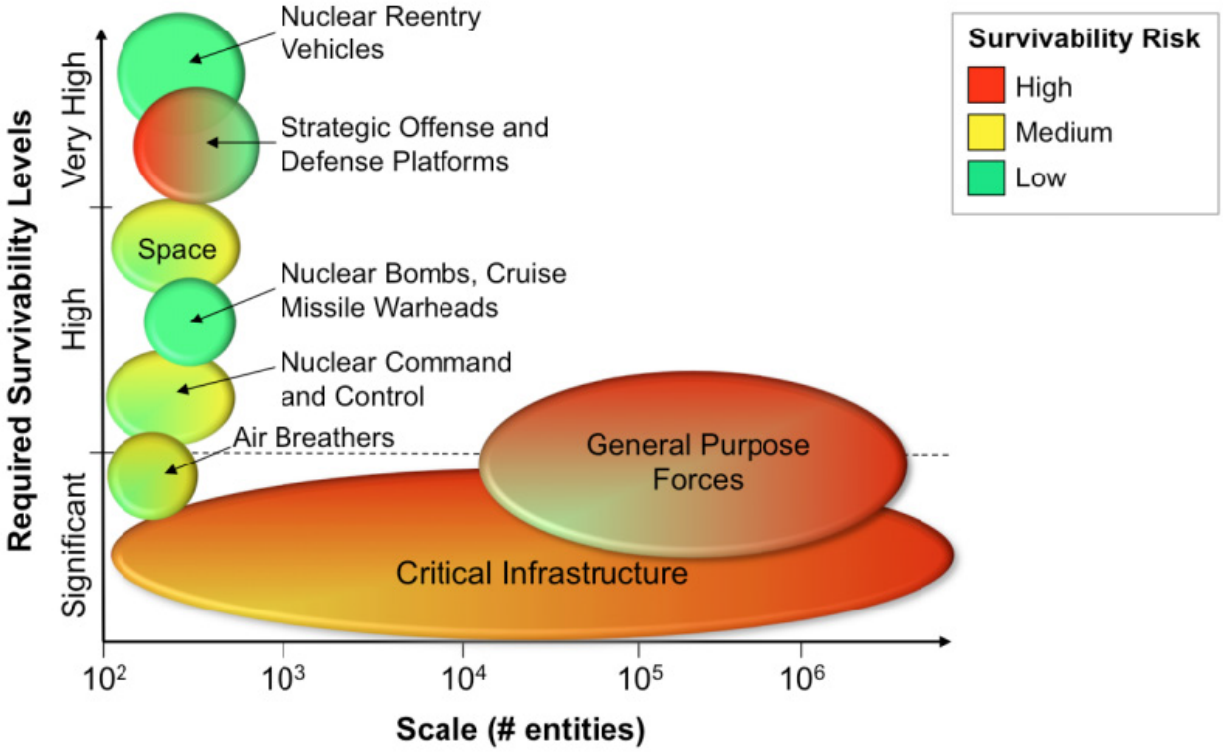

Figure 1.1: Current Survivability Risks of Critical Capabilities Against Nuclear Weapons [100].

poor spectral shape matching, the timing profile and intensity, which are important for annealing in radiation damage and second order reactions in nuclear reactions, is far from representative of a TN+PFNS. The National Ignition Facility (NIF) stands as a lone possible exception, with a significant flux that captures the TN portion of the TN+PFNS, though it lacks the PFNS portion at lower energies.

In light of these shortcomings, the DoD has solicited calls in 2006 and 2012 to develop a "technologically viable alternative to the Fast Burst Reactor (FBR) at White Sands Missile Range...capable of providing the neutron radiation environment required for Nuclear Survivability Testing" [52]. To date, this need has gone unfilled, and most approaches have used surrogate sources such as the Ion Beam Lab (IBL), which require benchmarking against NW or NW-like (FBR) sources. Additionally, the need for realistic synthetic debris and sample databases has been noted by the technical nuclear forensics (TNF) community [1, 101, 197].

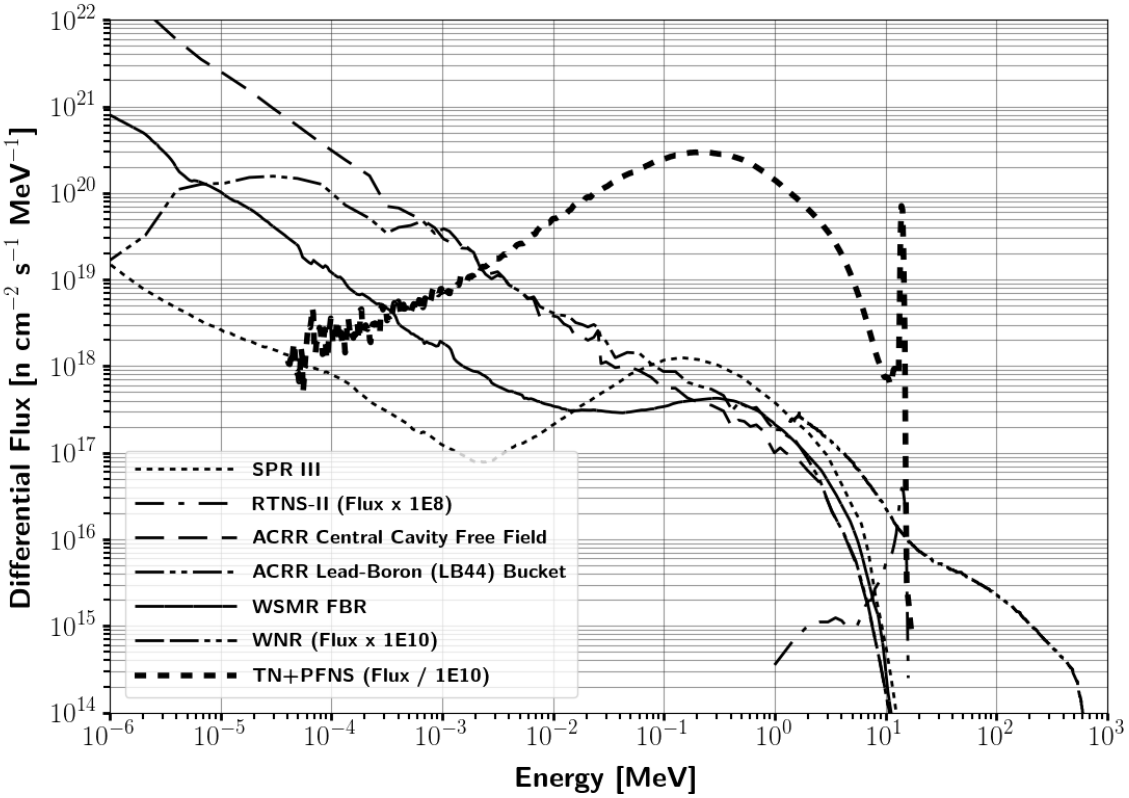

Figure 1.2: Neutron sources used to simulate the prompt NW neutron environment in comparison with a representative TN+PFNS [86, 87, 100, 104, 148, 160, 166, 169, 189, 202, 207, 225, 229]. In the figure, SPR is the Sandia Pulsed Reactor, RTNS is the Rotating Target Neutron Source, ACRR is the Annular Core Research Reactor, WSMR FBR is the White Sands Missile Range Fast Burst Reactor, and WNR is the Weapon Neutron Research Facility.

1.2 National Technical Nuclear Forensics and Synthetic Debris

Section 1.1 highlighted several areas of need where the current existing neutron sources left much to be desired in meeting the needs of the NW community. While each represents a pressing and timely need, this research focuses on methods that can be used to generate synthetic post-detonation debris. However, when considering possible solutions, approaches that are adaptable to needs other than synthetic debris (discussed further in Section 1.5) will be preferred all other things being equal.

According to the Joint Nuclear Forensics Working Group (JNFWG), "Nuclear forensics is the technical means by which nuclear materials, whether intercepted intact or retrieved

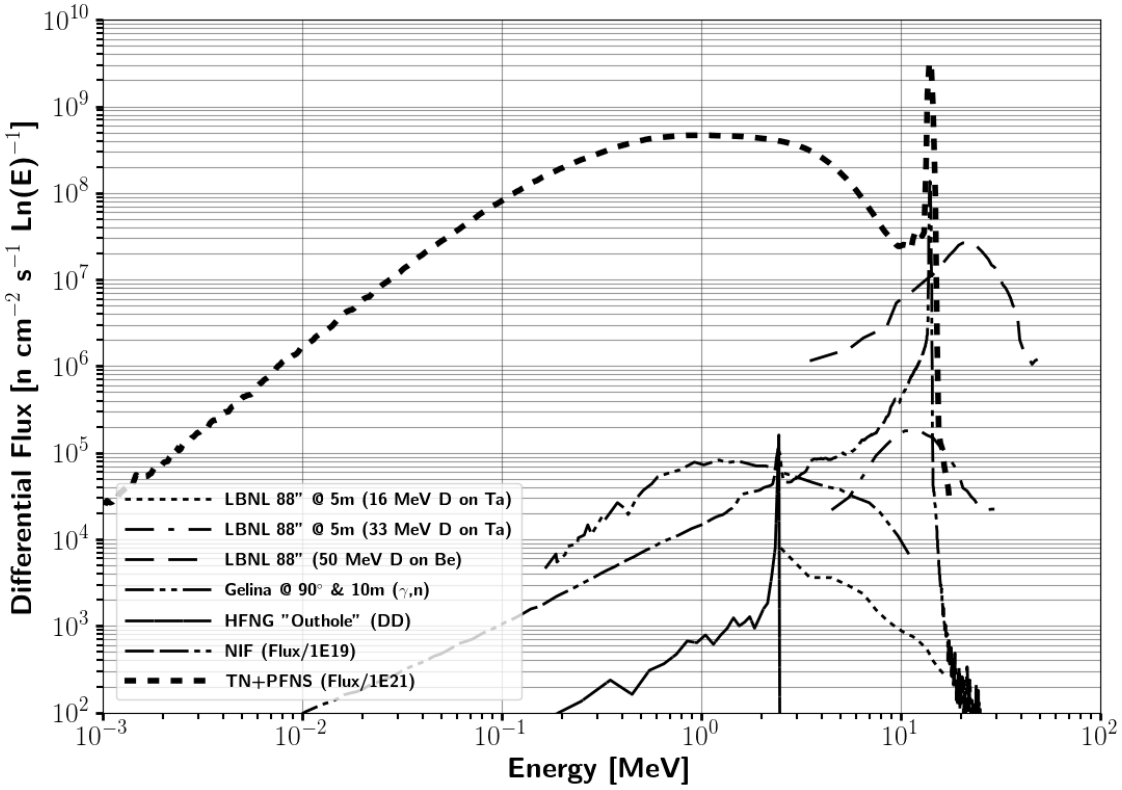

Figure 1.3: Alternative prompt neutron sources for NW environment applications [19, 35, 160, 169, 189].

from post-explosion debris, are characterized (as to composition, physical condition, age, provenance, history) and interpreted (as to provenance, industrial history, and implications for nuclear device design)" [101]. Nuclear forensics is seen as an enabling U.S. capability that enhances deterrence and discourages nuclear and radiological terrorism through attribution capabilities that identify the pathways and sources of material intercepted in either a pre- or post-detonation scenario. Because of this, the National Technical Nuclear Forensics Center states that, "Advancing nuclear forensics capabilities provides a means for governments around the world to work together to counter illicit trafficking in nuclear materials, deter nuclear terrorism, and promote global nuclear security" [159]. Additionally, nuclear forensics would continue to provide a strategic enabling capability through treaty verification and enforcement in any future nuclear-free world.

This research focuses on post-explosion TNF applications, which is far more limited in the availability of new, relevant samples than the pre-detonation community. In fact, JNFWG states that [101]:

> Current post-detonation debris analysis techniques derive largely from the nuclear

> weapons test programs of the Cold War. Leveraging the Cold War infrastructure enabled a baseline forensics capability to be established quickly, but has resulted in a capability that relies largely on science and technology developed in the nuclear-testing era, with timelines and priorities sometimes distinct from those of nuclear forensics. In addition, current analysis methods are often labor-intensive, and rely on education and training that are no longer prominent in the U.S. university system.

Clearly, an approach that can generate synthetic debris in general would be beneficial, while an approach that can generate synthetic debris where current benchmarks do not exist would be revolutionary. This could drive capability improvements in the TNF community, thereby strengthening attribution and deterrence.

It is important to further define synthetic debris in the context of this research. Here, a distinction is drawn between the glassy matrix and the radio-isotopic composition of the sample. The University of Tennessee and others have pursued research into generating synthetic nuclear melt glass that has "physical, chemical, and morphological properties very similar to trinitite[5]" [143, 144]. While the glassy matrix can contain a fingerprint about the temperature and pressure conditions under which it was formed, a preponderance of the matrix is formed from materials surrounding the detonation site that were consumed into the fireball. Conversely, the radio-isotopes contained within the matrix contain a fingerprint associated with the NW's characteristic neutron energy spectrum for materials ranging from the fissile core, to weapon structure, to the medium surrounding the detonation. Each contains forensics information relevant to attribution. According to the JNFWG [101]:

> By analyzing radioactive debris from an explosion and measuring the decay, nuclear forensics can determine the history of the fissile material, including when the plutonium underwent chemical separation and the uranium's radiochemical history. This, in turn, may indicate from where the fissile material came. Analysis of the debris may also identify other, non-fissionable materials used to construct the device, and something about the sophistication of the design, or lack thereof. The particular alloys or compounds used in making a device, or the impurities and contaminants found to be present, may also indicate the source of those materials or the industrial processes used to make them, which in turn may be indicative of the practices or techniques in certain parts of the world.

As much progress has been made in generating synthetic glassy matrices, this research is focusing solely on improving the quality of the radio-isotope distribution that can be obtained. While a completely representative radio-isotope distribution would be ideal, the scope is narrowed to solely reproducing the correct fission product (FP) distribution. This is because the radio-isotopes of interest are dependent on device construction, which is not openly available, and detonation location, which can be highly variable. However, when

[5]The greenish, glassy material left from the first NW test at Trinity, NM in 1945.

evaluating the techniques to generate the synthetic FP distribution, the applicability of the method to the broader synthetic debris question will be considered.

1.3 A Brief Survey of Options to Generate Sythetic FPs

There are four primary approaches that could be considered to generate a synthetic FP distribution:

1. Sample doping
2. Direct production using fission converters
3. Surrogate methods
4. Spectral modification of existing sources

Previous research and implementation of each, along with applicability to the problem of interest, is discussed in the sections below. After consideration of the advantages and limitations of each of the approaches, the option chosen to generate a synthetic FP distribution was the spectral modification method for reasons as discussed in Subsection 1.3.4.

1.3.1 Sample Doping

Sample doping is the fairly straightforward process of selectively building up a fission product distribution and other radionuclide inventory from irradiations at different facilities and/or times to generate a synthetic FP distribution. This is the current state-of-the-art method employed to generate samples for the forensics community. Sample doping is well understood, extremely customizable, and within the existing capabilities of current neutron sources and radio-chemistry labs.

However, sample doping is labor-intensive and tends to lock in Cold-War capabilities and procedures as noted by the JNFWG. Because of the required time to generate a sample, only certain mass chains are typically used, thereby limiting the realism of the sample and the usefulness for training and capability development. Another reason to limit the mass chains to well known ones is that the sample doping process is highly dependent on nuclear data, NW test history, and/or fission product models.

While the U.S. has the benefit of an extensive test history, historical documentation and measurements of interest do not always correspond to measurements of interest today. In many ways, the test history can be made irrelevant as long as a complete set of nuclear data exists to be able to model the FP distribution created under different irradiation conditions. However, as discussed in Section 3.1, FP data, especially the energy dependence aspect, is lacking. Correspondingly, the models, most of which are empirical or at best semi-empirical,

also are limited. The lack of data or suitable models makes it difficult to expand this approach to the entire fission product distribution or create a process whereby more samples can be generated for training and/or capability development.

Although technically a combination of sample doping and the direct production approach that is described next, it is worth mentioning the method being pursued by the University of Tennessee (UT) here. As described in Section 1.2, they have developed glassy surrogate debris matrix samples that are representative of trinitite [144, 197]. Recently, UT added uranyl nitrate hexahydrate to the melt glass sample and irradiated it in the High Flux Isotope Reactor (HFIR) at Oak Ridge [46]. Presumably, they could add highly enriched uranium (HEU) or other activation products of interest in the future as well. However, as the authors readily acknowledge, they have not overcome the issue that HFIR, or any other available neutron source, does not replicate the relevant neutron spectrum, and the resulting fission and activation products reflect this fact [46].

1.3.2 Direct Production

Direct production is the method used in NW testing. A direct production replacement using a fusion-fission source is theoretically attractive as it most closely represents the NW source term. D-T fusion sources with a fissionable conversion layer could be used to meet the requirements outlined in Section 2.1. However, it is very difficult to achieve the appropriate mixture of TN and PFNS neutrons expected in NWs[6] with small amounts of fissile or fissionable converter. Consider the following simple calculation assuming a point source of D-T neutrons[7]: a 1 cm^2 ^{235}U fission converter placed 1 cm from the source, a 10 cm optically thick converter ($t \approx 3$ mfp), and a HEU sample 15.24 cm away from the source:

$$\phi_f^{DT} = \frac{S_i}{4\pi r_1^2} e^{-n\sigma_T t} \tag{1.1}$$

$$\phi_f^{fission} = \frac{S_i}{4\pi(r_2 + 0.5t)^2} \left(1 - e^{-n\sigma_f t}\right) \nu \frac{1}{4\pi(r_1 - (r_2 + 0.5t))^2} e^{n(\sigma_T - \sigma_f)_{2MeV} 0.5t} \tag{1.2}$$

[6]The percentage of the spectrum due to TN varies based on the design of the NW. For this research, it is taken as 15% fusion. See Section 2.1 for how this was derived.

[7]This would be a high end estimate for the output available from the National Ignition Facility (NIF).

where:

$$\begin{aligned}
\phi_f^{DT} &= 1.98\text{x}10^{11} \text{ n cm}^{-2}\text{, fluence due to DT neutrons at sample} \\
\phi_f^{fission} &= 1.44\text{x}10^{10} \text{ n cm}^{-2}\text{, fluence due to fission neutrons at sample} \\
S_i &= 10^{16} \text{ n, initial point source of neutrons} \\
r_1 &= 15.24 \text{ cm, distance from point source to sample} \\
r_2 &= 1 \text{ cm, distance from point source to converter} \\
\sigma_T &= 5.85 \text{ b, total } ^{235}\text{U cross-section at 14.1 MeV} \\
\sigma_f &= 2.1 \text{ b, } ^{235}\text{U fission cross-section at 14.1 MeV} \\
(\sigma_T - \sigma_f)_{2MeV} &= 5.8 \text{ b, } ^{235}\text{U total minus fission cross-section at 2 MeV} \\
n &= 4.87\text{x}10^{22} \text{ atoms cm}^{-3}\text{, } ^{235}\text{U number density} \\
t &= 10 \text{ cm, fission converter thickness} \\
A_{surf} &= 1 \text{ cm}^2\text{, surface area of fission converter} \\
\nu &= 4.5\text{, neutrons produced per fission at 14.1 MeV}
\end{aligned}$$

The result is 93.2% fusion neutrons entering the sample after exiting the converter, which demonstrates the limitations of this approach. It is possible to have thicker converters or to cover larger surface areas, but the fissile or fissionable material mass quickly becomes prohibitive, which also reduces the overall flux available to irradiate the sample. The simple analytic calculation was confirmed with a Monte Carlo Neutral Particle (MCNP)[8] simulation that had $95.7 \pm 0.1\%$ fusion neutrons in the sample. Additionally, these converters are more efficient when using fissile material, and the DoD solicitation specifically calls for alternatives without using special nuclear material (SNM). For these reasons, direct production is impractical for high fission to fusion ratios and cannot fill the NW neutron source term need.

Another approach at direct production is using charged particle and breakup reactions to produce tailored neutron spectra [28, 130, 139, 221]. Due to the ability to tune the incident charged particle energy, these reactions can be designed to produce neutrons that vary from nearly monochromatic to a wide energy range. This is illustrated in Figure 1.3 for charged particle reactions by the HFNG and NIF neutron spectra and for breakup reactions by the three 88-Inch Cyclotron spectra. In addition to the tuning of the incident beam, the spectra can be modified by interchanging the type of beam or target. Finally, methods have been developed to shape the initial beam energy distribution to result in a wider neutron distribution [171].

However, the charged particle and breakup reactions are not suitable as replacement NW sources for several reasons. First, the reaction cross sections tend to be in the millibarn range, resulting in a low neutron flux compared to the desired spectrum[9]. For time-correlated

[8]MNCP version 6.1 was used with ENDF/B-VII.1 data libraries throughout this research effort.

[9]See Figure 1.3, where NIF stands out as the notable exception.

nuclear effects or reaction histories, the low flux can produce an end result that is not closely correlated with the expected result from a prompt, high flux source. Second, the energy range spanned by any given reaction is insufficient to cover the spectral range of the TN+PFNS. This necessitates multiple reactions be combined, resulting in the need for multiple beams and/or generators, an experimentally difficult and expensive proposition. Finally, any attempt to reproduce the TN+PFNS spectral shape solely with charged particle or breakup reactions is unlikely to succeed without modification of the incident charged particle or resulting neutron energy spectrum using methods described in Subsection 1.3.4 or Praena [171]. Although either direct production method is theoretically feasible, both are impractical, complex, and unlikely to be implemented for safety or technological limitations.

1.3.3 Surrogate Methods

An alternative method is to target reproducing the end state in the material using surrogate methods instead of reproducing the starting neutron spectrum via direct production. This approach has been successful in both radiation effects and nuclear physics to compensate for a lack of intensity and sources in important regions. For example, surrogate reactions in nuclear physics leverage the compound nucleus to study reactions that are otherwise inaccessible due to difficulty in producing the necessary isotopes, small cross-sections requiring a higher flux than may be practical, or radiation dose hazards due to short half-lives, among others [67, 102, 170]. However, the surrogate reaction method requires well known reference cross-sections to be able to infer the cross-section of interest [67, 170]. Additionally, surrogate reactions only approximate the reaction of interest, and details such as the spin-parity mismatch can lower the accuracy of the results obtained [67, 102].

Research at LLNL has explored the use of surrogate reactions to produce synthetic fission products using the Center for Accelerator Mass Spectrometry (CAMS). LLNL used 25.6 MeV α particles via the ^{232}Th(α, n)^{236}U reaction as a surrogate for ^{235}U fission from 14 MeV neutrons. Initial results have shown a strong correlation between the surrogate and 14 MeV neutron produced fission product distributions [74]. Assuming that there is similar overlap in the angular momentum distributions at other excitation energies, this is a promising area of further research as a viable alternative to produce realistic synthetic debris.

To consider the limitations of the charged particle surrogate approach if pursued in its fullest extent, it is worth considering their use in the radiation effects area. The Qualification Alternatives to the Sandia Pulsed Reactor (QASPR) program was started in 2005 due to the impending closure of SPR[10], a FBR that was a close approximation of spectral and temporal characteristics of the NW fission source term [182, 225]. The QASPR program aims to replace the SPR capability by using "available irradiation facilities combined with new, science-based modeling to predict time-dependent device and circuit performance under inaccessible conditions" [154].

[10]SPR-III was closed in September 2006 due to security concerns over the 258 kg of HEU it contained in its 18 fuel plates [186].

As part of the QASPR program, the IBL uses ions to simulate the late-time neutron-induced defect population to inform physics based modeling [86]. The key requirement is that the defect population resulting from a NW exposure is well understood, using techniques like deep-level transient spectroscopy (DLTS), thereby enabling defect reproduction using the surrogate ions at IBL. However, there is no current representative NW source term to generate the benchmark data for IBL, which was built in 2010. Instead, the ion-to-neutron damage equivalence for IBL is established using ACRR irradiations, which itself was benchmarked against SPR-III, which traces its pedigree to NW testing [86, 180]. Despite ten years of effort, to date QASPR simulations only "enabled a 'ranking' of the circuits in terms of vulnerability" [180]. This ranking, when compared to previous test history and experience, combined with a significant margin, provides the basis for our certification of components to survive in a NW neutron environment.

The QASPR approach is proof that the surrogate method is feasible and can be used to access previously "inaccessible conditions." However, each new device technology or material requires new benchmark data as well as significant effort to develop the device response models and establish the trace to NWs, a trace that gets more tenuous as the sources and device technology progresses further from those used in or shortly after the era of NW testing.

Table 1.1 is also useful to understand the benefits and shortcomings of this approach. While nuclear reentry vehicles, nuclear bombs, and cruise missile warheads have some of the highest requirements for survivability, they are also the least at risk thanks to programs like QASPR. However, these systems are among the smallest in scale for systems requiring capabilities against NW, and the level of effort and funding required for QASPR and similar programs is too high to allow for this effort to be extended directly to many other components in the NW Enterprise or critical infrastructure.

These same limitations were also present when looking at the surrogate method as applied by the nuclear physics and astrophysics communities. In general, surrogate methods are limited by the inability to replicate small order effects and the need for a priori knowledge. Additionally, each particular measurement of interest requires a full development effort to validate. Given the alternative in many cases, these limitations are acceptable, and surrogate methods could meet most of the needs for NW related nuclear effects and nuclear reaction based requirements. Nevertheless, a more affordable, adaptable method with closer ties to the NW source term, thereby reducing the need for a priori knowledge, is a more desirable approach.

1.3.4 Spectral Methods

Following the discovery of the neutron by James Chadwick in 1932, research into measuring the resulting (α,n) spectrum started the same year [22, 36]. Very early on, it was deemed desirable to modify neutron spectra, and hydrogen thermalization and cadmium filters were employed by 1935 to modify or remove portions of neutron spectra [37, 58]. Over 80 years later, neutron spectral modification techniques have advanced, but the same basic concepts are largely the state-of-the-art today. The history of spectral shaping, along with some

current, relevant examples are explored in detail in Chapter 4. However, it is worthwhile to note some key characteristics that make spectral shaping a desirable approach to realistic synthetic FP generation here, while leaving the background and examples to later.

Spectral shaping methods meet many of the high level design objectives described in Chapter 2 and the DoD solicitation in that they are inexpensive, flexible[11], and do not need to utilize SNM. Unlike surrogate approaches, a spectrally-shaped neutron beam could have many applications in the forensics, nuclear weapon effects, and stockpile stewardship communities. Spectral shaping also avoids the need for a priori knowledge, and all of the physics of interest are replicated to the extent that the spectral shape matches the objective spectrum. Ostensibly, surrogate debris materials, even the glassy matrix, could be irradiated, producing realistic synthetic fission *and* activation products.

There are some drawbacks to the spectral shaping approach. Like all of the previous methods, it is limited in the flux that is achievable, but spectral shaping does allow the leveraging of the most intense experimental neutron sources. Additionally, physics will impose limitations on what spectra are achievable, especially when considering practical engineering constraints on the design. However, the same is true for any of the three other methods discussed. In total, the spectral shaping's benefits, combined with the potential to reach a broader set of applications (see Section 1.5), outweigh the drawbacks. For these reasons, this research will pursue the spectral modification method.

1.4 Research Objective

The research objective is to develop a methodology to generate synthetic FPs for post-detonation nuclear forensic application. Specifically, the creation of synthetic FPs will be accomplished through spectral modification techniques that will generate a forensics relevant neutron energy spectrum from the NIF source. The end deliverables will be a novel spectral modification capability, a fabricated design, and an outlined test plan to prove the concept. The research objective, as phrased, is broad in scope, and it is worthwhile to explicitly narrow the scope of the problem and define the limitations associated with this research.

1.4.1 Scope and Limitations

The first major limitation is classification issues surrounding NWs. To avoid any potential issues, this research only uses NW data and information available in the U.S. Government open literature and uses surrogates or simplistic approximations for any NW related information. The research objective is to obtain an approximate solution that represents the desired end state, thereby enhancing the probability of success with minor tweaks when using real data. To this purpose, the more stressing conditions were chosen where they could

[11]This is evidenced by the wide range of sources that beam shaping assembly (BSA) designs have been developed to meet similar boron neutron capture therapy (BNCT) criteria, which is described further in Chapter 4.

be identified[12]. This limitation primarily affected the FP distribution data, TN+PFNS, and the range of variation for the TN+PFNS. Each of these is described in further detail below.

Several possible national security applications were covered in Section 1.1 and Section 1.2. This research will focus on the nuclear reaction applications, specifically the generation of FP distribution representative of exposure to a TN+PFNS. This approach was chosen because generation of the correct FP distribution is sensitive to the correct incident neutron energy across the entire spectrum, as described in Section 3.1, thereby allowing a point solution and validation of the correct spectrum[13]. These features make the FP distribution one of the most difficult national security applications, in keeping with the stated objective of pursing the most stressing conditions for the research.

Using the FP distribution as the target application is not without difficulties. The primary issue is that there are no FP data openly available for a TN+PFNS. This data would exist for the U.S. NW test program, but it is not available for this research. Instead, models, benchmarked to data where it does exist, are used to derive the expected FP distribution given the incident TN+PFNS neutron energy spectrum. The details of this derivation are described in Subsection 3.1.3.

A key component to this research is defining a suitable TN+PFNS. However, this information is not available in the open literature, and a strict derivation would run into classification issues. For these reasons, a simplified approach was taken, using critical assemblies as surrogate geometries to construct a MCNP model to determine a representative neutron spectrum. All associated weapon physics that would have temporal, spatial, or physical effects were ignored. Additionally, although bare and reflected ^{239}Pu and ^{235}U systems were explored, only a bare ^{235}U system, Godiva, was carried forward. The complete details, including several approximations and neglected attributes, are described further in Chapter 2. While this representative spectrum is likely not correct in many respects, the hope is that it will contain key features and approximate relative intensities that will result in a methodology that is adaptable to the actual neutron spectra of interest.

It is important to clarify what the range of interest in TN+PFNS entails. There are three broad classes of nuclear weapons: fission based, boosted, and TN [54]. Fission weapons only contain PFNS. Although a need exists for a prompt PFNS source, it is also the area that surrogate methods and alternative sources are most developed[14]. Boosted and TN weapons contain both the PFNS and TN portions of the spectrum, but TN weapons are multi-stage devices for which a critical assembly is a poor approximation. For the purposes of this research, a TN+PFNS representative of a boosted NW was chosen as the objective.

Within each broad major classification, there is a large variation in design that can result

[12]These choices are described in this section and Chapter 2, but two main examples are the use of bare critical assemblies and the FP distribution application.

[13]For all practical purposes, this statement is true. While surrogate spectra can be used to produce FP distributions within measurement uncertainty, these spectra are significantly different than the target spectra and unlikely to be obtained accidentally. The details of the FP sensitivity with respect to incident neutron energy are described in Section 3.1

[14]See Section 1.1 and Section 1.3

in different neutron spectra. For example, fission weapons can be broken down into two subcategories: implosion and gun-type. Each has different geometry, materials, and masses used that will affect the neutron spectrum. For the purposes of this research, only a point approximation is used. No attempt is made to quantify the range of neutron spectra that could result from this class, or any other class, of weapon.

The design optimization uses NIF as the ideal source of neutrons. However, fielding at NIF was unfeasible for this research. Instead, the spectral shaping capability was designed to the NIF source but tested at the Lawrence Berkeley National Laboratory (LBNL) 88-Inch Cyclotron. Testing at the 88-Inch will not result in producing a TN+PFNS relevant spectrum or a realistic synthetic FP distribution, but it will enable validation of the model and process using NIF relevant materials and designs.

The use of the 88-Inch Cyclotron and its associated facilities does complicate making the FP measurements of interest. First, the total fluence delivered at the 88-Inch Cyclotron is a factor of $\sim$50 less than the minimal NIF fluence considered in the experiment design. The lower flux, combined with the lack of radio-chemistry analysis capability, will make the measurement of valley and wing FPs extremely difficult. However, the 88-Inch Cyclotron adds flexibility in the use of multiple detectors and experimental set-ups as described in Chapter 8.

Finally, any design developed will be a point design subject to all of the nuances described in this section. In other words, the research demonstrates a proof of concept, not an all-encompassing solution. However, the methodology to generate spectral shaping designs is developed to be broadly applicable to generating new designs for TNF–or other national security–applications. This was a key consideration in developing and scoping the solution methodology.

1.4.2 Solution Methodology

Figure 1.4 shows a schematic overview of the solution methodology taken for this research. The figure shows three pathways. The first path, shown in black, is the modeling and optimization path that originates with the NW and culminates in the design of the Energy Tuning Assembly (ETA or η). The second path, shown in green, is the piece-wise experimental validation path that starts with the LBNL 88-Inch Cyclotron and finishes with pulse height spectrum (PHS) and FP measurements. The final path, shown in blue, is the integral test and generation of a realistic synthetic FP distribution at NIF. This section will provide a logical overview of each path.

The modeling and optimization path starts with defining a suitable NW neutron spectrum. Since this information is not available in the open literature, critical assemblies were used as a surrogate to construct a relevant TN+PFNS spectrum using MCNP[15]. The resulting TN+PFNS spectrum is used as the objective function, and the NIF source spectrum

[15]The complete derivation is described further in Chapter 2.

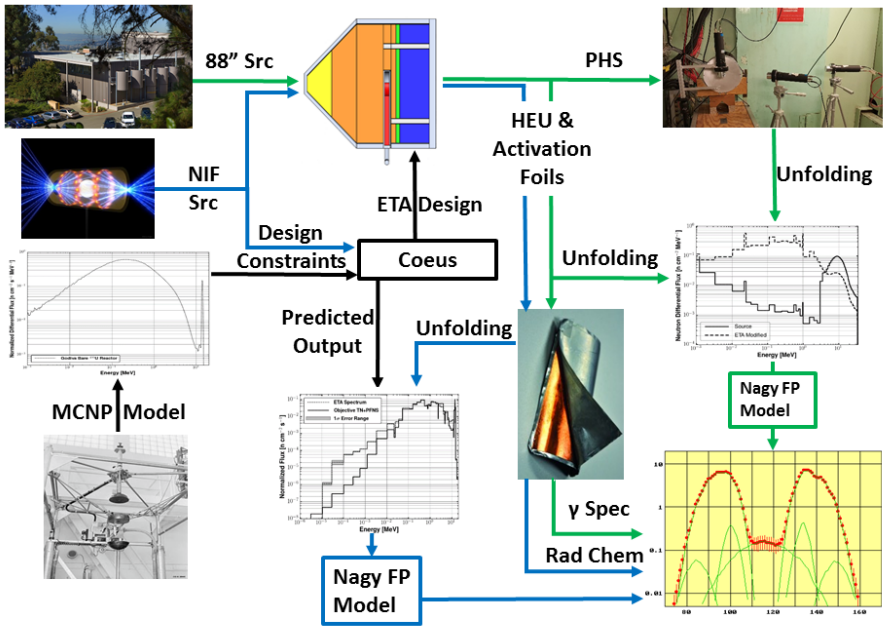

Figure 1.4: Schematic overview of the proposed solution approach. Black lines indicate the modeling and ETA design path, green lines represent the 88-Inch Cyclotron piece-wise, application-specific validation path, and the blue lines represent the integral NIF validation path.

and facility limitations are used as design constraints for the ETA design. The ETA design is generated with the Coeus optimization code developed for this research[16].

Due to difficulty of testing at NIF[17], the 88-Inch Cyclotron was chosen as the primary experimental facility for this research for initial validation efforts and method development[18]. Given the Coeus-generated ETA design, MCNP was used to predict the output spectrum expected when the ETA is exposed to the 88-Inch Cyclotron source spectrum instead of NIF. PHS and foil activation measurements were made in a variety of ETA configurations. These measurements were unfolded to provide complementary spectrum measurements that can be compared to the modeled spectral shaping predictions. The partial stack-ups of the ETA can be used as integral tests to understand how the nuclear data affects the ability to model ETA performance. Finally, irradiated ^{235}U foils will serve as a secondary diagnostic to measure the integral neutron spectrum.

The 88-Inch Cyclotron validation serves as the basis for future experiments at NIF to

[16]Coues, the Gnowee optimization engine, and the final ETA optimization are described fully in Chapter 6.

[17]The NIF proposal, vetting, and scheduling cycle to get a dedicated shot is long compared with the typical time of a dissertation if starting from scratch as is the case for this research.

[18]See Chapter 8 for the full experimental procedures.

produce representative TN+PFNS spectra for national security applications. At NIF, only the full ETA assembly is tested[19]. Additionally, only fission and activation foils are fielded as diagnostics. However, NIF enables the generation of synthetic FPs in quantities sufficient to be measured with radio-chemistry. The FPs themselves can be used as a measure of performance, and the fission and activation products can be used to unfold the ETA generated neutron spectrum.

1.5 Broader Applications

This chapter has focused on national security applications with an emphasis on TNF and realistic synthetic fission products in particular. Improvements in realistic synthetic fission products would enable advancement of forensic capabilities from the current baseline capability established from Cold War era science and tests to a more modern, adaptive capability with timelines appropriate for nuclear forensics. Additionally, better production methods for synthetic debris would move away from the current labor-intensive approaches and help bolster research and capability development to supplement the education and training that has lost prominence in the U.S. university system [101]. These capabilities enhance the ability of the U.S. to attribute the source of a nuclear weapon design and components, thereby strengthening deterrence and non-proliferation.

However, a secondary goal of this research is to look at solution methods that go beyond point designs and can be applicable to a range of applications. This secondary goal is also useful to the TNF and national security communities as the neutron spectra of interest changes based on weapon type and employment scenario thereby limiting the utility of any particular point design. This secondary goal also makes this research useful to many other problems in nuclear engineering, and it is worthwhile to acknowledge the broader potential before delving into the specific research thread pursued in this dissertation.

As will be described in much more detail in Chapter 5 and Chapter 6, the use of formal optimization techniques to generate the ETA design enables a framework under which future designs can be generated. Since the process uses metaheuristic optimization techniques, future ETA designs can differ significantly from the concepts developed for NIF in Section 6.3. Additionally, the metaheuristic optimization approach allows for a full design space to be considered, thereby allowing for non-intuitive designs that would be missed by common point design approaches.

More importantly, nothing about the radiation transport methods employed or the Gnowee optimization algorithm is specific to ETA design. While optimization performance gains might have resulted from the tailoring of the algorithms to ETA design, the exclusion of problem-specific information allows for any nuclear engineering optimization problem to be considered. The only real limitation is the compute resources required, which can be limiting for some large scale design problems if not properly scoped. In other words, while the bulk of this dissertation is devoted to the TNF synthetic FP application, the core of the research

[19] See Chapter 9 for the full experimental procedures.

has potential impacts for medical physics, nuclear data, radiation shielding, medical isotope production, detector network and mask configuration, and nuclear reactor designs, to name a few applications.

1.6 Innovations

This research advances the state-of-the-art on many different, disparate fronts, which are explicitly identified here. While perhaps not an all encompassing list, the key aspects of this research are

1. **Improve the ability to generate synthetic fission and activation products:** The primary stated goal of this research represents a dramatic improvement over the current sample doping techniques with respect to the ability to generate a full, realistic, synthetic FP distribution.

2. **Advance the field of neutron spectral shaping:** The ETA design represents a step forward in neutron spectral shaping design from previous experience with neutron filters, screens, and BSAs, as described in Chapter 4.

3. **Develop novel optimization algorithms:** The Gnowee algorithm developed is a robust, capable metaheuristic algorithm that has been shown to outperform existing metaheuristic algorithms across a range of objective functions and input variable types, as shown in Section 6.1.

4. **Demonstrate a nuclear engineering optimization framework:** Coeus is demonstrated to be a powerful ETA optimization tool in Section 6.2, and ongoing development is improving the generality and applicability to other nuclear engineering design problems. Coeus represents a significant improvement over existing nuclear optimization codes, as described in Chapter 5 and Section 6.2.

5. **Development of a spectral shaping test methodology:** The techniques used in Chapter 8 and Chapter 9 are not novel in and of themselves, but the full design of experiment, development of the techniques, and application to spectral shaping and integral nuclear data benchmarks are more thorough and nuanced than any previous spectral shaping concept experimental validation.

Each of these innovations will be expounded upon in great detail throughout the course of this dissertation. This starts with Chapter 2, explicitly defining the problem constraints and objectives to delineate the available ETA design space. Chapter 3 builds the foundation for the physics-based constraints and considerations for neutron energy modifying reactions and the current state of FP data and models. Chapter 4 then explores the previous spectral shaping literature and approaches to establish the current state-of-the-art and its associated limitations. Chapter 5 proposes a different approach to spectral shaping, the implementation

of which is described in Chapter 6. Chapter 7 outlines the experimental procedures to be used during the 88-Inch Cyclotron and NIF validation efforts, which are described in Chapter 8 and Chapter 9, respectively. The dissertation closes with a summary of the accomplishments of the research in Chapter 10 and an outline of future work required in Appendix A. Finally, an overview of the code and data locations are made available in accordance with reproducible science principles in Appendix B.

Chapter 2

Problem Definition

A problem defined, is a problem half solved.

- Albert Einstein

Development of an ETA design to create a TNF relevant synthetic fission product distribution begins with clearly defining the problem and desired objectives in quantifiable terms. This chapter starts with a derivation of the objective TN+PFNS spectrum. Next, key attributes of the NIF and 88-Inch Cyclotron sources are defined. This is followed by a discussion of experimental considerations and the constraints imposed on the solution by NIF. Finally, the chapter closes with a discussion of the design space considered within the bounds of the defined constraints and objectives.

2.1 PFNS+TN Target Spectrum Derivation

While there is an established need for a TN+PFNS source, precisely quantifying that need is difficult as most NW spectra are not openly published. Figure 2.1 shows the four commonly referenced, openly published fission weapon neutron spectra from Hiroshima, Nagasaki, Glasstone, and the Defense Nuclear Agency (DNA) [11, 77, 172]. In addition, Figure 2.2 shows the two published TN neutron spectra from Glasstone and DNA [11, 77]. All of these spectra are transmission, sometimes called leakage, spectra, where the neutron spectrum is taken at some point exterior to the bomb casing, resulting in varying thermalization of the neutrons.

For NW effects, this is appropriate, but the design and scenario details can result in different spectra depending on the application and scenario. For example, consider the different neutronics properties and areal densities of a 10,000 lb Fat Man versus a couple hundred pound modern inter-continental ballistic missile (ICBM) warhead. For studies looking at the nuclear reactions inside of the warhead for forensics, performance, secondary NW effects, or other purposes, the neutron spectrum can be significantly less thermalized than the open source transmission spectra shown in Figure 2.1 and Figure 2.2. Additionally, these

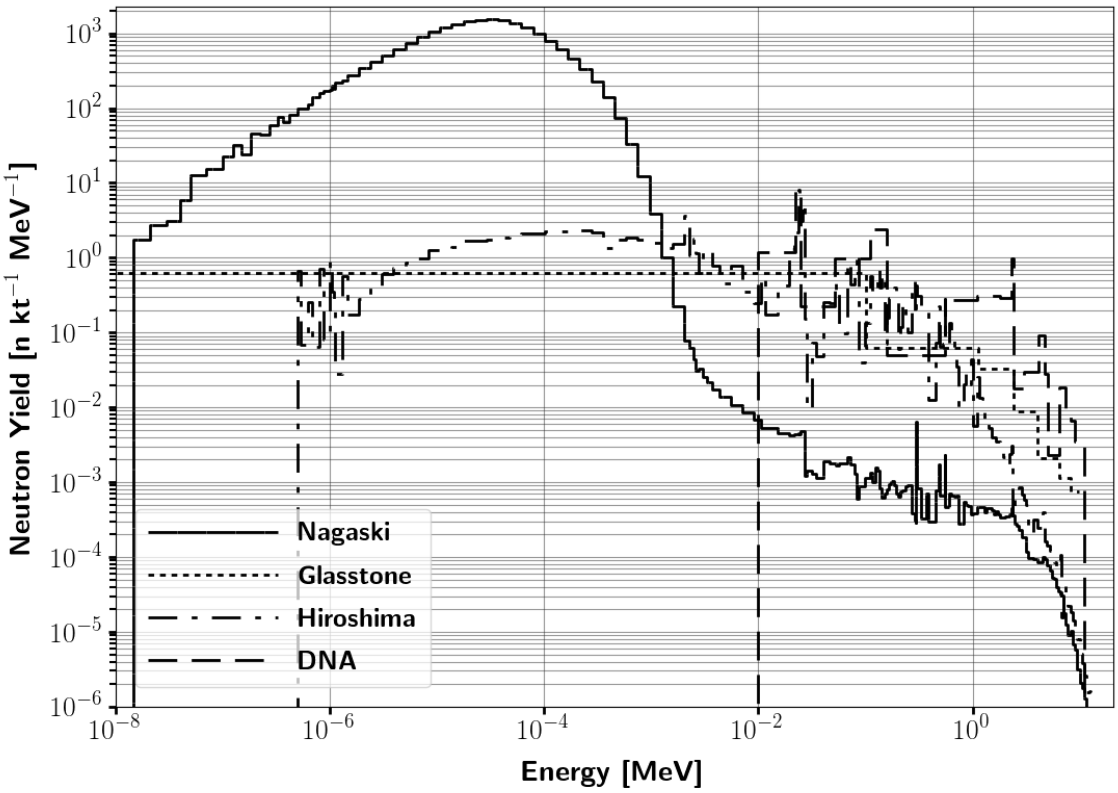

Figure 2.1: Open source fission based NW neutron spectra [11, 77, 172].

open source neutron spectra tend to have few energy groups, with the notable exception of Hiroshima and Nagasaki, which can miss important spectral information.

To avoid these issues, this research derived a simplistic approximation of the TN+PFNS from first principles. There were three primary factors affecting this derivation:

- Determine the class of NW.
- Quantify a zeroth-order spectrum.
- Correlate the FP results from an optically thin to an optically-thick geometry.

2.1.1 Determining NW Class

The first goal was to determine which class of NW to design to. NWs can be broadly classified into fission, boosted, or multi-stage TN devices, and the anticipated neutron spectra would vary significantly from one class to another [54]. Fission based devices are either implosion or "gun-type", and generate their yield purely from fissioning of fissile material [54, 189]. All neutrons are born with the PFNS. Boosted devices use the D-T fusion reaction to increase

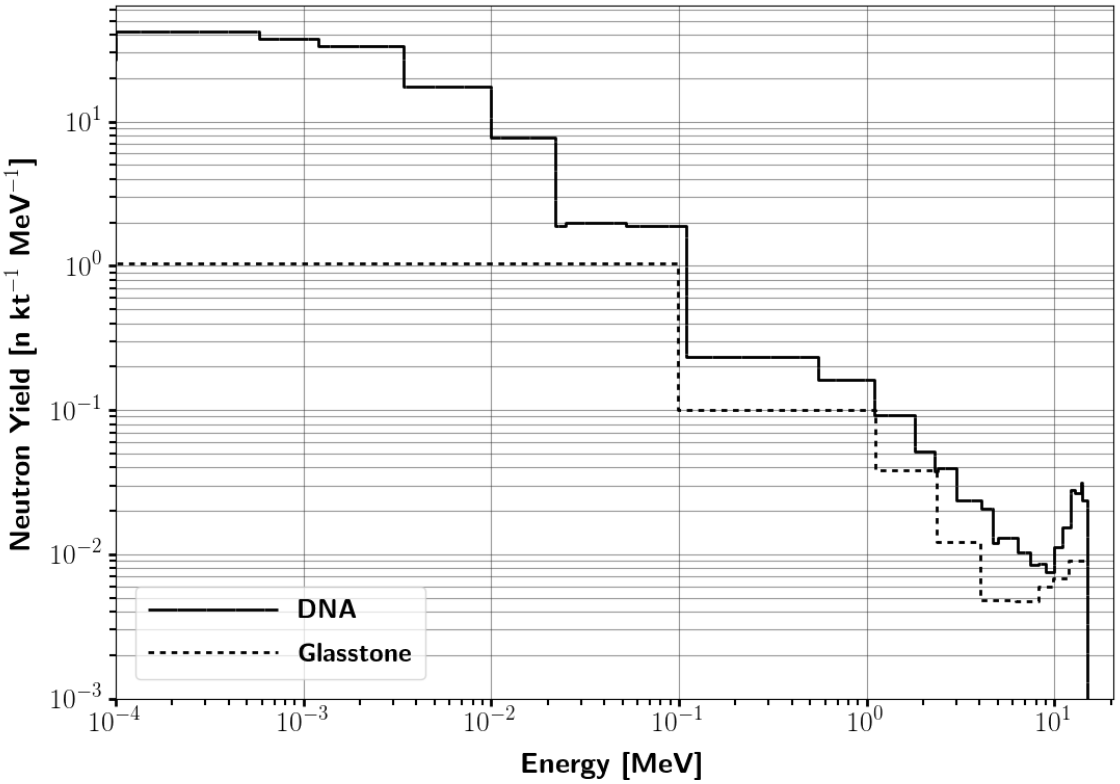

Figure 2.2: Open source TN based NW neutron spectra [11, 77].

the overall yield [54]. Consequently, neutrons are born with the prompt fission, 14.1 MeV D-T fusion, and, to a much lesser extent, 2.45 MeV D-D fusion distributions. Multi-stage TN devices have multiple fission and/or fusion stages, and the neutron birth energies will be comprised of the prompt fission, D-T, and/or D-D fusion distributions.

For the purposes of this research, the purely fission based class was eliminated. First, the use of NIF as the starting source makes this class difficult as it is impossible within practical constraints to fully eliminate the 14.1 MeV neutrons from the spectrum. Second, while a prompt PFNS source is needed, as per the DoD solicitation noted in Chapter 1, it is also the area for which surrogate methods and sources are the most developed [52]. Finally, fission based spectra are not the most challenging distribution to produce[1].

Multi-stage TN weapons were eliminated for the purpose of this research as there is inadequate published information available to determine a suitable method for ascertaining an appropriate spectrum to use. This left the boosted class as the basis for this research. However, purely knowing the birth spectra is insufficient for determining the proper TN+PFNS

[1]This is most easily accomplished by fast burst reactors, but could be done with fast reactors or, albeit at a much lower flux, with fissionable or fissile converters at the end of a thermal column of a research reactor.

to use. To develop a better approximation, a zeroth order surrogate was used to approximate the neutron transport characteristics.

2.1.2 Zeroth-order Neutron Spectrum Development

In developing the TN+PFNS, there are several questions that need to be answered:

- What is the appropriate fission and fusion mixture?
- How should the starting source terms be modeled?
- How do you model the impact of material interactions on the observed spectrum?
- What combinations of materials should be pursued as the transport matrix?

Question one does not have an easy, direct answer as it theoretically should vary by the design and class of the device of interest. Additionally, no device information accompanied the spectra shown in Figure 2.2 [11, 77]. Therefore, only a rough approximation can be used. It is possible to glean insight from the open-source TN spectra by integrating the fission and fusion components. As an approximation, the spectrum can be divided into fission from 0 - 5 MeV and fusion from 5 - 20 MeV. While this method is not exact, ignoring the down-scattered fusion contributions at lower energies and the tail of the PFNS at higher energies, it is a useful approximation and provides sufficient detail for this research. Integration of the DNA spectrum in Figure 2.2 from 5 - 20 MeV yields 15% fusion and 85% fission. These fusion and fission fractions are the ones carried forward in this research.

Knowing the appropriate starting source term fraction for each component is a useful starting place for a radiation transport model, but it is worthwhile to elaborate on how each of those source terms are implemented. The PFNS is generally described as the Watt, Maxwellian, or Madland-Nix spectrum [9, 200, 209]. The Watt spectrum's probability distribution as a function of energy is

$$p(E) = Ce^{-\frac{E}{a}} \sinh(\sqrt{bE}) \, . \tag{2.1}$$

In general, this is the dominant representation used in the evaluated nuclear data library (ENDL). This spectrum reproduces the experimental data more accurately for ^{235}U as demonstrated in Figure 2.3[2] [9, 94, 209]. In Equation 2.1, a, b, and C are normalization parameters that depend on the fissioning isotope and incident neutron energy. In this problem, there is not a single incident neutron energy, but a range of neutron energies spanning from weapon thermal to ∼14 MeV. Using the DNA spectrum from Figure 2.2, the average neutron energy is 1.7 MeV. Since the Watt distribution only varies weakly with energy, the MCNP built-in parameters for a Watt spectrum for a 1 MeV incident neutron were used for this research. Additionally, all spatial and temporal variations were ignored, and the fission source term was treated as a uniform volumetric source.

[2]The results are mixed for ^{239}Pu, with different models performing better in different energy regimes.

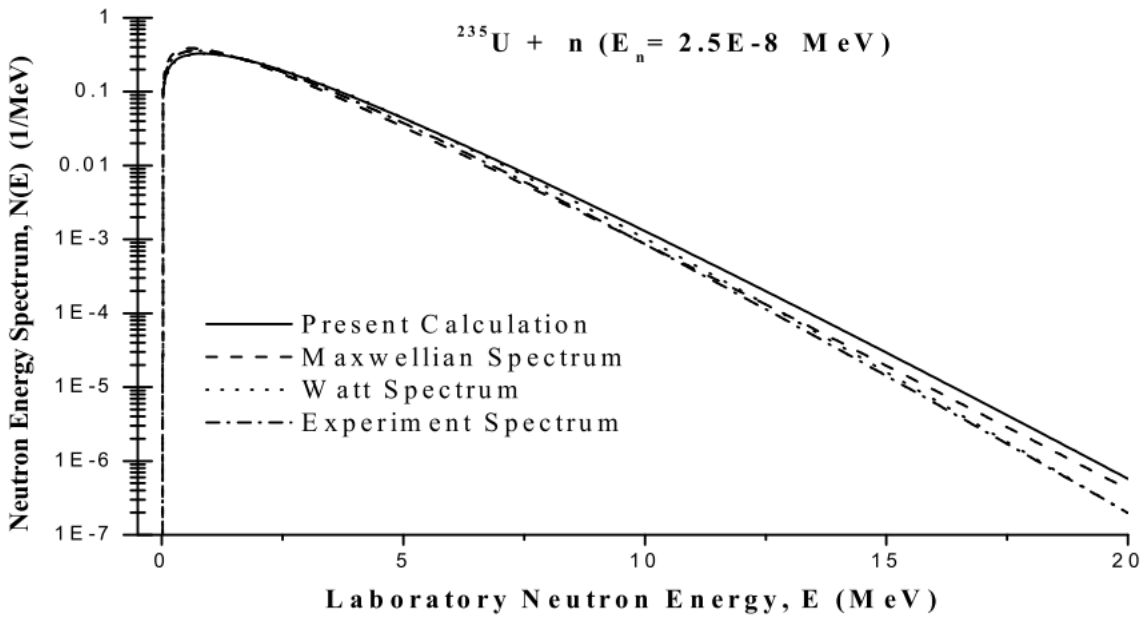

Figure 2.3: Comparison a different neutron energy distribution models for thermal neutron fission of ^{235}U; present calculation refers to the Madland-Nix model [9].

The fusion source term probability distirubtion as a function of energy is modeled as a Gaussian spectrum according to [200]

$$p(E) = Ce^{(-(\frac{E-b}{a})^2)} . \tag{2.2}$$

In Equation 2.2, a is the width of the distribution, and b is the average energy of the reaction. In general, these can be determined by the temperature at which the fusion reaction is taking place, but there is no suitable way to determine that parameter for this problem. As such, for this research, the fusion source term is assumed to be a D-T point source at 10 keV, the MCNP default parameter [200].

With the source fully outlined, the next step is to define the appropriate geometry on which to transport the TN and Watt birth spectra. This choice is important because the choice of material will impact the resulting objective neutron spectrum[3]. Neglecting the effect of neutron interactions completely will result in an arbitrarily artificial objective spectrum, but the inclusion of too much will result in a much softer spectrum than is likely to be of interest to TNF applications. Once again, openly published literature does not have many answers in terms of NW device designs that can be modeled here. However, all NWs will have to assemble at least one critical mass worth of fissile material to function. While there

[3]Elastic scattering, inelastic scattering, (n,xn), and (n,x) reactions will moderate the spectrum, changing and softening the initial birth distribution.

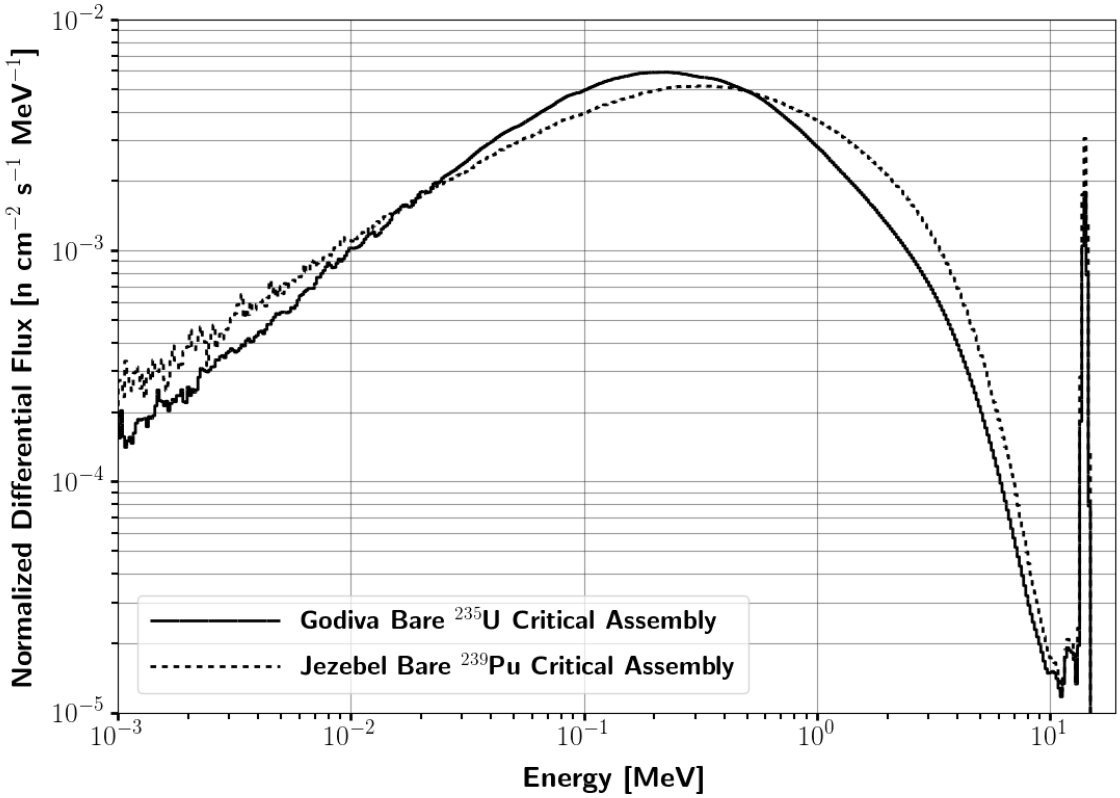

Figure 2.4: Comparison of the TN+PFNS obtained with the Godiva and Jezebel bare critical assembly geometries.

can be significant differences between the one critical mass assembled via implosion[4] and one critical mass assembled for a criticality experiment, there will be similar neutronics properties, allowing for a zeroth-order approximation of the spectrum.

Many experiments have been performed on bare and reflected critical assemblies of multiple isotopes [160, 168, 169, 183]. Jezebel and Godiva are bare metal spherical critical assembly benchmarks made of plutonium and highly enriched uranium (HEU), respectively [160]. Jezebel and Godiva were modeled with the D-T and fission source terms, and two possible TN+PFNS were determined as shown in Figure 2.4. Between the two, the Godiva-based TN+PFNS is softer due to the much larger mass of the critical assembly. This observed result is corroborated by the comparisons of the reported ^{238}U/^{235}U fission ratios for Jezebel and Godiva [160]. While the harder spectrum is the more difficult design target, HEU is chosen as the fissile material due to the difficulty of performing plutonium experiments at NIF.

In addition to bare critical assemblies, extensive work has been done to determine critical

[4]Implosion of the fissile material will result in spatial and temporal varations of the temperature, density, and source term. None of these variations are considered.

Table 2.1: Be and natural U reflected critical assembly dimensions [169].

Reflector	Thickness [cm]	Density [g cm^{-3}]	HEU mass [kg]	HEU Density [g cm^{-3}]
Be	5.1	1.84	20.8	17.6
Nat U	18.0	18.62	16.63	18.62

configurations for reflected, bare and hydrogen-moderated HEU, ^{233}U, and ^{239}Pu systems. Results for varying thickness of H_2O, D_2O, graphite, beryllium, polyethylene, wood, concrete, graphite, borated graphite, aluminum, steel, natural uranium, and other materials have been reported [76, 169, 183]. For this research, only beryllium and natural uranium critical assemblies, both of which are extensively characterized for varying thicknesses, were considered.

Table 2.1 shows the relevant details of the critical assemblies modeled, and Figure 2.5 shows the resulting TN+PFNS. Both reflectors "soften" the spectrum, although the impact is more pronounced for the low-Z beryllium. For the purposes of this research, the reflected geometries were eliminated, and the bare critical assembly was chosen. This resulted in the "hardest" TN+PFNS, which also represents the most difficult spectrum to reproduce as limiting the thermal and epi-thermal component while spectrally modifying the 14.1 MeV peak is difficult. If a bare TN+PFNS can be achieved with spectral shaping, modifications to account for the reflection, moderation, and/or leakage of the TN+PFNS for other national security applications is relatively straightforward.

The final volume-averaged TN+PFNS, as determined through transport of an 85% Watt fission and 15% Gaussian D-T source on the Godiva critical assembly, is shown in Figure 2.6. This spectrum is used as the objective function for the ETA design and optimization process as discussed in Chapter 5 and Chapter 6. In Figure 2.6, the group structure is changed to the DPLUS 46 group structure, which is based on the DABL69 library for use in defense-related radiation shielding problems [149]. This is necessary to work with the AutomateD VAriaNce reducTion Generator (ADVANTG) code, which is described further in Subsection 6.2.1.

2.1.3 Optically Thick to Optically Thin Geometry Correlation

An implicit assumption that has been carried forward to this point is that the replication of a representative TN+PFNS in a different sample geometry would result in the same observable effects and reactions. In the case of this research, the sample geometry is a HEU foil, and the observable is the FP distribution. The fission reaction rate is given by

$$R_f(\vec{r}, E, \vec{\Omega}, t) = \Phi(\vec{r}, E, \vec{\Omega}, t)\Sigma(\vec{r}, E)\ . \tag{2.3}$$

In Equation 2.3, $\vec{r}$, E, $\vec{\Omega}$, and t comprise the spacial, energy, angle, and time phase space. $\Sigma(\vec{r}, E)$ is the space and energy dependent macroscopic cross section. $R_f(\vec{r}, E, \vec{\Omega}, t)$ and $\Phi(\vec{r}, E, \vec{\Omega}, t)$ are the space, energy, angle, and time dependent fission reaction rate and

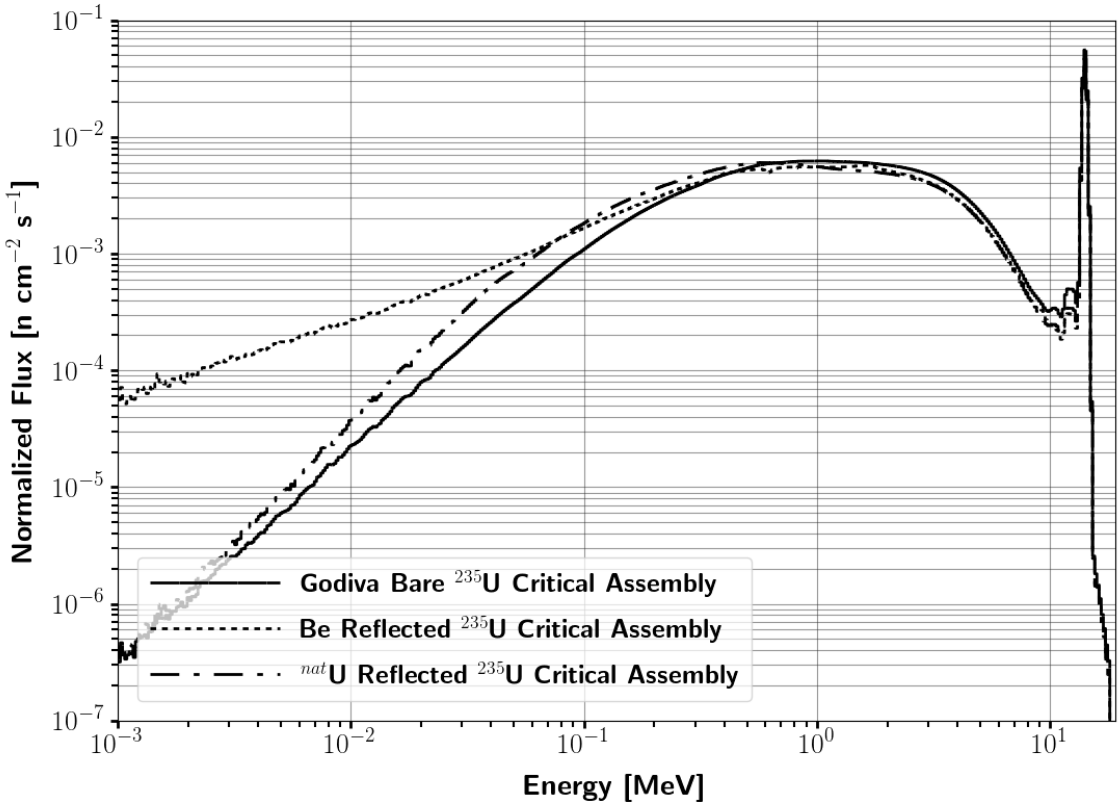

Figure 2.5: Comparison of the TN+PFNS obtained using bare and reflected critical assembly geometries.

neutron flux, respectively. If the flux is integrated over volume, angle, and time, the result is that the fission rate as a function of energy is only dependent on the energy-dependent cross-section, a fixed value[5], and the energy-dependent flux as shown in Equation 2.4. Mathematically, this shows that the fission rate is geometry independent and reproducing the volume averaged flux will reproduce the FP distribution.

$$R_f(E) = \iiint_V \Sigma(\vec{r}, E)\, dV \int_{4\pi} d\vec{\Omega} \int_0^{+\infty} \Phi(\vec{r}, E, \vec{\Omega}, t) dt = \Phi(E)\Sigma(E) \tag{2.4}$$

Noting that the goal is to reproduce the volume-averaged flux has important implications for ETA design and experimental validation. Conceptually, it is useful to draw the distinction between a neutron beam, in which the neutron energy spectrum is relatively constant at different points in a homogeneous medium, and a neutron field, in which the neutron energy

[5]This assumes a homogeneous material at room temperature, which is the case in this research as applied. However, neither of these will hold true for NWs.

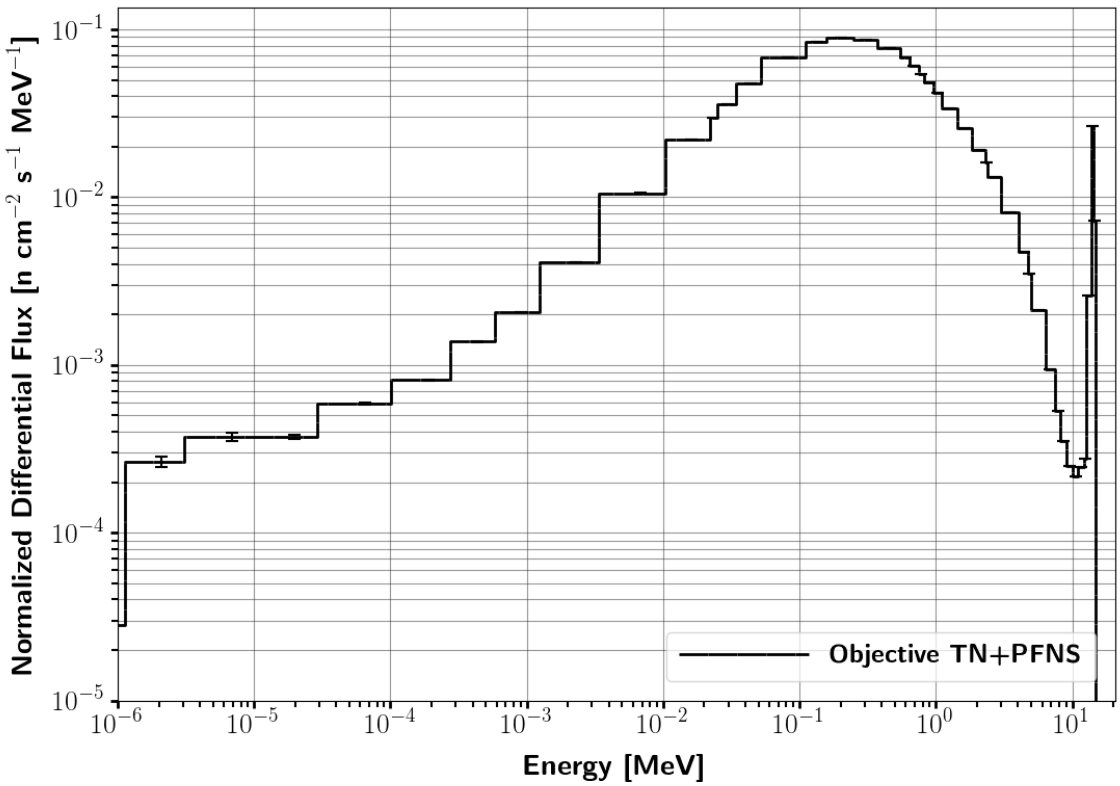

Figure 2.6: TN+PFNS derived from the Godiva critical assembly used as the objective spectrum for ETA optimization and design.

spectum varies, sometimes drastically, based on the location in a nonhomogeneous medium. Since the neutron field can vary significantly, it is important to consider the location of the measurement sample used to determine the volume-averaged flux.

For example, one approach is to treat the ETA as a beam modifier after which interchangeable samples can be placed. Under this construct, the design process would target replicating the objective TN+PFNS at the rear of the ETA. However, the resulting neutrons do not have beam-like characteristics and instead behave like a field where the energy spectrum is dependent on the additional materials and the location in proximity to the ETA. There will be small but measurable distortions introduced into the spectrum of the energy of the neutrons, causing fission inside of any sample added later based on the sample location and characteristics.

To avoid these errors and best produce the desired objective neutron spectrum, the ETA design goal is to produce a neutron field across a sample volume that is integral to the design. The sample volume will contain the HEU and other activation foils required for the measurement of the flux and FP distributions. The ETA design code will tally the volume-averaged flux across the HEU foil to compare with the objective TN+PFNS.

2.2 Input Spectrum

The starting point, whether one considers the computational optimization and design or experimental validation, is the input spectrum that is to be spectrally modified. NIF is an ideal starting source for this research and will be used for determining the ETA design, but the experimental validation at NIF was not accomplished as part of this research. Instead, an intermediate step of validation was pursued to test the ETA concept.

Other facilities such as OMEGA laser at the Laboratory for Laser Energetics and TANDEM at the Triangle Universities National Laboratory have intense D-T sources that could be used as a scaled down NIF test, but the 88-Inch Cyclotron at LBNL was chosen instead. The 88-Inch Cyclotron is able to achieve many of the same objectives that could be done at TANDEM and OMEGA and is subject to the same limitations in generating a realistic synthetic FP distribution[6]. While the 88-Inch Cyclotron has the additional drawback of having a different source spectrum than NIF, the facility accessibility was a driver for this stage of the research effort. The input source and spectrum chosen for the 88-Inch Cyclotron measurements is defined and discussed in Subsection 2.2.2.

2.2.1 NIF

When comparing various possible sources shown in Figure 1.2 and Figure 1.3, NIF stands out as an ideal starting point to reproduce the TN+PFNS due to the intensity and starting neutron energy distribution. Both are key features in any attempt to produce a TN+PFNS that will be relevant to national security applications, and there currently is no other neutron source that is even within orders of magnitude in intensity. A facility overview and description of the NIF source is provided in Section 9.1.

The highest yield shots as of 2017 were from the high-foot campaign. Of these, NIF shots 130927 and 140520 were selected as the basis for the NIF spectrum used in this research. Shot 140520 is shown in Figure 2.7 and compared with the desired final TN+PFNS.

2.2.2 88-Inch Cyclotron

The 88-Inch Cyclotron is a K=140 cyclotron pulsed ion source with both light- and heavy-ion capabilities. The accelerated ions can be used to generate neutrons through various nuclear reactions such as D-D fusion, D-T fusion, ^{7}Li(p, n), deuteron breakup, among others. A facility overview and description of the source and target is provided in Section 8.1.

The neutrons for this research were generated from 33 MeV deuteron breakup on a thick tantalum target, resulting in the neutron distribution shown in Figure 2.8. This process, and the spectral variations that result from changes in incident neutron energy and target choice,

[6]This is due to the orders of magnitude lower flux available at the three facilities in comparison with NIF. While TANDEM and the 88-Inch Cyclotron can be ran for longer times to compensate, the resulting FP distribution is perturbed by the differential decay as a result of the long irradiation time of several hours to days.

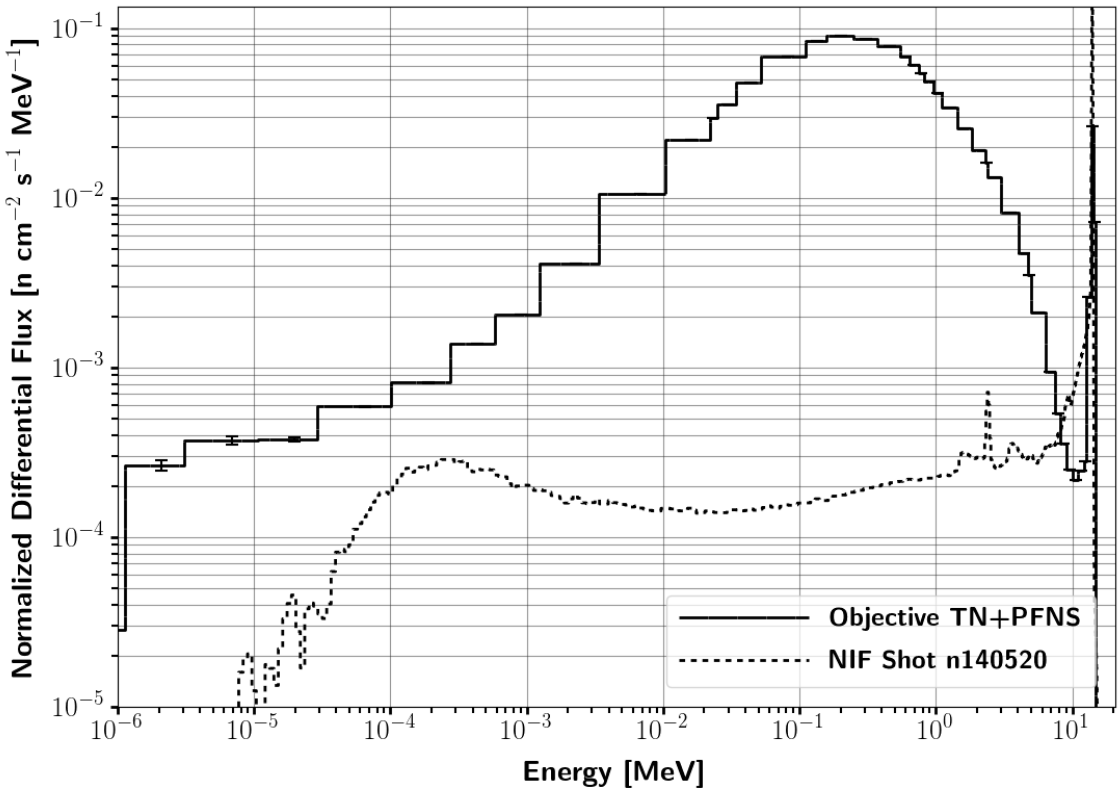

Figure 2.7: Comparison of the normalized NIF Shot 140520 vs the desired TN+PFNS [35].

are described in Section 8.1. This starting distribution is significantly different from the NIF source spectrum shown in Figure 2.7, and it has many undesirable characteristics for use as a starting source to achieve the objective TN+PFNS, as shown in Figure 2.9. However, the 33 MeV deuteron breakup spectrum does peak at about 10 MeV[7], has a small fraction of the total fluence above 20 MeV[8], and has sufficient intensity to be able to perform the pulse height and activation measurements.

2.3 NIF Constraints

Many constraints and considerations must be included when developing a spectral shaping capability for NIF or the design generated might not be able to be fielded. This section looks at the different factors that were considered and included in the development of an

[7]This means that a bulk of the nuclear cross-sections that are relevant for the neutron spectral shaping at the 88-Inch Cyclotron will also be relevant for NIF.

[8]This limits the relative contribution from reactions such as (n,3n) that would not be present at NIF. Additionally, it limits the reliance on reaction models instead of nuclear data for the simulations.

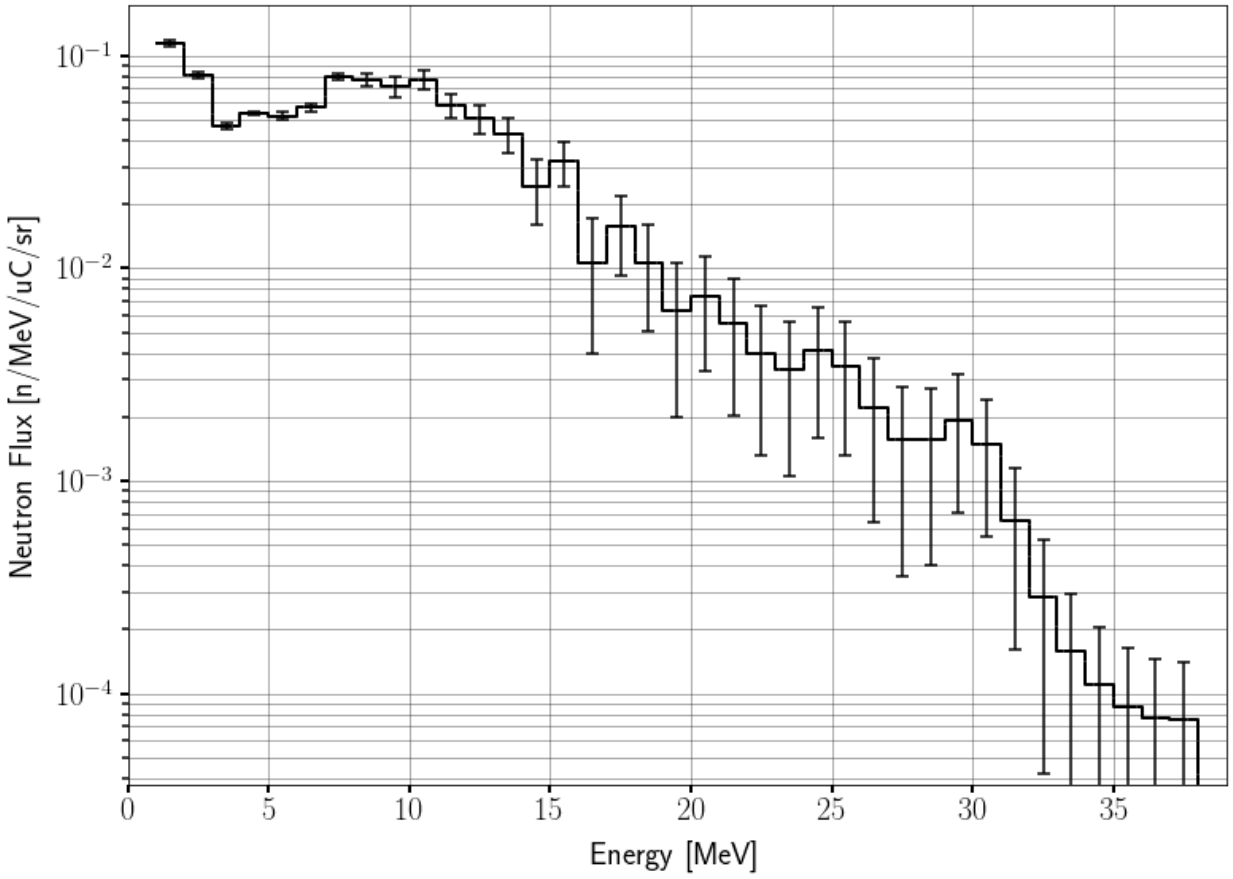

Figure 2.8: Neutron spectrum resulting from 33 MeV deuteron breakup in a thick Ta target.

ETA design. First, the diagnostic instrument manipulator (DIM) that will be used to place the ETA in the NIF target chamber (TC) and the associated mechanical limitations are evaluated. Next, a brief survey of the materials requirements and limitations are described. Finally, the limitations imposed on the foil diagnostic package are detailed[9].

2.3.1 DIM Limitations

Several design studies were conducted with LLNL to determine the design constraints for the ETA design. There are four primary mechanical considerations that must be met to field on any of the four DIMs: laser exclusion zone, target positioner (TarPos) sweepout, DIM weight limitations, and a maximum outer diameter. The laser exclusion and TarPos/Cryo-TarPos sweepout are combined here to yield a single exclusion zone expressed as a minimum distance from target chamber center (TCC) and a conical opening angle from that point.

[9]The permalink location of the full inputs and design results can be found in Appendix B.

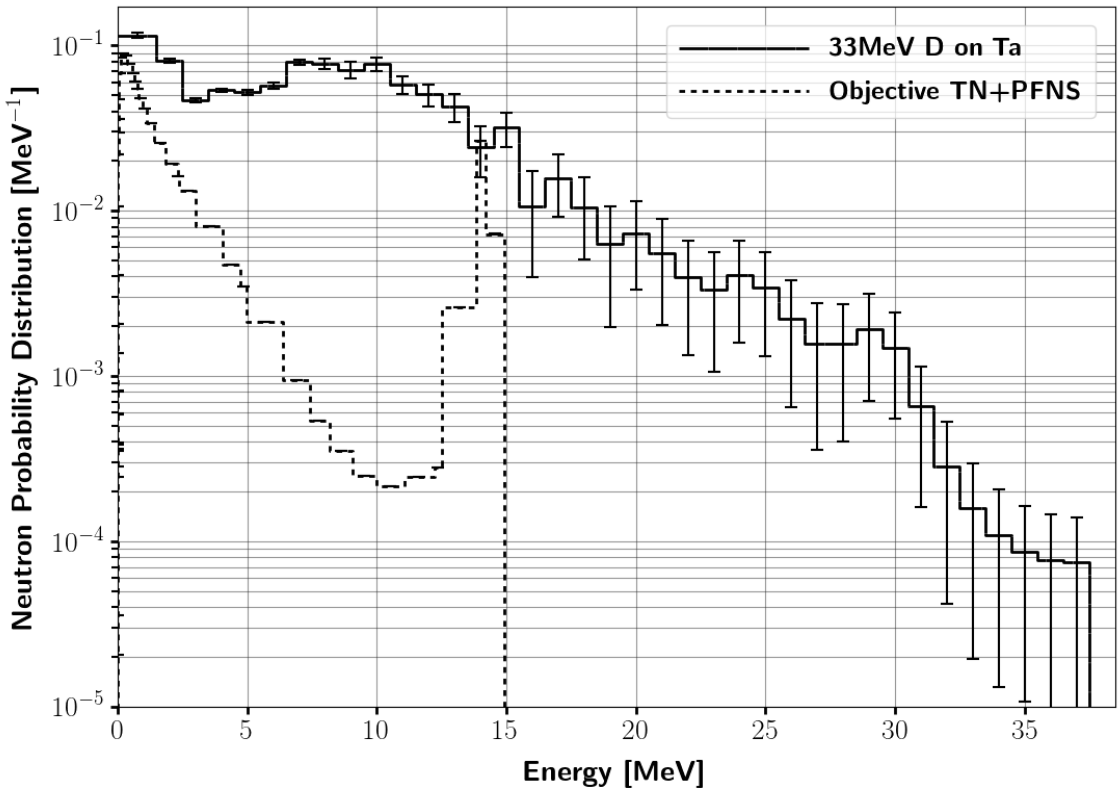

Figure 2.9: A comparison of the 88-Inch 33 MeV breakup neutron distribution and the desired TN+PFNS.

The weight limitation is expressed as a moment that is a function of the closest approach from TCC and the size of the ETA. The maximum outer diameter is 285 mm as set by the diagnostic load package (DLP) limitation.

NIF currently has four DIMs. The mechanical limitations for each are outlined in Table 2.2. It is worth noting that the closest approach and diagnostic volume listed are estimates that are subject to the design of the ETA. They are not the final answer, but are useful for comparing the relative and approximate distances that can be achieved for each DIM. The polar DIM (0-0) was immediately rejected as it has the most restrictive exclusion zone. NIF has three equatorial DIMs: 90-78, 90-315, and TANDEM (90-348). As of this writing, TANDEM was not yet certified for passive diagnostics, and the maximum moment was not specified during the initial scoping studies. However, it is expected to have the largest load capacity, which, coupled with the shorter reach into NIF, will make the moment non-limiting for any design capable of being fielded on 90-78 or 90-315.

DIM 90-78 is capable of a slightly closer approach than 90-315 for both TarPos and Cryo-

Table 2.2: DIM Mechanical Limitations.

DIM	Limiting Factor	Volume	Approach [mm]	τ [ft-lb]
Polar (0-0)	1Ω Beam	38.1°	220.50	1738
90-78	TarPos	72.1°	109.00	1792
	Cryo-TarPos	72.1°	134.50	1792
90-315	TarPos	72.1°	153.00	1792
	Cryo-TarPos	72.1°	156.25	1792
90-78	TarPos	72.1°	115.75	>1792
	Cryo-TarPos	72.1°	407.00	>1792

TarPos[10] while maintaining the same load bearing capacity. For the purposes of setting constraints, DIM 90-78 was chosen. Due to 90-78 being capable of achieving the closest possible approach, any design that meets the weight and moment limitations for 90-78 will meet the limitations for the remaining DIMs.

After design iteration, the design constraints determined for DIM 90-78 are shown graphically in Figure 2.10. The closest approach of 60 mm and opening angle of 102.3° corresponds to a weight limitation of 80 kg. The front nose cap is hollow, resulting in the front of the shaping assembly and materials being located $\sim$ 75 mm from TCC. The outer radius is limited to a maximum of 280 mm to allow for clearance on the DLP cart.

2.3.2 Materials

Due to the close approach of the ETA to TCC, additional requirements for the ETA case must also be specified. The conical section of the ETA case was required to be made of stainless steel 409 to be able to withstand debris impact. The aft conical section was made of aluminum alloy 6061 to minimize weight. Finally, the design requires a debris shield on the nose to partially deflect and thereby minimize the impulse from the shot on the DIM.

For the ETA internal materials, there are three primary NIF-imposed limitations. First, hazardous or carcinogenic materials such as lead or beryllium will need to be encapsulated. This does not preclude their use, and the subsequent encapsulation should have little impact on the neutronics properties of the ETA. Second, the materials will have to pass dose limit requirements post-irradiation. This analysis will be performed after the final ETA design is determined and will not limit any of the materials used for the ETA design.

However, HEU and plutonium, required for the generation of the synthetic FPs, fall under much stricter guidelines at NIF than typical activation products. To eliminate time-consuming and costly approvals, the approach was taken to adopt the use of 1.2 g HEU

[10]Cryo-TarPos is required for the highest yield, cryogenically-cooled shots.

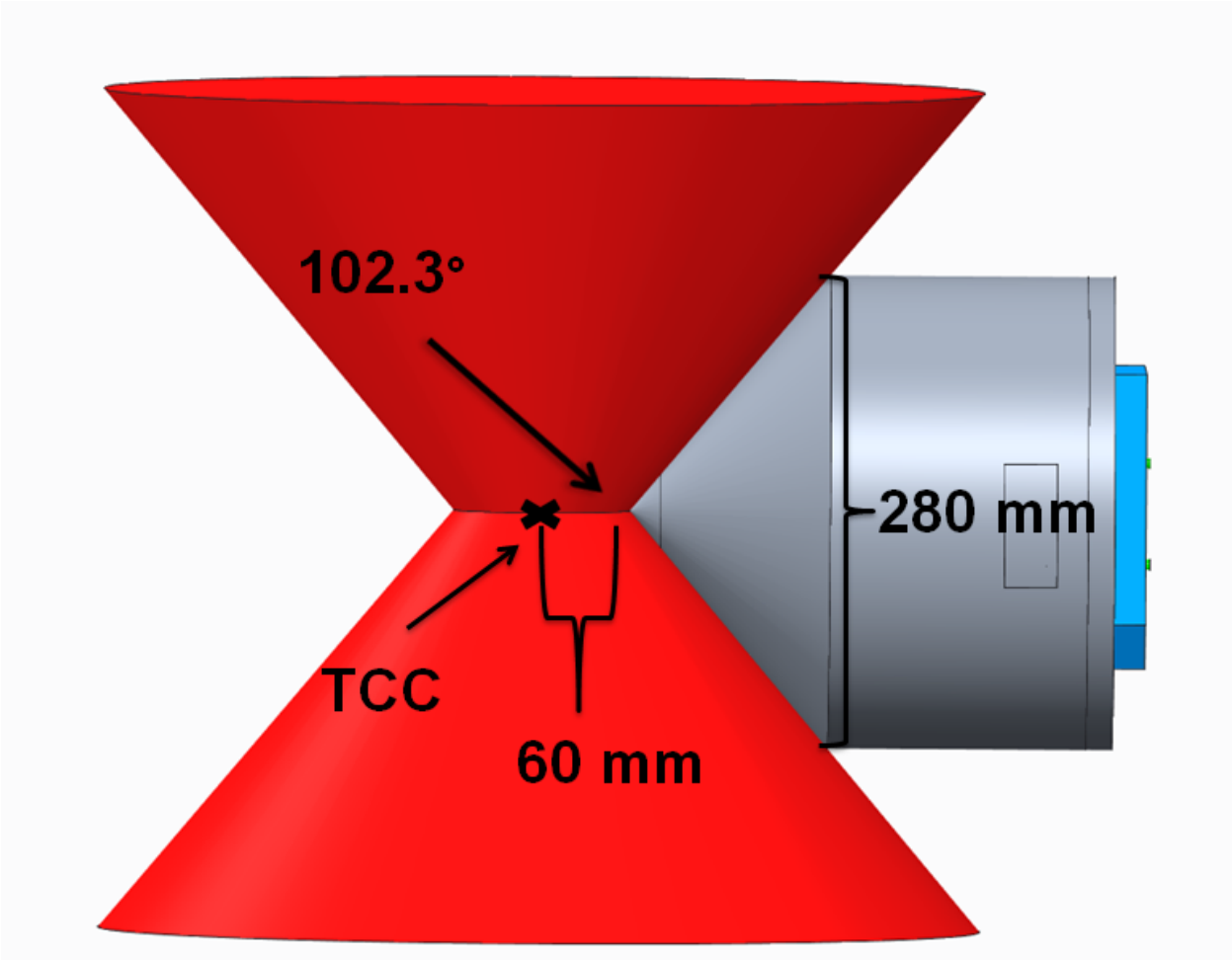

Figure 2.10: The final design constraints and envelope for DIM 90-78.

foils encapsulated in a Target Option Activation Device (TOAD). This approach has been approved on NIF for past radio-chemistry experiments [75, 190, 192].

Finally, any materials fielded in the ETA will have to pass NIF cleanliness and off-gassing tests. This can be limiting, but an alternative approach is to hermetically seal the ETA materials, thereby eliminating this concern. The choice was made that the materials library consist of elemental materials for both simplicity and a straightforward tie to the nuclear data. For practical considerations, the library consisted of a few compounds and alloys (6061 Al, LiF, high density polyethylene (HDPE), deuterated HDPE, Stainless 409, and boron carbide) as well. From the initial list of 83 elements, 35 undesirable materials such as gas, low-melting point, expensive, and reactive elements were removed. This resulted in a material library consisting of 54 elements, compounds, and alloys for potential use in the ETA design. As will be seen in Section 6.3, this library is a good starting point for future designs but needs to be further vetted for reactive metals. The addition of more alloys and

compounds should also be considered.

2.3.3 Diagnostics Limitations

As described in Subsection 2.1.3, the ETA will produce a neutron field that replicates the TN+PFNS objective spectra across the HEU and activation foils. Since activation foils are the measurement of interest for a NIF experiment, the ETA can be fielded as a passive diagnostic. This greatly simplifies the experiment and implementation on a DIM at NIF. However, the considerations of access time and determining the minimum number of acceptable reactions need to be addressed.

The timeline of access to the ETA after a shot is on the order of a few hours, and longer if a full unmounting is required. To avoid requiring an unmounting of the ETA to retrieve the samples, the ETA will be engineered with a drawer that provides quick access to the HEU and activation foils. Post-irradiation, the DIM will be removed from the TC, and the drawer containing the HEU and activation foils will be transported to the radio-chemistry and gamma spectroscopy facilities.

The logistical delay required before counting can begin limits the activation reactions and fission products that can be considered[11]. NIF designed a neutron activation spectrometer (NAS) with these limitations in mind, and it has been approved for use on previous NIF shots. A sample NAS is shown in Figure 2.11. A modified NAS foil pack was used for this research[12].

The final diagnostic consideration is the minimum number of atoms that need to be created for radio-chemical separation, which turns out to be on the order of 10^5 atoms [75]. Factoring in the valley and wing yield of $\sim$0.1%[13], the minimum number of fissions required is 10^8. To improve the statistics to a few percent for valley and wing FPs, the minimum number of fission was set to be 10^9. This is not the primary factor constraining the spectral match possible in ETA design, but it does influence the choice of materials utilized to improve the neutron economy.

This chapter has presented a full problem definition for the TNF synthetic fission products research problem. It outlined the derivation of the TN+PFNS objective spectrum, and the material, mechanical, and diagnostic constraints imposed on the ETA design by NIF. Next, the development of the fission and activation diagnostics, and achieving the NIF to TN+PFNS spectral shaping goals within the constraints specified, will be discussed from the perspective of neutron reaction and fission theory.

[11]See Section 3.1 for a description of the process used and considerations made in choosing the FPs to measure. While the half-life limitation is one factor, energy dependent fission product data tends to be a more limiting factor.

[12]See Section 7.2 for a full description of the activation foils and reaction channels used for the 88-Inch and NIF experiments.

[13]Approximate yield given the TN+PFNS spectrum. Exact yields are calculated in Subsection 3.1.3

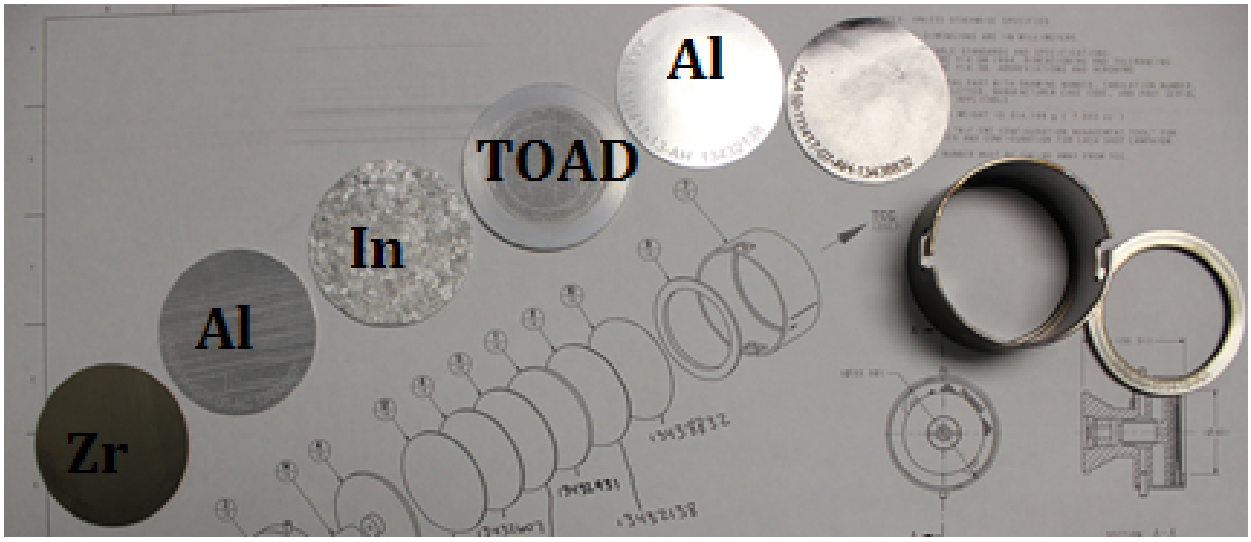

Figure 2.11: A sample NIF NAS configuration containing a TOAD.

Chapter 3

Neutron Reaction Theory

> *It is conceivable that the nucleus breaks up into several large fragments, which would of course be isotopes of known elements but would not be neighbors of the irradiated element.*
>
> - Ida Noddak, 1934

Neutron reactions are the fundamental physics underlying every aspect of the ETA from the spectral shaping to the fissioning process to the measurement of the neutron spectrum. As such, this chapter explores basic neutron reaction theory as applicable to the TNF ETA design and measurement. The chapter starts with an overview of fission theory[1], the fission product data, and fission models that could be used to determine the fission product distribution resulting from irradiation of HEU by TN+PFNS. Next, neutron reactions are described in the context of their kinetics and application to spectral shaping from the NIF spectrum to the TN+PFNS. Finally, activation-relevant reactions are described in the context of developing a neutron activation foil pack to be used as the primary diagnostic for the measurement of the TN+PFNS.

3.1 Fission Theory

Fission is the process by which heavy nuclei, either spontaneously or through the absorption of a neutron, photon, or charged particle, splits into varying combinations of two lighter fission fragments. This is shown schematically in Figure 3.1. In the process of fissioning, nuclei in the uranium-plutonium region release ∼200 MeV of energy in the form of fragment kinetic energy, gammas, and neutrons. Additional delayed neutrons, gammas, and beta particles are emitted from the subsequent decay of the neutron-rich fission fragments. The distribution of the fission fragments varies as a function of the isotope undergoing fission and

[1]This is a brief overview intended to provide context to the FP models available and the limitations of the current approaches available.

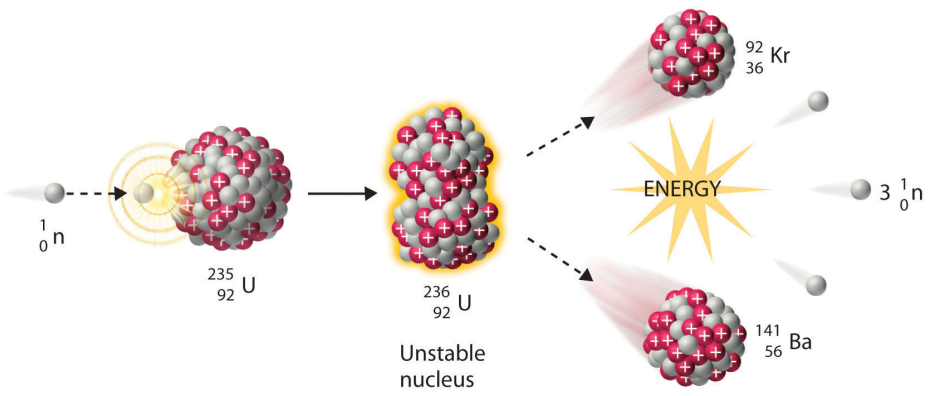

Figure 3.1: Schematic depiction of neutron induced fission depicting one possible fission fragment and neutron outcome [161].

the incident neutron energy as shown in Figure 3.2 and Figure 3.3, respectively. Similarly, the number of neutrons and their associated energy distribution are affected by the fissioning nucleus and incident neutron energy, as shown in Figure 3.4 and Figure 3.5, respectively.

Fission nominally produces two fission products (FPs) per fission event, and these FPs cover a large swath of the known neutron-rich isotopes, as shown in Figure 3.6. The FPs are neutron rich because the two fragments closely replicate the N/Z ratio of the fissioning nucleus shown in Figure 3.6, instead of being closer to the valley of stability and $N/Z \approx 1$. Virtually all of these are formed in an excited state, and some will also form long-lived isomers of the elements. Complicating the picture further, each of these elements will decay, often with sub-second half lives, resulting in the formation of new isotopes. Often this decay is via β^- decay channels due to an excess of neutrons in the FP. Finally, the FPs will emit both prompt and delayed neutrons on time scales ranging from 1×10^{-17} to 1×10^{4} seconds after the start of fission [108].

To ensure consistency when discussing the dynamic fission process and resulting fission fragment populations, several common definitions are worth defining explicitly. The term fission fragment is generally used to refer to the primary fragments pre-evaporative neutron emission, while fission product is used to refer to the resulting post-evaporative product nuclei. This terminology convention is adopted here, and the fission products are the observables of interest for TNF applications due to the time scale required for collection. This also corresponds to the commonly measured quantity in the literature.

The yield of the fission products can then be broken down into several sub-categorizations. The fractional independent yield, $f(A, Z)$, is the fractional yield of all isomers of (A, Z). The sum yield, $Y(A)$, is defined as the total independent yield, prior to delayed neutron emission, of all fission products of mass A. The isomeric yield ratio, $R(A, Z, I)$, is the fraction produced as isomer I for each value of (A, Z) [98].

The independent yield, $y(A, Z, I)$, is then given by [98]

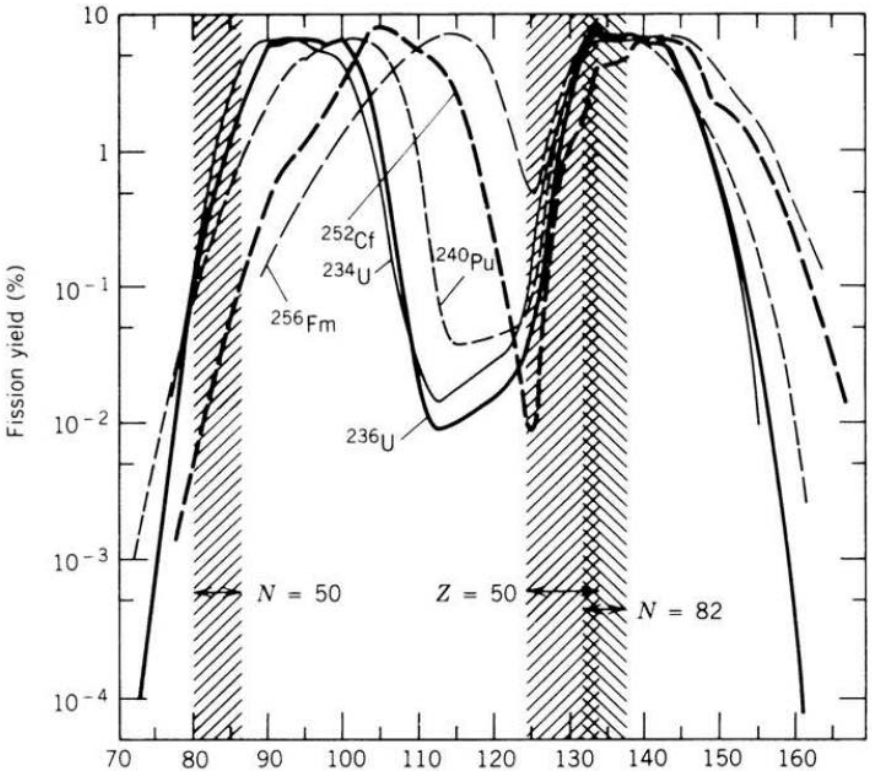

Figure 3.2: Impact of different fissioning isotopes on the resulting fission product distribution for thermal neutron induced fission of ^{233}U, ^{235}U, and ^{239}Pu and spontaneous fission of ^{242}Cf and ^{256}Fm [216].

$$y(A, Z, I) = Y(A) f(A, Z) R(A, Z, I) \,. \tag{3.1}$$

The sum yield is then given as [98]

$$Y(A) = \sum_{Z,I} y(A, Z, I) \quad \text{for all A} \,. \tag{3.2}$$

Given that fission is most commonly a binary process,

$$Y = \sum_{A} Y(A) = \sum_{A,Z,I} y(A, Z, I) = 2 \,. \tag{3.3}$$

In contrast, the cumulative yield, $Y_c u(A, Z, I)$ is defined as the number of atoms of (A, Z, I) produced over all time. This is typically the experimentally measured quantity. The chain yield for a mass chain is determined as the cumulative yield for the stable terminating isotope of the chain. For example, ^{137}Ba is the terminating stable element of the A=137 mass chain shown in Figure 3.7.

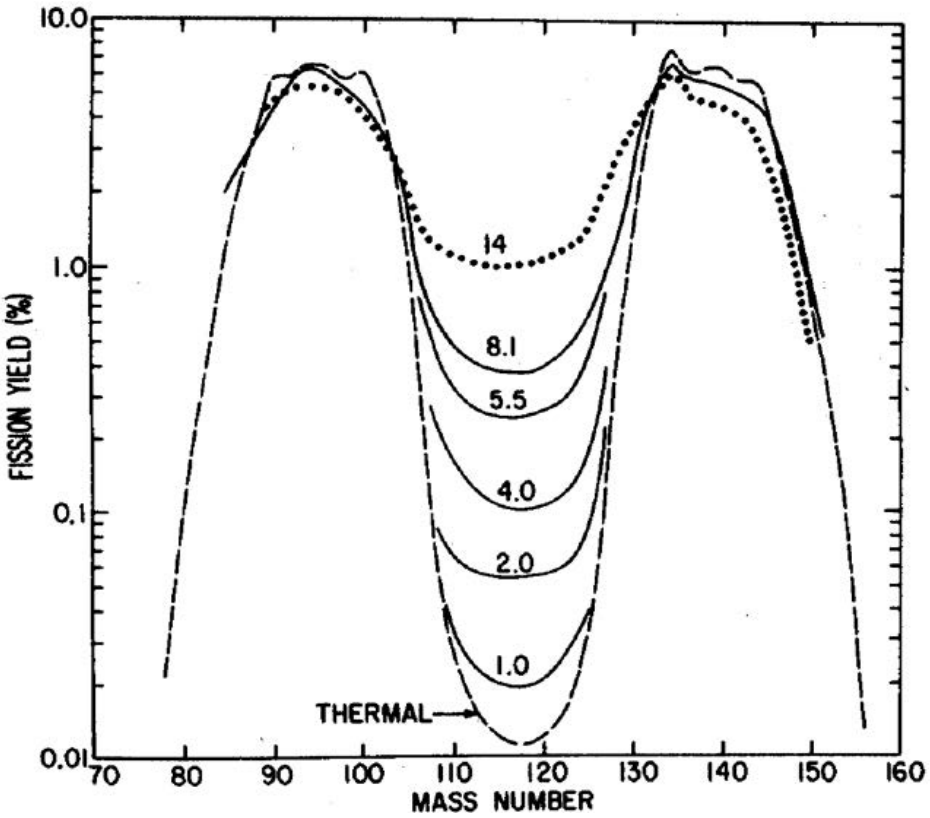

Figure 3.3: Impact of incident neutron energy on the fission product distribution for ^{235}U. Each curve is labeled energy of the neutron that induced fission [79].

The chain yield differs from the sum yield in accounting for exit and entry channels into the mass chain. Whereas the sum yield is given by Equation 3.2, the chain yield can be calculated from the independent yield by

$$Y_{ch}(A) = \sum_{Z,I} y(A,Z,I) * (1 - \alpha_{out}(A,Z)) + y(A+1,Z,I) * (\alpha_{in}(A+1,Z)) \ , \tag{3.4}$$

where α is the branching ratio out of or into the chain by delayed neutron emission B_n^-. Unless otherwise specified, the cumulative yield is used when referring to the distribution of fission products for the purposes of this research as these are the measurements of interest in a TNF application.

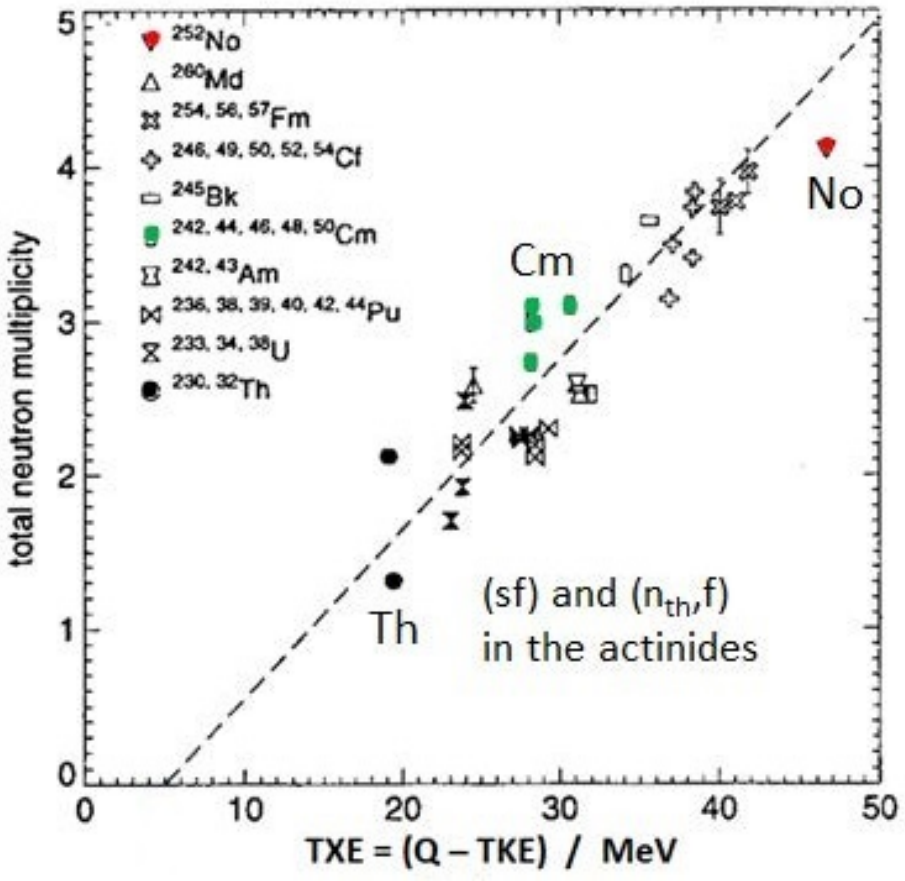

Figure 3.4: Emitted neutron multiplicity for different fissioning isotopes as a function of excitation energy left in the fission products [92].

3.1.1 Fission Models

Since fission was discovered by Strassman, Meitner, and Hahn in 1938, several models have been proposed to describe the fission process and the resulting observables, such as the fragment distribution, the number of neutrons, the overall energy partitioning, and the energy distribution of the emitted neutrons. Meitner and Frisch proposed the Liquid Drop Model (LDM) that was expounded upon by Bohr and Wheeler the very same year [20, 140]. In the LDM, the neutron adds excitation energy, causing the nucleus to elongate until it splits. The LDM allows for accurate calculation of bulk properties of fissioning systems but is insufficient to describe microscopic properties of the system. To move beyond the "macroscopic" LDM model to be able to predict "microscopic" properties of the fission system, a series of corrections were made to account for quantum effects on the system.

Quantum shell effects and deformation induced shell structure changes were added to models of the nucleus by Mayer and Nilsson, respectively. Strutinsky incorporated these

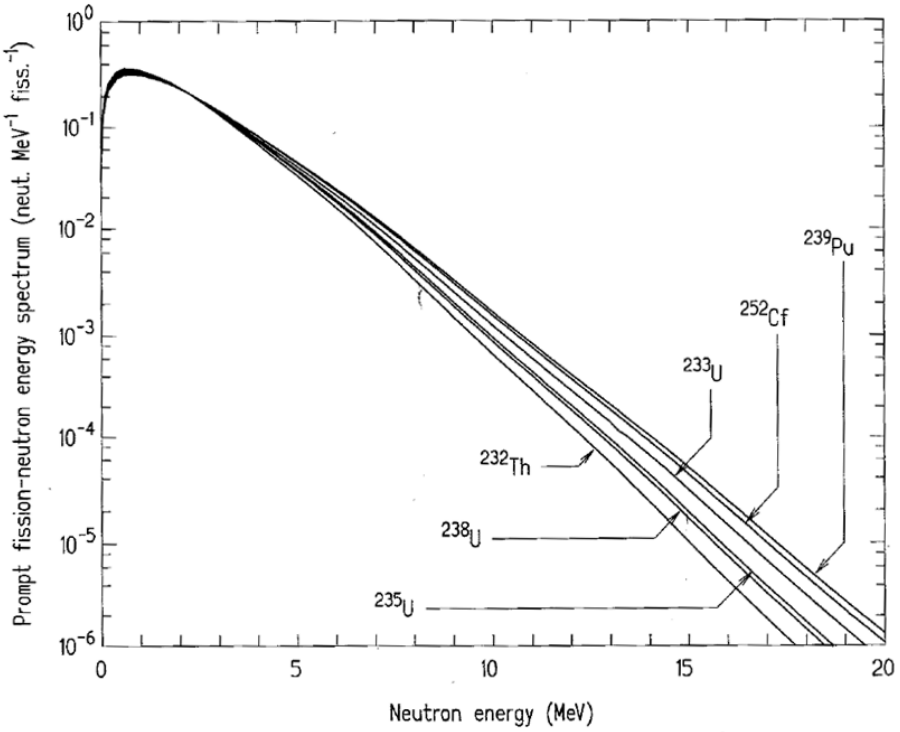

Figure 3.5: Prompt fission neutron energy distribution for various fissioning nuclei [218].

and pairing effects into a "macroscopic-microscopic" fission model. Many others have continued to refine macroscopic-microscopic fission models through addition of more realistic potentials, assymetric distribution of the protons and neutrons, etc. These models provide good agreement with macroscopic experimental results and are able to replicate microscopic trends that generally agree with experimental results for nuclei that have been well-studied [145].

One shortcoming of the LDM based models is their ability to model the dynamic process of scission that leads to the observables of interest to this research, namely the distribution of the fission products and their properties. Wilkins et al. overcame this limitation by using statistical arguments to simulate the dynamic scission process [224]. Continued improvement of this approach through improving the parameter selection, description of the scission geometry, statistical descriptions, and improved state density calculations have been incorporated. One example of a modern scission-point model is the scission-point yield (SPY) model developed by Lemaître et al. Despite the improvements of scission-point models at simulating the resulting particle and energy partitioning following scission, they still are unable to predict the fission fragement distribution with any accuracy useful for comparison with ETA experiments, as shown in Figure 3.8 [116].

The macroscopic and micro-macroscopic approaches are limited because they replace the

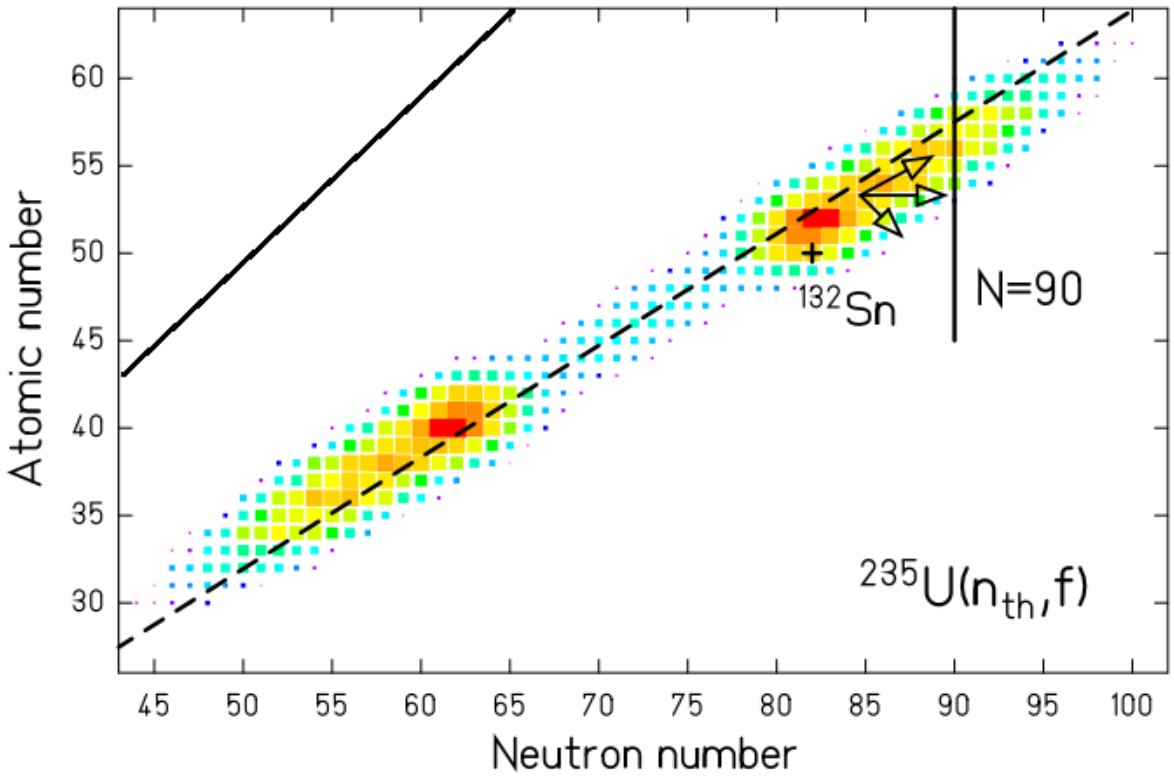

Figure 3.6: GEF calculated FP distribution prior to prompt neutron emission. The dashed line is the same N/Z ratio as the fissioning nucleus and the solid line is N/Z=1 [185].

fundamental physics of the interactions between protons and neutrons with approximations. "Microscopic" models seek to bridge this gap and fully describe the process of fission from first principles, starting with the effective nucleon interactions. However, microscopic models are computationally expensive and do not currently produce better correlations with the data for fission product distributions than phenomenological or semi-empirical models. Figure 3.9 shows a comparison of a microscopic calculation by Younes, experimental data from Schillebeeckx, and the GEneral description of Fission observables (GEF) code from Schmidt [184, 185, 235]. A combination of semi-empirical and phenomenological models are described next in terms of their general characteristics and ability to model the fission product distributions following neutron induced fission.

GEF

GEF calculates "pre-neutron and post-neutron fission-fragment nuclide yields, angular-momentum distributions, isomeric yields, prompt-neutron yields and prompt-neutron

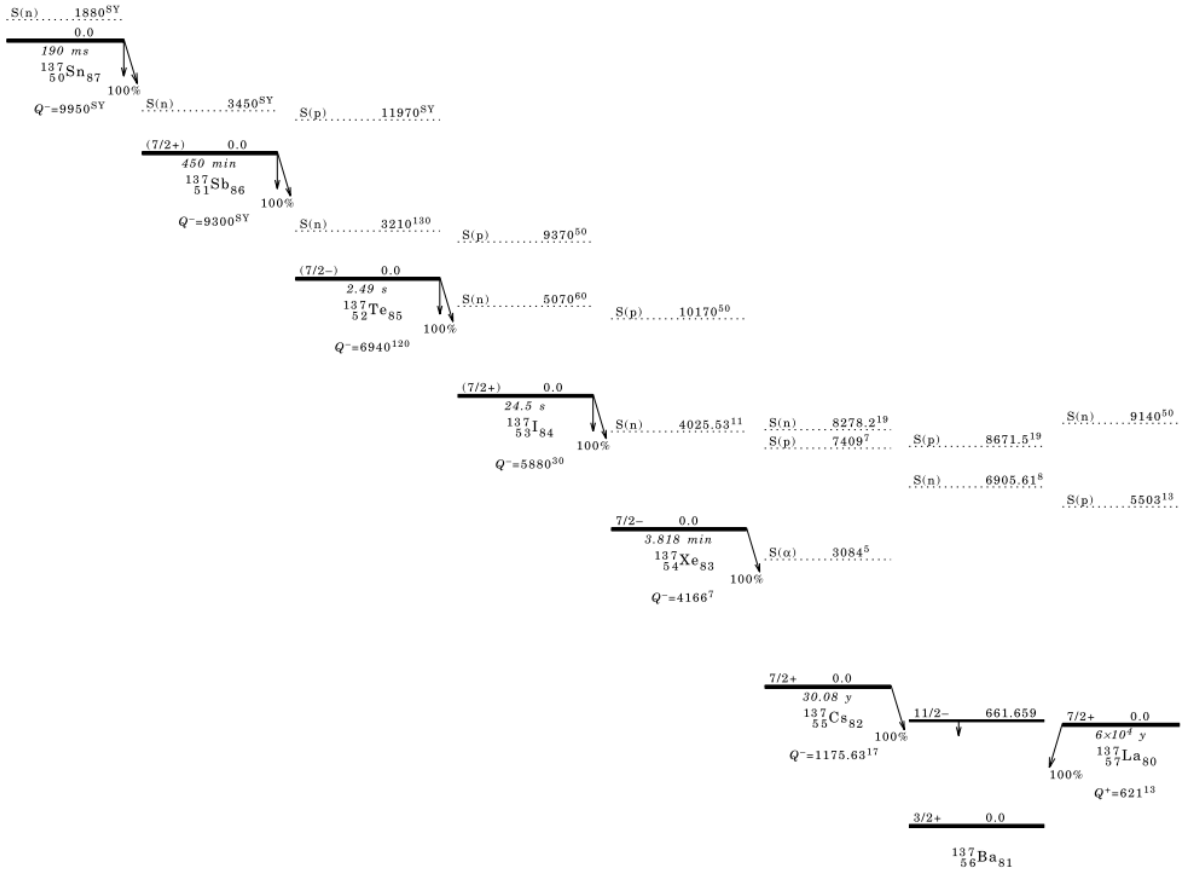

Figure 3.7: A=137 mass chain. Only the neutron rich side of the chain is shown for compactness [25].

spectra, prompt-gamma spectra, and several other quantities for a wide range of fissioning nuclei from polonium to seaborgium in spontaneous fission and neutron-induced fission" [185]. Additionally, GEF can model multi-chance fission, which is fission that follows after the emission of a neutron. Multi-chance fission is an important component for 14 MeV neutron induced fission. GEF also preserves the correlations between all of the fission observables modeled. This is accomplished through Monte-Carlo sampling of the multi-dimensional parameter space for each fission history [185].

GEF uses a combination of quantum, statistical mechanics, and experimental information tied together by a set of 50 adjustable parameter values. The full models for each fission observable are described in the GEF manual [185]. While this parameter set is large, it covers approximately 100 fissioning systems from spontaneous to 100 MeV induced fission. Most of these parameters are tied to physical properties of the fissioning system. Since GEF is a Monte-Carlo code, the parameter set can be sampled according to the prescribed

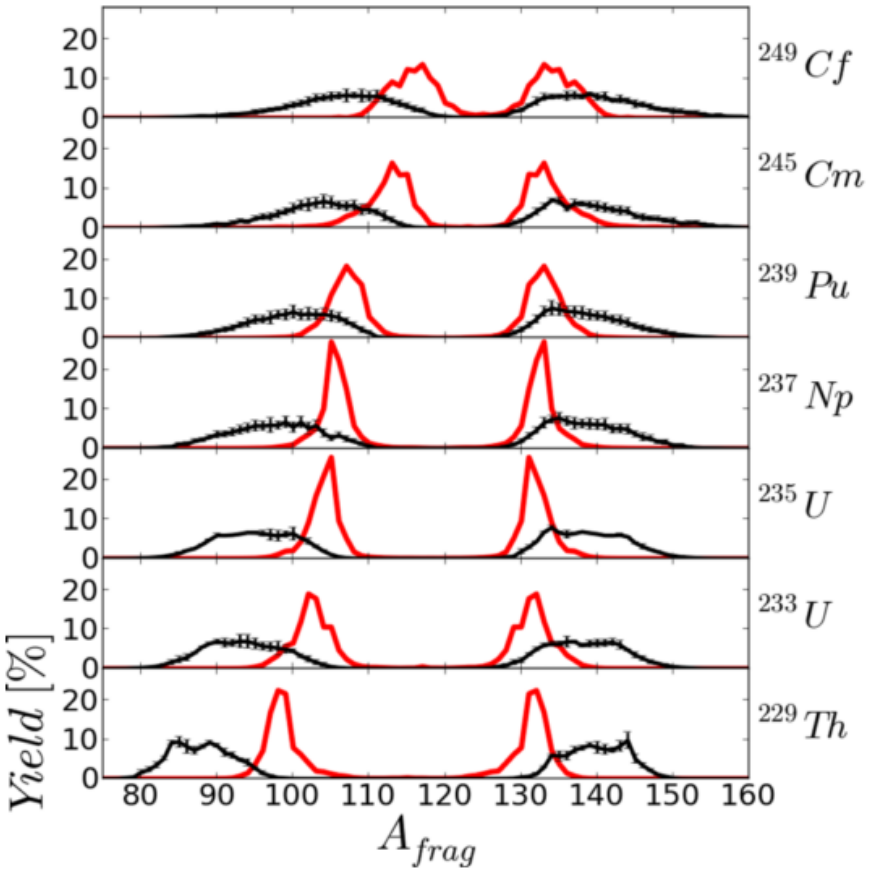

Figure 3.8: Comparison of thermal induced fission mass yield for different nuclei as calculated in SPY (red) and the evaluated data from ENDF/B-VII.1 (black) [38, 116].

uncertainties to develop a perturbed parameter set for estimation of model uncertainties [185].

In general, GEF does an excellent job of matching the fission product mass distribution, especially in regions where data exists. For example, the comparison between GEF and ENDF/B-VII evaluated data for thermal induced fission of ^{235}U is shown in Figure 3.10. However, GEF's performance varies when considering the energy dependence of individual fission products. This is shown in Figure 3.11 and Figure 3.12 for a valley (^{111}Ag) and heavy peak FP (^{140}Ba), respectively. While GEF replicates the overall trends well, the actual reduced χ^2 can vary significantly from one FP to the next[2].

[2] χ^2 is used as a "goodness of fit" statistic to describe how well a model fits a set of observed data and their associated uncertainty. It is given by $\frac{\chi^2}{\nu} = \frac{1}{\nu}\sum_i^N \frac{(x_i-\mu_i)^2}{\sigma_i^2}$ where ν is the degrees of freedom (N-model free parameters) and x_i, μ_i, and σ_i are the model estimate, the measure value, and the uncertainty of the i^{th} measurement.

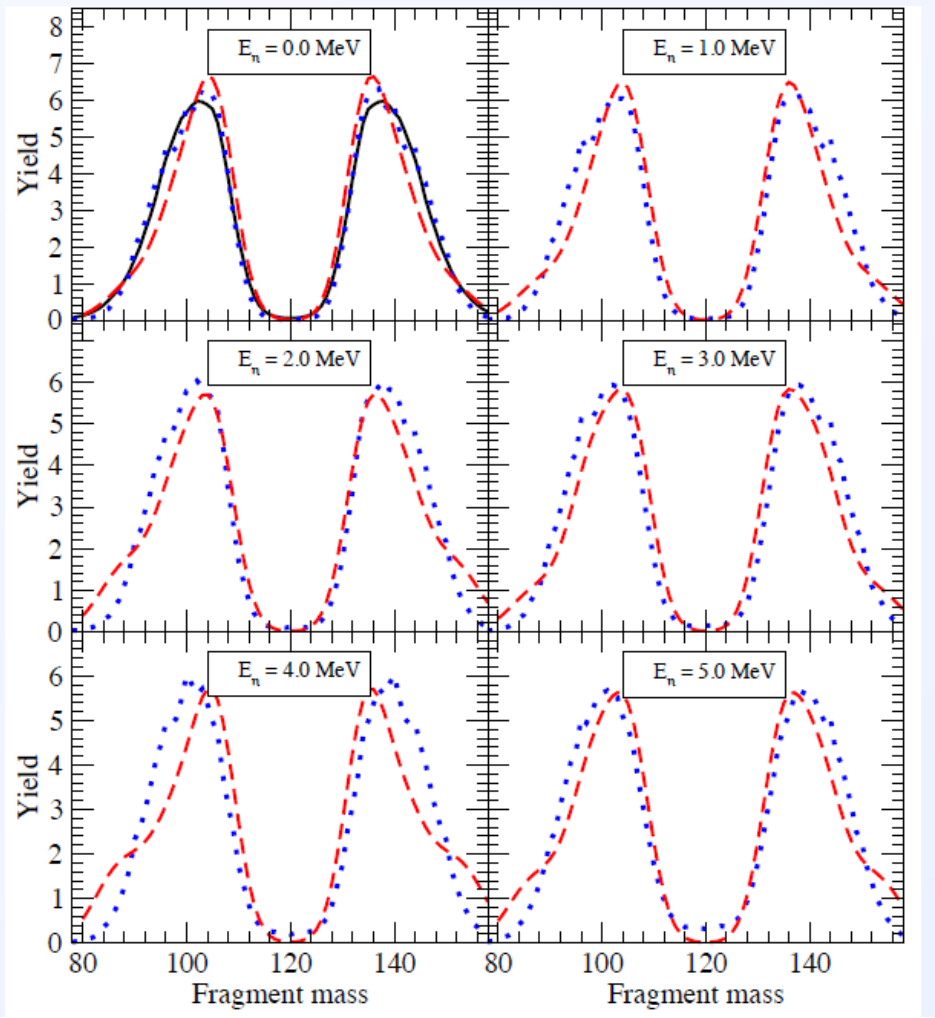

Figure 3.9: Comparison of the fission fragment mass distribution for neutron induced fission on ^{239}Pu at various incident energies. The red dashed line is a microscopic calculation by Younes, the solid blue line is experimental data from Schillebeeckx, and the blue dotted line is a calculation from the GEF code by Schmidt [184, 185, 235].

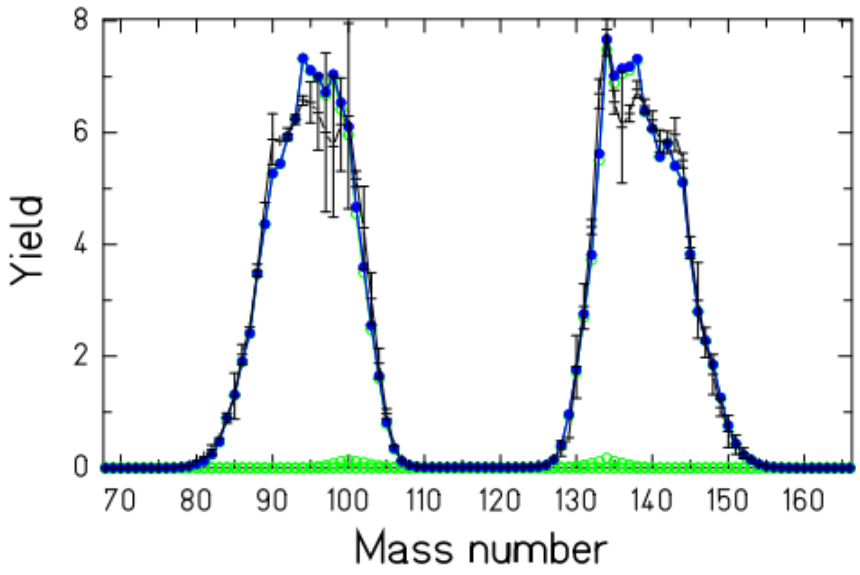

Figure 3.10: Comparison of the GEF calculations and ENDF/B-VII evaluated data [38] for the fission product mass distribution for thermal neutron induced fission on ^{235}U [185].

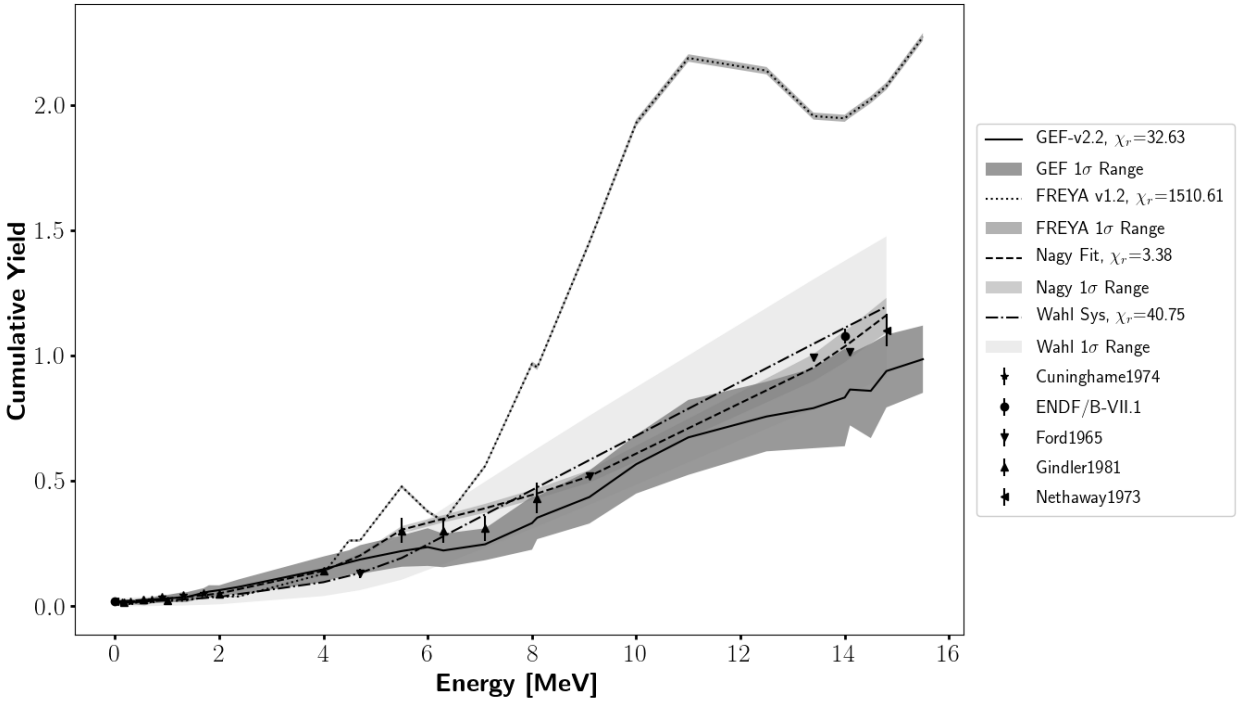

Figure 3.11: Comparison of the GEF, FREYA, Wahl, and Nagy energy dependence calculations to measured data for the energy dependent cumulative yield of ^{111}Ag [155, 185, 209, 217].

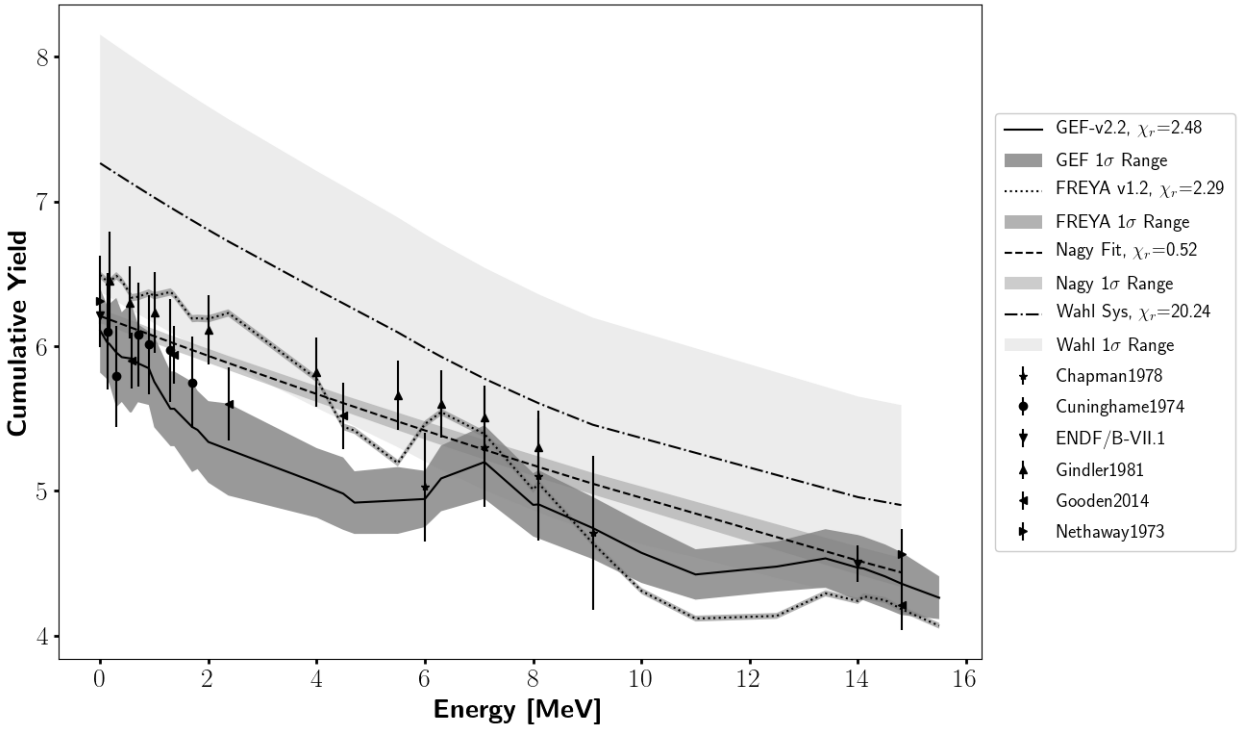

Figure 3.12: Comparison of the GEF, FREYA, Wahl, and Nagy energy dependence calculations to measured data for the energy dependent cumulative yield of ^{140}Ba [155, 185, 209, 217].

In Figure 3.11 and Figure 3.12, GEF is also compared to alternative options such as Fission Reaction Event Yield Algorithm (FREYA), Wahl systematics, and Nagy fits. Each of these is described further in the following sections.

FREYA

FREYA has many similarities to GEF in that it models the complete fission event history while maintaining correlations between observables and conserving energy and momentum. FREYA has the additional benefit of integration into MCNPX 2.7.0, MCNP6, and Geant 4.10, thereby allowing for a complete model of neutron transport, the fission process, and the resulting observables. FREYA's goal is to improve upon the previous state-of-the art processes implemented in MCNPX 2.7.0, MCNP6, and Geant 4.10 that sampled from average fission parameter distributions without maintaining correlations [175, 209].

Similar to GEF, FREYA uses a combination of models and approaches under a Monte-Carlo construct for simulating the fission observables. Fits to nuclear data are used for fission product mass and kinetic energy distributions, and statistical models are used for neutron and photon emission. Monte-Carlo sampling is used to maintain the correlations between

the fission products and the emission of neutrons and gammas. Of interest to this research, the fission product mass distributions are modeled with classical five-Gaussian fits given by

$$Y(A) = G_1(A) + G_2(A) + G_0(A)\,, \tag{3.5}$$

where A is the mass of a given fission product, G_1 and G_2 are the asymmetric fission modes associated with spherical shell closure at $N = 82$ and the deformed shell closure at $N = 88$, respectively, and G_0 is the symmetric fission mode. Equation 3.5 has eight free parameters and is given by

$$\begin{aligned} Y(A) =& \frac{N_1}{\sigma_1\sqrt{2\pi}}[e^{-\frac{(A-\bar{A}-D_1)^2}{2\sigma_1^2}} + e^{-\frac{(A-\bar{A}+D_1)^2}{2\sigma_1^2}}] \\ &+ \frac{N_2}{\sigma_2\sqrt{2\pi}}[e^{-\frac{(A-\bar{A}-D_2)^2}{2\sigma_2^2}} + e^{-\frac{(A-\bar{A}+D_2)^2}{2\sigma_2^2}}] \\ &+ \frac{N_3}{\sigma_3\sqrt{2\pi}}e^{-\frac{(A-\bar{A})^2}{2\sigma_3^2}}\,, \end{aligned} \tag{3.6}$$

where N_i is the coefficient of the i^{th} Gaussian, σ_i is the Gaussian width parameter, $\bar{A}$ is the mean mass of the distribution, and D_i is the separation of the i^{th} Gaussian peak from $\bar{A}$ [98]. $\bar{A}$ can also be calculated from the experimental data by

$$\bar{A} = \sum_A A * Y(A)\,. \tag{3.7}$$

This approach is quite adequate to reproduce the fission product distribution where there is underlying data, as shown in Figure 3.13. FREYA also does admirably in reproducing the correlated gamma and neutron observables, a primary objective for the code and its intended applications [213, 214]. However, similar to GEF, FREYA is limited by the available complete sets of nuclear data, and struggles to simulate the energy dependent cumulative yields for specific isotopes, as demonstrated in Figure 3.11 and Figure 3.12. In this aspect, GEF outperforms FREYA significantly. However, FREYA runs far more quickly than GEF and is integrated into neutron transport codes, often making it more appropriate for modeling an application where fission is only one aspect of the entire system of interest.

Wahl Systematics

Wahl developed a set of empirical equations to describe the systematics of fission-product yields that has been used for decades. Unlike GEF or FREYA, Wahl does not attempt to develop an all-encompassing model, nor is there an attempt to tie parameters of the model explicitly to nuclear and quantum physics. Nonetheless, the model is similarly effective in reproducing the fission product distribution, as shown in Figure 3.14 [217].

The model developed by Wahl is a multi-Gaussian (3-7) approach similar to that outlined in Section 3.1.1. The addition of two more Gaussians has been shown to improve the

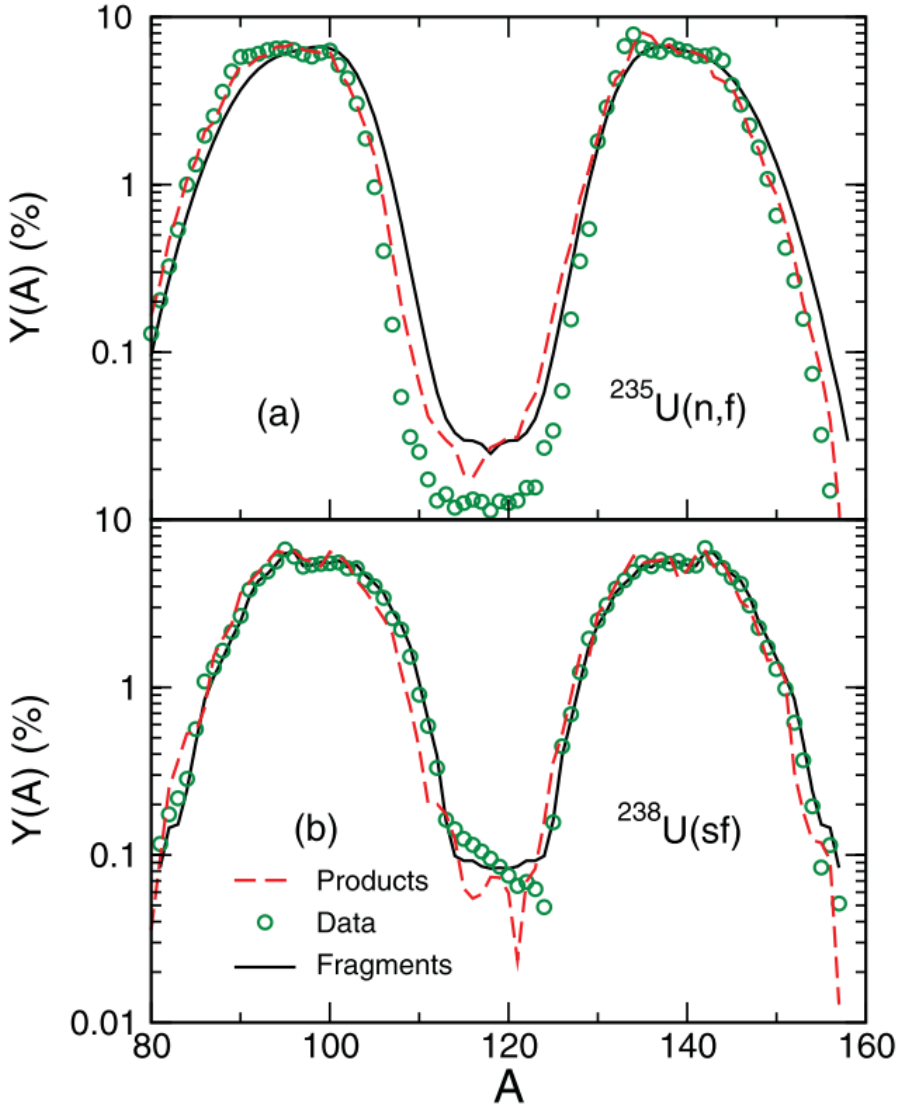

Figure 3.13: Comparison of the FREYA calculations and England and Rider evaluated data [64] for the mass distribution for thermal neutron induced fission on ^{235}U. The solid black curves are the five-Gaussian fits to the fragment distributions, while the red dashed curves are the results after neutron emission in FREYA [213].

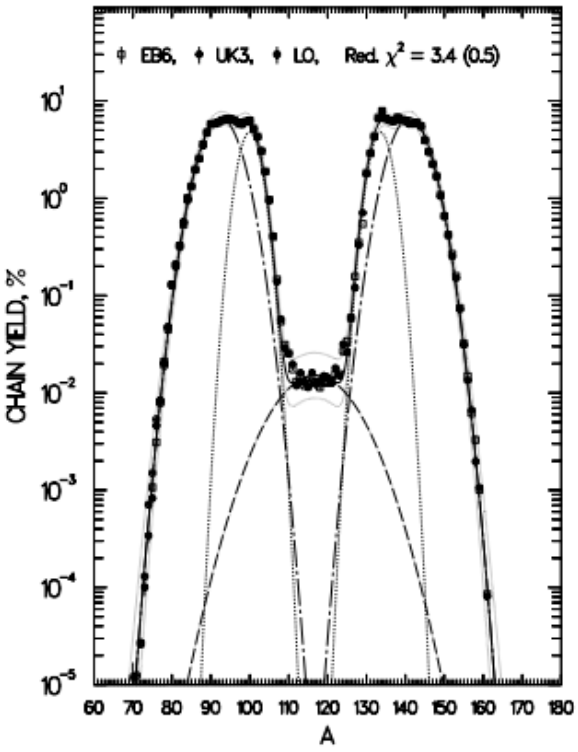

Figure 3.14: Comparison of the Wahl systematics and England and Rider evaluated data [64] for the mass distribution for thermal neutron induced fission on ^{235}U [217].

representation of $Y(A)$ on the wings of heavier fissioning nuclides (Z$\geq$94). Additionally, Wahl breaks the model parameters into the separate regions based on the Z and energy of the excited fissioning nucleus to improve the representation of the data. The multi-Gaussian functions are then fit to the available cumulative yield data using the method of least squares [217].

This is a large domain to fit, but Wahl's approach obtains more success in reproducing the fission product distributions over a wider range of fissioning nuclei and excitation energies than FREYA due to the more sophisticated approach to the same basic methodology. However, similar to FREYA, the lack of a tie to any fundamental physics limits the ability to extrapolate beyond the measured data. This is evident in Figure 3.11 and Figure 3.12 where GEF outperforms the Wahl systematics in reproducing the trends and values of the energy-dependent behavior for the fission product yield.

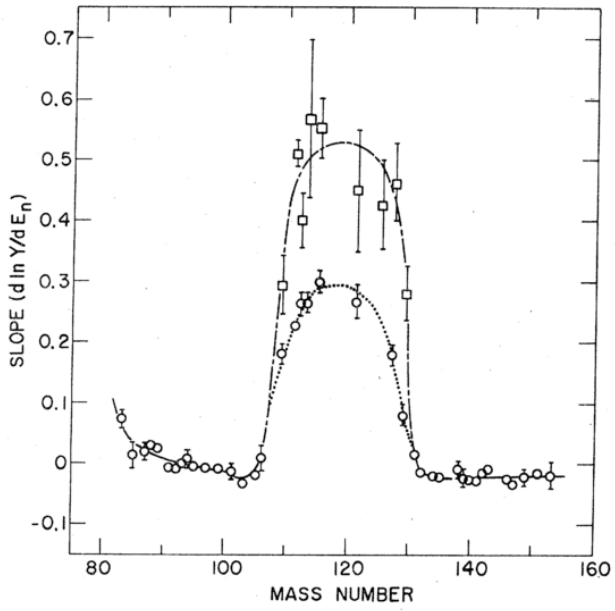

Figure 3.15: The constant in the exponential, b, from Equation 3.8 as a function of fission product mass for neutron induced fission on ^{235}U [155].

Nagy Fits

Nagy reduced the scale of the problem one step further and focused exclusively on an empirical model for the energy dependence of the fission product yield data. Nagy fit a series of fission product yield data against an exponential function of the form

$$Y(E_n) = Y_0 e^{bE_n}, \tag{3.8}$$

where b is a measure of the sensitivity of the fisson product yield to the incident neutron energy and Y_0 is the yield at thermal fission [155].

Equation 3.8 was then fit using the method of least squares to energy dependent data for each fission product of interest. For the asymmetric mass regions ($83 \leq A \leq 106$ and $131 \leq A \leq 153$), a single equation was used for all energies[3]. The symmetric mass region ($109 \leq A \leq 129$) was divided into the energy ranges corresponding to first chance fission (up to 5.5 MeV) and second chance fission (5.5 to 14.1 MeV). The resulting b parameters as a function of mass number are shown in Figure 3.15 [155].

As shown in Figure 3.11 and Figure 3.12, Nagy's approach is able to best model the energy dependence of the fission products. This is not surprising as it takes the most direct approach and does not try to fit the entire fission process with dozens of parameters. As such, it has limited predictive ability as the parameter values are determined empirically for

[3]Up to 14.1 MeV data was used for the fits.

a given mass change. However, interpolation between known parameters could be used to allow the Nagy approach to be used where limited data exists.

3.1.2 Fission Product Distribution Data

As seen in Subsection 3.1.1, the performance of fission models are heavily reliant on measured fission data. For this research, and fission model development in general, the most relevant measurements are those of the fission fragment and fission product yields and their dependence on the energy of the fissioning neutron [14]. Unfortunately, current evaluated nuclear data libraries, based on the original England and Rider evaluation with a literature cutoff date of 1989, only contain the fission product yield for thermal, fast (fission - like spectrum with average energy of 0.5 MeV), and high (14.1 MeV) energy neutrons [38, 64]. The limitation is manifested in the inability of most models to capture the energy dependence of the fission product yield, as illustrated by Figure 3.11 and Figure 3.12.

However, there have been a series of mono-energetic measurements for select fission products and the ^{236}U and ^{239}U fission systems done that could be used with the Nagy approach [40, 48, 72, 79, 82, 89, 121, 155, 157]. These measurements are generally only cumulative yields of select mass chains, but a few independent yields are reported as well. The limited data of select isotopes poses a significant limitation when considering which fission products to use for experimental validation purposes. While peak, or near peak, energy-dependent fission product data tends to be more abundant, the wing and valley fission products are more useful for measurement in the ETA context because they have far more energy sensitivity. Using available energy-dependent fission product data and the experimental limitations described in Subsection 2.3.3, a set of cumulative yield fission products are identified for use in the ETA experiments in the next section.

3.1.3 TNF Fission Product Estimates

Two approaches were taken to model the fission product distribution expected from exposure of a HEU sample to the objective TN+PFNS. First, the existing energy-dependent cumulative yield fission product measurements available were used to develop energy dependent fits according to the Nagy methodology [155]. This only allowed for specific fission products to be estimated based on the available data in the literature.

The fission products shown in Table 3.1 are a subset of the available data that were selected for this research based on the criteria of half-life, location on the FP yield distribution, and decay radiation characteristics. Key characteristics of each FP, according to the selection criteria, are listed in Table 3.1[4]. While a broader set of FPs could be analyzed, these represent the most accessible and easiest to measure while ensuring a diversity of energy dependence behavior[5].

[4]BR = branching ratio

[5]In general, the FP yield trends are: a) the light and heavy peaks have a slight linear decrease in yield

Table 3.1: Fission products of interest for this research.

A	**FP**	**Location**	$T_{1/2}$	E_γ	**BR** [%]
95	$^{95}_{40}$Zr	Light Peak	64.032 d	724.192/756.725 keV	44.27/54.38
97	$^{97}_{40}$Zr	Light Peak	16.75 hr	743.36 keV	93.09
111	$^{111}_{47}$Ag	Valley	7.45 d	342.13 keV	6.7
115	$^{115}_{48}$Cd	Valley	53.46 hr	933.84 keV	2.0
133	$^{133}_{53}$I	Heavy Peak	20.83 hr	529.87 keV	87.0
140	$^{140}_{56}$Ba	Heavy Peak	12.7527 day	537.26 keV	24.39
147	$^{147}_{60}$Nd	Heavy Wing	10.98 d	91.11/531.02 keV	28.1/13.4
151	$^{151}_{61}$Pm	Heavy Wing	28.40 hr	340.08 keV	22.5
153	$^{153}_{62}$Sm	Heavy Wing	46.50 hr	103.18	29.25

The cumulative yield data available from each FP listed in Table 3.1 was fit according to Equation 3.8 to develop mass-chain-specific Y_0 and b parameters. The cumulative yield for each FP for exposure of a 93.15% ^{235}U HEU sample to the TN+PFNS objective spectrum was then calculated as

$$Y(A,Z) = \sum_{i=1}^{4}\sum_{g=1}^{G} f_i Y_{i,0}(A,Z) e^{b_i(A,Z)E_g} * \frac{\phi_g}{\int \phi(E)\ dE}\,, \tag{3.9}$$

where f_i is the fission fraction of the i^{th} isotope, E_g is the mid-point energy of the g^{th} energy group, and ϕ_g is the fluence in the g^{th} group. The four isotopes considered are ^{234}U, ^{235}U, ^{236}U, and ^{238}U. Since ^{234}U and ^{236}U are minor and threshold fissioners, the fission fraction or each were summed with the fission fraction of ^{238}U. The FP yields calculated using Nagy fits weighted to the objective spectrum from Equation 3.10 are shown in Table 3.2.

The second method used to estimate the FP yield was with the GEF code and was calculated as

$$Y(A,Z) = \sum_{i=1}^{4}\sum_{g=1}^{G} f_i Y_i(A,Z,E_g) * \frac{\phi_g\,,}{\int \phi(E)\ dE} \tag{3.10}$$

where $Y_i(A,Z,E_g)$ is determined from GEF energy- and fission-system-dependent calculations. While not reproducing the energy dependence of the data quite as well as the Nagy fits, GEF was the next best option of the codes and methods considered. GEF has the

with increasing neutron energy, b) the valley has an exponential increase in yield with increasing neutron energy, and c) the wings range from flat to exponential increases in yield with increasing neutron energy.

Table 3.2: Nagy- and GEF-based fission product yield estimates for select FPs from a 93.15% ^{235}U HEU foil exposed to a TN+PFNS [155, 185].

FP	Nagy $f_{cum}(A, Z)$ [%]	GEF $f_{cum}(A, Z)$ [%]
$^{95}_{40}$Zr	6.17 ± 0.09	6.47 ± 0.30
$^{97}_{40}$Zr	5.75 ± 0.09	6.47 ± 0.28
$^{111}_{47}$Ag	0.25 ± 0.01	0.21 ± 0.12
$^{115}_{48}$Cd	0.25 ± 0.01	0.24 ± 0.11
$^{133}_{53}$I	6.41 ± 0.13	6.04 ± 0.37
$^{140}_{56}$Ba	5.71 ± 0.07	5.41 ± 0.28
$^{147}_{60}$Nd	2.12 ± 0.03	2.00 ± 0.22
$^{151}_{61}$Pm	0.47 ± 0.02	0.46 ± 0.10
$^{153}_{62}$Sm	0.18 ± 0.01	0.17 ± 0.05

benefit of allowing for the full fission product distribution to be estimated, as shown in Figure 3.16. The specific yields for the FPs that are to be measured for this research are shown in Table 3.2 in comparison with the Nagy estimated yields.

3.2 Neutron Reactions

Spectral shaping of an incident neutron energy distribution is governed by, and fundamentally limited by, the available neutron interactions that serve as the energy loss mechanisms. This section explores the major neutron interactions in this context to understand the underlying physics of spectral shaping. These concepts can be used to understand the selection of materials appropriate for an ETA design of a given application, and each will be described in relation to their applicability to the TNF synthetic debris application.

3.2.1 Elastic Scattering

The kinematics of elastic neutron scattering are well documented [109], but a couple of key outcomes are described here in the context of ETA design, specifically for the TNF TN+PFNS objective spectrum. First, the maximum energy loss for a neutron elastically scattering off of a nucleus is given by

$$Q_{max} = \left(1 - \frac{(A-1)^2}{(A+1)^2}\right) E \,, \tag{3.11}$$

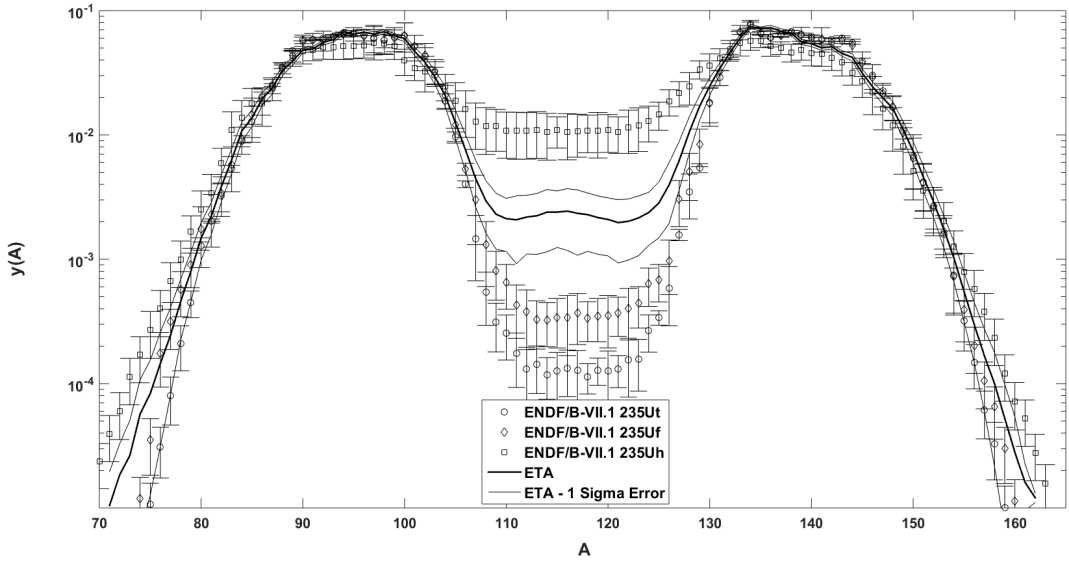

Figure 3.16: GEF-based fission product yield estimates for a 93.15% ^{235}U HEU foil exposed to a TN+PFNS [185].

where E is the initial neutron energy and A is the target atom mass. For perspective, elastic scattering on hydrogen can result in a complete loss of energy in one scatter, but scatter off of a ^{208}Pb nucleus will loose a maximum of 2% of the initial energy. The average energy loss, assuming isotropic scattering in the center-of-mass system, is then

$$Q_{avg} = 1 - \left(1 + \frac{(A-1)^2}{(A+1)^2}\right)\frac{E}{2}. \tag{3.12}$$

Because the TN+PFNS has very few thermal and low-energy neutrons, Equation 3.11 and Equation 3.12 indicate that low-A materials would be undesirable due to fewer scatters required for thermalization. Mid- to high-A materials provide more fine-tuned control over the neutron population for elastic scattering reactions and are likely to be better suited to this application.

High-A materials offer two additional advantages for the TN+PFNS application. One of the primary goals for any ETA generating the TN+PFNS from a NIF source spectrum is to down-scatter the 14.1 MeV neutrons. In the 10-15 MeV energy region, the trend is towards higher elastic scattering cross sections with increasing A, as shown in Figure 3.17. Additionally, the overall trend is for increasing atom density with increasing Z. Therefore, higher A materials will scatter the D-T fusion neutrons more frequently and be more beneficial for generating the TN+PFNS.

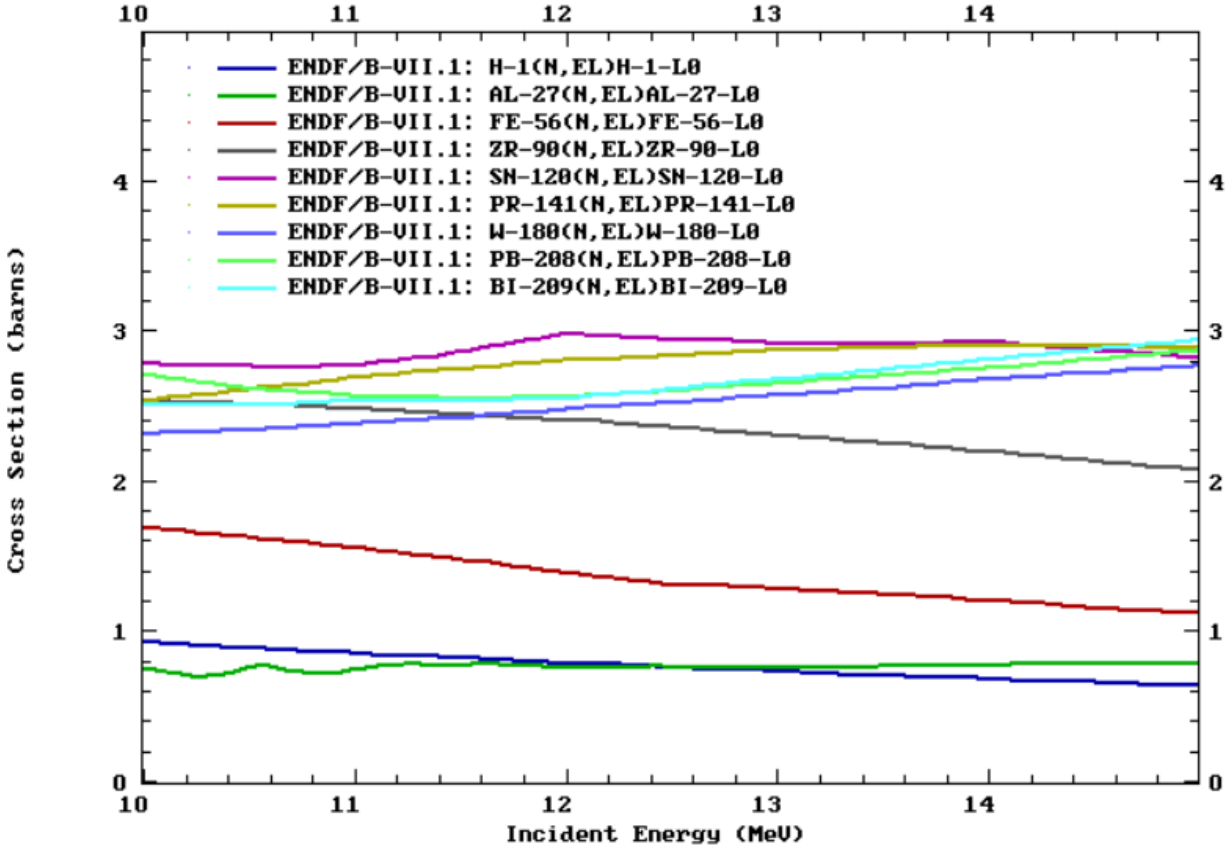

Figure 3.17: Comparison of the elastic scattering cross section of several isotopes spanning from A=1 to A=209 [38].

3.2.2 Inelastic Scattering

In inelastic neutron scattering, the total kinetic energy before and after interaction is not conserved, and a portion of the incident neutron energy is absorbed by the nucleus, resulting in the population of an excited state. The energy loss of the neutron depends on the states available for population in a given material. The lowest states can range from several keV in the actinides to several MeV in tightly bound nuclei such as ^{12}C, and the highest states range up to neutron separations energies in the range of several MeV. Generally speaking, the majority of the transitions available tend to be in the hundreds of keV to a few MeV range.

The overall trends are a decrease in the energy of the lowest lying state and an increase in the number of states with increasing Z. The increase in the number of states translates to a general increase in the inelastic scattering cross section for high Z materials, but these global trends are subject to significant local deviations because of shell and nuclear structure effects. The differentiation of the cross-section and variable energy loss can be exploited to

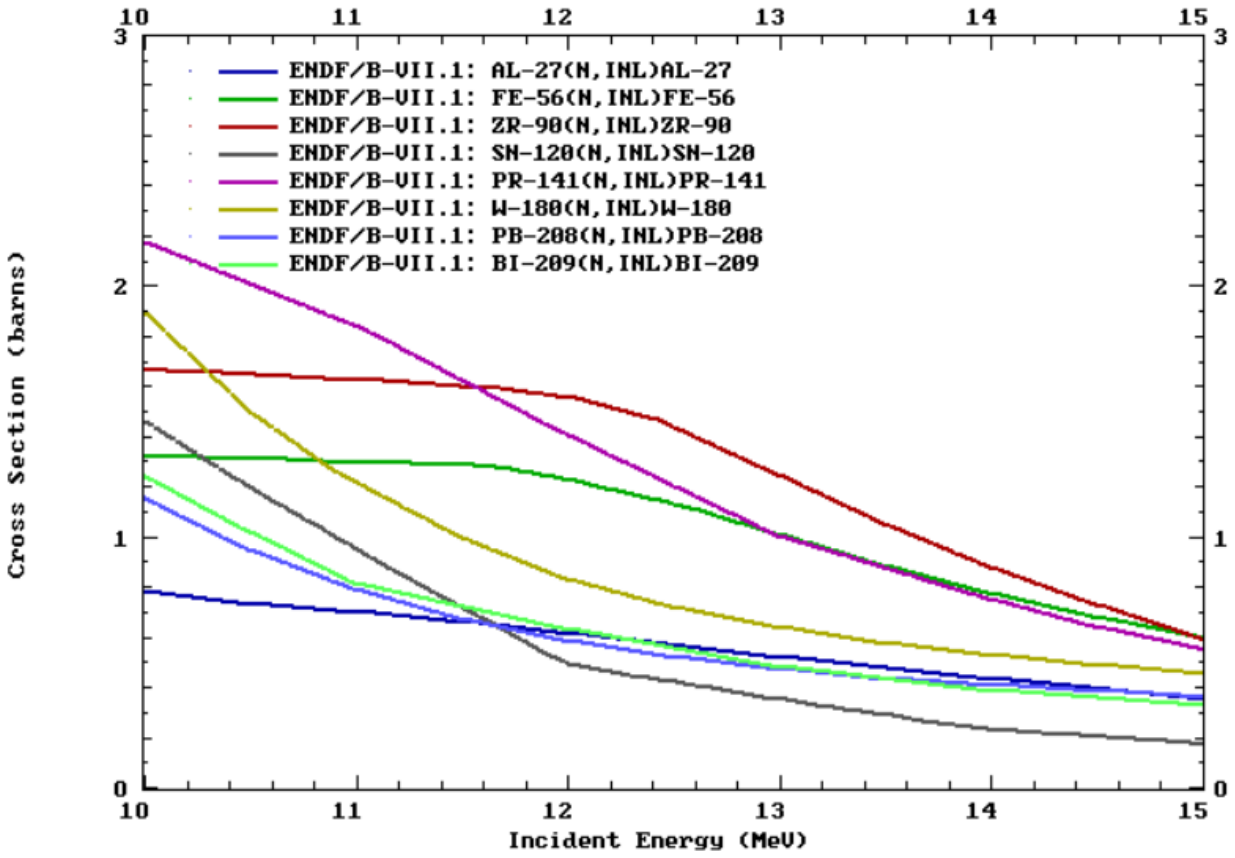

Figure 3.18: Comparison of the inelastic scattering cross section of several isotopes spanning from A=13 to A=209 [38].

fine tune the spectral shaping of the 100s of keV to several MeV range.

However, there is little differentiation of the inelastic cross section in the 14.1 MeV range important for depopulation of the D-T fusion peak, as illustrated in Figure 3.18. High-Z materials will still maintain an advantage due to increased reaction rates from a generally higher atom density. In contrast to elastic scattering, this gain in reaction rate for high-Z materials is not necessarily offset by a reduction in the energy loss per reaction, which is useful to move neutrons from the TN to Watt portion of the objective TN+PFNS.

3.2.3 (n, xn)

(n, xn) reactions result in the absorption of one neutron followed by the emission of two or more neutrons, through the compound nucleus formation process or pre-compound emission of a neutron with lower energy. For the TN+PFNS objective spectrum, the formation of a compound nucleus is a beneficial attribute of the (n, xn) reactions. In the compound nucleus, the neutron shares its kinetic and binding energy with many nucleons thereby “heating up”

the nucleus. The subsequent interaction of the "hot" nucleus results in a probability for one or more neutrons to "boil off." This is the same process for prompt neutrons emitted from the primary fission fragments[6], and the resulting neutrons have an "evaporation" spectrum. While the spectrum for neutrons evaporated at temperatures associated with fission differs than that at temperatures associated with (n, xn) reactions from neutrons with up to 14 MeV of kinetic energy, the differences are small making the (n, xn) reaction a key component for any ETA design for the TN+PFNS application.

Nature grants another favor in addition to the favorable resulting neutron energy distribution in the form of favorable cross-section trends. The (n, 2n) cross-section is on the order of the elastic scattering cross-section near 14.1 MeV making it a viable reaction in this region. The higher-A materials also tend to have higher overall cross-sections as shown in Figure 3.19. This, combined with higher atom densities, results in the most favorable combination of reaction rate and energy loss of any neutron interaction mechanism available in the 14 MeV energy range.

3.2.4 (n,γ)

The final reaction that needs mentioning is the (n,γ), or more generally (n, abs) reaction. These reactions absorb a neutron and generally form a compound nucleus, but they emit a non-neutron particle. As such, they are parasitic reactions, which lowers the overall neutron economy of the spectral shaping system. The reduction in neutron economy is generally not beneficial in the TNF application where higher efficiencies and fission yields are desired.

However, these reactions can be useful in three ways. First, the (n, x) reactions can be useful as an interaction mechanism for high energy neutrons. This is not necessary when NIF is the source, but it would be for a white source like the deuteron breakup reaction at the 88-Inch Cyclotron. Second, the (n,γ) reactions are useful to "clean-up" any low energy neutrons resulting from over thermalization of the spectrum. Finally, (n,γ) reactions are useful as a diagnostic to measure the spectrum generated through activation analysis, which is discussed further in Chapter 7.

[6]It is worth noting that this is not true for the scission and delayed neutrons which contribute to the observed Watt spectrum.

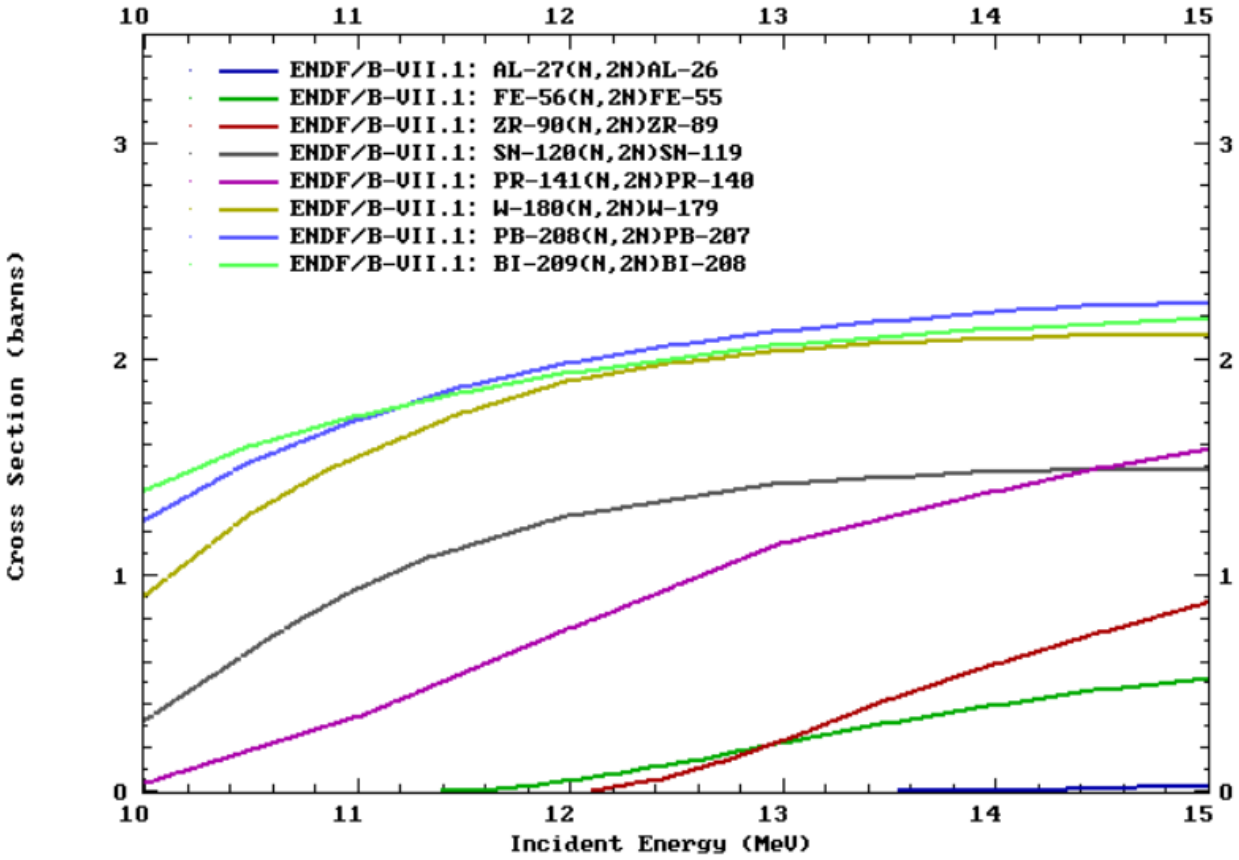

Figure 3.19: Comparison of the (n, 2n) reaction cross section of several isotopes spanning from A=13 to A=209 [38].

Chapter 4

Neutron Spectral Shaping Background

If the neutron did not exist, it would need to be invented.

- Bertram Brockhouse, 1994 Nobel Laureate in Physics

Very early on, it was deemed desirable to modify neutron spectra. By 1935, only three years after the discovery of the neutron itself, hydrogen thermalization and cadmium filters were employed to modify or remove portions of neutron spectra [37, 58]. Over 80 years later, neutron spectral modification techniques have advanced, but the same basic concepts are largely the state-of-the-art today. This chapter starts with a description of modern applications of the neutron filter and screen concepts. Next, the most sophisticated approach to targeted neutron spectral shaping, beam shaping assemblies (BSAs) designed primarily for boron neutron capture therapy (BNCT), are described. Finally, the chapter closes with a description of the limitations to the BSA approach and the areas where this research aims to advance the state-of-the-art for designing neutron spectral shaping assemblies.

4.1 Neutron Filters and Screens

Neutron filters, sometimes called neutron screens, have been used in a wide variety of nuclear science and engineering applications. In activation analysis, highly absorbing filters employing Cd, B, Gd, Hf, etc. are often used to suppress the thermal neutron flux, allowing for epi-thermal reactions to dominate [179]. Materials science and nuclear physics have used neutron filters on cold neutron beams to filter neutrons with wavelengths less than the critical wavelength, resulting in a high purity, low energy beam [3, 61]. To certify epi-thermal and fast reactor designs, solid and liquid neutron filters have been used for irradiation degradation and power transient studies, respectively [42]. In the field of radiation detection, filters have been used to enhance the gamma signal by suppressing high neutron fields and to selectively detect thermal and fast neutrons [24, 107]. Neutron filters can be used to produce

quasi-monochromatic neutron beams with V, Mn, S, ^{56}Fe, or other nuclei that have deep interference minima [153]. Optimized, sometimes layered, neutron filter designs for several applications such as neutron radiography and neutron transmutation doping of silicon have also been developed by combining multiple elements from the list of applications above [106, 152].

Despite the broad range of applications requiring spectral and different nuclear properties that are employed for each application, the unifying feature of all filters is that they modify an incoming neutron spectrum by removing portions of that spectrum. This technique is insufficient for this research, as there is not a suitable starting neutron source in which cuts alone can be used to achieve the TN+PFNS. Additionally, cutting a neutron spectrum reduces the available flux on target, an area where all available neutron sources are currently deficient compared to the desired source term.

In contrast to filters, moderation can be used to soften a neutron spectrum without cutting flux. The most notable example of this is nuclear reactors, which thermalize a starting PFNS to reactor thermal energies while minimizing non-fission absorption. This concept is also regularly employed in neutron detection to take advantage of the high thermal absorption cross section of several materials, or to help unfold the incident neutron spectrum [15, 109].

4.2 Beam Shaping Assemblies

Perhaps the most advanced employment of neutron filters and moderation for the purpose of spectral modification has been done in BSA development for BNCT research [**Goff2003**, 6, 18, 27, 142, 173, 210, 208]. BNCT uses the capture of neutrons on boron, a process that is maximized at thermal neutron energies, to deposit large doses locally in brain tumors to kill cancer cells [**Goff2003**, 208]. To maximize dose to the tumor while minimizing the overall dose to the patient, it was determined that an optimal neutron spectrum peaked at approximately 10 keV was needed, but neutron sources with this characteristic spectrum and suitable treatment times do not exist [142, 208, 210]. BSAs have been used to shape the neutron spectra from subcritical assemblies, research reactors, ^{7}Li(p,n)^{7}Be, ^{9}Be(d,n)^{10}B, (γ, n), D-D, and/or D-T sources to a spectrum that meets the clinical needs for BNCT [**Goff2003**, 18, 31, 173, 208]. Figure 4.1 shows one of the BSA designs proposed for modification of a ^{7}Li(p,n) source, and Figure 4.2 shows the resulting neutron energy spectrum from this design [142].

The BNCT BSA design methodology differs significantly from the surrogate debris applications in the target objectives and design optimization[1]. First, the target objective of BSAs for BNCT was not a spectrum but a ratio of the dose to a tumor and the dose to the patient. This was often represented as a quasi-monoenergetic source at approximately 10 keV, but that was not the controlling figure of merit for the design. This distinction is important because there is no guarantee that the spectrum to achieve a given dose ratio

[1]For a full description of ETA design objectives, see Chapter 2.

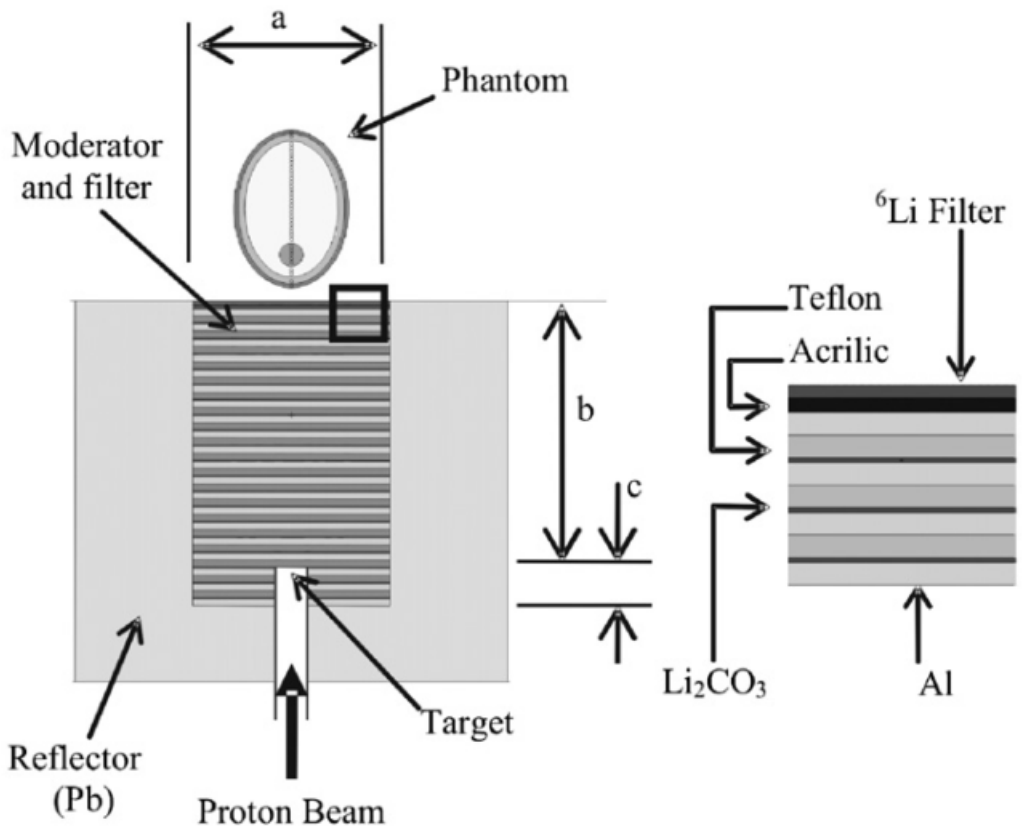

Figure 4.1: Example BSA configuration for modification of a ^{7}Li(p,n) source [142].

is not degenerate. While this does not matter for the BNCT application, it does for the TN+PFNS where the same spectrum would be useful for many other applications besides the specific TNF application to generate synthetic FPs pursued in this research.

Additionally, BCNT sources can be made sufficiently intense, or boosted using subcritical assemblies, to allow filtering techniques to significantly reduce the flux and still obtain enough neutrons at the target. In contrast, the potential sources for TN+PFNS applications do not have sufficiently intense starting neutron sources, limiting the choice of filtering and moderating materials because of neutron economy needs.

However, the concept of using spectral modification of an existing source to become representative of the TN+PFNS shows promise. The BSA concept meets many of the high level design objectives described in Chapter 2 and the DoD solicitation described in Chapter 1 in that BSAs are inexpensive, flexible[2], and do not need to utilize SNM. For these reasons, this research will pursue neutron spectral modification methods and aim to improve upon

[2]This is evidenced by the wide range of sources that BSA designs have been developed for to meet criteria similar to those needed for BNCT.

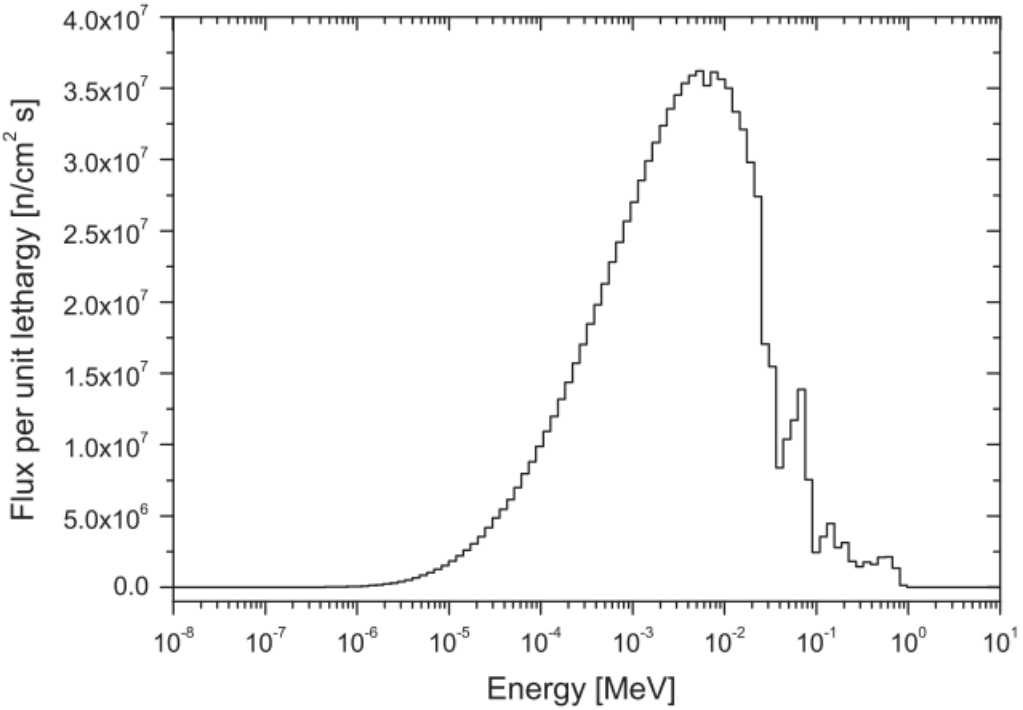

Figure 4.2: Neutron spectrum resulting from modification of a ^{7}Li(p,n)^{7}Be source using the BSA configuration shown in Figure 4.1 [142].

the limitations of previous employment methods.

4.3 Limitations to Current State-of-the-Art

Based on the wide array of different applications for neutron spectral shaping detailed in this chapter and Section 1.5 as well as the long history of their use, one might think that the field is fairly mature. In reality, the previous approaches of neutron screens, filters, moderators, and BSAs have had limited neutron spectral shaping goals, if any explicit spectrum shaping objectives at all. None of the approaches sought to design a complicated spectrum such as the TN+PFNS objective spectrum used in this research. At most, the best that has been achieved is either hardening a spectrum, softening a spectrum, or generating a quasi-monoenergetic spectrum. Here, we aim to design a complete spectrum, which is a significant advance on the previous applications in the literature.

How the design of the energy tuning assembly (ETA) is approached also is a significant departure from the current methodologies in the literature. Previous approaches have relied on either analytic or parametric approaches to the design of the neutron filter, screen, moderator, or BSA. In most cases, this is possible due to the design being considered – i.e.

a single material where the only design parameter is the thickness. Even those applications which have sought complicated, multi-layered designs to achieve their objectives have used the parametric approach [15, 95, 106, 152, 208]. As the complexity of the design space and objective increase, the parametric approach becomes increasingly less desirable.

The benefits and drawbacks of enumerative (parametric) design approaches for complicated designs are detailed further in Subsection 5.2.1. To illustrate the drawbacks, consider the extensive work that has gone into the BNCT application over the course of ∼60 years [12]. One reason for the sheer volume of BSA papers, dissertations, and theses, is that numerous starting neutron sources and desired tumor treatment locations have been considered for the BNCT application. Because each design process tends to be parametric, future design efforts for new sources or tumor locations are not greatly enhanced by the previous work. In fact, there are many examples in the literature of multiple BSA designs for essentially the same neutron source and treatment scenario. For example, the BSA shown in Figure 4.1 was designed for a ^{7}Li(p,n) source for treatment of brain tumors [142]. There were previous papers describing the same process that came up with the design shown in Figure 4.3 instead. While the Minsky design (Figure 4.1) did improve upon the patient outcomes in some regards, such as patient treatment times and treatable depth, the overall dose to tumor / dose to patient ratio is approximately the same at the peak, as shown in Figure 4.4.

One of the reasons that revisiting previous work can result in design improvements is that the parametric design process tends to result in the investigation of limited geometries and materials, often based on those that worked for previous designs. This unnecessarily limits the design space in ways that can drastically impact the overall performance of the design. The benefits of pursuing a true optimization process was highlighted by work done at UC Berkeley in the early 2000's by Vujic and Greenspan. In the late 1990s and early 2000s, two Ph.D. dissertations and a Masters thesis were performed at UCB to design BSAs [**Goff2003**, 17, 208]. Following this work, initial efforts at formal optimization of these and similar BSA deigns were pursued using the SWAN code. Despite 2-D convergence issues and a limited library of materials considered, the SWAN study was able to identify new materials and BSA geometries that outperformed previous work [215].

This research will expand upon the initial SWAN studies to develop an optimization methodology to design spectral shaping assemblies. Through framing the design as a formal optimization problem, the design space can be expanded to materials and/or geometries that were not previously considered. Additionally, through the use of global or nearly-global optimization techniques, designs developed will have the maximum performance under the constraints and objectives considered. Finally, the development of optimization software will enable future designs to be generated at a fraction of the cost in terms of manpower and research effort, thereby greatly accelerating the pace of development in this field. Chapter 5 explores optimization approaches available and selects one that is the most applicable to a wide range of spectral shaping applications.

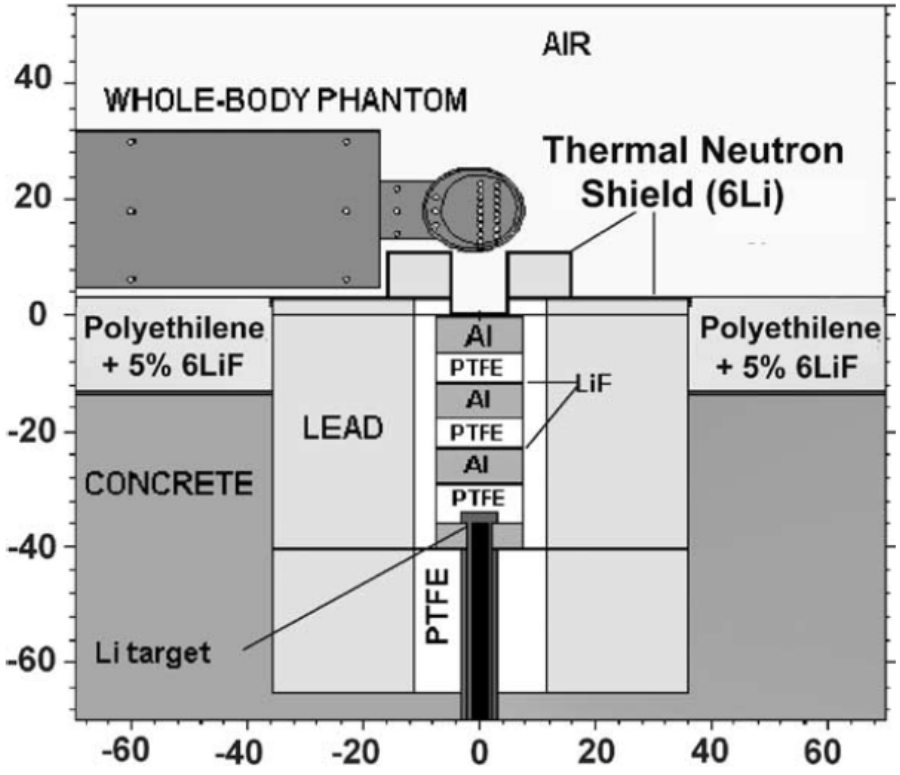

Figure 4.3: Alternate BSA configuration for a ^{7}Li(p,n) source [27].

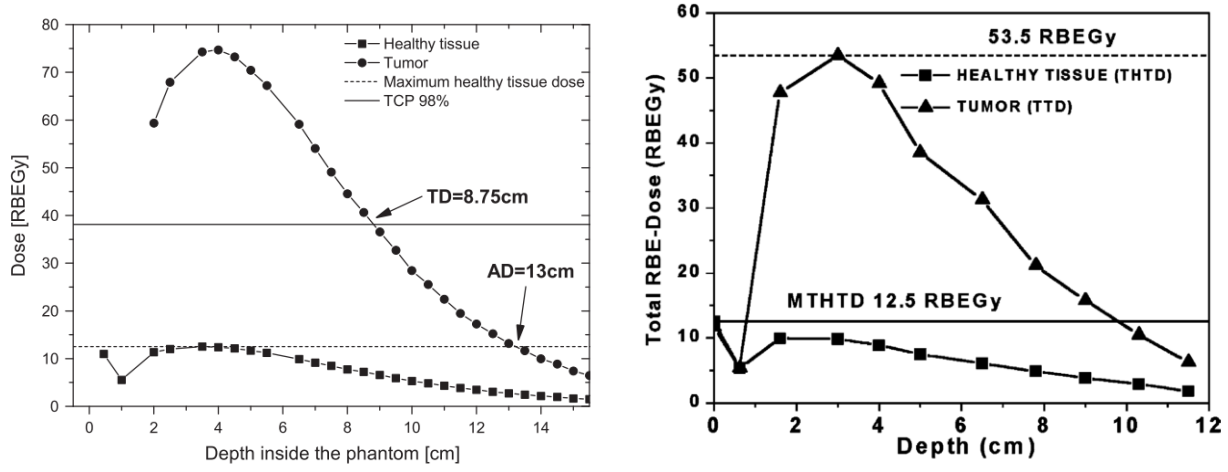

(a) a) (b) b)

Figure 4.4: Comparison of the dose profiles achieved for the BSA design shown in a) Figure 4.1 and b) Figure 4.3 for a ^{7}Li(p,n) source applied to brain tumors for BNCT [27, 142].

Chapter 5

Optimization Theory and Background

For rarely are sons similar to their fathers:
most are worse, and a few are better than their fathers

- Homer, The Odyssey

The question of how to best improve upon shaping assemblies' (BSAs') or energy tuning assemblies' (ETAs') ability to shape a neutron beam's characteristic energy distribution to another desired distribution, or spectrum, is difficult to answer analytically or from intuition for many reasons. First, the problem space is large and many dimensional. Second, there are multiple competing neutron interactions with widely varying and often rapid changes in probability of occurrence. Finally, any answers that are derived from either approach will be extremely problem specific and require starting anew when the problem changes. Conversely, formal optimization techniques are designed to answer such questions, can be made more or less general, and bring a level of reproducibility to the design process. In other words, if done appropriately, the application of optimization to the ETA design processes can be extended to cover a broad set of design problems to generate ideal, or nearly ideal, solutions as opposed to a one-off point design.

This chapter starts by defining general optimization problems and frames ETA design within this construct. General approaches to optimization are then described along with some high level benefits and drawbacks. The state of the art for mixed-integer nonlinear programming (MINLP) is explored in detail to consider options available. Finally, the chapter closes by discussing metaheuristic optimization, the technique chosen for application to the ETA design problem.

5.1 ETA Optimization Problem Definition

Many engineering problems and processes can be described by multi-dimensional surfaces that form the "fitness" landscape of the solution [55, 115, 146, 230]. An example of a potential

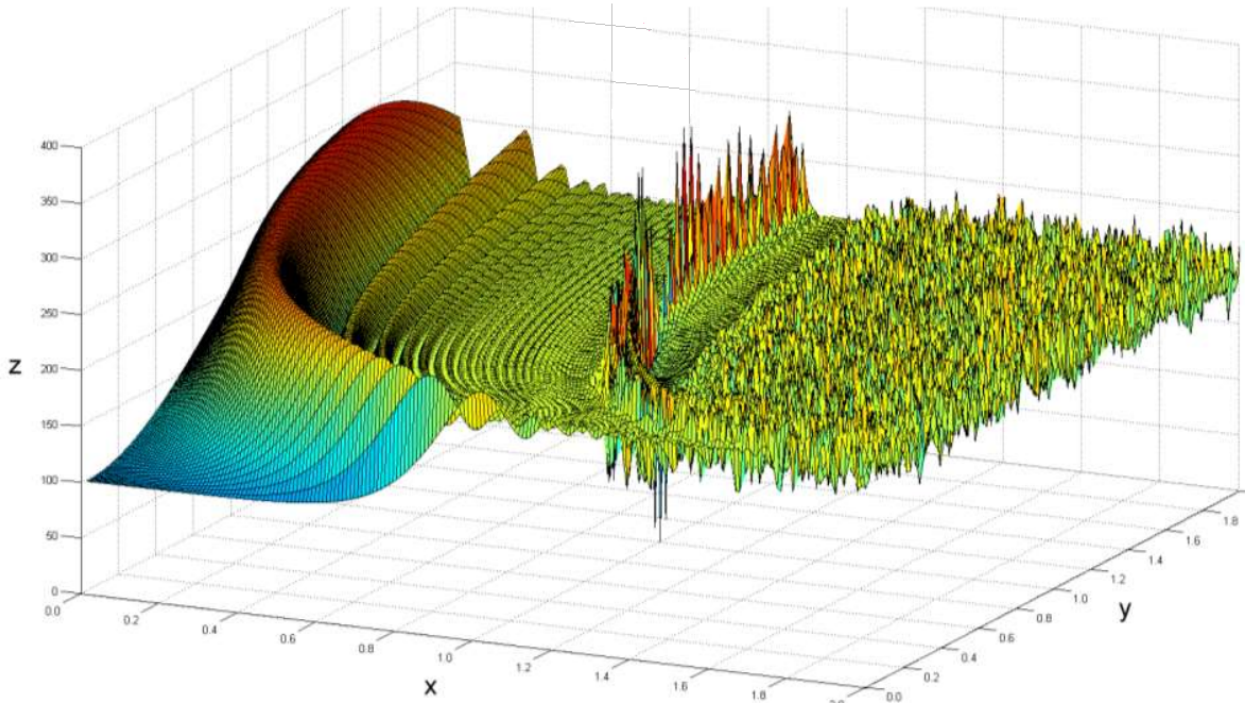

Figure 5.1: Example of a noisy, multi-modal fitness landscape.

landscape is shown in Figure 5.1. A single point on the fitness landscape is obtained through evaluation of one n-dimensional solution set against desired objectives such as performance, size, cost, etc. All solution sets that meet the given design constraints of a problem form the complete fitness landscape, which can have many locally-optimum solution sets (multi-modal). The combination of a large n-dimensional search space, a noisy, multi-modal fitness landscape, and a complex objective function evaluation, often via a black box code, makes the determination of the globally optimum solution virtually impossible via intuition or parametric studies. Formal optimization techniques are required to solve these types of problems.

At its most basic, an optimization problem can be stated as

$$\underset{\vec{x}\in\mathbb{R}^d}{\text{Minimize}} \quad f_i(\vec{x}), \qquad (i = 1,\ 2,\ \ldots,\ I)^T, \tag{5.1}$$

$$\text{Subject to:} \quad g_j(\vec{x}) \leq 0, \qquad (j = 1,\ 2,\ \ldots,\ J), \tag{5.2}$$

$$h_k(\vec{x}) = 0, \qquad (k = 1,\ 2,\ \ldots,\ K), \tag{5.3}$$

where I, J, and K are the number of objective functions, inequality, and equality constraints, respectively. $\vec{x}$ is the candidate design solution given by $\vec{x} = (x_1, x_2, \ldots, x_n)^T \in \mathbb{R}^d$, where $\mathbb{R}^d$ is the design space. Optimization problems can be classified by sub-setting the mathematical formulation in ways that are illustrative to assessing the requirements for a given optimization algorithm. Some of the more general classifications are considered here: single

objective ($I = 1$) versus multi-objective ($I > 1$); linear versus nonlinear objective function(s); differentiable versus derivative free objective function(s); unconstrained ($J = K = 0$) versus constrained ($J|K > 0$); continuous, discrete, combinatorial, or mixed-integer (MI) design space ($\mathbb{R}^d$); and uni-modal (convex) versus multi-modal (non-convex) fitness landscapes ($f(\vec{x})$) [88].

For the ETA design problem being considered, Equation 5.1 can be formulated as a flux-weighted relative least squares minimization given by

$$f_1(\vec{x}) = \sum_{g=1}^{G} \left(\frac{\phi_g^{TNF} - \phi_g^C(\vec{x})}{\phi_g^{TNF}} \right)^2 * \frac{\phi_g^{TNF}}{\phi^{TNF}} \,, \tag{5.4}$$

where ϕ^{TNF} is the technical nuclear forensics (TNF) relevant fluence, ϕ_g^{TNF} is the TNF fluence in a given energy bin g, and $\phi_g^C(\vec{x})$ is the fluence in a given bin g for the spectrum obtained from a candidate design. Equation 5.2 can be formulated as

$$g_1(\vec{x}) = \sum_{n=1}^{N} \rho_n V_n - W \leq 0 \tag{5.5}$$

for the weight constraint, where ρ_n and V_n are the mass and volume of the n^{th} component, respectively, and W is the maximum system weight allowed. The minimum reactions constraint can be formulated as

$$g_2(\vec{x}) = N_f^{min} - \phi^C(\vec{x}) V \Sigma_f^{HEU} \leq 0 \,, \tag{5.6}$$

where $\phi^C(\vec{x})$ is the candidate design's neutron spectrum produced across the highly enriched uranium (HEU) foil, V and Σ_f^{HEU} are the volume and macroscopic cross-section of the HEU foil, respectively, and N_f^{min} is the minimum number of fissions required. It is worth noting in this problem formulation that $\phi^C(\vec{x})$ from Equation 5.4 and Equation 5.6 are informed by black-box radiation transport calculations.

The design vector $\vec{x}$ contains all of the variables describing the system (ETA design). $\vec{x}$ for a 2-D ETA design is given by

$$\begin{aligned} \vec{x} = \{ & Cell_1[M_1, \rho_1, IR_1, OR_1, Z1_1, Z2_1],\ Cell_2[\ldots],\ \ldots, \\ & Cell_N[M_N, \rho_N, IR_N, OR_N, Z1_N, Z2_N],\ R_{foil},\ Z_{foil}\} \,, \end{aligned} \tag{5.7}$$

where M_i is the material for the i^{th} cell (discrete variable of size m, where m is the number of materials being considered); ρ_i is the density corresponding to M_i (discrete variable of varying size depending on the allowable densities for a given material); IR_i and OR_i are the inner and outer radii, respectively (continuous variables); $Z1_i$ and $Z2_i$ are the initial and final Z locations, respectively (continuous variables); R_{foil} and Z_{foil} specify the foil's location (continuous variable); and N is the number of cells, or components, in the geometry (integer variable). Additionally, the location of the materials within the construct of each component or cell can be treated as a combinatorial variable such that the material ordering within the cells can be swapped.

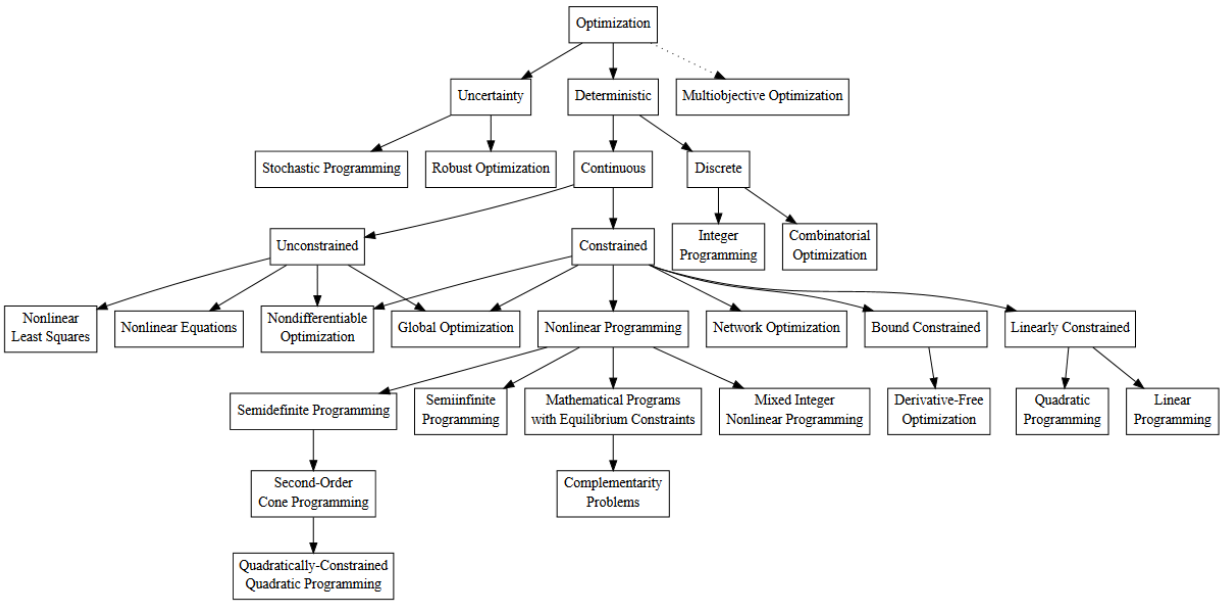

Figure 5.2: Optimization taxonomy with an emphasis on deterministic techniques [162].

In summary, the ETA design is best formulated as a single objective, nonlinear, derivative-free, constrained, combinatorial *and* mixed-integer, multi-modal optimization problem. Additionally, the constraints and objective function are informed by black box radiation transport calculations that may not be continuous and can be very noisy due to limitations in the model or underlying data. With the problem definitions and categorizations in mind, a survey of the literature for optimization approaches can be undertaken.

5.2 General Optimization Methods

The optimization field can be subdivided in many ways. Often, the literature is broken out based on the categorizations outlined in Section 5.1, but most taxonomies converge to three top level techniques: deterministic (calculus-based), stochastic (random), or enumeratives (parametric) [162, 226]. An example taxonomy with an emphasis towards deterministic approaches is shown in Figure 5.2, and another with emphasis towards stochastic approaches is shown in Figure 5.3. Each of these three general classifications is explored in broad strokes with respect to the ETA design optimization in the following sections.

5.2.1 Enumerative Optimization

Enumerative optimization techniques involve breaking down the variable space into all possible solutions [26, 178]. These can range from unguided parametric studies where the search space is discretized, to computing all possible combinations, to guided approaches such as

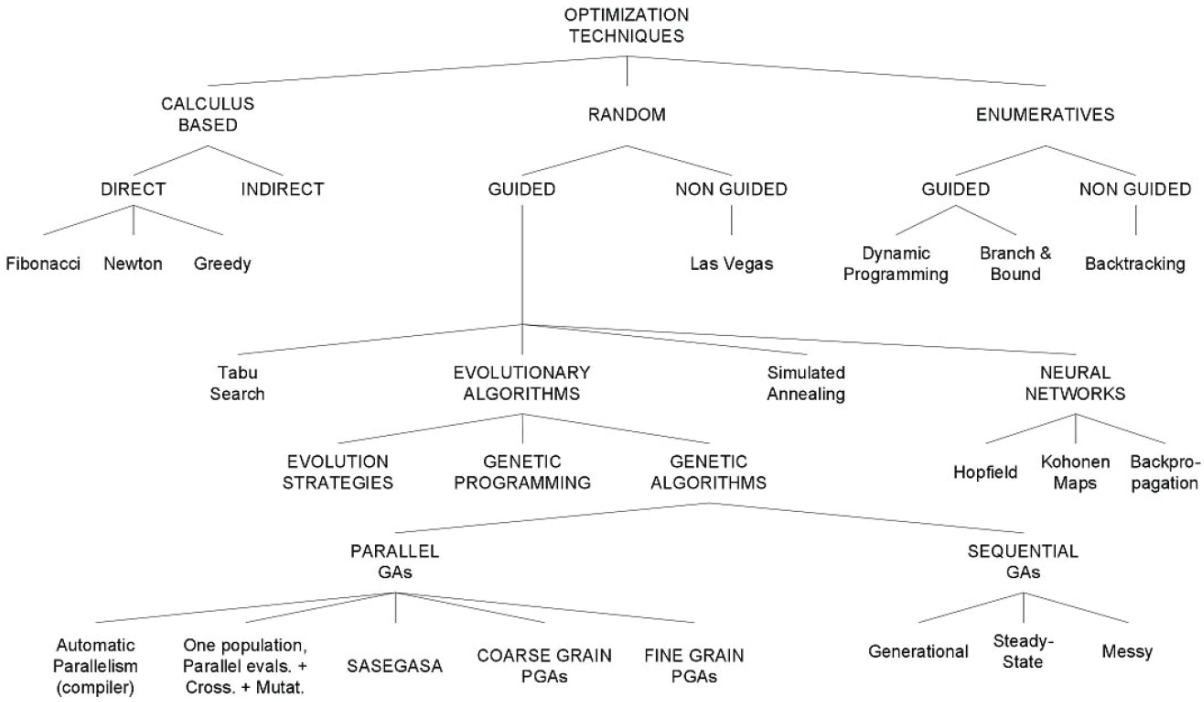

Figure 5.3: Optimization taxonomy with an emphasis on stochastic techniques [226].

branch and bound [34, 120]. Branch and bound techniques are considered further in Section 5.3.

Parametric studies are common in engineering design [42, 95, 208]. The approaches are attractive because their use requires little to no formal framework – i.e. every competent engineer comes equipped with the knowledge and insight required by this approach. When only considering one or two variables and convex problems, nearly-optimal solutions can be obtained with very few function evaluations. Finally, knowledge of a problem or previous solutions is easy to apply to the optimization process, further accelerating the convergence to a suitable point design.

However, enumerative techniques are problem specific and do not accelerate the pace of future research or design development unless a very analogous problem is considered. Additionally, they do not scale well to large, multi-dimensional variable sets. Consider the design space for the ETA problem as described by Equation 5.7. If the continuous variables are discretized, the number of possible permutations is given by

$$P = (|M| \times |\rho| \times |IR| \times |OR| \times |Z1| \times |Z2|)^{|N|} \times |R_{foil}| \times |Z_{foil}| \,, \tag{5.8}$$

where $|\,|$ represents the number of allowed values for a given variable. For a simple 1-D ETA design with 5 layered cells ($|N| = 5$, $|IR| = 1$, $|Z1| = 1$), a material set consisting of the 83 naturally occurring elements and no compounds ($|M| = 83$), a single allowed density for

each ($|\rho| = 1$), a fixed outer radius ($|OR = 1|$, ten possible thicknesses ($|Z2| = 10$), and a foil located on the X-Y axis $|R_{foil}| = 1$) that is allowed to be placed at ten different heights ($|Z_{foil}| = 10$), the number of possible ETA designs is 3.94×10^{15} Therefore, any realistic ETA design that fully considers the available design space is far too complex to be considered using these enumerative techniques.

5.2.2 Deterministic Optimization

Deterministic optimization techniques, also referred to as calculus-based or mathematical programming, follow a rigorous mathematical formulation of the problem to move towards the optimum solution. The methods generally involve computation of the gradient or Hessian to guide the next selection of design variables. Some common deterministic algorithms are Newton's Method, Gradient Decent, and the Simplex Method [34, 178, 231].

In the nuclear field, SWAN is a 1-D deterministic solver developed originally to optimize nucleonic characteristics of fusion reactor blankets. It obtains approximations to the gradient through the use of perturbation theory [83]. Later algorithm versions extended SWAN's capabilities to criticality and shielding problems [84]. Attempts were made to extend SWAN to 2-D to address BSA design with mixed results [215].

SWAN, like all deterministic methods, has many advantages. Deterministic solvers have a tremendous advantage in the number of function evaluations required for convergence as compared to stochastic solvers. They are also mathematically guaranteed to find a *local* optimum within a given set of bounds, which is not always true for stochastic or enumerative methods. Finally, the results are reproducible given an initial set of conditions used as input to the solver [34, 178, 231].

However, there are also drawbacks to deterministic approaches. First, the requirement for a rigorous mathematical formulation makes each approach problem specific – especially in the case where constraints or objectives are derivative-free and/or evaluated by black box codes. Next, while *local* convergence is guaranteed, *global* convergence is not. In fact, which optima is found is highly dependent on the starting conditions, which is non-ideal. This can be overcome with several methods, but all either increase the number of function evaluations, often through the addition of a stochastic component, or further entrench the problem specific-nature of the implemented solver. Finally, deterministic approaches are intrinsically single objective [34, 178, 231].

A strong case can be made for using deterministic approaches for ETA design. First, a preliminary capability exists in SWAN. Second, radiation transport is expensive computationally, which is an important fact when hundreds or thousands of transport calculations are required, and deterministic methods could reduce the number of calculations required compared to stochastic methods.

However, the combination of noisy, potentially discontinuous, and highly multi-modal fitness landscape makes obtaining global or nearly global optimum solutions difficult. Additionally, this deterministic approaches would not generate a general optimization approach that could be applied more broadly than this specific ETA design problem. Finally, existing

literature suggests a need to limit the design space considered, which challenges the idea of extending the existing approaches to 2- or 3-D [215]. In other words, a deterministic approach would generate a fantastic, problem-dependent, local solver, but would struggle to serve as a general, global or nearly-global optimization technique given the problem definitions of interest. For these reasons, deterministic approaches were not pursued.

5.2.3 Stochastic Optimization

Stochastic optimization uses random search methodologies or patterns to sample the design space. This can be in the form of modifications to deterministic methods to overcome local convergence issues or algorithms whose entire search process is based on random moves. Here, the focus is on completely stochastic algorithms. The most common of these techniques are embodied in the class of evolutionary or metaheuristic algorithms [125, 231]. For the purposes of this dissertation, the term metaheuristic will be used to described guided stochastic optimization methods.

The term metaheuristic was coined by Glover in 1986 by combining the Greek prefix meta- (metá, beyond in the sense of high-level) with heuristic (from the Greek heuriskein or euriskein, to search) [80, 193]. Sorensen and Glover define metaheuristic as "a high-level problem-independent algorithmic framework that provides a set of guidelines or strategies to develop heuristic optimization algorithms" [193]. Originally intended to describe the framework of search strategies, the term metaheuristic is commonly used as being synonymous with nature-inspired stochastic algorithms of which there are numerous and varied implementations in the literature [69, 231]. For the purposes of this dissertation, metaheuristics will be used to refer to the search technique framework developed, and heuristic will be used to refer to the specific search technique used.

Metaheuristics have several advantages over deterministic and enumeration methods. First, metaheuristics can efficiently explore large design spaces without requiring a gradient or discretization. This efficient exploration, coupled with the random walks, enables metaheuristic algorithms to overcome local convergence issues rather well. Second, unlike deterministic methods, limited, if any, *a priori* knowledge is required. In this way, metaheuristic frameworks can be developed that are generally applicable to a wide range of problems. Metaheuristic approaches are also not intrinsically limited to a single objective function as is the case with deterministic approaches. Finally, metaheuristic approaches lend themselves to building a population of candidates, which can simultaneously perform their individual random walks either in isolation or with information sharing. Because of this, metaheuristic algorithms are generally "embarrassingly parallel" [34, 69, 231].

Alas, there are also significant drawbacks worth considering. In isolation, stochastic processes will always, on average, require more function evaluations than properly defined deterministic approaches given that there are suitable gradients to follow. Because the solution process is stochastic, the design process is not repeatable outside the partial caveat of seeding random number generators [34, 69, 231]. Finally, there exists a "no free lunch" theorem, which states that "any elevated performance over one class of problems is offset

by performance over another class". This is important to keep in mind for metaheuristic algorithms that are developed to be general-purpose [228].

On the balance, metaheuristic optimization's benefits outweigh its drawbacks for ETA optimization and design, and this was the optimization approach chosen for this research. Most importantly, these techniques are capable of solving the complex class of optimization that characterize ETA design (see Section 5.3 for more details). In addition, metaheuristic algorithms can be made general while still obtaining global or nearly global optimization results. Finally, the intrinsically parallel nature of the algorithm allows the decreased rate of convergence to be overcome with high-performance computing (HPC) resources.

5.3 MINLP

Section 5.2 explored optimization taxonomy at the highest levels, but it is also worthwhile to explore a cross-cutting, categorization-based taxonomy slice that most closely addresses the ETA design problem in more detail. MINLP addresses nonlinear optimization of design problems informed by continuous, integer/binary, and discrete variables. Most approaches require continuous, convex functions or that the problem can be decomposed into a set of continuous, convex functions [91, 120]. The existing techniques generally struggle with noise and black box objective function evaluations, but advances have been made in both areas [71, 91].

A full reproduction of all of the different approaches to MINLP is beyond the scope of this work. Several good review papers and books exist on this topic, and a large majority of the techniques have little to no applicability to the ETA optimization problem under consideration [13, 21, 71, 120, 178]. Instead, a survey of two broad techniques that were the most promising for ETA design are considered: surrogates and metaheuristics.

5.3.1 Surrogate Methods

Surrogate methods aim to minimize function evaluation costs for computationally expensive, black box objective functions or constraints. They accomplish this through the use of either a simplified model or interpolation of previously evaluated design points to develop response surfaces. The results of the surrogate evaluation can then be used to guide the optimization to perform the computationally expensive function evaluations in promising portions of the design space. This can be accomplished directly through developing a seed population that is handed off to a local optimizer, or can be used with branch and bound techniques to selectively remove unproductive regions of the design space by generating sub-regions or constricting the bounds of individual variables [23, 49, 91, 151].

Surrogate models are attractive because many applications have suitable, lower-fidelity alternative codes available. In areas where lower-fidelity models do not exists, regression methods, such as kriging, can be used to develop response surfaces with limited initial design points. Additionally, response surfaces can incorporate uncertainty estimates that can be

used to identify regions requiring additional sampling, further increasing the robustness of this approach [2, 49].

However, the development of fast running models suitable as surrogates often significantly lags that of their high-fidelity peers. The lack of development has left behind assumptions tied to computer memory or computational speed that are unnecessary for today's computers. These simplifying assumptions used in the lower-fidelity models can lead to added noise or can misguide the optimization process completely, resulting in more function evaluations. This is especially true for the potential surrogate options that could be applied to the ETA problem. Diffusion theory, the lower-fidelity version of transport theory, is limited in this application because assumptions of the finite size of potential ETA designs, the possibility of inclusion of sources and sinks within the ETA, and the proximity of the ETA to rapidly time-varying sources. An alternative surrogate option could be deterministic methods. However, the discretization of the phase space required by deterministic solvers can lead the optimization process astray. This can be especially true for cross section discretization; some candidate ETA designs utilize resonances to populate or depopulate select portions of the neutron energy spectrum, so the cross sections must be captured accurately for this to work. While surrogate models were not incorporated into the optimization process directly through evaluating objective or constraint functions, they were used to reduce the computation expense of the evaluations as described in Subsection 6.2.1.

Response surface techniques also struggle with noisy and discontinuous response surfaces. Continued development of response surface techniques has improved their ability to address noise, handle constraints, and address problems that do not decompose to convex functions. However, for high-dimensionality problems with many of these features, most of these methods are best used to provide seed populations at best [23, 49, 91, 151]. Response surface techniques were not explored directly in this work, but are address in Chapter 10 for possible future research.

5.3.2 Metaheuristic Methods

Metaheuristic techniques have been adapted to solved MINLP problems to great success [59, 60, 68, 71, 131, 234]. For the reasons outlined in Subsection 5.2.3, metaheuristic techniques are perfect for the complicated MINLP design space in many ways. For example, they are not limited by non-convexities, readily handle constraints, can handle noise, and are extensible to large dimensions – all of which can be problems for surrogate or deterministic methods of solution.

Despite this, there is a surprisingly limited amount of metaheuristic development or tools in the MINLP realm [60, 193]. Work has been done to extend scatter search (eSS), tabu search, and particle swarm optimization (PSO) to biomedical and chemical engineering MINLP design problems [59, 60, 68, 234]. However, of Matlab's five solvers in its Global Optimization Toolbox, only GA is capable of handling mixed-integer design vectors [131]. Even more limiting to research, only the MEtaheuristics for bIoinformatics Global Optimization (MEIGO) algorithm (eSS based) was found to be openly available [60].

Metaheuristic techniques applied to MINLP only magnify the short comings that are characteristic of the metaheuristic techniques. If the number of function evaluations was limiting in a simpler design space, they can become prohibitive in a more complex one. Additionally, the performance of the algorithm is highly driven by the selection of the heuristics used and the settings of the tunable parameter set associated with that algorithm. Following the principles of the no free lunch theorem, heuristics and parameters tuned to perform well for one problem will result in poor performance for others. Mitigation of these limitations will be a focal point of the optimization method development in this work.

5.4 Metaheuristic Algorithms

The goal, then, for any metaheuristic optimization development should be to overcome the method limitations through careful selection and balancing of search heuristics. The chosen mix of search heuristics should emphasize general applicability and global search while maintaining sufficient intensification, or local convergence, to minimize the required number of function evaluations. However, this development approach is rarely explicitly taken [193]. Instead, most algorithm development starts with metaphors, often based on natural processes, with no eye towards the fundamental reasons why mimicking that process will work as an optimization technique. Subsequent iterations often stray from this metaphor, but few approaches identify the key characteristics of the heurstics that are being utilized that enable an algorithm's success.

Some authors have gone so far as to claim that a bulk of the metaheuristic literature is better described as art than science [193]. Some of this is rooted in the stochastic nature of the field and the limitations imposed by the no free lunch theorem. Some is driven by apples and oranges comparisons between stochastic and deterministic method development and the stark differences in the mathematical underpinnings. Some is purely driven by the proliferation of algorithms in the literature that make it difficult for designers and engineers to use the methods developed due to information overload or a lack of transition from academic papers to useful tools [91, 125, 193]. In spite of all of this, it is hard to argue against the success that metaheuristics have had in solving complex global optimization problems.

To continue improving upon that success in a responsible way, Lones and Sorensen have proposed ways to advance the state of the field. Some of the proposed ideas within the scope of this research include [125, 193]:

1. Analysis and explicit identification of the characteristics of the heuristics employed in an algorithm.
2. The development of hyper-metaheuristics that can be used to evaluate the effectiveness of different combinations of heuristics.
3. The establishment of consistent, adequate testing standards.
4. The requirement to disclose source code.

An attempt to address the spirit of the second suggestion is described in Subsection 6.1.3, but it falls far short of the large research and development effort they envisioned. The code developed in this research is open-source, documented, and available[1,2]. Complete details for all of the data, analysis and code locations for this research are described in Appendix B. The third step is also beyond the scope of this research, at least in the sense that no attempt was made to establish testing standards across the metaheuristic optimization field, but a coherent benchmarking strategy across a range of established optimization benchmarks is developed and presented in Subsection 6.1.5. Additionally, the full results of the benchmarks are made available for review[3].

The first suggestion is worth expanded discussion as it provides the framework for the development of the algorithms discussed in Chapter 6. Lones lays out an argument for considering metaheuristics a framework under which specific heuristics are combined to achieve the appropriate diversification and intensification strategies. He then identifies ten common search strategies employed in metaheuristic algorithms. Although Lones also calls these ten strategies metaheuristics, this work adopts a more nuanced definition as proposed by Sorensen, where metaheuristics refers to the overall framework and heuristics to the specific search strategies [125, 193]. A specific algorithmic implementation of one or more heuristics is then referred to as a search operator (i.e. mutation or crossover).

Lones's list is not all inclusive or a universally adopted, complete classification of the different possible strategies. The ten strategies considered in this work as proposed by Lones are [125]:

- **Neighborhood Search:** New solutions developed are a move, or step change, away from current solutions. A move can be defined as a change in a single variable or the entire solution. While the neighborhood can be defined and sampled multiple ways, the search carried out typically is local in nature.
- **Hill Climbing:** A sequence of moves is used to find a locally optimum solution where moves are only accepted if they lead to an improvement in fitness. The acceptance of only positive moves along a search path can lead to local optima trapping if not combined with another global search heuristic.
- **Accepting Negative Moves:** Allows moves to worse fitness solutions. Often used to prevent premature convergence at local optima.
- **Multi-Start:** Restart the search process with a new starting location once it converges at a local optimum. The use of a population can be considered a form of multi-start. The use of restarts and/or population-based techniques reduces local optima trapping in large search spaces.

[1] `https://github.com/SlaybaughLab/Gnowee`
[2] `https://github.com/SlaybaughLab/Coeus`
[3] `https://github.com/SlaybaughLab/Gnowee/tree/master/Benchmarks/results`

- **Adaptive Memory Programming:** Uses past search experience to guide development of the next move. This can range from calculating random steps from the current design point to stored histories of recent moves. These strategies can help guide the search away from well explored regions, preventing cyclical patterns.
- **Population-Based Search:** Multiple search processes that are often cooperative and executed in parallel. In cooperative executions, information sharing can be tightly or loosely coupled. For large, multi-modal search spaces, this can accelerate global convergence, though it can be inefficient in relatively easy problems.
- **Intermediate Search:** Explores the space between two or more high fitness solutions. This can either lead to exploration of new regions between two local optima or faster local convergence if both solutions reside in the region of the same optimum. Particular implementations of this may not be universal as defining a logical "middle" between different types of design variables will differ.
- **Directional Search:** Carries out moves according to identified productive directions of search. Implementation can be guided by gradients, known locations of high fitness solutions, or estimates of the derivatives. This can lead to faster convergence, but, if not scaled properly for the size and complexity of the problem, can lead to premature convergence.
- **Variable Neighborhood Search:** Explores different neighborhoods around the current search point. The definition of different neighborhoods can vary from using moves of variable size to fixed definitions of search neighborhoods. This can help reduce local trapping and increase search efficiency in large, complex problems.
- **Search Space Mapping:** Constructs a map or partitions on the search space to guide the search process. This can aid in the efficiency of convergence but can require knowledge of the problem to devise the correct mapping or partitioning.

With these descriptions of the heuristics in mind, it is worth exploring some well traveled metaheuristic algorithms. When considering each of the algorithms, it is important to note that these heuristics are not fixed in stone, prescriptive search procedures, but instead describe the general features and characteristics of a given method of search methodology. Consequently, while two algorithms may employ the same heuristic, the implementation may vary in nature and effectiveness. With that in mind, the following sections describe the basic algorithm, give a brief description of the search operators, and annotate which heuristics are employed. These descriptions are not intended to be all inclusive, and make no attempt to document the many variations and extensions of the foundational algorithms made in the literature.

5.4.1 Evolutionary Algorithms

Evolutionary algorithms can trace their early development to the late 1950s and early 1960s [34, 193]. The basic concept behind evolutionary algorithms is to replicate the evolutionary process through blending of two parent chromosomes, mutation of chromosomes, and natural selection processes. Two popular forms of evolutionary algorithms are explored here: genetic algorithms (GA) and differential evolution (DE).

GAs have been around in their modern form since their formulation in Holland's seminal 1975 book [93]. They represent some of the first algorithms developed in the metaheuristic and evolutionary computation field [193]. They represent the basis for numerous other branches of algorithms, and there continues to be active research of GA variants [226].

The basic GA concept is the encoding of the design space into binary strings or chromosomes. This mapping to binary space allows tremendous flexibility in addressing continuous, binary, integer, discrete, and combinatorial variables, but it does require discretization of the continuous design space [34]. Some more modern methods have removed the requirements to map to binary space to generate the chromosomes, thereby eliminating the discretization issues [226, 231].

GAs generally employ the mutation and crossover operators, with the common addition of the elitism, to guide the search process [34, 231]. Crossover is the primary operator, with mutation taking a secondary role. In crossover, one segment of chromosome from one parent is swapped with the corresponding segment in the other parent. In mutation, random bits are selectively flipped from a zero to one, or vice versa. Elitism is used in many ways: from the selection of the parents used for the operators to the selection of the next generation's population [231].

DE can be considered an extension of GA. DE was first introduced by Storn and Price in 1996 and 1997, and active development of variants and derivative methods continues [34, 195]. DE differers from GA in two primary ways. First, the DE search vectors, called chromosomes in GA, are real valued and require no binary coding or decoding. This enables DE to avoid discretizing the search space. Second, DE utilizes mutation as the primary operator, with crossover taking a secondary role.

Evolutionary algorithms employ several of the heuristics described in Section 5.4. First, crossover uses the intermediate search algorithm looking for design solutions that lie between two sets of parent chromosomes. Second, mutation, as described above, uses the neighborhood search heuristic through exploration of small moves around a given chromosome. Both utilize the adaptive memory programming heuristic in that the subsequent moves are informed by the current chromosomes. The selection process for the subsequent generation is an implementation of hill climbing. Finally, the construct of GA around a population of chromosomes is supported by the multi-start and population-based search heuristics [125, 231].

5.4.2 Particle Swarm Optimization

Particle swarm optimization (PSO) was introduced by Kennedy and Eberhard in 1995 to apply swarm theory to optimization [105]. This technique seeks to use the swarm behavior of fish, birds, or insects looking for food to optimally search a design space for productive regions. Many variants of PSO have been developed, and it has become the basis for several other algorithms, including the Firefly Algorithm and Cuckoo Search (CS) [231].

As opposed to GA and DE, PSO uses real-number random search operators and information sharing among particles to search the design space. Each particle has an attractiveness factor based on the quality of its current solution. This information is shared among the swarm and used to alter the velocity vector of each particle to bias the velocity vector toward those particles with better solutions. The addition of randomness to the alteration of the velocity vectors limits trapping in local minima. Additionally, the strength of the attractiveness factor can vary as a function of generation to allow for enhanced early time global exploration and accelerated late time convergence [34, 105, 231].

PSO leverages population-based search and mulit-start heuristics extensively through its formulation and theoretical foundation in swarm theory. Similar to evolutionary algorithms, it also uses hill climbing selection strategies. Intermediate search and adaptive memory programming is used through the information sharing among the swarm in each generation, and the use of different velocities, specifically different magnitudes of velocity, for each particle is an implementation of the variable neighborhood heuristic. Finally, the concept of attractiveness enables the use of a directional search heuristic, which can accelerate convergence and enable efficient search of the design space [125, 231].

5.4.3 Cuckoo Search

Cuckoo Search (CS) is a nature-inspired metaheuristic algorithm that was introduced in 2009 by Yang [232]. The basic concept seeks to mimic the obligate brood parasitism behavior of some cuckoo species, where the cuckoo tricks a host bird into raising its young. The method has proven to be highly effective and has compared favorably to other metaheuristic algorithms [45, 232, 231]. As a result, CS has quickly spawned dozens of variants and hybrid methods based on the original CS algorithm [70].

Although not explicitly stated, part of the reason for CS's success is that it blends PSO and GA/DE behavior in its search operators. It's primary operator uses random walk processes governed by Lévy flights based on animal, and human, foraging behavior. Lévy flights are heavy tailed probability distributions that enable efficient exploration of the design space (see Subsection 6.1.1 for more details). The secondary operator is referred to as a "nest abandon" operator by Yang. This operator is essentially a real-valued, population based mutation strategy where portions of each design vector are replaced. The nest abandon operator seeks to identify a fraction of the nests, mutate them, and discard the worst solutions.

The core of the CS algorithm is supported by population-based search and multi-start heuristics. Updating strategies utilize the hill climbing heuristic. Lévy flight operators are

a form a variable neighborhood search supported by adaptive memory programming. The abandon nests operator uses the intermediate search and mulit-start heuristics [125].

5.4.4 Ant Colony Optimization

Ant colony optimization (ACO) was introduced by Dorigo in 1992 [57]. This algorithm draws inspiration from the foraging and social behavior of ants that enable them to find the shortest route to a food source. The shortest route information is shared via deposited pheromones that increase in strength as more and more ants traverse a given path. Like all of the other algorithms, many variants of ACO can be found in the literature [57, 62].

ACO encodes the solution space into a set of discrete variables, each with an associated pheromone concentration. The initial pheromone levels are populated after objective function evaluation of a randomly generated starting population. The search operator then updates the population using on a biased random walk based on the pheromone concentrations. Another operator is introduced through pheromone decay. The pheromone levels are allowed to decay over time so that only well worn paths, highly used variables, maintain their pheromone levels, thereby increasing intensification [57, 62, 125].

Like the other algorithms discussed to this point, ACO is supported by population-based search and multi-start heuristics. The used of pheromones is based on the adaptive memory programming, directional search, and search space mapping heuristics [125].

5.5 Optimization Strategies for ETA Design

The ETA design problem is best described as a single objective, nonlinear, derivative-free, constrained, combinatorial *and* mixed-integer, multi-modal optimization problem with noisy, discontinuous, black box objective function and constraint evaluations. This chapter detailed an overview of the current optimization approaches in the literature and how they would apply to the ETA optimization problem. From the options outlined, metaheuristic techniques were chosen for their generality, robustness, compatibility with derivative free optimization, and extensibility to multi-objective optimization, and ease of parallelization. To overcome the cost of increased functions evaluations, a characteristic of metaheuristic algorithms in comparison with deterministic approaches, a balanced global search and intensification strategy was employed using Lones heuristic classification as a guide. The next chapter explores the specific implementation of the metaheuristic concepts into the Gnowee algorithm in detail.

Chapter 6

Energy Tuning Assembly Design

I love it when a plan comes together!

- Hannibal Smith, A-Team

The previous chapters outlined the TNF relevant ETA problem definition (Chapter 2), the physics behind and past experiences with neutron spectral shaping (Chapter 3 and Chapter 4), and the optimization approaches available for ETA design (Chapter 5). This chapter brings it all together to describe the ETA design tools developed in this research. It is organized into three major sections. Section 6.1 describes Gnowee, a general-purpose metaheuristic optimization code. Section 6.1 describes the algorithmic framework, each of the search operators and associated heuristics, tuning of Gnowee's parameters, and the benchmarks used to show the effectiveness of the algorithm. Section 6.2 outlines Coeus, a nuclear engineering design package. Section 6.2 describes the radiation transport models implemented, the method of parallelization, and ongoing development. Finally, Section 6.3 shows the ETA design developed using Coeus.

6.1 Gnowee

Eternally looking for her son she lost while gathering yams using her powerful torch from her perch high up in the sky.

- Australian Aboriginal mythology

Gnowee is a modular, Python-based, open-source hybrid metaheuristic optimization algorithm[1]. Gnowee is designed for rapid convergence to nearly globally optimum solutions

[1]Open source and available from `https://github.com/SlaybaughLab/Gnowee`. Code documentation, installation procedures, how to run, and an overview of the outputs is in the README file located here as well.

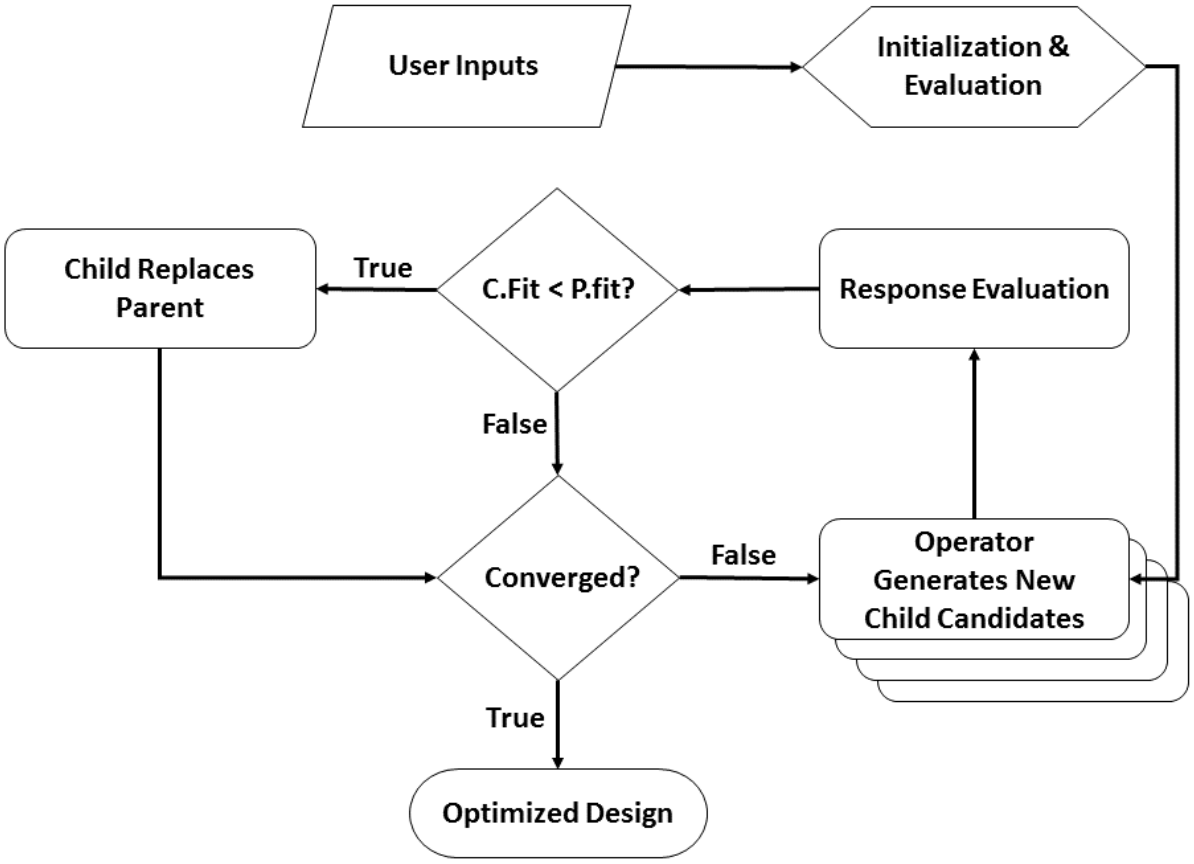

Figure 6.1: Gnowee flowgorithm.

for complex, constrained engineering problems with mixed-integer and combinatorial design vectors and high-cost, noisy, discontinuous, black box objective function evaluations. Gnowee's hybrid metaheuristic framework is based on a set of diverse, robust heuristics that appropriately balance diversification and intensification strategies across a wide range of optimization problems. While developed with ETA design in mind, the approaches outlined here are generally applicable across a wide range of engineering design problems as shown by the benchmarks used in Subsection 6.1.5.

The general flow and decision process for Gnowee is presented in Figure 6.1. This is a high level overview of the Gnowee optimization process detailing the algorithm's logic and primary steps. The stacked search operators indicate an internal loop through each of the operators described in Subsection 6.1.2. This loop through the operators can be better shown in the algorithm framework outlined in Algorithm 1. Operators of the algorithm have been simplified in Algorithm 1 for conciseness.

A key feature that underpins many of the operators displayed in Algorithm 1 are Lévy flights. Subsection 6.1.1 introduces the concept of Lévy flights and how the probability

Algorithm 1: Gnowee Algorithm

Input : User defined objective function, f; constraints, g and h; design space, $\vec{x}$; and algorithm settings (see Table 6.1)

begin
  $P.\vec{x} \leftarrow$ initialization(n) `// P is the parent population of size n`
  $P.fit \leftarrow$ population_update($P.\vec{x}$) `// fit is the assessed fitness`
  while *convergence criterion is not met* **do**
    $C.\vec{x} \leftarrow$ three_opt($P.\vec{x_x}$)
    $P.fit \leftarrow$ population_update($C.\vec{x}$)

    $C.\vec{x_c} \leftarrow$ cont_lévy_flight($P.\vec{x_c}$) `// C is the child population and` $\vec{x_c}$ `is the subset of the design vector containing continuous variables`
    $C.\vec{x_d} \leftarrow$ disc_lévy_flight($P.\vec{x_d}$) `//` $\vec{x_d}$ `is the subset of the design vector containing discrete, integer, and binary variables`
    $C.\vec{x_x} \leftarrow$ comb_lévy_flight($P.\vec{x_x}$) `//` $\vec{x_x}$ `is the subset of the design vector containing combinatorial variables`
    $P.fit \leftarrow$ population_update($C.\vec{x}$, mh) `//` mh `indicates a Metropolis-Hastings algorithm is to be used`

    $C.\vec{x} \leftarrow$ crossover($P.\vec{x_c}$, $P.\vec{x_d}$)
    $P.fit \leftarrow$ population_update($C.\vec{x}$)

    $C.\vec{x} \leftarrow$ scatter_search($P.\vec{x_c}$, $P.\vec{x_d}$)
    $P.fit \leftarrow$ population_update($C.\vec{x}$)

    $C.\vec{x} \leftarrow$ mutation($P.\vec{x_c}$, $P.\vec{x_d}$)
    $P.fit \leftarrow$ population_update($C.\vec{x}$)

    $C.\vec{x} \leftarrow$ inversion_crossover($P.\vec{x_c}$, $P.\vec{x_d}$, $P.\vec{x_x}$)
    $P.fit \leftarrow$ population_update($C.\vec{x}$)

    $C.\vec{x} \leftarrow$ two_opt($P.\vec{x_x}$)
    $P.fit \leftarrow$ population_update($C.\vec{x}$)

distribution is sampled. Subsection 6.1.2 expounds upon and then implements these concepts into many of the search operators.

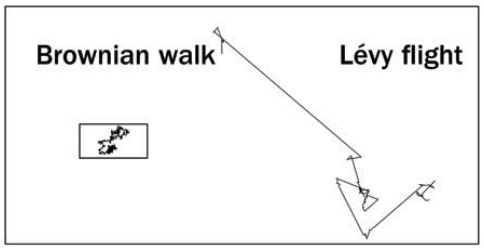

Figure 6.2: Comparison of equal length paths for a Lévy flight and a normally distributed Brownian walk [227].

6.1.1 Lévy Flights

Metaheuristic implementations are often stochastic, with a preponderance of implementations sampling from variations of uniform or normally distributed processes. As many algorithms are built on metaphors of physical, nature-inspired processes, this is a convenient choice as there are many naturally occurring phenomena that follow a normal distribution. An alternative is the Lévy distribution, which also has a basis in animal foraging behavior [127, 203, 237]. Lévy Flights are implemented as the basis for the random walk processes in the Cuckoo Search (CS) optimization algorithm and its variants [232].

The Lévy distribution is given by

$$L_{\alpha,\gamma}(z) = \frac{1}{\pi} \int_0^{+\infty} e^{-\gamma q^{\alpha}} \cos(qz) dq, \tag{6.1}$$

where α defines the index of the distribution and γ selects the scale of the process. Lévy distributions are heavy-tailed probability distributions where the wings are characterized by a power law behavior. This enables a more efficient global search of the phase space to be conducted through a higher probability of medium and large step sizes. Not only does the Lévy flight cover more of the phase space, it also avoids revisiting the same design point multiple times. This is shown graphically in Figure 6.2 for a Lévy flight and Brownian walk of the same path length.

Several algorithms have been developed to draw a stochastic sample with the correct probability density from a Lévy stable distribution. In this work, we chose the Mantegna algorithm for its speed and accuracy in sampling a Lévy distribution [127, 165]. We show the key steps for the original, full algorithm, as some implementations vary in the literature [127, 232]. First the stochastic variable, ν, is calculated by

$$\nu = \frac{x}{y^{\frac{1}{\alpha}}}, \tag{6.2}$$

where x and y are normally distributed stochastic variables with standard deviations σ_x and σ_y. Since σ_x and σ_y cannot be chosen independently for arbitrary values of α, $\sigma_y = 1$ is

chosen and

$$\sigma_x(\alpha) = \left[\frac{\Gamma(1+\alpha)\sin(\pi\alpha/2)}{\Gamma\left(((1+\alpha)/2\right)\alpha 2^{(\alpha-1)/2}} \right]^{\frac{1}{\alpha}}. \tag{6.3}$$

A nonlinear transformation can be done to speed up the convergence to a Lévy stable process by

$$w = \nu \left[(K(\alpha) - 1)e^{(-\nu/C(\alpha))} + 1 \right], \tag{6.4}$$

where $K(\alpha)$ is given by

$$K(\alpha) = \frac{\alpha\Gamma((\alpha+1)/2\alpha)}{\Gamma(1/\alpha)} \left[\frac{\alpha\Gamma((\alpha+1)/2)}{\Gamma(1+\alpha)\sin(\pi\alpha/2)} \right]^{\frac{1}{\alpha}}, \tag{6.5}$$

and $C(\alpha)$ is obtained by numerically solving

$$\begin{aligned} &\frac{1}{\pi\sigma_x} \int_0^\infty q^{1/\alpha} \exp\left[-\frac{q^2}{2} - \frac{q^{2/\alpha} C(\alpha)^2}{2\sigma_x^2(\alpha)} \right] dq \\ &\qquad = \frac{1}{\pi} \int_0^\infty \cos\left[\left(\frac{K(\alpha) - 1}{e} + 1 \right) C(\alpha) \right] e^{-q^\alpha} dq. \end{aligned} \tag{6.6}$$

The stochastic Lévy sample is then given by

$$z = \gamma^{1/\alpha} \frac{1}{n^{1/\alpha}} \sum_{k=1}^{n} w_k, \tag{6.7}$$

where n is the number of independent stochastic variables.

6.1.2 Search Operators

Gnowee operators implement the neighborhood search, hill climbing, accepting negative moves, multi-start, adaptive memory programming, population based search, intermediate search, directional search, and variable neighborhood search heuristics. Search space mapping was not implemented as it generally required discretization of the phase space. A balance was struck between directional search, which can increase the rate of convergence, and accepting negative moves, which can increase the global search capabilities, to accomplish a fast, nearly global convergence within the design criterion described more fully in Subsection 6.1.3.

Initialization

The Gnowee algorithm has flexible user-selected initialization through random draws from a uniform distribution, nearly orthogonal Latin hypercube (NOLH), NOLH with random permutation, NOLH with Cioppa and Da Rainville permutations, and Latin hypercube (LHC) [44, 174, 212]. The use of LHC and NOLH sampling techniques increases the diversity of initial solution sets by better covering the design space. Increased diversity in the population improves global search while minimizing premature local convergence. This can dramatically improve early time (i.e. few function evaluations) convergence rates, but at late time, only minor differences were noted. However, improvements in the early time convergence can be useful for the high cost objection function evaluation applications for which Gnowee was designed, and LHC was selected as the default initialization method.

The efficiency of the LHC algorithm to sample the design space is dictated by the number of population members. Larger populations provide a more robust sampling but are cumbersome to carry throughout the optimization process due to the increased number of function evaluations performed on "dead weight" members (see Subsection 6.1.3 for further discussion on the selection of the population size). Here, a compromise is struck to allow for robust LHC sampling by generating a number of LHC samples equal to the greater of twice the population size or three times the length of the design vector. After evaluating the fitness of the candidate designs, only the best p designs are carried forward into the optimization process.

3-opt

The 3-opt is in the family of heuristics introduced by Lin and Kernighan that has been applied to a wide variety of different algorithms [122]. For the Gnowee algorithm, the 3-opt heuristic is ideal as it is largely problem independent – requiring minimal, if any, knowledge of the problem – and can be implemented rather generically. Three-opt implements the neighborhood search, adaptive memory programming, hill climbing, and population based search heuristics. To explain 3-opt, consider the following non-looping parent sequence:

$$P_1 = \boxed{\text{A}|\text{H}|\text{B}|\text{D}|\text{G}|\text{F}|\text{C}|\text{E}}$$

Three random, unique break points are selected from within the parent. For this example, H, G, and C. To simplify the diagram, consider the following sequence:

$$P_1 = \boxed{\text{S1}|\text{S2}|\text{S3}|\text{S4}}$$

where $S1$ is the sub-sequence given from A to the first break point $(A - H)$, $S2$ is the sub-sequence given from the point following the first break point, B, through the second break point $(B - D - G)$, $S3$ is the sub-sequence given from the point following the second break point, F, through the third break point $(F - C)$, and $S4$ is the renaming sub-sequence (E). Gnowee considers two re-orderings of the parent sequence around the three chosen break points. The first child, C_1 is defined as

$$C_1 = \boxed{\text{S1}}\boxed{\text{S3}}\boxed{\text{S2}}\boxed{\text{S4}}$$

If the fitness of C_1 improves upon the fitness of P_1, then C_1 replaces P_1 in the parent population. The second permutation is then determined to be

$$C_2 = \boxed{\text{S1}}\boxed{\text{S2}^{-1}}\boxed{\text{S3}^{-1}}\boxed{\text{S4}}$$

where $S2^{-1}$ and $S3^{-1}$ is the inverse of the original sub-segment. If C_2 improves the fitness, C_2 replaces P_1 in the parent population. This continues for each parent in the initial population.

Continuous Lévy Flights

Lévy flights are used to develop Markov chains that sample the design space. Lévy flights have primarily been employed in CS algorithms, but stochastic sampling of the search space is a commonly employed heuristic [231]. Lévy flights implement the variable neighborhood search, adaptive memory programming, hill climbing, directional search, accepting negative moves, multi-start, and population based search heuristics described in Section 5.4. Lévy flights on continuous variables are performed on a fraction of parents, f_l, as

$$\vec{x}_r^{g+1} = \vec{x}_r^{g} + \frac{1}{\beta}\vec{L}_{\alpha,\gamma}, \tag{6.8}$$

where g is the generation number, r is a unique random index, $r \in \{1, 2, \ldots, p\}$, β is a step size scaling factor, and the procedure to determine $\vec{L}_{\alpha,\gamma}$ was described in Equation 6.2 - Equation 6.7. Including β is typically necessary to avoid consistently taking steps that are large relative to the dimensions of the problem, which can result in oscillatory behavior. The recommended value for β reported in the literature varies from $\beta = 1$ to $\beta = L/100$ where L is the characteristic scale of the problem being considered [231, 232, 238]. This can be problematic when the scales vary significantly for different variables of the design vector, a fact often ignored.

Instead of scaling β to the characteristic scale of the problem, the Gnowee algorithm takes a slightly different approach. First, the updated design vector is calculated using Equation 6.8. Next, a boundary rejection and re-sampling algorithm is implemented to check the resulting design vector's validity. If the step returns a valid result within the boundary of the problem for a given variable of the design vector, the value is accepted and no further action is taken. However, if that step is outside the problem boundary for a given design variable, that solution is rejected and a new $L_{\alpha,\gamma}$ is generated. Finally, the value of the optimal β under this approach was determined using a hyper-optimization technique described in Subsection 6.1.3. This method showed drastic improvement in decreasing the sensitivity of the optimization performance with changes in β, allowing a constant value to be chosen without any impact on the algorithm's performance.

Finally, within the Lévy flights heuristic, a form of the Metropolis-Hastings rejection sampling algorithm is implemented [90]. All children that improve upon the fitness of the parent are automatically accepted. A fraction, $f_m h$, of the children that would normally be discarded due to lower fitness than their parent are instead compared against another

random parent in the population. If the fitness of the child is an improvement over the random parent, the child replaces that parent. This technique works well when coupled with Lévy flights. For small steps, accepting a fraction of the solutions that would normally be discarded increases the local convergence rate through the directional search heuristic. For large steps, this can increase the global exploration through the acceptance of negative moves and multi-start heuristics. However, even with Lévy flights, care must be taken not to set $f_m h$ too large or the population diversity will decrease, resulting in premature convergence.

Discrete Lévy Flight

Lévy flights on discrete, integer, and binary variables are performed as described in Equation 6.8, but $L_{\alpha,\gamma}$ is calculated from

$$L_{\alpha,\gamma} = ROUND(TLF_{\alpha,\gamma} * D(x)), \tag{6.9}$$

where $TLF_{\alpha,\gamma}$ is a truncated Lévy flight on the interval $[0, 1]$ and D is a variable describing the scale of the discrete variable, x, being considered [128]. In this way, the TLF can be used to map a Lévy distribution onto a discrete variable by eliminating arbitrarily large steps. D can be kept general, such as the relative current location indexes, or problem specific knowledge relevant to the objective function can be leveraged.

For the Gnowee algorithm, one child is generated per $f_l * p$ parents. The Metropolis-Hasting algorithm is employed to accept a fraction of the children that do not improve upon their parent's fitness.

Combinatorial Lévy Flight

Combinatorial Lévy Flight combines Equation 6.9 from Discrete Inversion Lévy Flight with an inversion operator. Inversion operators are common in Genetic Algorithm (GA) implementations, and they have been adopted by other algorithms such as Cuckoo Search (CS) [194, 198, 238]. Combinatorial Lévy Flight implements the neighborhood search, hill climbing, adaptive memory programming, directional search, accepting negative moves, multi-start, and population based search heuristics described in Section 5.4 by creating new solutions through inverting a portion of the original solution set. For example, consider the parent sequence below:

$$P_1 = \boxed{\text{A}}\boxed{\text{H}}\boxed{\text{B}}\boxed{\text{D}}\boxed{\text{G}}\boxed{\text{F}}\boxed{\text{C}}\boxed{\text{E}}$$

The inversion points can be selected randomly, based on current location indexes, or by using a problem-specific quantity related to the minimization of the objective function such as distance. For example, if H and G are chosen as the cut points, the child would be:

$$C_1 = \boxed{\text{A}}\boxed{\text{H}}\boxed{\text{G}}\boxed{\text{D}}\boxed{\text{B}}\boxed{\text{F}}\boxed{\text{C}}\boxed{\text{E}}$$

For the Gnowee algorithm, one child is generated per $f_l * p$ parents. The Metropolis-Hasting algorithm is employed to accept a fraction of the children that do not improve upon their parent's fitness.

Crossover

Crossover is a common feature of GA and Differential Evolution (DE) algorithms implemented in a variety of manners [195, 198]. Variations of the crossover concept have been applied in Particle Swarm Optimization (PSO) and CS algorithms as well [105, 219]. For Gnowee, a version of the implementation adopted by Walton is employed for continuous, integer, and discrete variables where the child solution is calculated as [219]

$$\vec{x}_r^{g+1} = \vec{x}_0^g + \frac{(\vec{x}_0^g - \vec{x}_r^g)}{\Phi}, \tag{6.10}$$

where r is a unique random index, $r \in \{1, 2, \ldots, f_e * n\}$, f_e corresponds to the fraction of parents in the elite subset of high fitness designs, and Φ is the golden ration given by $\Phi = (1 + \sqrt{5})/2$. The golden ratio is used as it has been found to increase convergence over other choices in the range of $[0, 2]$ for similar strategies [195, 219].

As implemented, this method executes the intermediate search, adaptive memory programming, hill climbing, directional search, and population based search heuristics described in Section 5.4. The addition of intermediate and directional search through elitism increases overall population fitness and allows for rapid search of promising localities but can lead to premature convergence if f_e is not chosen properly due to the loss of population diversity.

Scatter Search

Gnowee uses an adaptation of scatter search pioneered by Egea et al. [59]. The scatter search approach leverages the information of the population to build variable search spaces based on the relative fitness of selected population members. In Gnowee, the scatter search heuristic is applied to continuous, integer, binary, and discrete variables. Scatter search implements intermediate search, variable neighborhood search, adaptive memory programming, hill climbing, and population based search heuristics described in Section 5.4. The scatter search heuristic updates the design vector according to

$$x^{g+1} = c_1 + (c_2 - c_1)r, \tag{6.11}$$

where x^{g+1} is the updated design vector and r is a vector of uniformly distributed random variables. c_1 and c_2 are given by

$$c_1 = x_i - d(1 + \alpha\beta), \tag{6.12}$$

$$c_2 = x_i - d(1 - \alpha\beta), \tag{6.13}$$

where x_i is a member of the elite sub-population. d is given by

$$d = \frac{x_j - x_i}{2}, \tag{6.14}$$

where x_j is a randomly chosen member of the population. From Equation 7.13 and Equation 7.14, α and β are calculated as

$$\alpha = \begin{cases} 1, & \text{if } i < j \\ -1, & \text{otherwise,} \end{cases} \tag{6.15}$$

$$\beta = \frac{|j - i| - 1}{p - 2}, \tag{6.16}$$

where p is the size of the population.

This process is continued for $f_e * p$ parents. If the generated children have a better assessed fitness than their parents, they are accepted into the population and replace their parents.

Mutation

Mutation is another foundational search heuristic of GA and DE algorithms that has been modified and adopted by a wide variety of other approaches [10, 195, 231]. The Gnowee algorithm implements mutations for continuous, integer, binary, and discrete variables. The mutation method implements intermediate search, variable neighborhood search, adaptive memory programming, hill climbing, and population based search heuristics described in Section 5.4. The mutation method employed is calculated as

$$\boldsymbol{X}^{g+1} = \boldsymbol{X}^{g} + r\boldsymbol{D}(\boldsymbol{P}_1 - \boldsymbol{P}_2), \tag{6.17}$$

where $\boldsymbol{X}$ is the population solution vectors, $\vec{x}$; r is a uniformly distributed random variable; $\boldsymbol{D}$ is a matrix of 0s and 1s where each value is determined through a random draw from a uniform distribution, with 0 obtained if $< f_m$ and 1 otherwise; and $\boldsymbol{P}_1$ and $\boldsymbol{P}_2$ are random permutation of the original $\boldsymbol{X}$.

Inversion Crossover

Inversion and crossover is used in GA and DE algorithms to copy portions of one parent into another to create a unique child [10, 195, 198]. When combined with elitism, crossover can be used to copy traits of high fitness parents into the population. In Gnowee, crossover with elitism for the continuous, integer, binary, discrete, and combinatorial variables implements the intermediate search, adaptive memory programming, hill climbing, directional search, and population based search heuristics described in Section 5.4. Gnowee uses random search to determine the sub-segment to crossover in order to allow for general applicability. This

can be kept general, such as the relative current location indices, or can be problem specific so knowledge relevant to the objective function can be leveraged [198, 238]. Consider the following sequences: P_1, chosen randomly from elite sub-population, and P_2, a unique, randomly-chosen parent from the entire population:

$$P_1 = \boxed{\text{A}|\text{H}|\text{G}|\text{D}|\text{B}|\text{F}|\text{C}|\text{E}}$$

$$P_2 = \boxed{\text{E}|\text{A}|\text{G}|\text{C}|\text{H}|\text{B}|\text{D}|\text{F}}$$

Point H is chosen randomly as the first inversion point from P_1. The second inversion point is determined by the location that follows H in P_2, which is B in this example. After inversion, the child sequence is

$$C_1 = \boxed{\text{A}|\text{H}|\text{B}|\text{D}|\text{G}|\text{F}|\text{C}|\text{E}}$$

Only children that improve upon their parent's fitness are accepted. Next, the previous second inversion point, B, is taken as the starting inversion point in P_2, and the new second inversion point is determined from the location that follows B in P_1, which is F. The new child sequence generated is

$$C_2 = \boxed{\text{E}|\text{A}|\text{G}|\text{C}|\text{H}|\text{B}|\text{F}|\text{D}}$$

If C_2 improves upon the fitness of P_2, then the child replaces the parent in the population. This process is continued over each location in the elite parent for $f_e * p$ elite parents.

2-opt

Two-opt is one of a family of heuristics introduced by Lin and Kernighan that has been applied to a wide variety of different algorithms [122]. The Gnowee algorithm adopts an implementation similar to that described by Zhou by adding Lévy flights and elitism to the selection process [238]. As implemented, 2-opt employs the neighborhood search, adaptive memory programming, hill climbing, directional search, and population based search heuristics.

To understand 2-opt, consider the following parent sequence

$$P_1 = \boxed{\text{A}|\text{H}|\text{B}|\text{D}|\text{G}|\text{F}|\text{C}|\text{E}}$$

The first break point is chosen as A. The second break point, G for this example, is chosen from a TLF mapped onto the length of the sequence. The re-connection is made where the first break point connects to the second break point and inverts the sequence between the two points. The point originally following the first break point, H, then connects to the point originally following the second break point, F as shown in the sequence

$$C_1 = \boxed{\text{A}|\text{G}|\text{D}|\text{B}|\text{H}|\text{F}|\text{C}|\text{E}}$$

If the child improves upon the parent's fitness, then the solution is accepted. The starting break point then cycles through the list up to the n^{th} item in the sequence (or $n-2$ for non-looping sequence) for each parent in the elite subset given by the top $f_e * p$ parents.

Population Update

The descriptions of the individual operators describe the population update procedures used, but it is worth expounding upon this process. Update strategies typically follow a couple of approaches. First, a common approach is to select p new parents from the generated c children plus p existing parents. In this approach, the p best solutions are taken regardless of their origin, which can result in faster convergence at the expense of reduced diversity and increased chances of premature local convergence. An alternative approach is to select the new p population members from the c children. This approach increases diversity and limits premature convergence but may require more function evaluations as a large number of negative steps can be accepted.

The approach adopted by Gnowee attempts to strike a balance by *mostly* only allowing children to replace their parents. This keeps diversity high and avoids negative moves. However, elitism based heuristics, while serving to increase convergence, can also themselves decrease the diversity of the population. This is offset employing the Metropolis-Hastings algorithm once a generation to allow for negative moves that, due to the nature of Lévy flights, can increase the diversity of the population.

6.1.3 Parameter Selection

One of the challenges for metaheuristic algorithms is that the performance for a given problem type is generally highly dependent on the set of algorithm specific parameters chosen. Gnowee's use of a diverse set of heuristics compounds this by adding in the issue of selecting the proper mixing of the heuristics and operators. One of the key points made by Lones and Sorensen (point #2 in Section 5.4) cited the need for hyper-metaheuristics to be able to address these questions [125, 193].

For the Gnowee algorithm development, true hyper-optimization techniques were not used. Instead, Gnowee's parameters were determined from the set of benchmarks described in Subsection 6.1.5 using iterative parametric studies. Most of the parameters have large stable regions making this approach sufficient, but it is subject to the limitations of numeratives described in Subsection 5.2.1. The Gnowee program-specific settings found from this approach are shown in Table 6.1.

For brevity, only the results of the population size p are presented in Figure 6.3 as it is the most sensitive and complex parameter[2]. Each class of problem, described further in Subsection 6.1.5, could have a different optimal population size, but 25 was chosen as it maximized benefits for the largest number of considered benchmark problems while minimizing the loss of performance for the remaining problems.

[2]The IPython notebooks containing the output results and methods used to develop the psuedo-hyper-optimization are available at `https://github.com/SlaybaughLab/Gnowee/tree/master/Benchmarks`. The full set of plotted results is available at `https://github.com/SlaybaughLab/Gnowee/tree/master/Benchmarks/plots/HyperOptimization`.

Table 6.1: Gnowee algorithm settings.

Parameter	Gnowee
$\boldsymbol{P}$	25
$\boldsymbol{S_i}$	LHC
$\boldsymbol{\alpha}$	0.5
$\boldsymbol{\gamma}$	1
$\boldsymbol{\beta}$	10
$\boldsymbol{f_1}$	1.0
$\boldsymbol{f_d}$	0.2
$\boldsymbol{f_e}$	0.2

6.1.4 Benchmarking Methodology

Several well-established, openly available algorithms were chosen to benchmark the performance of Gnowee. This section describes the algorithms chosen, the origin of the specific implementation chosen, and any modifications made to the original algorithm.

It is beyond the scope of this discussion to describe each algorithm implemented for benchmarking in detail. However, with the exception of Discrete Cuckoo Search (DCS), all algorithms were adopted directly from their authors with modifications only to the convergence criteria, described below, and output information. References for the source location of each algorithm are given below. The algorithms chosen for benchmarking represent a diverse set of approaches with both unique and sometimes overlapping heuristic search strategies. However, we do not claim the implementations chosen represent the best possible implementation of a given algorithm. Instead, preference is given to well characterized algorithms readily available for use in engineering design problems.

For comparison against continuous vector algorithms, GA, simulated annealing (SA), PSO, CS, modified cuckoo search (MCS), and MEIGO were selected. GA, SA, and PSO were implemented using the Global Optimization Toolbox in Matlab® R2015b [131]. A Matlab® implementation of Yang's CS[3] and Walton's MCS[4] algorithms were obtained through the Mathworks® File and Link exchanges [219, 232]. The Matlab® implementation of MEIGO[5], openly available from the author's website, was used [60].

For comparison against mixed-integer vectors, GA and MEIGO were chosen. GA was

[3]Available from `https://www.mathworks.com/matlabcentral/fileexchange/29809-cuckoo-search--cs--algorithm`

[4]Available from `https://www.mathworks.com/matlabcentral/linkexchange/links/2999-modified-cuckoo-search-mcs-open-source-gradient-free-optimiser`

[5]`http://www.iim.csic.es/~gingproc/meigo.html`

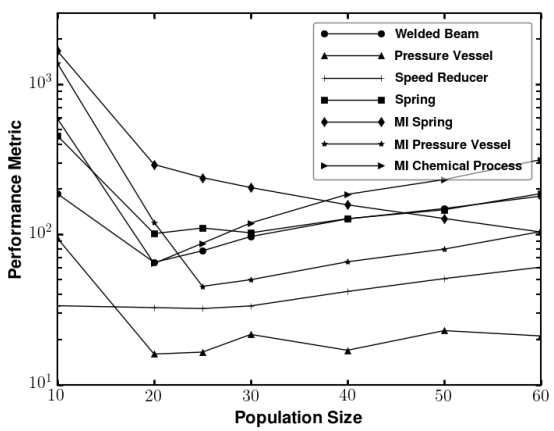

(a) Mixed-Integer and Continuous Constrained

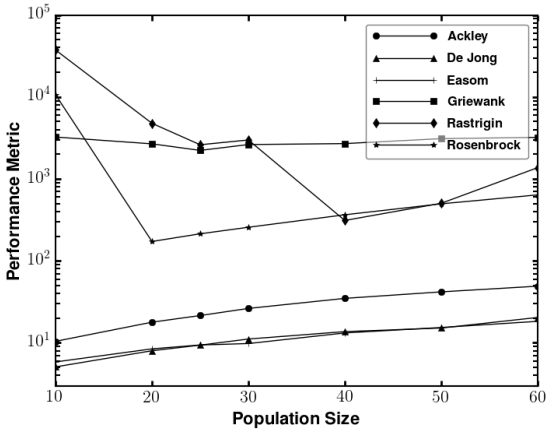

(b) Continuous Unconstrained

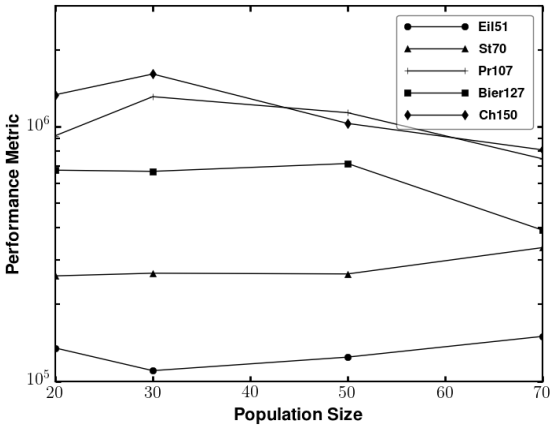

(c) TSP

Figure 6.3: Parametric hyper-optimization results for Gnowee population size. Each algorithm and benchmark was run for 100 iterations.

implemented using the Global Optimization Toolbox in Matlab® R2015b [131]. A Matlab® implementation of MEIGO was obtained through the MEIGO website [60].

Finally, for combinatorial vector algorithms, Discrete GA and DCS were chosen. The Discrete GA algorithm for TSP was obtained through the Mathworks® File exchange[6]. No available implementation of the DCS algorithm was found, so the authors implemented their best interpretation of the algorithm by Zhou [164, 238]. Results from this implementation are consistent with those reported by Zhou [238].

Each of the considered comparison algorithms has many possible user directed modifications that can be made through adjustment of algorithm parameters. For this study,

[6]Available from `https://www.mathworks.com/matlabcentral/fileexchange/13680-traveling-salesman-problem-genetic-algorithm`

all non-convergence related model parameters for the comparison algorithms are set to the defaults recommended by that software package and/or author [60, 131, 219, 232, 238].

The convergence criteria were set to ensure fair comparisons were made among the algorithms. The maximum number of function evaluations, F_{max}^{eval}, is capped at 200,000 for all algorithms. The stall convergence criteria is set at 1E-6, with the maximum number of stall evaluations, F_{stall}^{eval}, set at 10,000. The fitness convergence is set at 1% of the known optimal fitness. Finally, because the solution process is stochastic, each problem was run 100 times to get the representative mean and standard deviation behavior. No attempt was made to attempt to control for or quantify run time, as the intended applications will have high objective function evaluation costs that dwarf the metaheuristic framework costs.

Using this prescribed approach, four sets of benchmark problems were considered: continuous constrained, continuous unconstrained, mixed-integer, and combinatorial. The origin and formulation of these benchmarks is described in the sections that follow. The complete description of each problem is not presented, but the mathematical formulation of the objective function, constraints, and the optimal fitness is shown for an example problem from each set. References to literature are provided for the remaining benchmarks.

Continuous Contrained Benchmarks

The first set of benchmarks consists of four continuous, constrained engineering problems well described in the literature: optimization of a welded beam [30], pressure vessel [4, 30], speed reducer [4, 30], and spring [30, 231]. The pressure vessel design problem is stated as

$$\begin{aligned}
\text{Minimize:} \qquad & f(\vec{x}) = 0.6224RLt_s + 1.7781R^2t_h + 3.1611Lt_s^2 \\
& \qquad + 19.8621Rt_h^2 \\
\text{Subject to:} \qquad & g_1(\vec{x}) = -t_s + 0.01932R \leq 0 \\
& g_2(\vec{x}) = -t_h + 0.00954R \leq 0 \\
& g_3(\vec{x}) = -\pi R^2 L - \frac{4}{3}\pi R^3 750 * 1728 \leq 0 \\
& g_4(\vec{x}) = -240 + L \,,
\end{aligned}$$

where $\vec{x}$, the upper, and the lower bounds are given by

$$\begin{aligned}
\vec{x} &= [R, L, t_s, t_h] \\
\vec{x}_{lb} &= \left[10, 1 \times 10^{-8}, 0.0625, 0.0625\right] \\
\vec{x}_{ub} &= [50, 200, 6.1875, 6.1875] \,,
\end{aligned}$$

and R is the pressure vessel inner radius, L is the length of the pressure vessel, t_s is the thickness of the pressure vessel shell, and t_h is the head thickness. All variables are treated as continuous.

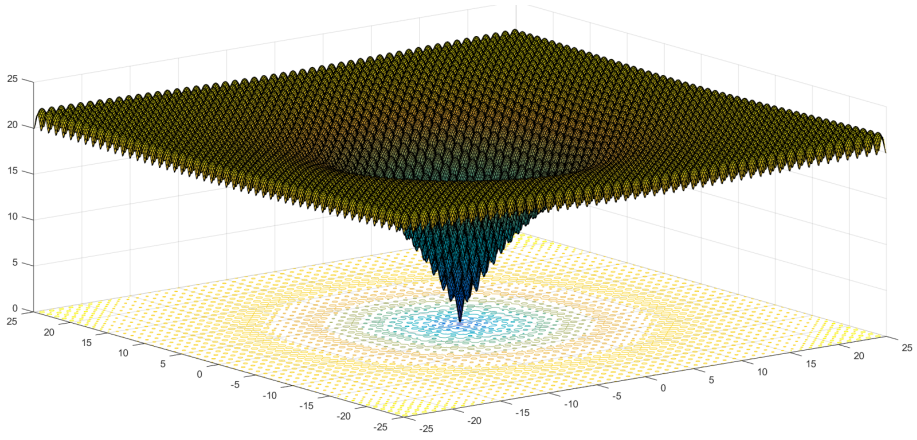

Figure 6.4: Two-dimensional Ackley function.

Continuous Uncontrained Benchmarks

The second set of benchmarks consists of six continuous, unconstrained functions well described in the literature as benchmarks: Ackley, De Jong, Easom, Griewank, Rastrigin, Rosenbrock [131, 219, 231]. Ackley's function is a multi-modal, n-dimensional function with a global minimum of $f_{opt} = 0$. This function is shown in Figure 6.4 for $n = 2$ and given by

$$f(\vec{x}) = -20exp\left[-0.2\sqrt{\frac{1}{d}\Sigma_{i=1}^{d}x_i^2}\right] - exp\left[\frac{1}{d}\Sigma_{i=1}^{d}cos(2\pi x_i)\right] + (20 + e) \qquad x_i \in [-32.768, 32.768].$$

Mixed-Integer Benchmark Problems

Mixed-integer optimization problems combine continuous, binary, integer, and/or discrete variables. Here, three engineering design benchmarks are considered: MI spring [111], MI pressure vessel [30], and a MI chemical process design [234]. For brevity, only the pressure vessel is described in detail.

The MI pressure vessel design is similar to the continuous pressure vessel design specified in Section 6.1.4 with the exception that two variables, t_s and t_h, can only take discretized values. The $\vec{x}$, the upper, and the lower bounds are the same as specified in Section 6.1.4, but for the mixed-integer case, t_s and t_h can only take values that are discrete multiples of 0.0625.

Combinatorial Benchmark Problems

The traveling salesman problem (TSP) was chosen for the combinatorial optimization benchmarks. TSP problems were drawn from TSPLIB[7] and were chosen to span a range of city lengths without being excessively large given the intended engineering design applications. For this study, the Eil51, St70, Pr107, Bier127, and Ch150 TSP problems were chosen.

6.1.5 Benchmarking Results

Benchmarks were carried out as described in Subsection 6.1.4 for continuous constrained, continuous unconstrained, mixed-integer, and combinatorial (TSP) benchmark problems. The results presented here highlight the optimization performance of Gnowee against the eight algorithms described in Subsection 6.1.4. For brevity, we have only included a subset of the results; the full results set is available[8]. Here, specific results are presented for the continuous constrained spring optimization to serve as an example, and summary results are presented for the remaining problems.

For Gnowee, success is measured by consistent, rapid convergence to nearly-globally-optimal solutions. To benchmark in a method consistent with the Gnowee design objectives, convergence criteria were set to a "limited" number of function evaluations (200,000), a threshold of 1% of the best known optimal fitness, or a "limited" function evaluation stall limit (10,000) as described in Subsection 6.1.4. To quantitatively capture the performance of a given algorithm and to facilitate comparison of algorithm performance, a figure of merit (FOM) was defined as

$$FOM = \frac{f_{avg}(\vec{x}) - f_{opt}}{f_{opt}} \left(N^{avg}_{f(\vec{x})} + 3\sigma_{N_{avg}} \right) . \tag{6.18}$$

This formulation of the FOM emphasizes the convergence rate and width of the functional evaluation distribution while also penalizing prematurely convergent algorithms for poor fitness solutions. The choice of using the 3σ number of function evaluations emphasizes the importance of minimizing the total number of function evaluations, an key factor for the high-cost objective function evaluation applications for which Gnowee was designed. In these applications, an optimization is often only performed a few times, perhaps even just once, making the edge cases more interesting than the average behavior of the algorithm.

In the results presented below, bolded values indicate premature convergence where the fitness achieved is $> 1\%$ from the optimal solution. The underlined values indicate the best performing algorithm according to the FOM.

[7] Available from urlhttp://comopt.ifi.uni-heidelberg.de/software/TSPLIB95/

[8] Available from `https://github.com/SlaybaughLab/Gnowee/tree/master/Benchmarks/results`

Continuous Constrained Benchmark Results

The continuous benchmarks considered are subdivided into constrained and unconstrained classes for ease of comparison. First, the detailed results for the spring optimization problem are shown in Table 6.2 for the run conditions and convergence criteria specified in Subsection 6.1.3. Table 6.2 presents design variable values (x_*), fitness ($f(\vec{x})$), number of function evaluations ($N_{f(\vec{x})}$), and FOM for both the average and best performance obtained over the 100 optimization iterations performed by each algorithm. For the spring optimization, Gnowee outperformed the other algorithms on average by reducing the number and standard deviation of function evaluations required, while MEIGO and SA had the best single performance optimizations.

The summary of FOM results obtained for the continuous, constrained benchmark problems are shown in Table 6.3. Across all of the benchmarks in this category, Gnowee had the best performance twice and never finished worse than third. Additionally, Gnowee did not suffer from premature convergence issues that affected all of the other algorithms except CS. Rapid yet continual convergence across a wide range of problems is a key feature of Gnowee enabled by the diverse set of hybrid heuristics.

One way to better visualize the results from Table 6.3 is to look at the histogram of converged solutions as shown in Figure 6.5 for SA and Gnowee. The histogram includes optimization results for 1000 iterations of the best average performer, Gnowee, and one of the top individual performers, SA. SA heavily relies on the directional search, neighborhood search, and hill climbing heuristics resulting in rapid convergence to a *local* optima. However, this comes at the expense of robust global search, often resulting in a solution that stalls short of the global, or in this case nearly global, optimum. Gnowee, on the other hand, does not achieve nearly as rapid initial convergence, but its convergence is more consistent due to the balancing of local and global search heuristics.

The effect of the balanced heuristics on the convergence can be shown throughout the complete optimization evolution as illustrated in Figure 6.6 for the spring benchmark. This figure shows the average fitness versus fixed function evaluation intervals for up to 10,000 function evaluations, illustrating some key points. First, while Gnowee is not the best algorithm at all fitness convergence levels, it is competitive across the full range considered. Second, Gnowee maintains its convergence rate and continues to converge while other algorithms start to plateau. Finally, this highlights a potential area for future work. In this example, and across several others, Gnowee's initial solution is among the worst. Work to improve the initial starting solution could accelerate Gnowee's convergence and improve performance.

Finally, a look at the convergence history of the design parameters illustrates the importance of balancing local and global search. Convergence history is shown in Figure 6.7 for a single optimization of the spring benchmark using Gnowee. In Figure 6.7, each point represents an improvement in overall fitness (top subplot) and the corresponding values for each of the three design variables (bottom three subplots). When there are periods of gradual change in the design variables with improvements in fitness, the solution is improving via

Table 6.2: Spring optimization results. Bold results indicate fitness greater than 1% from the global optimum. Underlined results indicate the best performance for the average and the overall best run. Optimum fitness = 0.012665.

	GA[131]	**SA[131]**	**PSO[131]**	**CS [231]**	**MCS[219]**	**MEIGO[60]**	**Gnowee**
x_1^{avg}	**0.060063 ± 0.00558**	0.050810 ± 0.00090	**0.052298 ± 0.00314**	0.051703 ± 0.00127	**0.058462 ± 0.00592**	0.052817 ± 0.00133	0.051620 ± 0.00119
x_2^{avg}	**0.610416 ± 0.18392**	0.335680 ± 0.02133	**0.375903 ± 0.08398**	0.357026 ± 0.03064	**0.560899 ± 0.18946**	0.385194 ± 0.03386	0.355059 ± 0.02874
x_3^{avg}	**5.461663 ± 3.19803**	12.840958 ± 1.32526	**11.363353 ± 3.39514**	11.560822 ± 1.83294	**6.573904 ± 3.75091**	9.997362 ± 1.53760	11.648626 ± 1.72111
$f_{avg}(\vec{x})$	**0.014398 ± 0.00161**	0.012778 ± 0.00002	**0.012890 ± 0.00030**	0.012771 ± 0.00004	**0.014068 ± 0.00156**	0.012785 ± 0.00006	0.012763 ± 0.00002
$N_{f(\vec{x})}^{avg}$	**16947 ± 6379**	5820 ± 5085	**7959 ± 10523**	16948 ± 7174	**19013 ± 13684**	10279 ± 9835	4738 ± 1836
FOM_{avg}	**4938**	188.3	**702.9**	323.2	**6654**	376.7	79.0
x_1^{best}	0.051341	0.050318	0.052021	0.051230	0.051768	0.052121	0.051092
x_2^{best}	0.348240	0.324492	0.364483	0.345779	0.358488	0.367169	0.342205
x_3^{best}	11.878832	13.476806	10.886333	11.987921	11.224128	10.703094	12.210091
$f_{best}(\vec{x})$	0.012740	0.012715	0.012711	0.012694	0.012705	0.012691	0.012694
$N_{f(\vec{x})}^{best}$	7900	835	27900	5225	4328	1090	3813
FOM_{best}	47	3.3	100.3	12.1	13.5	2.2	8.7

Table 6.3: Summary of FOM results for continuous constrained optimization benchmarks. Bold results indicate fitness greater than 1% from the global optimum. Underlined results indicate the best performance for the average and the overall best run.

	Welded Beam [30]	**Pressure Vessel [30]**	**Speed Reducer [30]**	**Spring [30]**
GA[131]	**106667.6**	**762.0**	56.5	**4938**
SA[131]	**5125.8**	**8488.6**	**1437.1**	188.3
PSO[131]	329.4	**1209.5**	62.2	**702.9**
CS[231]	442.6	529.4	51.3	323.2
MCS[219]	**2933.8**	**1472.6**	26.0	**6654**
MEIGO[60]	<u>35.0</u>	**1567.4**	<u>11.7</u>	355.3
Gnowee	80.6	<u>108.4</u>	29.7	<u>79.0</u>

local search heuristics. When there are large changes in one or more design variables from one point to the next, the solution is improving via global search heuristics.

This combination of local and global improvement is the reason that Gnowee outperforms most other algorithms most of the time. Unlike GA, PSO, or MCS, which tend to prematurely converge for some problems due to shifts towards local search with increasing generation/evaluations as shown in Figure 6.6, Gnowee maintains global search heuristics throughout the optimization as illustrated by the jumping between local optima throughout the optimization history shown in Figure 6.7.

Continuous Unconstrained Benchmark Results

The other subset of continuous benchmarks was the unconstrained functions described in Section 6.1.4. The summary of the FOM results obtained for these benchmark problems are shown in Table 6.4. Each column of the table indicates the benchmark function and the dimensionality considered. Here, Gnowee obtains the best performance for the Rastrigin and Rosenbrock functions and the second best performance for the remaining functions. Similar to the continuous constrained benchmark results shown in Section 6.1.5, Gnowee maintains consistent continual convergence throughout the optimization process for all problems except for the Rastrigin function. For the easier problems, Gnowee's poor early time solutions slow the convergence process slightly, thereby hindering its performance when compared to the other algorithms.

The results in Table 6.4 are useful for understanding the interplay of the well defined fitness landscape and the search heuristics used. For example, consider the Griewank function results. The Greiwank function is a high-frequency multi-modal landscape super-imposed

Table 6.4: Summary of FOM results for continuous unconstrained optimization benchmarks. Bold results indicate fitness greater than 1% from the global optimum. Underlined results indicate the best performance for the average and the overall best run.

	Ackley (3-D)	**De Jong (4-D)**	**Easom (2-D)**	**Griewank (6-D)**	**Rastrigin (5-D)**	**Rosenbrock (5-D)**
GA[131]	**1666.8**	10.7	**6809.3**	92.1	**15843**	**181239**
SA[131]	109.7	53.7	**22415.2**	**27654.5**	**122362**	**12420**
PSO[131]	33.7	15.2	11.9	**3665.4**	**29436**	**25884**
CS[231]	85.9	30.5	58.8	**13956.8**	**274627**	**47472**
MCS[219]	**1955.5**	12.6	54.4	**16746.4**	**155804**	**143587**
MEIGO[60]	12.5	3.5	3.2	**2597.3**	**11514.8**	224.4
Gnowee	19.7	8.9	6.5	**1549.7**	**1753.0**	152.2

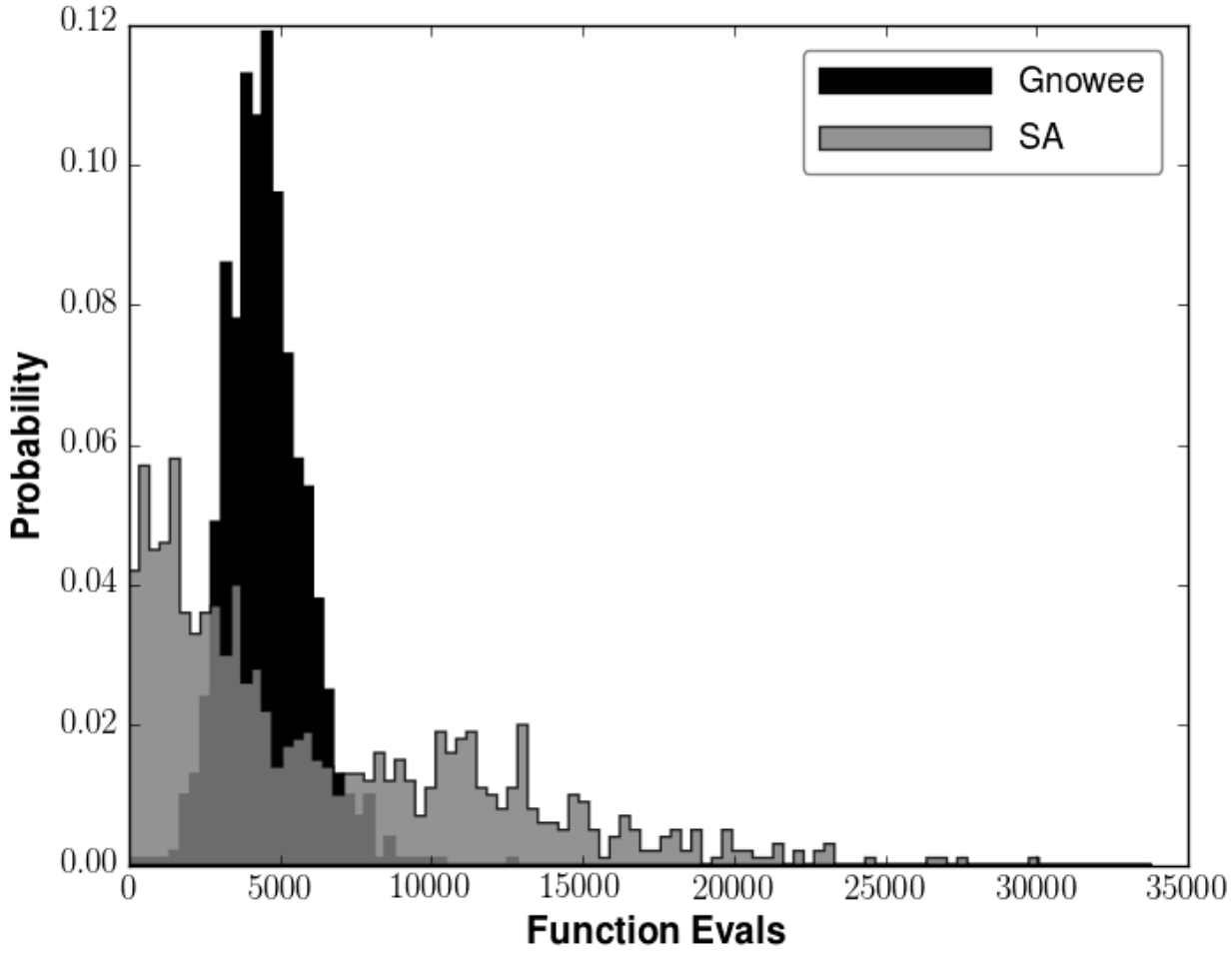

Figure 6.5: Histogram of the number of function evaluations performed before meeting the convergence or stall criteria specified in Subsection 6.1.4.

on a convex design landscape. When solving this problem, an initial population is likely to be formed in the large convex region and funneled to the edges of the flatter, center multi-modal region. GA's focus on intermediate search heuristics is highly effective in a problem like Griewank. Intermediate search allows for pairs of solutions at opposite edges to effectively traverse the complex multi-modal region in the center. Conversely, algorithms that use neighborhood or variable neighborhood search heuristics will have to traverse many local optima that can trap individual members. Algorithms incorporating intermediate or directional search heuristics such as PSO, MEIGO, and Gnowee do better on this problem. Algorithms that focus on neighborhood or variable neighborhood search, like SA and CS, do poorly. Finally, SA and MCS use "cooling" parameters that limit the range of the neighborhood and variable neighborhood search heuristics as the number of generations progresses. This can lead to local trapping and premature convergence on large, highly multi-modal

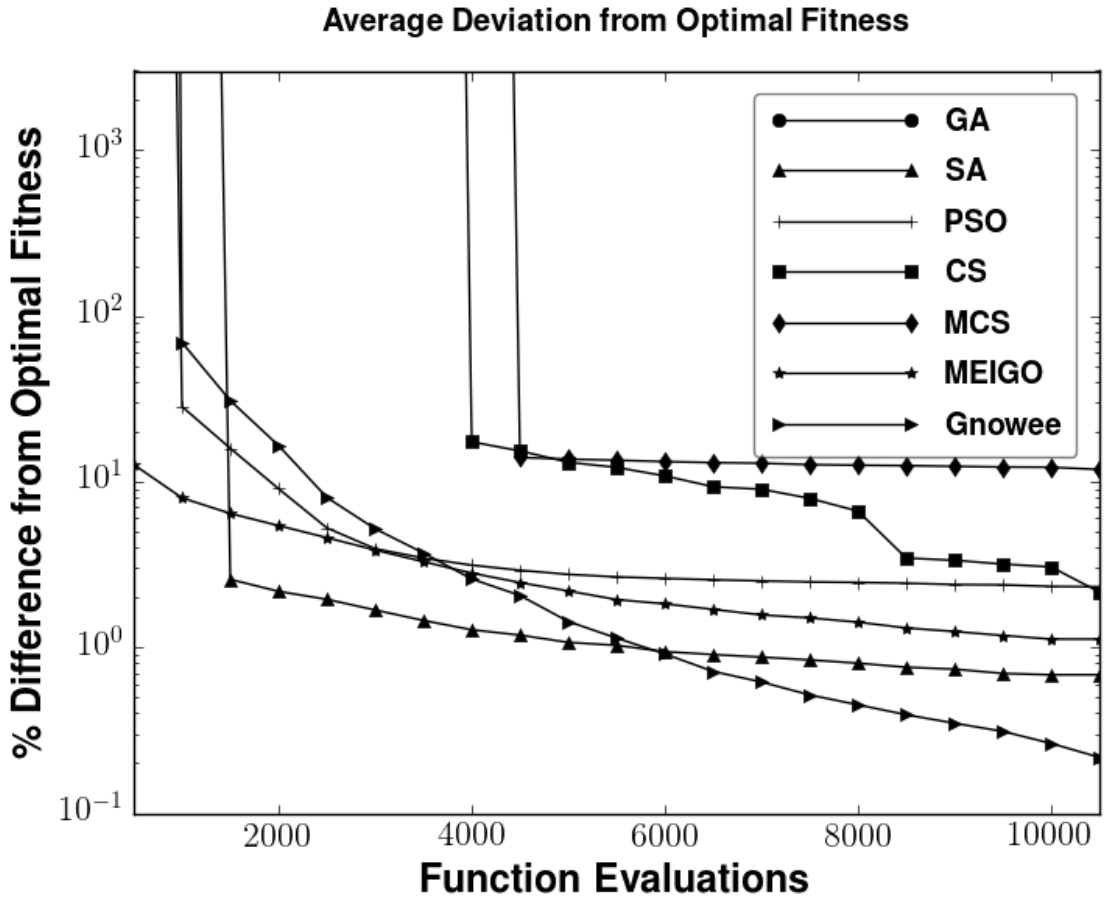

Figure 6.6: Spring optimization fitness convergence. 1σ standard deviation in fitness is generally comparable or smaller than the plot markers.

problems like Griewank, which is another factor in their poor performance.

Mixed-Integer Benchmark Results

The mixed-integer benchmarks allow for the performance of Gnowee to be assessed in problems containing a combination of continuous, integer, binary, and discrete variables. The summary of the FOM results obtained for the mixed-integer benchmark problems are shown in Table 6.5.

Here, Gnowee obtains the best performance across all benchmarks considered. Similar to the previous benchmarks, Gnowee maintains rapid, consistent continual convergence throughout the optimization process across the range of the benchmarks considered. Although MEIGO performs similarly well for the spring and chemical process problems, it pre-maturely converges more often than not for the pressure vessel design. Once again,

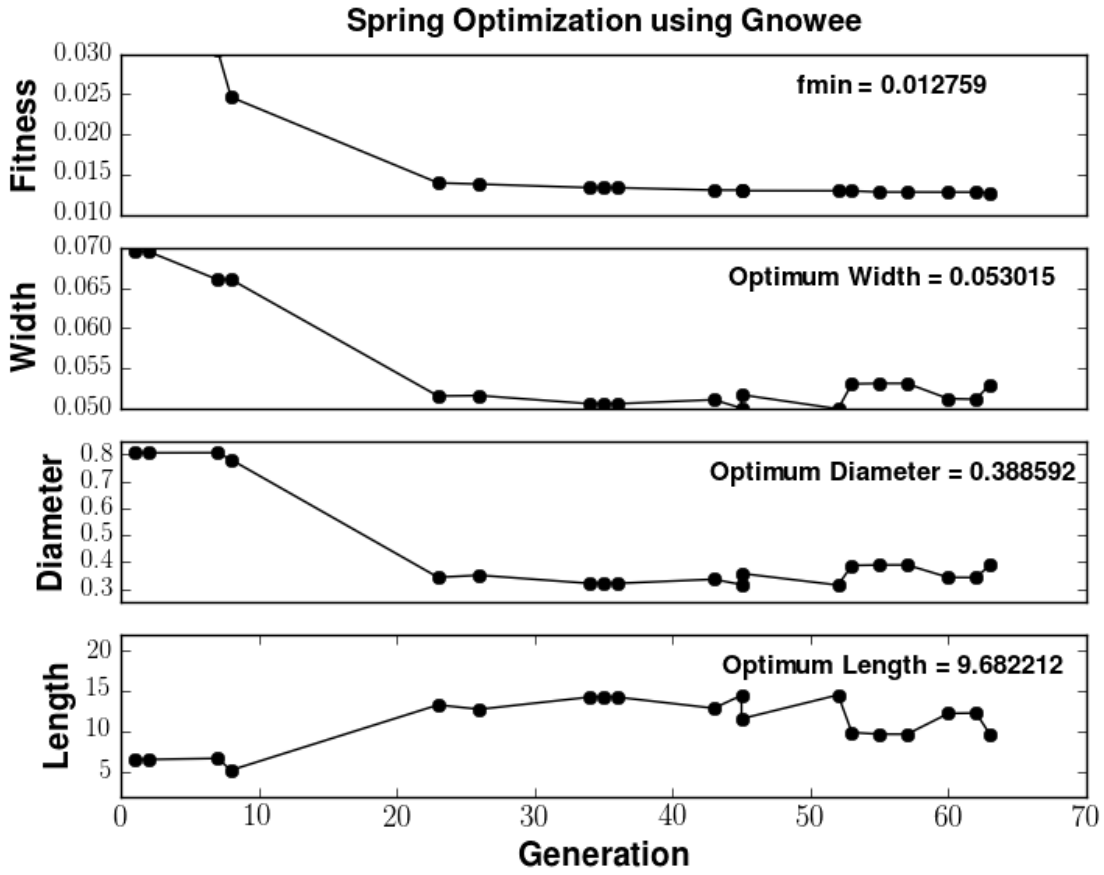

Figure 6.7: Spring optimization history for a single Gnowee run showing the convergence of the fitness and each design parameter.

Table 6.5: Summary of FOM results for constrained mixed-integer optimization benchmarks. Bold values indicate average fitness greater than 1% from the global optimum. Underlined values indicate the best average performance.

	Pressure Vessel [30]	**Spring [111]**	**Chemical Process [234]**
GA[131]	**897.9**	**1697.9**	**18890.1**
MEIGO[60]	**358.3**	330.1	95.2
Gnowee	<u>40.4</u>	<u>219.2</u>	<u>92.1</u>

Gnowee's diverse, robust set of heuristics limits premature convergence across all bench-

Table 6.6: Summary of FOM results for TSP optimization benchmarks. Bold indicates fitness greater than 1% from the global optimum. Underlined indicates the best average performance.

	GA[131]	DCS[238]	Gnowee
Eil51	**10940.4**	1509.7	**555.6**
St70	**27452.0**	3804.6	**1403.1**
Pr107	**36563.1**	**6067.9**	**3380.5**
Bier127	**49869.9**	**8337.3**	**3918.6**
Ch150	**115495.0**	**14396.6**	**5261.4**

marks considered.

Combinatorial Benchmark Results

The combinatorial aspects of Gnowee were benchmarked using the TSP problems described in Section 6.1.4. Unlike the algorithms used to solve the previous benchmarks, the GA and DCS algorithms used TSP specific information, i.e. the distance between pairs of cities, to guide the search process. To enable a coherent comparison between the algorithms, distance based searches were also incorporated into the Gnowee heuristics.

The summary of the FOM results obtained for the TSP benchmark problems are shown in Table 6.6. Each row of the table indicates the benchmark TSP route considered. The dimensionality of the TSP problems is indicated by the number in the problem name. Due to the high dimensionality, the solution space is extremely large, making 1% convergence results with limited function evaluations difficult. This is illustrated in Table 6.6 by the fact that 13 of the 15 cases do not meet the 1% convergence criterion. While not meeting the stated convergence criteria, Gnowee does outperform DCS and GA across all of the TSP benchmarks according the defined FOM.

The primary driver for Gnowee's increased performance is a reduction in the number of function evaluations needed as shown in Table 6.7. Gnowee reduces the number of function evaluations by a factor of ∼4-10 over the DCS and GA algorithms. The reduction in function evaluations will enable nearly-global solutions with limited function evaluations in the smaller sets of combinatorial variables found in typical engineering design problems.

Table 6.7: Summary of function evaluation results for TSP optimization benchmarks. Bold results indicate fitness greater than 1% from the global optimum. Underlined results indicate the best performance for the average and the overall best run.

	GA[131]	DCS[238]	Gnowee
Eil51	**103415 ± 24218**	104341 ± 39398	**9294 ± 6033**
St70	**157455 ± 30426**	174362 ± 37953	**16238 ± 9823**
Pr107	**159692 ± 37900**	**198006 ± 15497**	**27447 ± 16157**
Bier127	**197340 ± 10306**	**228991 ± 6345**	**37483 ± 18077**
Ch150	**199603 ± 3276**	**231786 ± 5338**	**48757 ± 24725**

6.2 Coeus

Titan god of intellect, wisdom, and heavenly oracles who pierces beyond the fog of prevailing obviosities with his inquisitive mind to amass new truths.

- Greek mythology

Coeus[9] provides the interface between Gnowee, the optimization alogithm, the radiation transport codes required to evaluate the ETA objective function and constraints, and the job scheduling system used to submit jobs on HPCs. The Coeus interfaces can be best visualized through the flowgorithm shown in Figure 6.8. In Figure 6.8, the dashed lines indicate paths that are taken either at the very start of the program or at the conclusion of each generation. The completion of each generation is defined as a cycle through the operators described in Subsection 6.1.2.

This section starts with a discussion of the use of surrogate methods to accelerate the black box radiation transport calculations using the AutomateD VarianCe reducTion Generator v3.0.3 (ADVANTG) code [149]. It then describes how Gnowee design variables and the search process is interfaced with the Monte Carlo Neutral Particle (MCNP) radiation transport code [200]. Both codes were run with the ENDF/B-VII.1 evaluated nuclear data libraries. A full description of either code and the transport methods employed is not presented as these are available in their respective manuals [149, 200]. Instead, the discussion for both is centered around their use and interfaced within the Coeus construct. Next, a description of the method of parallelization employed is presented. Finally, this section closes by highlighting future improvements that can be made to Coeus to improve its adaptability to other nuclear engineering application.

[9]Open source and available from `https://github.com/SlaybaughLab/Coeus`. Code documentation, installation procedures, how to run, and an overview of the outputs is in the README file located here as well.

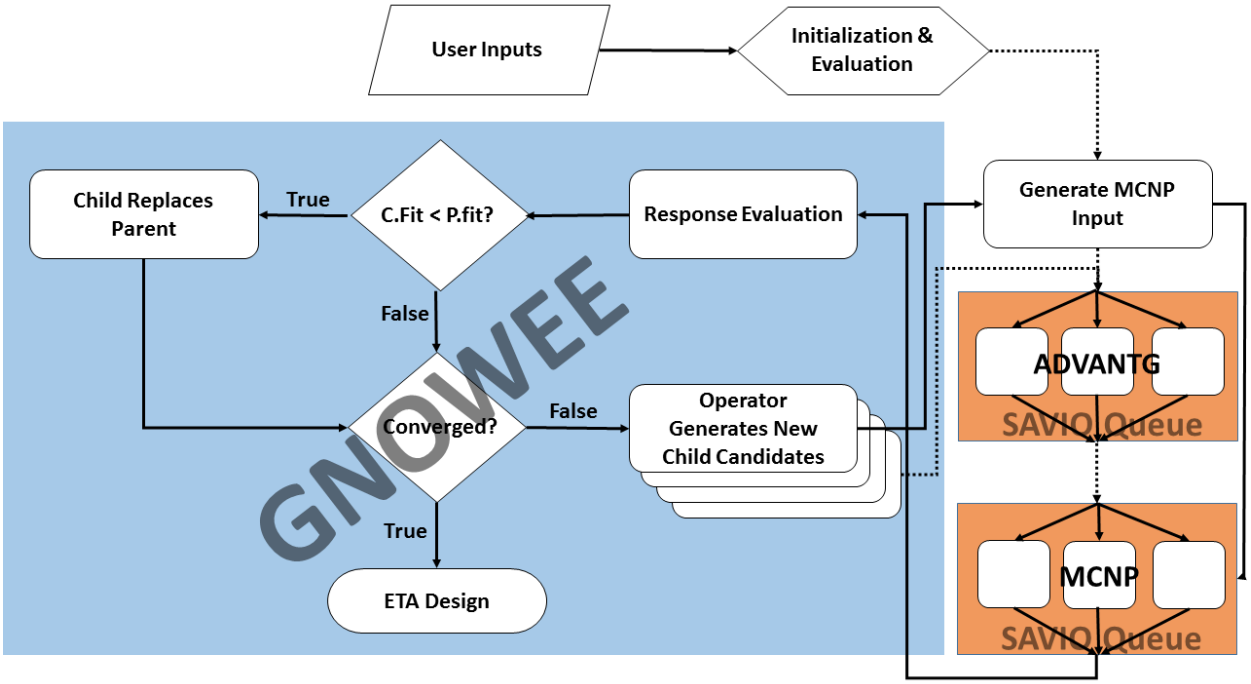

Figure 6.8: Coeus flowgorithm showing the interfaces between Gnowee, the radiation transport codes, and the parrallelization for HPC.

6.2.1 ADVANTG

ADVANTG determines space and energy dependent weight windows and biased source distributions for use in MCNP based on approximate 3-D, multigroup, discrete ordinates adjoint transport solutions generated by Denovo. ADVANTG automatically converts the continuous MCNP input to a discrete Denovo input, develops the variance reduction parameters, and outputs an updated MCNP and weight window input file. ADVANTG is compatible with all MCNP features and can handle one or more cell tallies (F4, F6, F8), surface tallies (F1 and F2), point-detector tallies (F5), and Cartesian mesh tallies (FMESH) [149].

The tally variance reduction parameters are generated with the Consistent Adjoint Driven Importance Sampling (CADIS) method, which has been demonstrated to improve the tally FOM by $O(10^1 - 10^4)$ [149]. The tally FOM is defined as

$$FOM = \frac{1}{\sigma^2 t} \tag{6.19}$$

where σ is the relative error of the tally and t is computer time in minutes. CADIS is designed to improve one particular outcome in a calculation, e.g. detector response, flux at a small volume, etc. For global solutions, e.g. flux everywhere, variance reduction parameters are generated using the Forward-Weighted CADIS (FW-CADIS) method. Details about CADIS and FW-CADIS can be found in the ADVANTG manual [149].

Coeus leverages ADVANTG's seamless integration with MCNP to generate weight windows and baised source solutions for nuclear engineering optimization problems. The weight windows and biased source solutions are then used to improve the FOM of MCNP calculations, see Subsection 6.2.2, to specified levels of tally statistics. Each member of the population in Gnowee carries an associated weight window map and biased source distribution. These are updated once per generation, which is once every few design calculations in Gnowee (the actual number varies based on the type of variables, and the selection of the f_l, f_e, and f_m Gnowee parameters). Using the parameters recommended in Table 6.1, this has been shown to be sufficient for the ETA design inputs and constraints shown in Section 6.3 as the importance maps do not change significantly from design to design.

The user can control the selection of the ADVANTG run parameters through an ADVANTG settings input file. The user must have some familiarity with ADVANTG and the correct settings to appropriately set these parameters – Coeus does not automatically generate default parameters. The input file uses ADVANTG keywords to enable the changing of key parameters such as the discrete cross-section library, the method used to generate the weight windows, the tallies for which to optimize the weight windows, outputs desired, the source characteristics, and the deterministic discretization levels. It also allows for specification of three levels of spatial discretization granularity, but these are currently tied to the ETA optimization problem. Future improvements will allow the levels of discretization to be tied to start and stop points that are either fixed or associated with design variables. The ability to have multiple levels of discretization is important for creating sufficiently useful weight window maps while controlling deterministic computation time and storage requirements, which can be several GB per ADVANTG calculation. Coeus manages the storage requirements by deleting all of the ADVANTG ancillary files after the completion of the ADVANTG run, but the weight window maps themselves, which must be kept for the MCNP simulations, can be 100s of MB to a couple of GB each. Since Gnowee uses a population based approach, the required storage can grow rapidly beyond the local user allotments.

Since extensibility beyond ETA design problems is desired, it is worth considering the limitations and benefits of the variance reduction approaches employed in the context of other nuclear engineering optimization problems. First, the use of ADVANTG allows for the incorporation of many tallies through the FW-CADIS method. This allows Coeus to generate weight windows for problems whose objective function and/or constraints are informed by multiple tallies spread throughout the problem geometry. Using ADVANTG would also integrate seamlessly with any future expansion of Coeus and Gnowee to multi-objection function optimization.

However, the use of once-per-generation updates of the weight window map can be inadequate for problems with dynamic boundaries. Large shifts in the scale of the problem, especially those that also move the tallies in space, would be problematic with the current approach. To address this, each calculation tests the level of statistics for consistency between the previous parent design and the current child design being considered. If there is a decrease in the level of statistics for the tallies being considered in ADVANTG by a factor of two, a new weight window map is generated and the MCNP calculation is re-performed

for the child solution. As long as the weight windows do not fail often, this approach is sufficient.

Finally, this approach does limit the choice of radiation transport engine to MCNP in order to achieve the acceleration of the design optimization. While Coeus is modular and could integrate additional radiation transport codes, alternative strategies to improve the FOM for the transport calculations needed by the optimization methods would need to be employed.

6.2.2 MCNP

MCNP is the chosen radiation transport engine for Coeus. It is a Monte Carlo based, continuous energy, continuous space, coupled neutral and charged particle transport code [200]. The flexibility, wide adoption, extensive bench-marking, and test history make MCNP an ideal choice for Coeus. Additionally, by using MCNP as the primary transport and geometry specification mechanism, the learning curve associated with Coeus is greatly reduced for large segments of the nuclear engineering community. For the ETA optimization, MCNP 6.1 with only neutron physics was used. While the current user-specified MCNP physics parameters are geared towards the neutron physics applications, nothing about the structure of Coeus or Gnowee prohibits extension to the use of MCNPX and charged particle transport.

As shown in Figure 6.8, the primary purpose of Coeus is to manage the interaction with Gnowee, creation of MCNP inputs, submitting of jobs, reading of MCNP outputs, and updating the population and results. Coeus also has to manage the creation of the ADVANTG inputs, submission of jobs, and reading of the ADVANTG outputs, but these are essentially just extensions of the MCNP processes due to the tight integration between MCNP and ADVANTG. This makes the interface between Gnowee and MCNP a crucial aspect of Coeus.

Currently, the interaction between the Gnowee variable update operators and the creation of the MCNP input files is hard-coded into Coeus for the ETA application. Coeus initializes surface and geometry objects with the specific 2-D ETA geometry used for the NIF application in mind. For each operator, the variables associated with each surface are sampled as described in Section 6.1. All of the surface and cell object updating and MCNP geometry logic is handled within each operator as needed for the variables under consideration for that particular operator. The MCNP parameters, surface, and cell objects are then passed to a function that prints the associated MCNP input. However, nothing about Coeus or Gnowee requires the tight integration of the search operators and cell update, and this can be handled in a much more generic, modular fashion (see Subsection 6.2.5 for more details).

After each MCNP calculation, the specified MCNP tallies are read and used to calculate the objective function and constraints. After assessing the fitness, the population is updated as described in Algorithm 1. Based on the assessed fitness, Coeus will increase the number

of particles used for that parent[10], rerun MCNP, and reevaluate the fitness of the considered design. The number of particles used in this second calculation with this parent design will be used for all future MCNP calculations involving that parent. This is true even if the increase of particles results in a worse fitness, which is possible due to the increased accuracy of the solution. Fixing the number of particles for future generations prevents oscillations and excessive inter-generational MCNP calculations.

The variation of the number of particles used as a function of fitness of a given design allows for the bulk of the computational cost to be spent on promising designs. For example, if a current design is outside the constraints imposed on the system, there is not any reason to spend time getting the statistical uncertainty to reasonable values. On the other hand, if the entire process is run at higher uncertainty for the sake of speed, Coeus may not be able to appropriately rank designs due to the large uncertainty in the tallies for each. This has a ripple effect beyond the inaccurate ranking that affects the subsequent generations. Since the Gnowee algorithm relies heavily on elitism, which requires an accurate ranking, for its intensification (local convergence) efforts, the inaccurate ranking will propagate less desirable characteristics throughout the population and spend extra function evaluations attempting to improve upon a less promising design.

When evaluating the fitness and constraints, Coeus handles two different tally types: scalars and vectors. The scalars are point values that represent the total from a tally, and the vectors are generally energy-dependent spectra but can be any tally that varies as a function of another MCNP-talliable variable, such as energy, time, or angle. For the vector variables, MCNP represents them as a normalized, group-wise binned results. However, the user may often have the desired objective in a different form (unnormalized, differential, lethargy, etc.). Coeus handles all of these conversions internally based on the user specified input and objective function type, thereby making the standard MCNP tallies adaptable to a wide variety of user objectives.

6.2.3 Method of Parallelization

Coeus takes advantage of the "embarrassingly parallel" nature of both Gnowee and MCNP to achieve efficient parallel computation. This results in a bi-level task based master-slave approach to parallelization where the regroup points are at the end of each operator. Since the computational requirements change over time for a given parent (due to increases in accuracy for high fitness solutions) and operator (due to varying number of designs generated by an operator), this represents a very efficient use of HPC computing time as only the number of nodes required at any given time are requested. Additionally, this is a very "courteous" approach as Coeus will surge to fill whatever nodes are available at the time, but it will not lock up a large chunk of compute power for long periods of time.

[10]The user specifies the starting number of particles; future code improvements will have the starting number of particles determined automatically.

An alternative approach that was considered was to make each member of the population its own thread that ran at its own speed. Coeus itself would hold a block of compute nodes and divide them up according to the needs of the individual threads. The threads would communicate via a bulletin board that would contain the design vectors for each thread to enable the information sharing required for some operators. In this construct, there is no requirement for the individual threads to be at the same operator or generation as another thread. When the optimization converges, each thread will be at a different generation and have performed a different number of function evaluations than if they had moved in lockstep through the Gnowee algorithm. The understanding of the interaction of the heuristics with out-of-sync threads is further complicated by the fact that the best fitness threads will have higher numbers of particles (i.e. higher computational requirements) and take longer to run unless some effort is spent on load balancing. While this threading and load balancing strategy would require significant modifications to Coeus and Gnowee, and perhaps a rethinking of the Gnowee operators altogether, this approach would be beneficial in applications where time, not compute power, was the resource that required conservation.

Gnowee itself is not parallelized as the compute time for each variable updating operator is a small fraction of the time required for the associated radiation transport calculation. It is here that the first level of parallelization occurs. Coeus builds the job scripts and submits slave jobs for each child generated by the current operator. The number of nodes allocated to each job is dependent on the number of particles being used for the MCNP simulation of that child design. This enables some semblance of load balancing. MCNP's task-based parallelization then provides the second level of parallelization within the allotted nodes and cpus. Coeus monitors the submitted slave jobs waiting for their completion before moving to evaluate the objective function and constraints. Coeus then continues to move through the algorithm with serial calculations in Gnowee and parallel calculations when evaluating the radiation transport codes required for weight window generation (ADVANTG) or objective function and constraint evaluation (MCNP).

This parallelization method has been successfully implemented on Savio[11], but it is not limited to Savio and is flexible implementation compatible on a wide range of HPC assets. The job submission script, currently adapted for the Slurm Workload Manager, is modular and can be changed for different scheduling systems. Additionally, the inputs required for the specific partition, user, or account are Coeus inputs, allowing for ease of use within a given architecture. Finally, this parallelization method allows for Coeus to run on very few nodes or to surge to run on many nodes, depending on the HPC capabilities and availability.

6.2.4 Alternate Use Cases

Gnowee was designed to be very general from initial development, as evidenced by the wide variety of benchmarks considered. However, Coeus, in its first incarnation, did not

[11]Savio is UC-Berkeley's 385-node, 8,040 processor-core (plus 169,728 GPU-provided CUDA cores) Linux cluster rated at nearly 350 peak teraFLOPS.

leverage this development fully. Instead, Coeus is currently limited to ETA design for 2-D cylindrical and/or conical geometries. This is an artificially imposed constraint – "Premature optimization is the root of all evil" after all – that can be removed in future development of Coeus (see Subsection 6.2.5 for more details). Possible alternative use examples for Coeus beyond the TNF ETA design considered in this work include:

1. Boron neutron capture therapy (BNCT)
2. Space radiation shielding design
3. Radiation converters
4. Medical isotope production targets
5. Fusion blanket design
6. Detector network configurations
7. Neutron spectrometers with matrixed detectors
8. Reactor design

6.2.5 Ongoing Development

Development of Coeus is ongoing to extend beyond ETA design applications to those mentioned in Subsection 6.2.4 and beyond. The aim is to develop a general purpose nuclear engineering code that is flexible enough to accommodate different transport engines, HPC architectures, modeled geometries, objective functions, and constraints. Some of the changes required for this transition have been mentioned throughout Section 6.2. The following is a brief summary of several of the major changes currently or soon to be underway that will enable the transition to a more general purpose code:

1. **A more general geometry:** This is a two step process. First, the tight integration of the Gnowee operators and the MCNP geometry modification must be separated. This is basically done, but the MCNP geometry logic piece is lacking. Next, the input needs to be modified to allow for a more generic geometry specification. The concept is that a standard MCNP input file will serve as the main input, with special formats used to identify inputs that are variables to be sampled. A parser then pulls the variable vector definition from the file, passes it to Gnowee, and the updated vector replaces the corresponding variables in the MCNP input file. A beta version of this is in place.
2. **Expand ADVANTG input options:** Currently, the user-selectable ADVANTG inputs are limited to a subset of the ADVANTG options. This will be expanded to include all ADVANTG options with two methods of spatial discretization: (1) predefined fixed bounds and intervals for static problems and (2) the current variable-based bounds and intervals for dynamic problems.

3. **Automatic ADVANTG switch:** This would enable the calculation of ADVANTG weight windows to automatically change from once-per-generation to once-per-evaluation for very dynamic problems where the weight windows rapidly become non-ideal.

4. **Make file:** While not overly complicated, Coeus currently has dependencies on other non-standard packages. Adding a make file would make it easier and more repeatable to use the software by building the dependencies and adding the appropriate environment variables.

5. **Remove PyNE dependency:** PyNE is currently used for the material definition support. However, it is a rather cumbersome dependency to have, and the format it uses to add materials to the library is tedious at best. The goal is to build a small elemental material library that can be used instead. This library can then be expanded by users to fit their needs.

6. **User defined constraints and objective functions:** In order to extend to other applications, the user must be able to add their own objective functions and constraints to be used in the optimization process. This currently exists for Gnowee, and it needs to be extended and integrated into Coeus. A beta version of this exists currently.

6.3 ETA Design Results

Gnowee and Coeus were not developed as ends unto themselves but instead as a set of tools to enable ETA design. This section outlines the ETA design developed, how it performs with respect to the objective spectrum and constraints, the process of converting an idealized model into an engineering design, and lessons learned for future ETA development. Although the objectives and constraints for this optimization were discussed in Chapter 2 and Section 5.1 in detail, some of the key parameters are mentioned here to aid in the discussion.

6.3.1 From Optimized Design to Engineered Product

Coeus was ran on Savio to generate a TNF relevant ETA design. The optimization run computed $\sim$ 4500 designs over the course of 76 hours (wall time). No attempt was made at the time to characterize the compute time used, which should be tracked for future improvements in Coeus. The end result was a time history of the top design as a function of the number of function evaluations and their associated fitness, which is shown in Figure 6.9. The fitness shown in Figure 6.9 can be compared with the snapshots of the top designs at various points in the optimization process shown in Figure 6.10. These snapshots are not an inclusive set of each top design generated but represent some of the points of major improvements from the optimization.

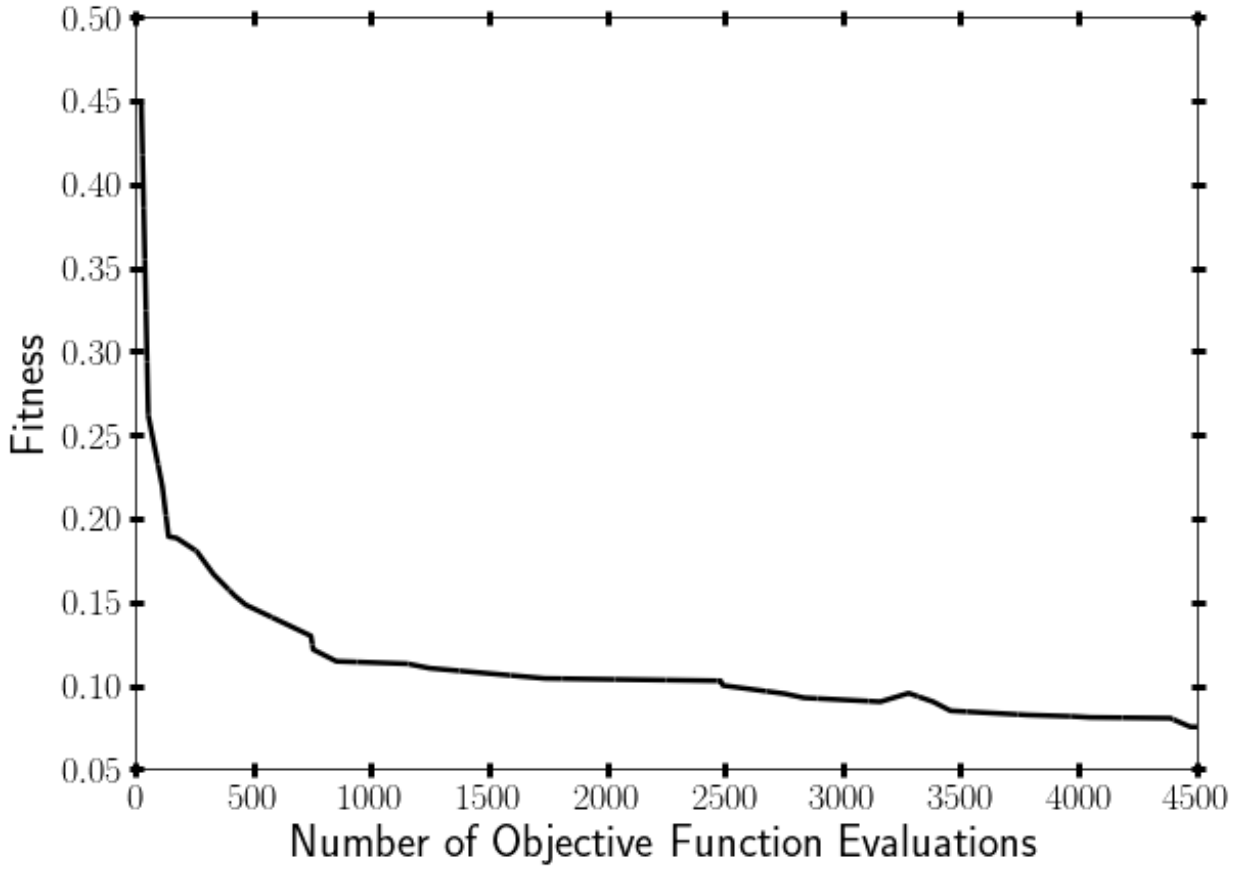

Figure 6.9: Coeus convergence history for the ETA optimization problem.

Since Coeus is a population-based optimization, Coeus also returns the final set of 25 designs and their associated fitness. The final fitness of each of the 25 designs is shown in Figure 6.11. This complete set of designs, along with the stored time history, can be useful when transitioning from a computer model to an engineering design and evaluating trade-offs not captured in the optimization, such as material costs. The top design generated, population member #0, is shown in Figure 6.12.

The ETA design shown in Figure 6.12 is not very practical from an engineering perspective as the materials library used for the optimization was not properly vetted. The library consisted of a few compounds and alloys (6061 Al, LiF, high density polyethylene (HDPE), deuterated HDPE, Stainless 409, and boron carbide) and every naturally occurring element. From the list of 83 elements, 35 gases and elements that had a low-melting point, were expensive, and/or reactive were removed. However, some undesirable materials were not removed from the library and some of those were used in the most optimal the ETA design. Thus, modifications were made to the design to remove problematic materials.

The first change that was made to the ETA design obtained by Coeus was to remove the

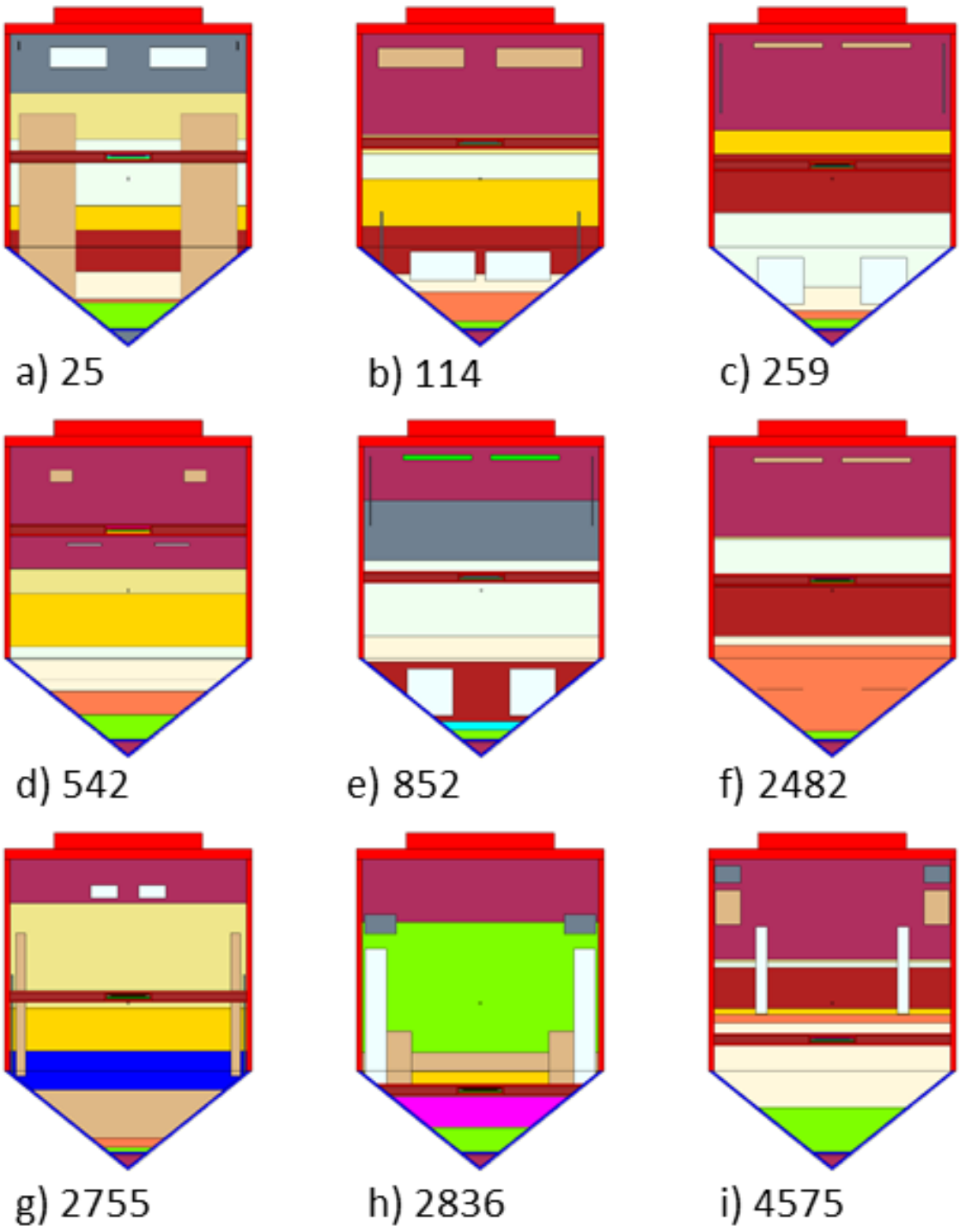

Figure 6.10: Snapshots of the best candidate designs at various points in the optimization process. The number under each plot represents the number of function evaluations up to that design point.

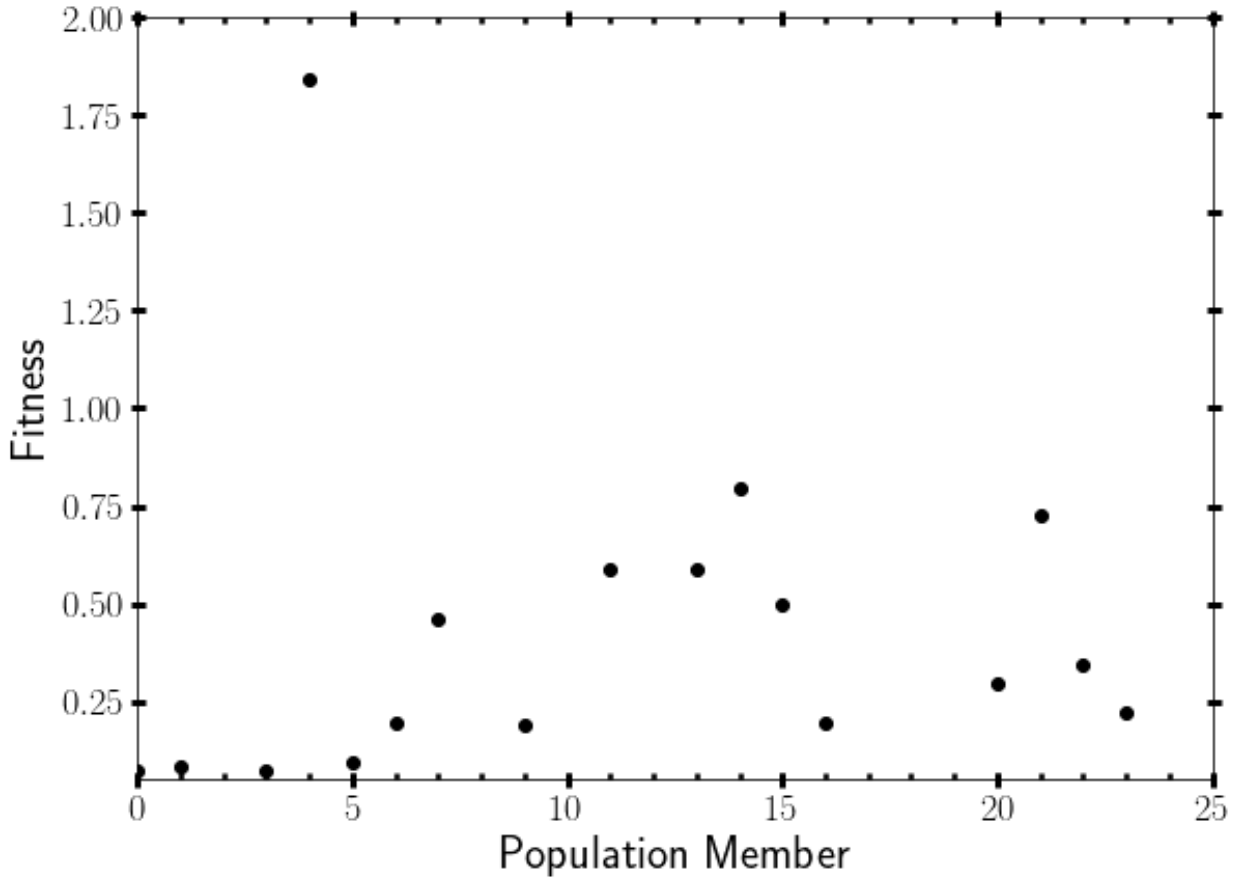

Figure 6.11: The final design fitness for each member of the population. Points that are at fitness > 2.0 are not plotted for conciseness.

iodine (I) layer. Iodine readily sublimes and is of limited availability in pure elemental form. To make this change, the history of the top design was leveraged. Design #4390, shown in Figure 6.13, was the last design that did not have iodine in the design, and this design was used as the basis for future engineering design decisions. The use of design #4390 resulted in a loss of 5.5% in fitness from the optimal design found by Coeus.

Similarly, potassium (K) is a difficult material to work with as it oxidizes rapidly in air and reacts vigorously with water. Since potassium was present in many designs, it was replaced with its nearest neighbor, bismuth (Bi), instead of choosing an alternative design. Additionally, the construction and emplacement of floating aluminum and chromium (Cr) rings was unnecessarily complex. The extra void space was removed, and the aluminum and chromium rings were moved to be in contact with the barium (Ba) layer. Finally, the lead layer containing the foil pack was turned into a drawer. These three changes resulted in the design shown in Figure 6.14, which improved upon design #4390's fitness a bit and was only 4.2% worse than the optimal design found by Gnowee.

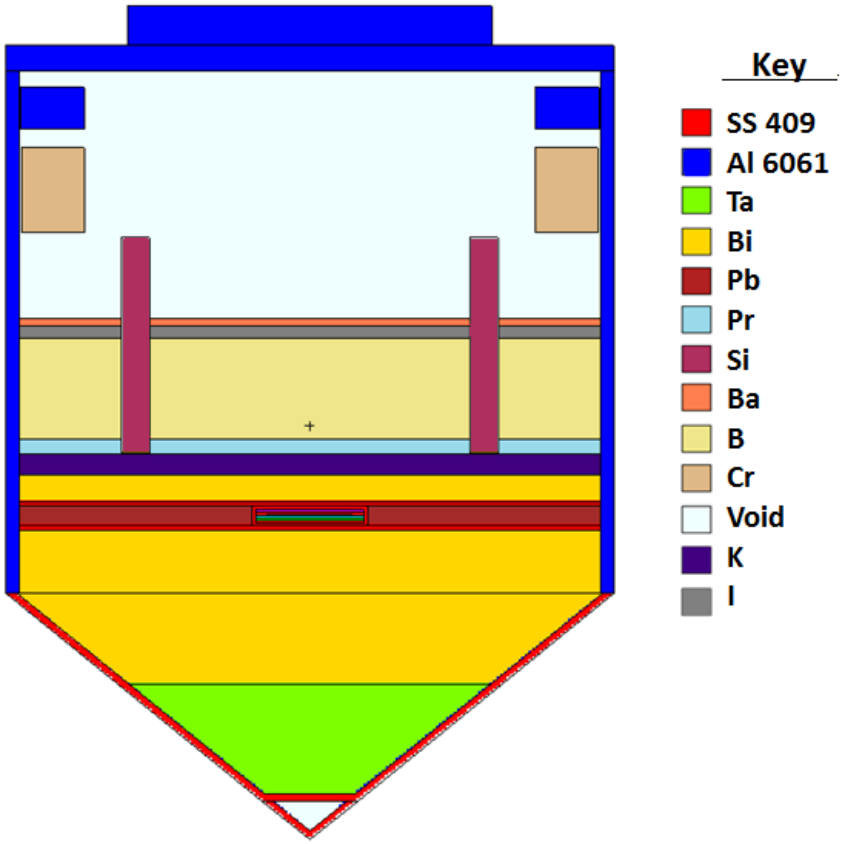

Figure 6.12: The top ETA design generated by Coeus (#4575) at the end of the optimization.

This design was sent out for cost estimates, but the overall cost (∼$64,000 for materials alone without the case or any machining costs) was prohibitive. To lower the cost, some design changes were made:

- Remove barium layer (difficult to machine and highly reactive): ∼$2,500 material cost savings plus machining
- Remove chromium ring: ∼$4,300 material cost savings plus machining
- Remove aluminum ring: ∼$400 material cost savings plus machining
- Exchange boron (B) for boron carbide (BC): ∼$20,800 material cost savings
- Exchange tantalum (Ta) for tungsten (W): ∼$15,200 material cost savings
- Remove nose cap, remove snout mount, and make case all aluminum (all were requirements for NIF but not required for 88-Inch Cyclotron experiments): machining cost savings

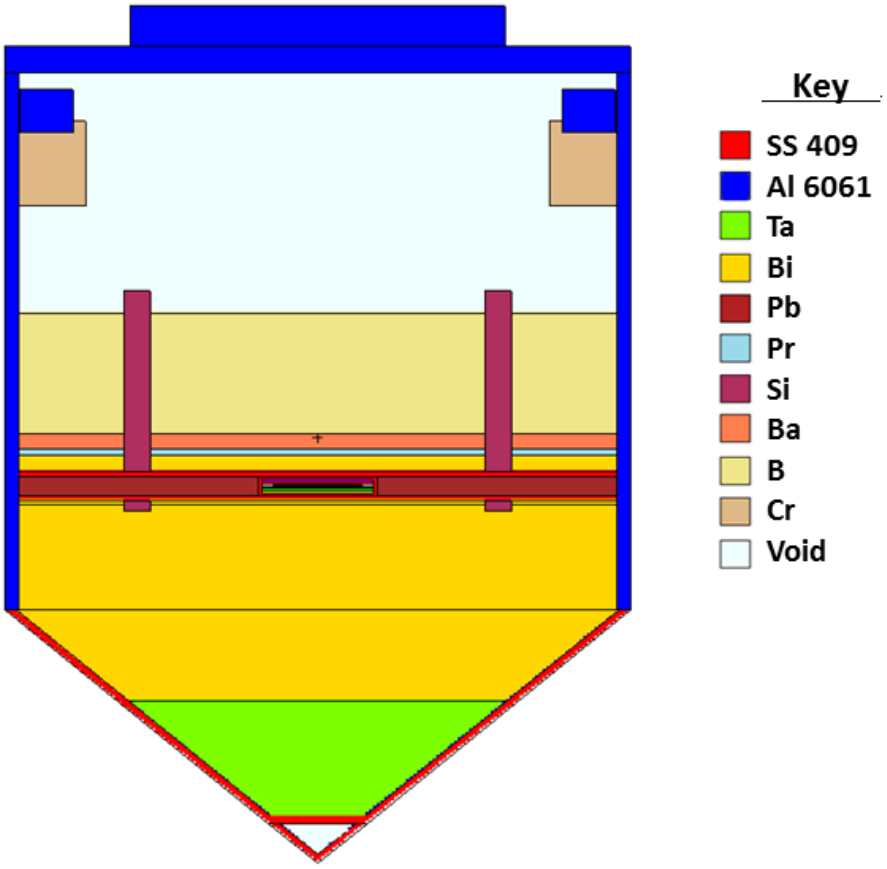

Figure 6.13: Design #4390.

The final assessed fitness of the as-constructed design was 3.9% worse than best design Coeus found, but it cost approximately 2-3 times less. The final design, shown in Figure 6.15, cost ~$57,600. The full specifications of the as constructed ETA are provided in Appendix B.

6.3.2 ETA Performance

While the computation of the fitness according to a defined objective function is useful to guide an optimization process, it conveys little actual insight into what was specifically achieved. This section details the expected performance of the ETA given the motivation of this work.

The objective function measures how well a particular candidate design matches the TN+PFNS objective defined in Chapter 2. This comparison is shown graphically in Figure 6.16. A more quantitative assessment is shown in Table 6.8. All uncertainties in Figure 6.16 and Table 6.8 are 1σ statistical uncertainties. For Table 6.8, the spectrum is divided

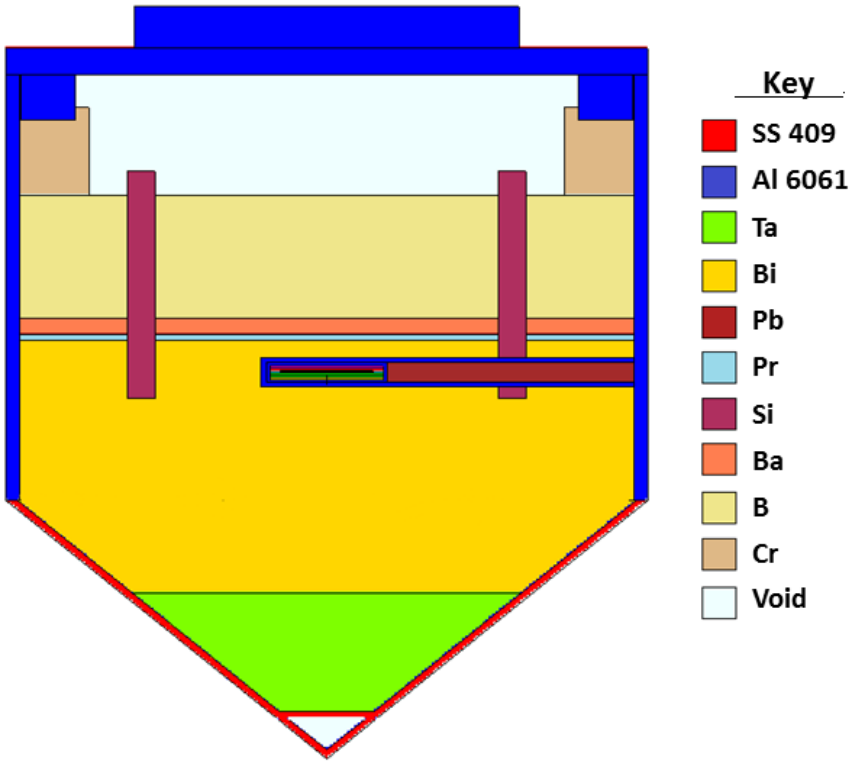

Figure 6.14: Design #4390 with engineering modifications to remove the potassium layer and extra void space.

into five bins that correspond to key features of the ^{235}U cross-section and TN+PFNS. It is worth noting that the worst performing bin, 0-3 keV, has minimal effect on the resulting fission product distribution because the neutrons in this bin account for only 0.06% of the overall spectrum achieved in the ETA.

In general, the weight limit imposed by NIF, $\sim$ 75 kg, is the factor limiting the spectral shaping performance, especially for the energies at the 14.1 MeV peak and below 10 keV. The increase in the fraction of neutrons below 10 keV is due to the introduction of low Z materials, B_4C and Si, that are non-ideal from an elastic scattering perspective but enable the design to meet the NIF weight constraints. Additionally, the constraint on mass limits the fraction of neutrons that can be removed from the 14.1 MeV peak as the interaction cross-sections for all materials are roughly the same, making the atom density the key factor. For this spectrum, there is also a physics limit constraining the performance in the 7-12 MeV range. This is an artifact of the manner in which the representative TN+PFNS was generated using transport in a bare Godiva critical assembly. The lack of any mid- or low-Z moderator resulted in an artificially low flux in the 7-12 MeV range due to the many scatters required by uranium to populate this region and the approximately equal probability for (n, 2n) reactions to occur,

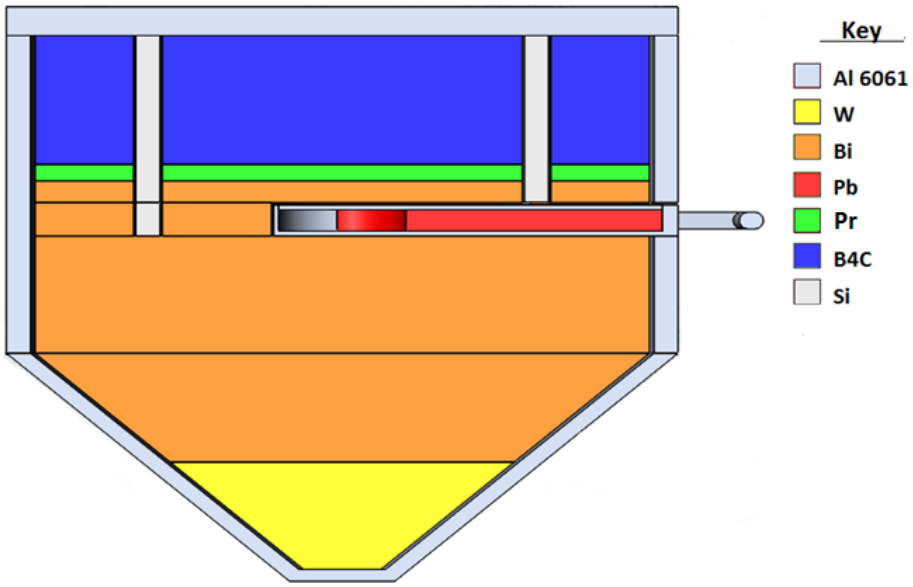

Figure 6.15: Final ETA design.

Table 6.8: ETA design spectrum results compared to the objective TN+PFNS

Energy Range	**TN+PFNS Fractional ϕ**	**ETA Fractional ϕ**
0-3 keV	7.23×10^{-5}	$6.20 \pm 0.23 \times 10^{-4}$
3-100 keV	3.80×10^{-2}	$5.02 \pm 0.01 \times 10^{-2}$
0.1-6 MeV	8.03×10^{-1}	$7.65 \pm 0.01 \times 10^{-1}$
6-10 MeV	3.33×10^{-2}	$4.01 \pm 0.01 \times 10^{-2}$
10-20 MeV	1.26×10^{-1}	$1.44 \pm 0.01 \times 10^{-1}$

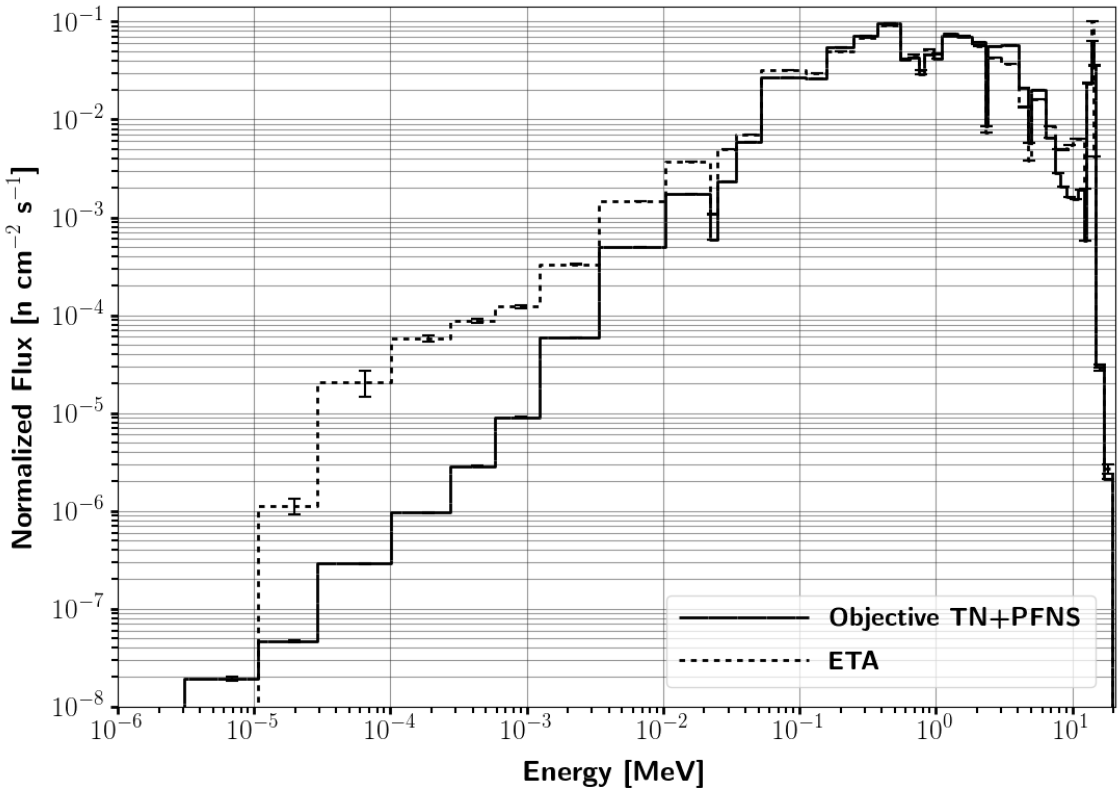

Figure 6.16: A comparison of the modeled ETA flux spectrum achieved across the foil pack and the TN+PFNS objective spectrum. All errors reported are Monte Carlo statistical errors only.

which bypass this region entirely. Any real world TNF applications would introduce some moderator which would fill in the 7-12 MeV region with elastic and inelastic scattering and bring the objective spectrum more in-line with what the ETA was able to achieve.

The neutron spectrum objective function was a surrogate for the real item of interest – the fission product distribution. The use of the neutron spectrum as the objective function was necessitated by the lack of comparison fission product data for the spectrum of interest. However, it is useful to compare the fission product estimates from Nagy fits (described in Chapter 2 from 93.15% HEU exposed to the objective TNF spectrum and the ETA spectrum. Nagy and GEF FP yield estimates for the objective and ETA spectrum are shown in Table 6.9. The difference in the FP distribution between the two spectra are well within the precision of the computational methods and any experimental procedures available.

The full FP distribution calculated using GEF is shown in Figure 6.17. The top half of Figure 6.17 compares the ETA and objective spectrum generated fission product distribution along with error bars for the objective spectrum generated FPs. The bottom half of Figure 6.17 shows the residuals $(Y_{Obj}(A) - Y_{ETA}(A))$ in comparison with the error bars

Table 6.9: Nagy and GEF based fission product cumulative yield ($f_{cum}(A, Z)$) estimates of select FPs from a 93.15% ^{235}U HEU foil exposed to the TN+PFNS objective and the TN+PFNS achieved by the ETA [155, 185].

FP	**Nagy**		**GEF**	
FP	**Objective**	**ETA**	**Objective**	**ETA**
$^{95}_{40}$Zr	6.17 ± 0.09	6.15 ± 0.09	6.47 ± 0.30	6.47 ± 0.30
$^{97}_{40}$Zr	5.75 ± 0.09	5.74 ± 0.09	6.47 ± 0.28	6.46 ± 0.28
$^{111}_{47}$Ag	0.25 ± 0.01	0.26 ± 0.01	0.21 ± 0.12	0.22 ± 0.12
$^{115}_{48}$Cd	0.25 ± 0.01	0.26 ± 0.01	0.24 ± 0.11	0.26 ± 0.16
$^{133}_{53}$I	6.41 ± 0.13	6.38 ± 0.14	6.04 ± 0.37	6.01 ± 0.37
$^{140}_{56}$Ba	5.71 ± 0.07	5.68 ± 0.07	5.41 ± 0.28	5.41 ± 0.28
$^{147}_{60}$Nd	2.12 ± 0.03	2.11 ± 0.03	2.00 ± 0.22	1.99 ± 0.23
$^{151}_{61}$Pm	0.47 ± 0.02	0.47 ± 0.02	0.46 ± 0.10	0.46 ± 0.10
$^{153}_{62}$Sm	0.18 ± 0.01	0.18 ± 0.01	0.17 ± 0.05	0.17 ± 0.05

from the objective spectrum FP yield calculations. The ETA generated FP distribution is remarkably similar to the TN+PFNS generated FP distribution, but the valley fission products are ∼10% higher for the ETA. This is due to the 10-20 MeV flux in the ETA spectrum being ∼14% higher than the TN+PFNS objective, which was a limitation based on the mass requirements to field on NIF.

These modeled results show promise for improving TNF outcomes and the ability to generate realistic synthetic fission products and debris. To move from a promising model to a useful capability, validation of the proposed methodology and specific ETA design must be conducted. This validation is approached from different angles using two sets of experiments, one at the 88-Inch cyclotron at LBNL and one at the NIF at LLNL. Chapter 8 and Chapter 9 describe these experiments in further detail, but first, experimental techniques available for neutron spectroscopy, required to measure the neutron spectrum produced by the ETA, are explored.

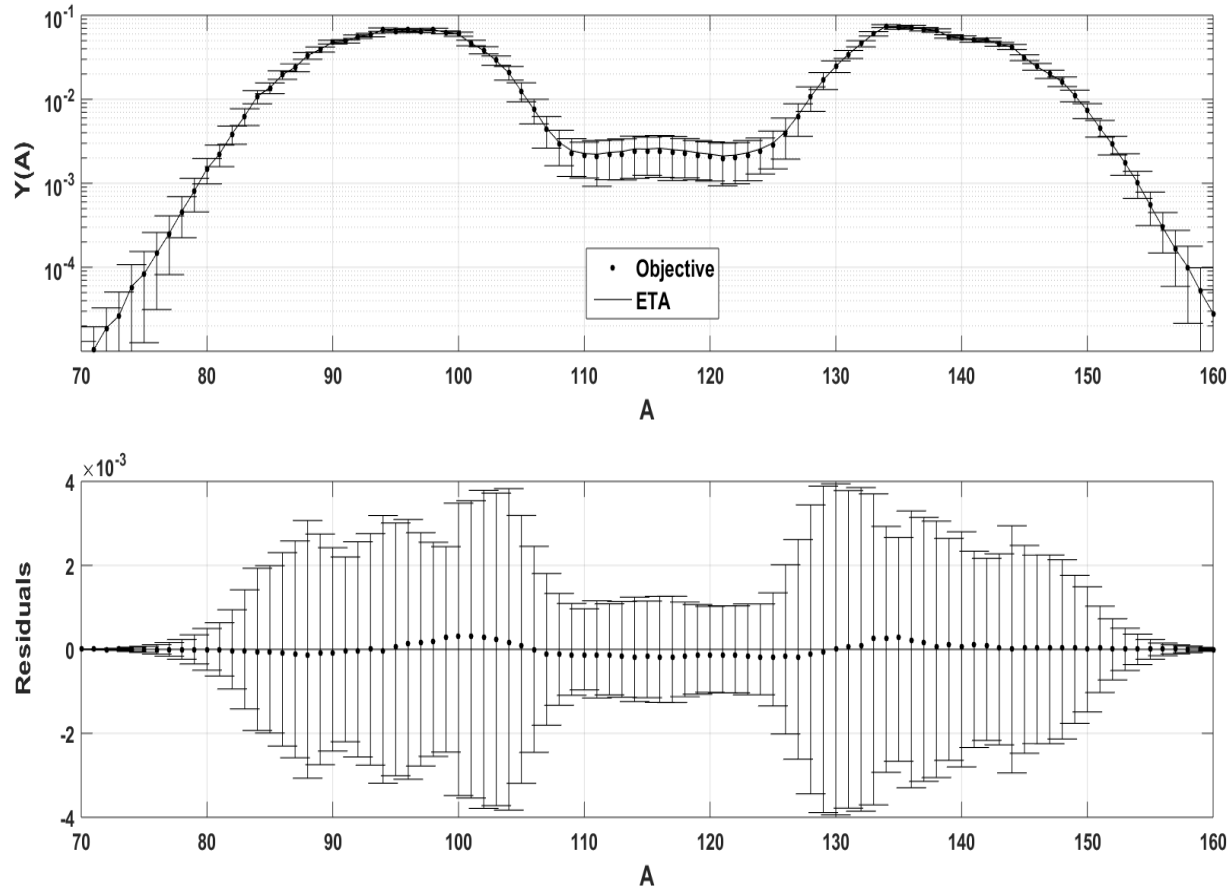

Figure 6.17: Comparison of GEF based fission product yield estimates for a 93.15% ^{235}U HEU foil exposed to a TN+PFNS and the ETA spectrum [185]. The bottom plot compares the residuals with the TN+PFNS objective FP yield error bars from GEF.

Chapter 7

Neutron Spectroscopy

In retrospect you will see that everything is unfolding perfectly.

- Shakti Gawain

Following the discovery of the neutron by James Chadwick in 1932, research into measuring the resulting (α,n) spectrum started the same year [22, 36]. Efforts to perform neutron spectroscopy are fundamentally limited by the lack of a full energy deposition mechanism that leads to a signal that is proportional to the energy of the incident neutron, such as the photoelectric effect for gamma rays. To overcome this limitation, many different techniques have been proposed, each with their own set of limitations.

One of the first methods employed was the time-of-flight technique. These techniques use the time between the source generation, either measured from an accelerator beam or a chopper, and the time of detection to reconstruct the detected energy from the kinetic energy formula [47]. Time-of-flight methods are considered the gold standard for neutron spectroscopy and can have very high measurement precision given the right combination of accelerator timing, flight path length, and fast detector response. Time-of-flight techniques are currently used at NIF and the 88-Inch Cyclotron to measure the source term [78, 138]. In the ETA application, all of the initial timing is lost during the dozens to hundreds of interactions that occur within the ETA. Therefore, other techniques must be considered.

Proton recoil telescopes are another common neutron spectroscopy option. These telescopes use a thin hydrogenous material to scatter the neutrons into a detector located at a sufficient distance to cover a small angle, thereby allowing reconstruction of the incident neutron energy from

$$E_p = E_n cos^2(\theta)\,, \tag{7.1}$$

where E_p is the detected energy of the recoiling proton, E_n is the incident neutron energy, and θ is the angle between the incident neutron beam and the detector. There is a trade-off between energy resolution and efficiency, but proton recoil telescopes generally have

extremely low detection efficiencies [43, 109]. More importantly, they will not work in the ETA application due to the lack of a incident collimated neutron beam.

Another option is capture-gated spectrometers. The basic concept is to record the total neutron energy through a series of multiple scatters within the detection volume, followed by capture with a highly absorbing dopant material such as ^{10}B. This approach has been successfully employed in many different configurations, and it would work for the 88-Inch Cyclotron neutron field measurements [109, 112, 129]. However, it could not be used to measure the TN+PFNS directly due to the size of detector needed to obtain sufficient overall detection efficiencies for the high energy neutrons. Additionally, since organic scintillators are typically used, the energy resolution is worse than the single scatter options due to the non-linearity of the response function as described in Section 7.3.

The final option considered was neutron spectrum unfolding. This method has been employed with a variety of detection methods including Bonner spheres [132, 201], gas proportional counters [109], activation foils [5, 126, 181, 188], and liquid scintillators [41, 66, 114, 211]. The foil activation method is perfect for measuring the volume averaged TN+PFNS spectrum internal to the ETA, and it is described in further detail in Section 7.2. While Bonner spheres and gas proportional counters could be used to measure the external neutron field, liquid organic scintillators where chosen due to the higher detection efficiencies and concurrent light yield measurements being conducted at the University of California - Berkeley [113]. Unfolding using liquid scintillators is described further in Section 7.3.

7.1 Unfolding

Unfolding seeks to solve the "inverse problem" to determine the unknown incident energy-dependent neutron flux given a set of measurements and a known detector response function. Mathematically this is formulated as

$$\mathcal{M}_i = \int R_i(E)\phi(E)dE \qquad \text{i=1,...,M}\,, \tag{7.2}$$

where $\mathcal{M}_i$ is the measured value of the detector system for the i^{th} channel, $R_i(E)$ is the energy dependent response function for the i^{th} measured channel, and $\phi(E)$ is the incident neutron energy spectrum. In the forward version of the problem, $R(E)$ and $\phi(E)$ are known and M has a unique solution. In the inverse problem, $\phi(E)$ is unknown, and Equation 7.2 has no unique solution due to the degeneracy created by representing a continuous function with a finite number of measurements [133].

An approximate transformation of Equation 7.2 can be made to the linear matrix equation

$$\vec{\mathcal{M}} = \boldsymbol{R}\vec{\phi} \tag{7.3}$$

$$\begin{pmatrix} \mathcal{M}_1 \\ \mathcal{M}_2 \\ \vdots \\ \mathcal{M}_M \end{pmatrix} = \begin{pmatrix} R_{11} & R_{12} & \cdots & R_{1N} \\ R_{21} & R_{22} & \cdots & R_{2N} \\ \vdots & \vdots & \ddots & \vdots \\ R_{M1} & R_{M2} & \cdots & R_{MN} \end{pmatrix} \begin{pmatrix} \phi_1 \\ \phi_2 \\ \vdots \\ \phi_N \end{pmatrix}, \tag{7.4}$$

where M is the number of measurements and N is the number of neutron energy groups. Equation 7.3 also has no unique solution when $N > M$, and often not for $N < M$ due to the correlations between the response functions [126, 133, 136].

Instead, Equation 7.3 is often solved using iterative minimization approaches using the method of least squares, or χ^2, which is given by

$$\frac{\chi^2}{n} = \frac{1}{n} \sum_i^M \frac{\left(\sum_j^N R_{ij}\phi_j^g - \mathcal{M}_i\right)^2}{\sigma_i^2}. \tag{7.5}$$

In Equation 7.5, $n = (N-1)$, the number of the degrees of freedom, and σ_i is the uncertainty of the i^{th} measurement [41, 133]. These methods are often modified to account for the non-negative flux requirements, smoothness of the solution, and the addition of *a priori information* [114, 133]. Each of these modifications, if done properly, is useful in overcoming the degeneracy of the solution space to unfold spectra that are consistent with TOF measured spectra. One example comparison is shown is Figure 7.1, where the unfolded NE-213 liquid scintillator pulse height spectrum (PHS) matches the smoothed TOF data across a broad portion of the spectrum.

One limitation of the direct application of minimization or "goodness of fit" methods is the difficulty in assessing the uncertainty of the unfold [114, 133]. To overcome this limitation, maximum likelihood estimation and maximum entropy techniques were introduced [133, 135, 176, 223]. These approaches construct a probability distribution over the degenerate solution space, thereby allowing for the estimation of uncertainty.

Many computer programs have been developed to solve spectrum unfolding problems using variations of the basic mathematics described above [5, 135, 163, 177, 204]. Some modern codes have started to incorporate metaheuristic minimization methods such as those described in Chapter 5 [56, 150]. Each code differs in the treatment of the uncertainty and the requirement for *a priori* information, such as a guess starting spectrum. In Section 7.2, STAYSL is discussed in the context of unfolding for neutron activation. In Section 7.3, HEPROW is described for the purposes of unfolding pulse height spectra from liquid organic scintillators.

7.2 Neutron Activation

One option for neutron detection is through measurement of the induced activity in different materials [109, 110]. A sample material, exposed to a flux of neutrons, will undergo neutron reactions such as those described in Chapter 3. The reactions can form a radioactive isotope

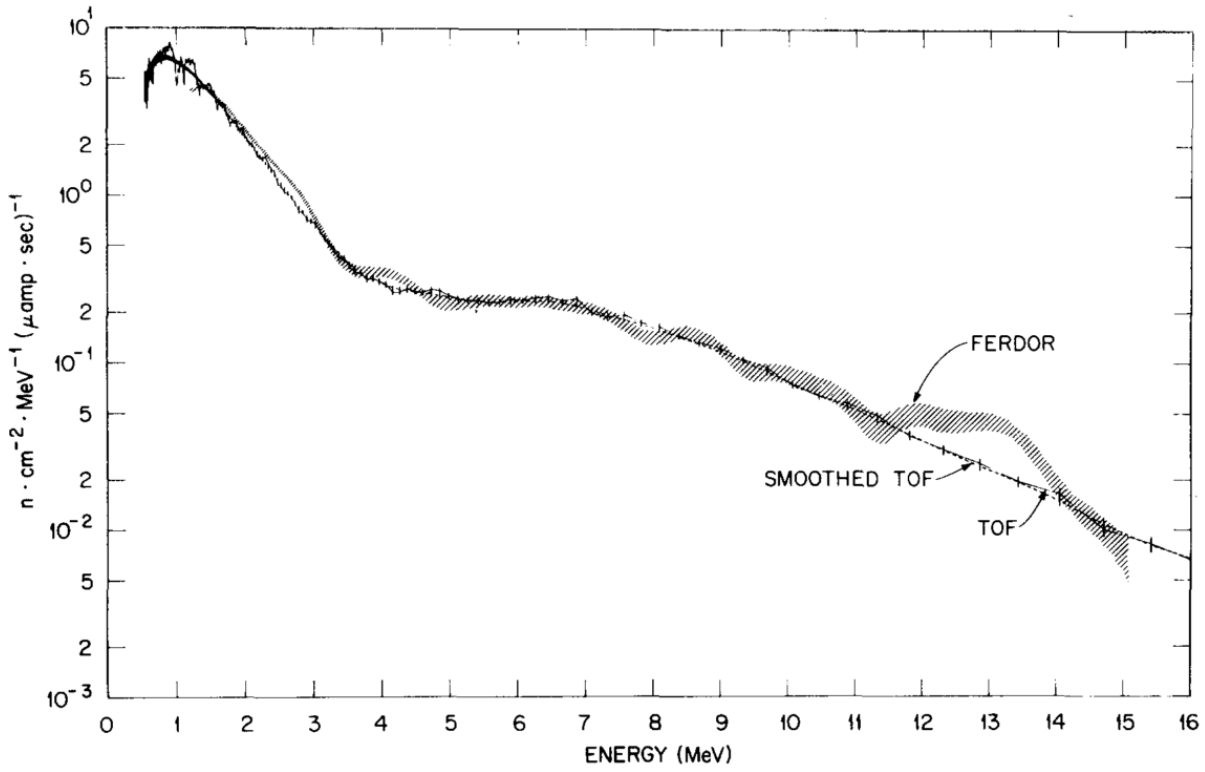

Figure 7.1: Comparison of a TOF, smoothed TOF, and FERDOR unfolded PHS for a ^{238}U neutron spectrum [196].

whose radiation can be measured to either inform the makeup of the material or the energy distribution of the neutron flux.

Here, we focus on the techniques and procedures necessary to use neutron activation as an integrating detector to measure the neutron flux. This method is especially well suited for the ETA application. Neutron activation foils are a passive measurement that can easily be placed in the sample volume of the ETA shown in Figure 6.15. Additionally, neutron activation foils can span the full TN+PFNS energy range. This allows this technique to directly measure the full TN+PFNS spectrum generated by the ETA.

The neutron flux can be assessed through comparison of the measured reaction rates with those from a model of the expected reaction rates based on the calculated neutron energy distribution [17]. This method is highly degenerate and requires knowledge of the expected neutron spectrum. For the ETA application, the expected neutron spectrum is known, and the use of a variety of foils with varying cross sections can help break the degeneracy. The steps required for this analysis are described in Subsection 7.2.1, while the parameters to consider when choosing the activation foils are discussed in Subsection 7.2.2.

If a statistical test such as χ^2 or the t-test shows the activation rates to be consistent

with the modeled activation rates, then the measured flux can be said to be consistent with the expectation from the model. However, if the measured rates differ, this approach does not offer insight into the actual spectrum measured. Subsection 7.2.3 describes how the measured reaction rates, along with their known response functions (i.e. cross section) can be used to unfold the incident neutron spectrum.

7.2.1 Activation Analysis

The fundamental goal of activation analysis is to measure the induced activity to determine the rate, R, at which interactions occurred in the foil during irradiation. The interaction rate for a given reaction channel is given by

$$R_{rx} = \int \Phi(E)\Sigma_{rx}(E)V dE \,, \tag{7.6}$$

where ϕ is the volume-averaged, energy-dependent neutron flux, Σ_{rx} is the energy-dependent macroscopic reaction-channel-specific cross section, and V is the volume of the foil. It is more useful, however, to work in terms of the activity instead because both production and decay occur throughout the radiation period. The activity for a given reaction channel at the end of irradiation is given by

$$A_0 = R\left(1 - e^{\lambda t_0}\right) \,, \tag{7.7}$$

where λ is the decay constant for the activation product and t_0 is the irradiation time.

Counting systems are subject to several correction factors to be able to arrive at A_0 from the observed counting rate. The total counts in a given peak seen during a counting interval is given by Equation 7.8 [109, 110, 119, 206]. The correction factors highlighted in Equation 7.8 are discussed in further detail below.

$$C = \epsilon_i \times \Omega_{pt} \times T \times \int_0^d \int_0^\theta e^{\frac{-\mu_f \ x}{cos\alpha}} d\alpha dx \times C_{CS} \times e^{-(\sum_{i=1}^{N} \mu_i \ d_i)} \times BR \times \int_{t_1}^{t_2} A_0 e^{-\lambda(t-t_0)} dt + B, \tag{7.8}$$

where

ϵ_i = the intrinsic detector efficiency

Ω_{pt} = the fractional solid angle at the counting location assuming a point source

T = the geometry transfer coefficient for a volume source

$\int_0^d \int_0^\theta e^{\frac{-\mu_f \ x}{cos\alpha}} d\alpha dx$ = the gamma self-shielding factor

C_{CS} = the coincident summing correction factor

BR = the gamma branching ratio

$e^{-(\sum_{i=1}^{N} \mu_i \ d_i)}$ = the attenuation of the gamma through the $N \cdot d_i$ thick attenuator materials

A_0 = the initial activity of the source at creation

t_0 = the irradiation time

t_1 = the counting start time

t_2 = the counting stop time

B = the background counts .

Each detection system has an intrinsic detection efficiency, ϵ_i that is a function of the active volume geometry and type, energy of the incident γ, counting geometry, and the gain settings. Generally, the absolute efficiency, $\epsilon_{abs} = \epsilon_i \Omega$, is measured using calibration sources of known intensity. From this measurement, the intrinsic efficiency of the system can be calculated. It is worth highlighting that the intrinsic efficiency can be dependent on the counting geometry as the average path varies based on the incident angle of the radiation. For a point source with no coincidence summing and negligible attenuation, the intrinsic efficiency can be calculated from

$$\epsilon_i = \frac{\dot{C}}{A} \frac{4\pi}{\Omega} \,, \tag{7.9}$$

where $\dot{C}$ is the observed count rate for a given γ line and A is the activity of the known source.

Ideal counting geometries are those where the foil is counted at a distance where it is functionally a point source with respect to the detector. However, some applications require large foils or close counting geometries in order to achieve counting statistics and count times that are in line with experimental goals. In these cases, the solid angle must be adjusted to account for the volume of the source. This can be done with a model or analytically through the calculation of the transfer coefficient [119]

$$T_\gamma = \frac{\Omega_{vol}}{\Omega_{pt}} \,. \tag{7.10}$$

T can also be found experimentally as

$$T_\gamma = \frac{\dot{C}_c \epsilon_{i,f} \Omega_{pt,f}}{\dot{C}_f \epsilon_{i,c} \Omega_{pt,c}} \,, \tag{7.11}$$

where c is the counting location corresponding to a volumetric source geometry and f is the counting location corresponding to a point source geometry.

The intrinsic efficiency as a function of counting geometry and energy must be determined to use Equation 7.11. This can be done with a radiation transport model such as MCNP or experimentally with the double ratio method:

$$T_\gamma = \frac{\epsilon^{pt}_{abs,c}}{\epsilon^{pt}_{abs,f}} / \frac{\epsilon^{vol}_{abs,c}}{\epsilon^{vol}_{abs,f}} \,. \tag{7.12}$$

However, Equation 7.12 can be difficult to implement in practice since point and volumetric sources of the same radioactive isotope are not always available. One work around is to fit the available point source efficiency ratios with a functional form [50].

Coincidence summing occurs when true coincidences from multiple gamma cascade transitions are detected within the resolving time of the detector [50, 117, 119, 187]. This results in a reduction of the gamma line peak counts as the energy deposition is recorded as the sum of the two (or more) observed gammas. The coincident summing factor can be calculated from models such as Efficiency Transfer for Nuclide Activity (ETNA) [117, 118, 119] or experimentally [50, 187]. The coincident summing correction factor obtained is specific to a given gamma line and is not valid for other gamma lines of similar energy due to the differences in their cascades. For a simple two line cascade from $E_2 \rightarrow E_1 \rightarrow E_g$, the coincidence summing factor for the $E_2 \rightarrow E_1$ transition is given by

$$C_{CS,1} = \frac{\dot{C}_1'}{\dot{C}_1} = \frac{1}{1 - \epsilon_{T2}} \,, \tag{7.13}$$

where $\dot{C}_1'$ is the expected count rate in the absence of coincidence summing and ϵ_{T2} is the total efficiency for detection of the second transition. For the $E_1 \rightarrow E_g$ transition, the coincidence summing correction is

$$C_{CS,2} = \frac{1}{1 - \frac{BR_1}{BR_2}\epsilon_{T1}} \,. \tag{7.14}$$

The same process can be followed for gamma cascades with more transitions [50, 187].

The main challenge for using Equation 7.13 and Equation 7.14 is determining the total detection efficiency for a given line. This can be accomplished using a series of "monoenergetic" sources such as ^{57}Co, ^{203}Hg, ^{113}Sn, ^{85}Sr, ^{137}Cs, ^{54}Mn, and ^{65}Zn to determine the total efficiency as a function of the incident gamma energy. Unfortunately, most of these sources are short lived and were not available for the experiments conducted. Since the detection probability for true coincidences falls off as Ω^2, the coincident summing factor can

be calculated as a ratio of the detection efficiencies from a far (where coincidence summing is negligible) and close distance. Assuming negligible change in the source activity between the counting periods and negligible attenuation differences, the count rate in the absence of coincident summing at position c can be related to that at a position f by

$$\dot{C}'_c = \frac{\dot{C}_f \epsilon_{i,c} \Omega_{pt,c}}{\epsilon_{i,f} \Omega_{pt,f}} \,. \tag{7.15}$$

The coincidence summing correction factor is then given by

$$C_{CS} = \frac{\dot{C}_f \epsilon_{i,c} \Omega_{pt,c}}{\dot{C}_c \epsilon_{i,f} \Omega_{pt,f}} \,. \tag{7.16}$$

It is worth noting that Equation 7.16 will also include the volumetric source correction factor, if present. Similar to Equation 7.11, Equation 7.16 depends on knowing the geometry- and energy-dependent intrinsic efficiency of the system. The same double ratio approach used in Equation 7.12 can be used here as well [50]. In this case, the reference ratio in the numerator must be monoenergetic sources such as those mentioned above. If point sources are used for the reference efficiency ratio, the transfer coefficient will be simultaneously captured with this method.

Equation 7.8 simplifies greatly with ideal foils that avoid the correction factors discussed in this chapter. Unfortunately, the foils used in this experiment for compatibility with NIF and reaction efficiency are not ideal for use with the 88-inch cyclotron. The foils chosen and their attributes are described next.

7.2.2 Activation Foil Selection

Not all neutron induced reactions are suitable for use as integrating detectors for activation analysis. Some of the important properties to consider are [109, 126]:

1. **Cross section:** The cross-section energy dependence is a function of the material and reaction channel being used. For the purposes of unfolding, it is desirable to have unique cross sections for each activation foil that, in combination, span the range of the neutron spectrum being measured. Additionally, the magnitude of the cross section is important to ensure that sufficient activity is created for measurement. If possible, validated dosimetry reactions are desirable due to the pedigree and energy range of their cross section data.

2. **Foil Composition:** The foil should be well characterized from an elemental perspective to be able to properly account for the number of atoms available for reaction within the foil. Additionally, impurities can have competing gamma lines that overlap the line of interest. When considering neutron energies exceeding 20 MeV, multiple feeding of a given isotope becomes possible in foils that are not mono-isotopic. Due

to the lack of data for many reactions above (n,2n), this can be difficult to deconvolve with reasonable precision.

3. **Induced Activity Half-Life:** The half-life of the induced activity is important to consider in relation to the experimental set-up and the ability to access the foils post-irradiation. Short half-lives will be difficult to count with sufficient statistics if there is any delay between irradiation and counting. Long half-lives can require long irradiation times. Ideal half-lives are typically on the order of several hours, but foil stacks will benefit from a range of half-lives to facilitate pain-free counting plans.

4. **Decay Radiation:** In general, activation products that emit gamma radiation during decay are preferred. Energies in the range of several hundred keV are ideal due to high counting efficiencies and a lack of background radiation in a well-shielded counting geometry. Additionally, the branching ratio of the lines should be considered as low branching ratios will make it difficult to detect sufficient decays to generate good counting statistics.

5. **Foil Geometry:** The foil should be of a size that ensures even irradiation across the foil while allowing for sufficient activity to be built up for measurement. Additionally, the foil should be small enough that the neutron flux is constant across the foil volume.

Several lists of possible activation reactions have been compiled [5, 85, 109, 110]. These are a good place to start before pouring through the chart of the nuclides. For this research, the foils used are based on the standard NIF NAS foil pack and geometry. This is helpful for the design approval process, but the foils have also been selected with the above criteria in mind given the NIF source spectra and experimental constraints.

The standard NAS uses aluminum (Al), indium (In), tantalum (Ta), and Zirconium (Zr). Other foils that have been used in the NAS are vanadium (V), titanium (Ti), nickel (Ni), bismuth (Bi), thulium (Tm), and gold (Au). Each foil is 50 mm in diameter, and thicknesses used have ranged from 0.1 - 5 mm.

For the ETA experiment, the Ta foil was removed due to the lack of dosimetry standard cross section data. This resulted in its non-inclusion in STAYSL. Ni and Au foils were added to extend the range of cross section coverage and improve the unfold characteristics. The resulting cross sections for the chosen foil set and reaction channels are shown in Figure 7.2. Key parameters for each reaction channel are shown in Table 7.1.

As shown in Figure 7.2 and Table 7.1, the reaction channels chosen have a spread of threshold energies that cover the range of the TN+PFNS energy region. This is the ideal for unfolding the activation foils. The code chosen for the foil activation unfolding, STAYSL, is described next.

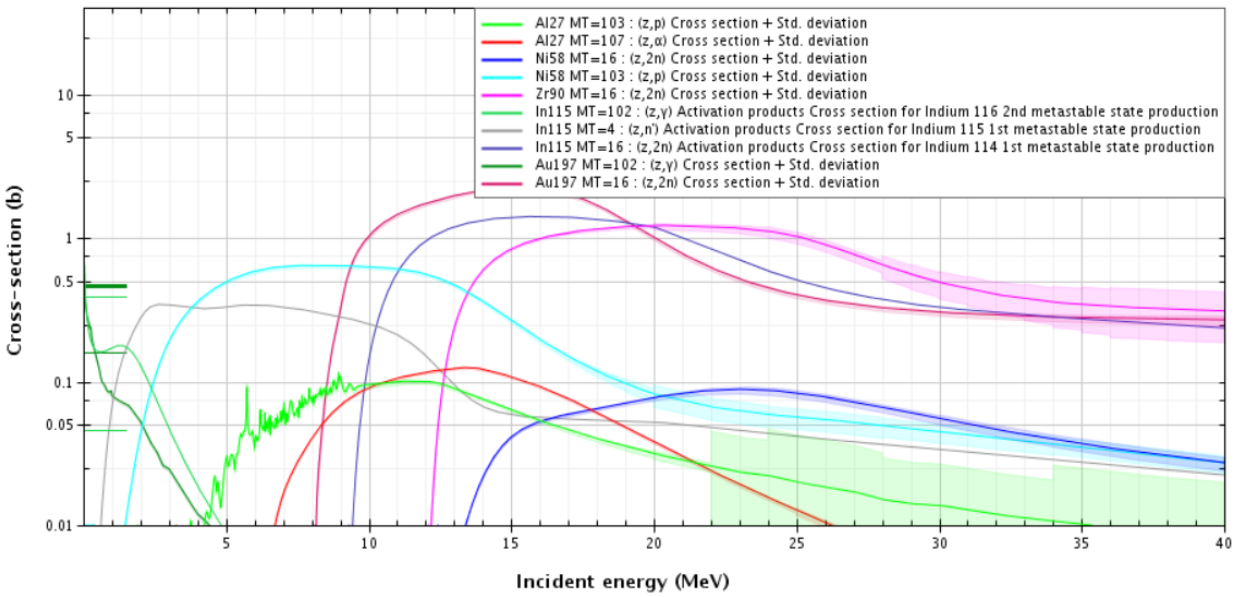

Figure 7.2: IRDFF v. 1.05 cross sections for the reaction channels for the Al, Au, In, Ni, and Zr foils chosen for this research [97].

7.2.3 STAYSL

STAYSL PNNL Suite v. 1.2.0 (hereafter referred to simply as STAYSL) was developed by Pacific Northwest National Laboratory for determining the neutron flux from foil activation [85]. It uses the method of least squares described in Section 7.1 to perturb an initial guess spectrum based on the measured activation rates and their uncertainties. The response functions are the IRDFF v. 1.05 cross sections and their associated covariances [97]. The initial guess spectrum is expected to be a close approximation to the true spectrum, where the initial guess is usually obtained from a radiation transport model. STAYSL propagates the measurement and response function uncertainties to the output flux spectra [85].

STAYSL was developed to handle multiple types of irradiation environments, including nuclear reactors and accelerator beams. The sub-modules allow for the calculation of neutron and gamma self-shielding (SHIELD), corrections for a time-varying flux (BCF), and re-binning of the nuclear data into arbitrary energy groups structures (NJOY99/NJpp). The software package comes with pre-compiled cross section data in the STAYSL PNNL 140-group, 69-group (WIMS/EPRI-CPM), 129-group (for 14 MeV source), 175-group (VITAMIN-J), and 640-/725-group (SAND IIa) energy grid structures. Complete documentation for STAYSL can be found in the STAYSL User Guide [85]. Examples of STAYSL unfolded results from activation simulations are included in Chapter 8 and Chapter 9.

The primary limitation to unfolding neutron spectra from foil activation is that there is limited information available. For example, in the proposed foil pack, there is a maximum of ten different response functions. This is compensated for by providing additional *a priori*

Table 7.1: Key parameters for the activation foils chosen for the NIF and 88-Inch Cyclotron activation analysis experiments.

Foil (thickness)	**Reaction**	**$T_{1/2}$**	**Threshold** (@10 mb)	**Gamma**	**Nat. (γ) Abund.**
In (1 mm)	^{115}In(n,n')^{115m}In	4.486 hr	336 (597) keV	336.24 keV	95.71 (45.9)
	^{115}In(n,g)^{116m}In	54.29 min	Thermal+	1293.56	95.7 (84.8)
	^{115}In(n,2n)^{114m}In	49.51 days	9.1 MeV (9.3 MeV)	190.27	95.7 (15.56)
Ni (1 mm)	^{58}Ni(n,p)^{58g}Co	70.86 days	0 (1.3) MeV	810.76 keV	68.08 (99.45)
	^{58}Ni(n,2n)^{57}Ni	35.60 hr	12.4 (13.3) MeV	1.378 MeV	68.08 (81.7)
Al (1 mm)	^{27}Al(n,p)^{27}Mg	9.458 min	1.90 (4.2) MeV	843.76 keV	100 (71.8)
	^{27}Al(n,a)^{24}Na	14.997 hr	3.25 (6.7) MeV	1368.63 keV	100 (99.99)
Au (10 mil)	^{197}Au(n,g)^{198}Au	2.694 days	Thermal+	411.8 keV	100 (95.62)
	^{197}Au(n,2n)^{196}Au	6.1167 days	8.11 (8.3) MeV	355.7 keV[1]	100 (80.9)
Zr (1 mm)	^{90}Zr(n,2n)^{89}Zr	78.41 hr	12.1 (12.1) MeV	909.15 keV	51.45 (99.04)

information to the unfold process in the form of a realistic guess spectrum. An alternative approach is to use detection systems that contain a more dynamic response. Liquid scintillators are one approach to introduce more information to the unfold process, allowing the removal of the realistic *a priori* spectrum requirement.

7.3 Liquid Scintillators

Scintillators are one of the oldest methods of detecting radiation, and several useful books and papers have been written discussing their application [16, 109, 222]. Scintillators work on the principle that incident radiation populates excited states in the molecule. The states

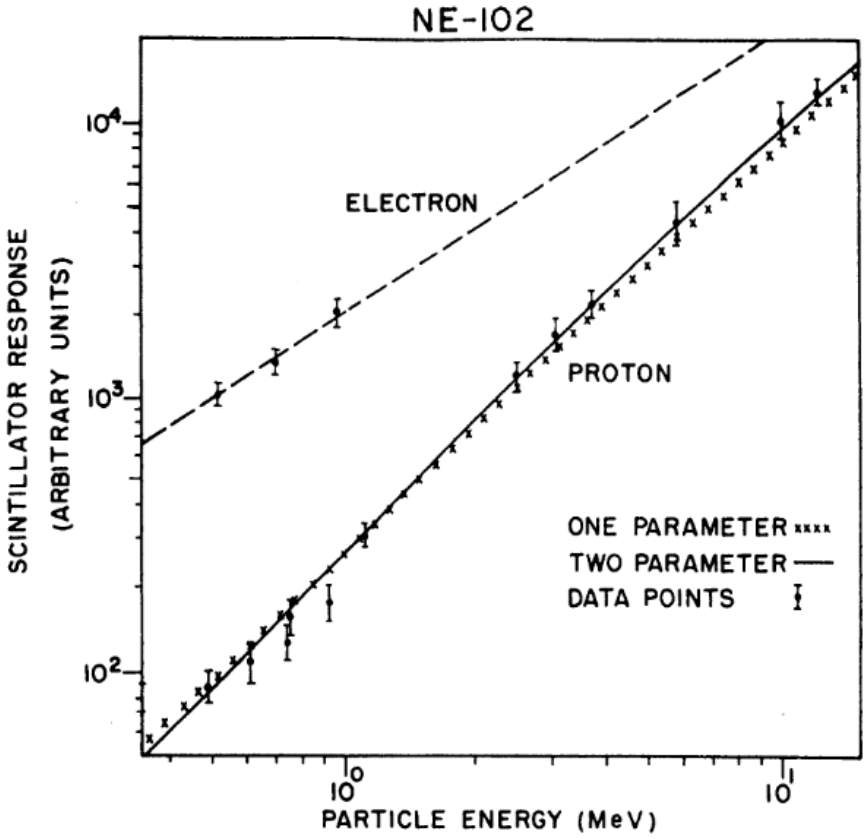

Figure 7.3: Comparison of the light yield from electron and proton energy deposition in NE-102 [109].

then depopulate via flourescence. These emitted photons can be collected and converted to an electrical signal to allow for quantitative measurement of the energy deposited.

The relation between the deposited energy and the light output of the scintillator varies by scintillator and is dependent on the particle depositing the energy, as shown in Figure 7.3. In Figure 7.3, electrons and protons are the primary energy deposition mechanism from gamma and neutron interactions in the scintillator, respectively. The electron yield is linear down to ∼100 keV, but the proton yield is nonlinear over a large energy range [109]. Accurately expressing the relationship between the energy deposition and light yield is crucial for unfolding the incident neutron flux and is described further in Subsection 7.3.2.

One drawback of liquid scintillators for the ETA application is their size. This limits their employment to outside of the ETA, which eliminates the ability to measure the TN+PFNS directly. However, they can measure the perturbed neutron field around the ETA, thereby providing secondary and complementary experimental validation for the spectral shaping performance of the ETA.

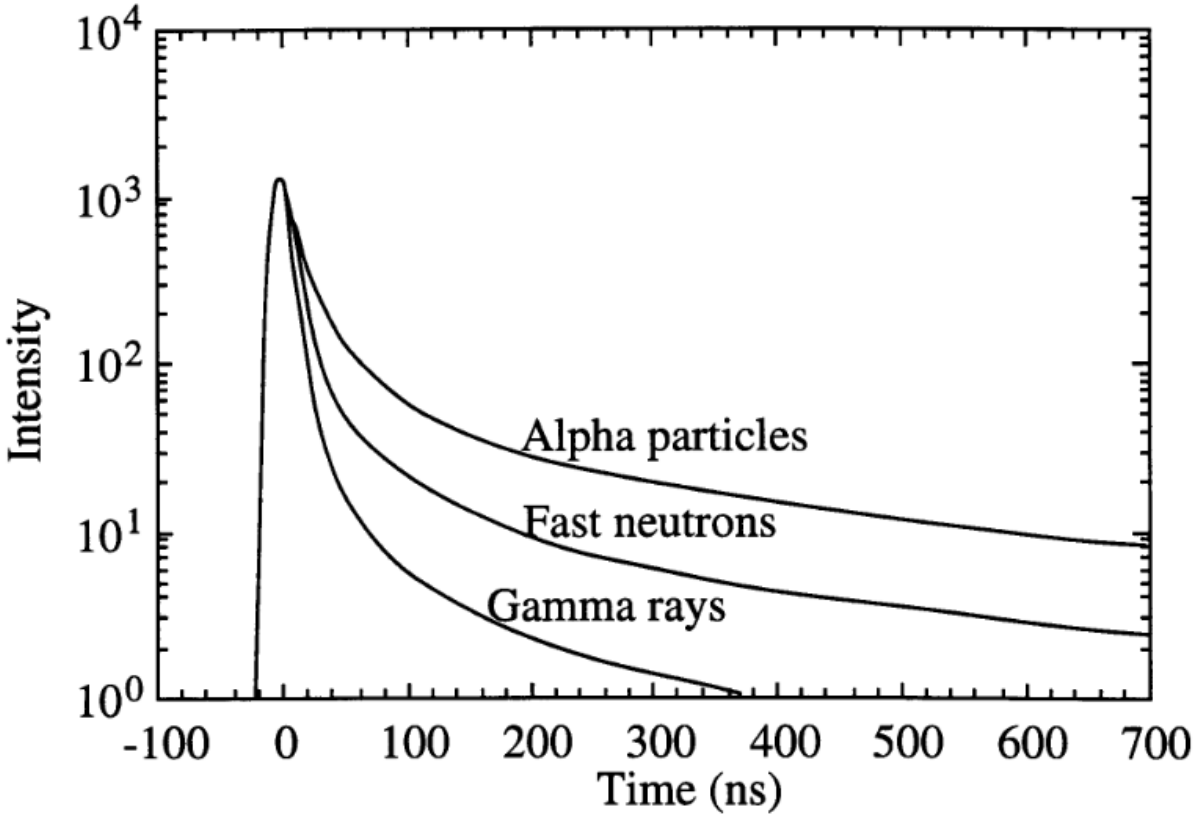

Figure 7.4: Comparison of the delayed light emission fraction as a function of the type of incident radiation [109].

Another drawback of liquid scintillators is their sensitivity to both neutron and gamma radiation. This can limit the ability to measure the neutron spectrum in a mixed field such as those present at NIF and the 88-Inch Cyclotron. A useful feature of some scintillators is the ability to use a technique called pulse shape discrimination to separate out the neutron and gamma responses.

7.3.1 Pulse Shape Discrimination

The vast majority of light emitted from scintillators has a characteristic decay time of a few nanoseconds, but a longer lived component does exist with a decay time of a few hundred nanoseconds. The fraction of the delayed component is dependent on the type of incident radiation causing the initial excitation, as shown in Figure 7.4 [109]. Use of this information to selectively remove certain particles from the data set is known as pulse shape discrimination (PSD).

The most common method of PSD is the charge integration method. This method

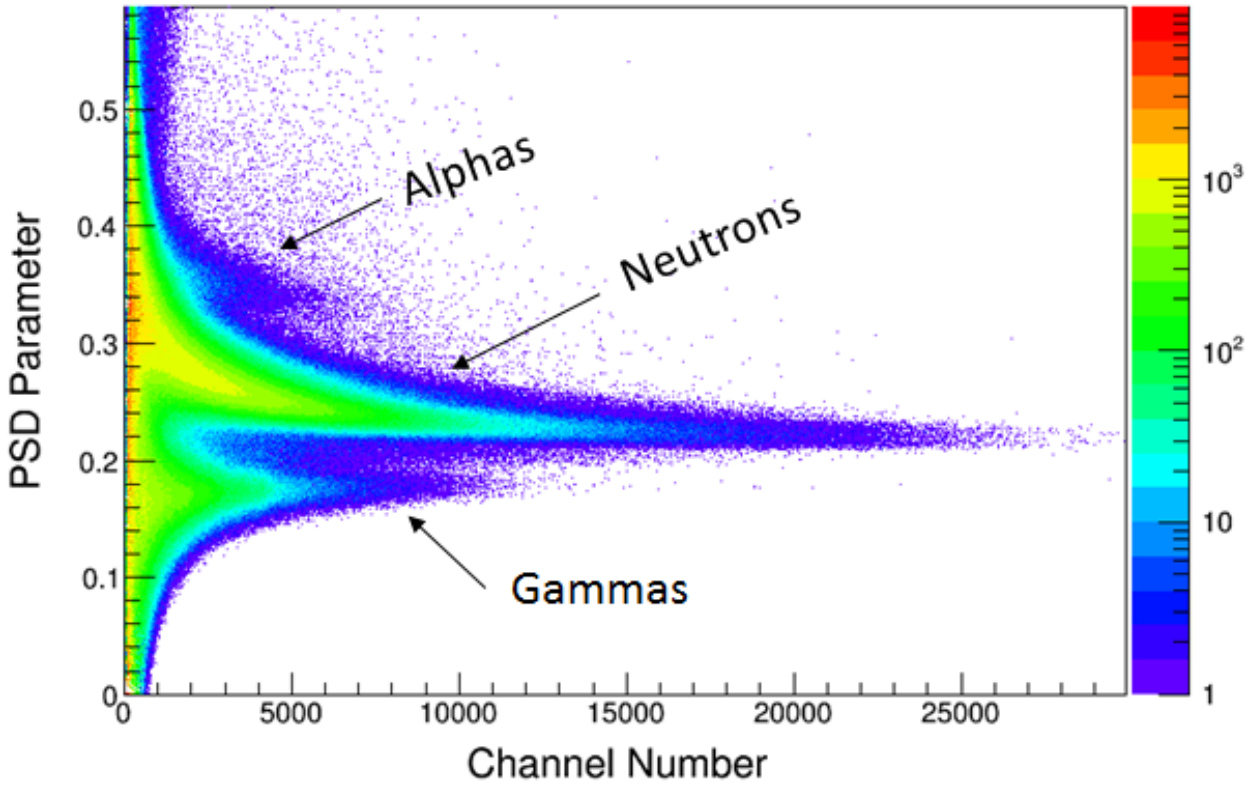

Figure 7.5: PSD plot using tail-to-total PSD method from Equation 7.17 for a EJ-309 detector.

develops a ratio of the tail-to-total integrated charge as the PSD parameter through

$$PSD = \frac{\int_{gate2_{start}}^{gate2_{end}} Q(t)dt}{\int_{gate1_{start}}^{gate1_{end}} Q(t)dt} \,. \tag{7.17}$$

Commonly, $gate1_{start}$ is set to the start of the pulse and $gate1_{end} = gate2_{end}$, but alternative gating methodologies for Equation 7.17 can be used [39, 63, 103, 167]. Other approaches include the application of Bayes' Theorem [147], discrete wavelet transformation [236], zero-crossing techniques [156], and pulse gradient analysis [7]. A typical PSD plot using the charge integration method is shown in Figure 7.5.

The efficacy of different approaches and gates can be evaluated using a figure of merit (FOM) defined as

$$FOM(E) = \frac{\Delta_{Peak}(E)}{FWHM_{\gamma}(E) + FWHM_{n}(E)} \,, \tag{7.18}$$

where $\Delta_{Peak}(E)$ is the distance in PSD parameter of the two peaks at a given deposition energy and $FWHM_{\gamma}(E)$ and $FWHM_{n}(E)$ are the full width at half maximum of the gamma

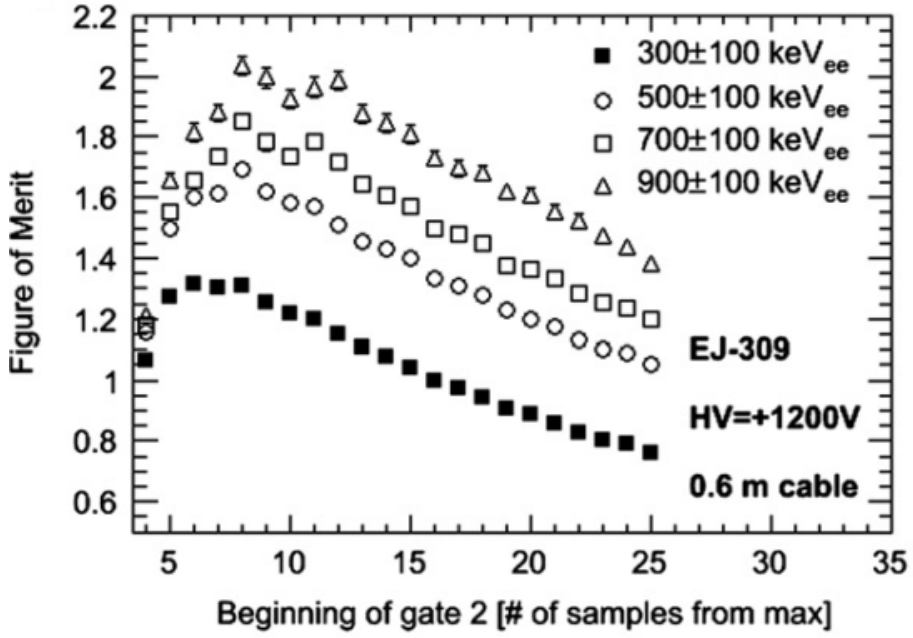

Figure 7.6: FOM for the starting gate time as a function of four different deposition energies [167].

and neutron distributions, respectively [167]. An example outcome of the analysis using Equation 7.18 is shown in Figure 7.6. The fact that the FOM is energy dependent also gives rise to the idea that different PSD parameters for different energy regions might improve the PSD performance, which has been shown in [66].

7.3.2 Light Response

One of the benefits of organic scintillators is a more robust set of unique response functions that can be used to unfold the neutron energy spectrum. A sample set of EJ-309 response functions is shown in Figure 7.7. This diverse response provides significantly more information to the unfolding problem than a set of activation foils.

The light yield response does not have the pedigree of dosimetry cross sections, and quantifying the light response is a key component in analyzing the PHS for the purposes of unfolding. As figure Figure 7.3 shows, the response for non-electron particles is nonlinear, and models have been proposed to capture this nonlinearity [16, 158, 222]. However, these models diverge significantly beyond the benchmark experimental data, as shown in Figure 7.8. This divergence creates a lower neutron energy bound above the physical detection threshold. Below the 1 MeV proton recoil threshold, the ability to accurately assess the incident neutron flux spectra rapidly degrades.

Recent work at LBNL and UC-Berkeley has sought to address this limitation by driving

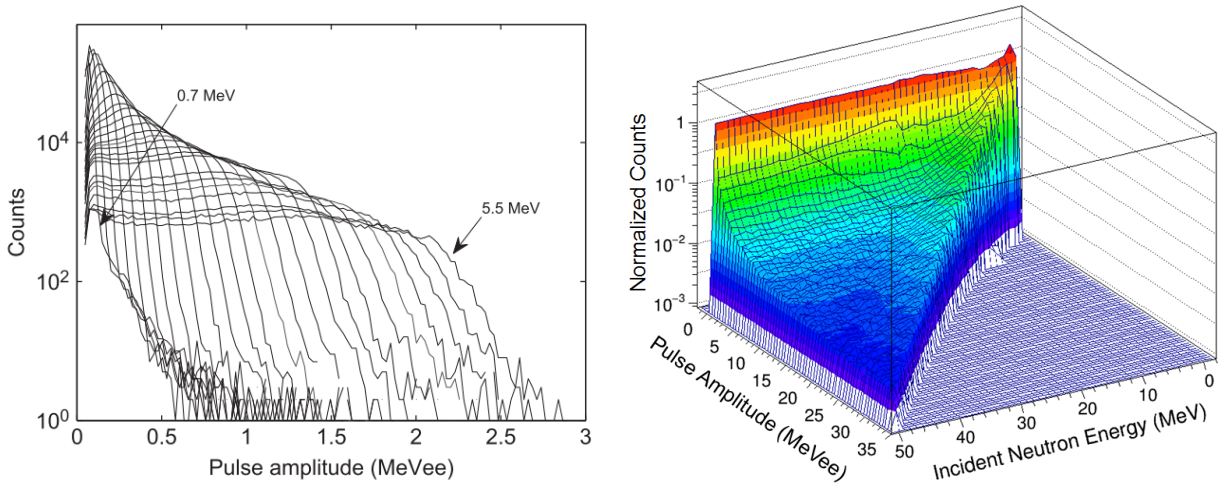

(a) a) (b) b)

Figure 7.7: EJ-309 response as a function of incident neutron energies for a) discrete curves from 0.7 to 5.5 MeV [65] and b) a complete normalized response matrix for 0-50 MeV neutrons.

the measured experimental light output down to a few hundred keV in proton recoil energy [113]. This allows EJ-309 scintillators to be used as a complementary and independent measurement of the ETA-generated neutron field at energies in the PFNS energy range.

7.3.3 HEPROW

HEPROW is written with unfolding experimentally measured PHS in mind, but it can be used to unfold "few channel" methods such as Bonner spheres or foil activation results as well [134, 135]. It contains several sub-modules that can be used for the manipulation of the required input such as UMSPHW to convert measures PHS to HEPROW format, OPERAW to combine and perform basic math operations on PHS and response files, RSPGW to perform rebinning and Gaussian smearing of ideal response matrices, and FALTW to perform the folding on the unfolded fluence with the response matrix to generate the comparison PHS. The core of the code is formed by the GRAVELW, MEIKEW, and UFANAW programs, which perform unfolding and error propagation [134].

GRAVELW is based on the methods from SAND-II, which are described in Section 7.1. GRAVELW expands on the original SAND-II approach and incorporates weightings proportional to the relative variances of the measured PHS bins into a logarithmic version of Equation 7.5[1]. An iterative approach is taken to minimizing χ^2, which requires an initial guess spectrum. Guesses close to the expected spectrum increase the convergence rate, but uniform spectra can be used to avoid biasing the solution. The solution does depend on the

[1]The logarithm of the PHS values are taken to enforce the condition of positive flux.

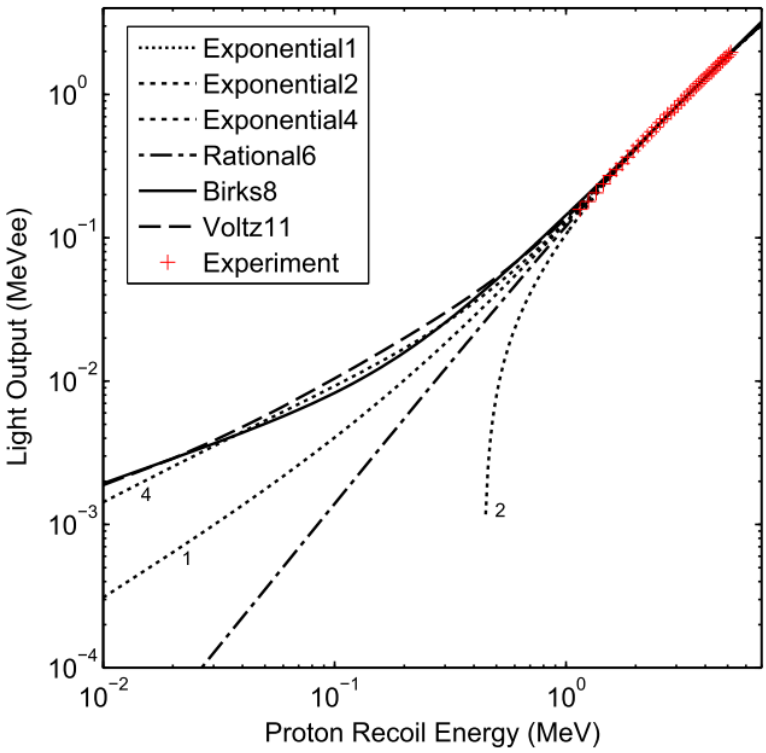

Figure 7.8: Comparison of 6 models and experimental data for EJ-309 light output as a function of proton recoil energy [158].

initial guess, which makes the determination of the uncertainty difficult with the GRAVELW code alone [134].

MIEKEW takes the unfolded GRAVELW spectrum and performs the uncertainty quantification. It accomplished this through assessing the probability density of the GRAVELW neutron spectrum unfold using Bayseian and Maximum Entropy inference methods and Monte Carlo sampling to inform expectation values. The full math behind this approach is laid out in several of the HEPRO papers [133, 134, 135, 136, 137].

UNFANAW was introduced to provide an analytical approach to uncertainty quantification due to the run time requirements of the MIEKEW code [134]. However, modern computers make the run times completely tractable[2], so the more robust MIEKEW code was used instead for this research.

This chapter outlined several approaches that could be used to measure the neutron energy spectrum for the ETA. Unfolding methods were determined to be the most appropriate based on the lack of timing information, experimental limitations such as a limited sample volume, and overall detection efficiencies. The foil activation and PHS unfolding methods

[2]MIEKEW run times were less than a minute for all problems considered.

outlined in this chapter will be applied to the 88-Inch Cyclotron and NIF ETA validation experiments in Chapter 8 and Chapter 9, respectively.

Chapter 8

88-Inch Cyclotron Experimental Validation

An experiment is a question which science poses to Nature, and a measurement is the recording of Nature's answer.

- Max Planck

Experiments for validation of the ETA were carried out 29-31 March, 2017 and 25-27 April, 2017 at the LBNL 88-Inch Cyclotron. The experimental goals were the validation of the NIF ETA design's spectral shaping capability and the testing of the neutron spectroscopy techniques. Additional partial ETA measurements were taken to understand the impact of nuclear data deficiencies on the ability to model the ETA performance. This chapter describes an overview of the 88-Inch Cyclotron facility, the experiment set-up and procedures, and modeling results of expected outcomes. Complete analysis of the results will be presented in future publications.

8.1 Facility Overview

The 88-Inch Cyclotron is a variable energy, multi-particle cyclotron capable of accelerating deuterons up to ∼65 MeV with maximum currents on the order of 10 μA. The Cave 0 beamline can be used to produce a collimated neutron beam through deuteron breakup. The facility has experience with multiple breakup targets including beryllium (Be), titanium (Ti), and tantalum (Ta). A schematic representation of the cyclotron vault and Cave 0 beam line experimental facilities is shown in Figure 8.1.

Deuterons, with a neutron separation energy of 2.22 MeV, are weakly bound and will produce neutrons via breakup in the Coulombic field of a heavier nucleus (elastic breakup), proton stripping reactions (inelastic breakup), and pre-equilibrium and evaporation emission from the excited compound nucleus formed by deuteron absorption [8, 32, 138, 220]. Each

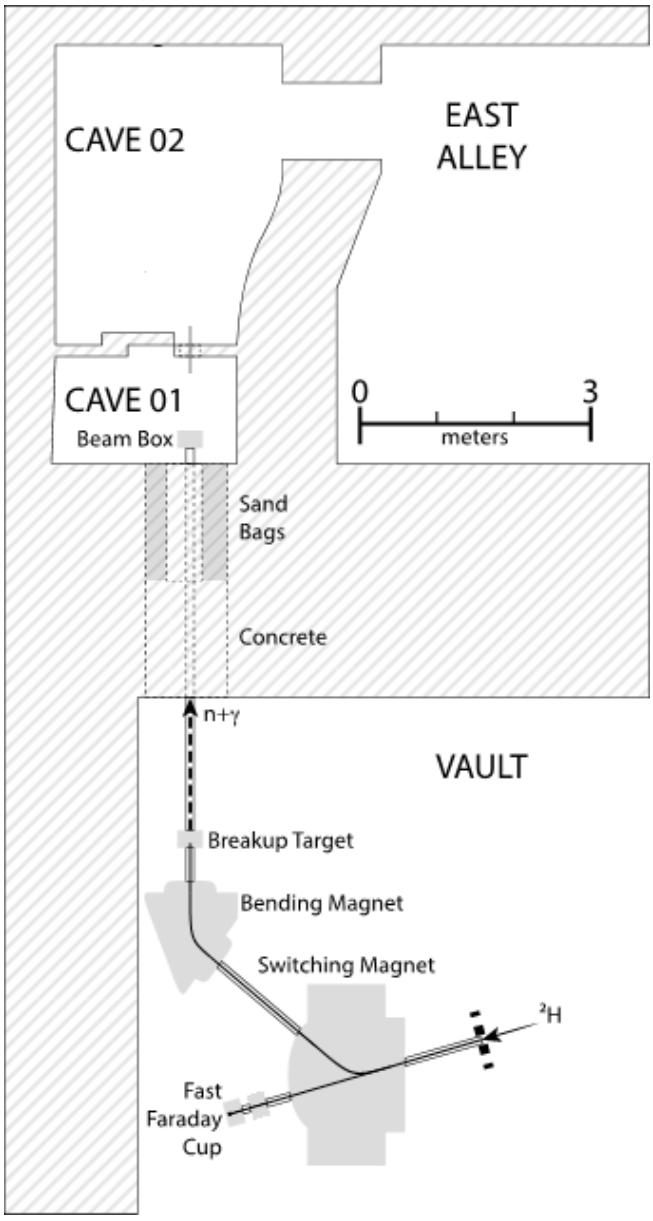

Figure 8.1: Schematic representation of the 88-Inch Cyclotron vault and beam line to Cave 0.

production mechanism produces neutrons with different angular and energy distributions. The elastic and inelastic breakup reactions result in neutron distributions that are highly forward peaked with an average energy of

$$E_n = \frac{1}{2}\left(E_d - \frac{Ze^2}{R_{bu}} - \epsilon_d\right) , \tag{8.1}$$

where R_{bu} is the breakup radius, E_d is the energy of the deuteron, and ϵ_d is the Q value of the reaction [32, 138].

Equation 8.1 describes the downward shift in the peak and average neutron energy with increasing Z. The neutron distribution is less broad with increasing Z due to the higher dE/dZ of the heavier target nucleus and the increasing relative fraction of the elastic channels [32, 141, 233]. In contrast, the pre-equilibrium and evaporative emission channels will be roughly isotropic and have energy distributions peaked at much lower energies based on the characteristic temperature of the nucleus [110, 220, 233]. As the neutron emission angle increases, the relative contribution of the pre-equilibrium and evaporative emission channels increase, and the resulting energy distribution is far broader and less intense [124, 141, 220, 233].

This diversity in neutron spectra as a function of incoming deuteron energy, outgoing angle, and the target enables the 88-Inch Cyclotron to be used to perform a variety of neutron related experiments. For the ETA experiments, a beam was designed to have a neutron spectrum that is well-characterized in the literature, peaked near 14.1 MeV, NIF-relevant energies, and had as limited a high energy component as possible. The beam used and experimental set-up for the ETA experiments at the 88-Inch Cyclotron are described in the next section.

8.2 Experimental Procedures

For this experiment, $^2H^+$ ions were accelerated to 33 MeV with currents ranging up to 12 μA. The deuteron beam was directed along the Cave 0 beam line and optically aligned using a phosphor located in the Cave 01 beam box, as shown in Figure 8.1. A Faraday cup located inside the cyclotron vault was outfitted with a 50 mm in diameter, 4-mm-thick tantalum breakup target. The tantalum target is backed by a 14.5 mm thick copper cooling assembly with a 38 mm diameter center cutout and an outer diameter of 101.5 mm. The resulting neutrons and photons entering the experimental area were collimated by ∼3 m of concrete and ∼1.5 m of sand bags encasing the beam pipe, producing a high-contrast, open-air neutron beam in the experimental area [138].

The setup resulted in a neutron beam that peaked at ∼10 MeV, extended to ∼38 MeV, and had ∼7% of the total fluence ≥ 20 MeV [141, 220]. The neutron intensity was ∼ 2×10^{10} n per μC per steradian at the breakup target and ∼ 3.5×10^7 n per second at the front face of the ETA. The neutron intensity from this configuration is over six orders of magnitude less than the NIF fluence on the front ETA face from the configuration described

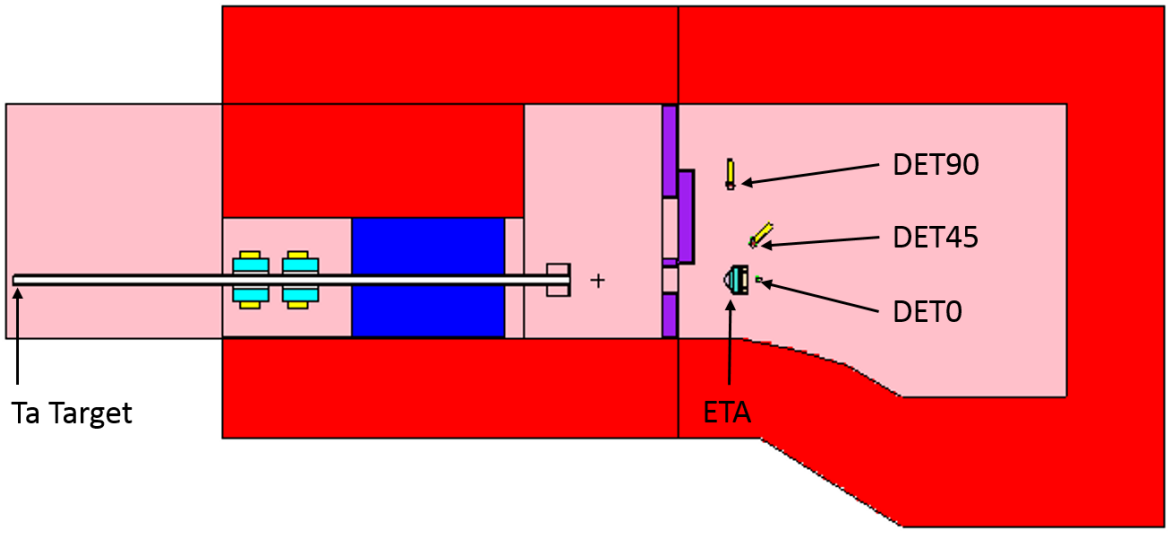

Figure 8.2: Experimental configuration for the PHS measurements. In the figure, concrete walls are red, sandbags are blue, lead walls are purple, and the air is pink. Det0 is oriented along the Z-axis.

in Chapter 9, but longer run times at the 88-Inch Cyclotron can make up for some of this difference.

A series of PHS and activation measurements were made from 25-27 April, 2017, and the experimental configuration for each is described in detail in Section 8.3 and Section 8.4 below. The simulated results expected from these experiments are described in Section 8.5. Additionally, a set of pulse-amplitude-time (PAT) PHS measurements were taken on 29-31 March. The experimental set-up is described in Subsection 8.3.1.

8.3 Pulse Height Spectroscopy Experiments

Two sets of PHS data sets were taken on 29-31 March and 25-27 April, 2017. Both measurements had essentially the same experimental setup, which is shown in Figure 8.2. The primary difference between the two experiments was the form in which the data were taken. The 29-31 March experiment took PAT data, whereas the 25-27 April experiment took full waveform (WF) data. Each data set contained a measurement of the 33 MeV deuteron on Ta distribution with no ETA in place, a measurement with the full ETA in place (depicted in Figure 8.2), and a series of measurements where the ETA was built-up component by component. Due to slight differences, the exact locations of each detector and the ETA are described in Subsection 8.3.1 and Subsection 8.3.2 for the 29-31 March and 25-27 April experiments, respectively.

Table 8.1: Locations of the EJ-309 detectors and ETA for the 29-31 March PHS experiments. All measurements are relative to BLC in the Y and Z directions and the Cave 02 side of the Cave 01/02 wall (540 cm from the Ta breakup target) in the X direction.

	X [cm]	**Y [cm]**	**Z [cm]**
ETA	44.0	0	0
Det0	81.0	0	0
Det45	73.4	34.7	0
Det90	52.4	91.4	0

The open-source locations for all of the PHS calibration data, experimental data, beam current monitor (BCM) files, and associated data taken during these experiments are described in Appendix B.

8.3.1 29-31 March, 2017 Pulse-Amplitude-Time Data

During 29-31 March run, data were taken in PAT mode using the CAEN V1730 digital data acquisition (DAQ) system and EJ-309 organic liquid scintillators. The 2-inch right circular cylinder (RCC) EJ-309 detectors with Hamamatsu H1949-50 photo-multiplier tubes (PMTs) were placed at beam line center (BLC), ∼45°, and 90° and are referred to as Det0, Det45, and Det90, respectively. The locations of the three detectors and the ETA for this experiment are listed in Table 8.1. The ETA and detectors were placed using lasers aligned to BLC, and the measurements were made relative to the Cave 02 side of the Cave 01/02 wall and BLC. This side of the wall is 540 cm from the breakup target located in the vault as shown in Figure 8.1. For the detectors, the distance measured is to the center of the face. Det0 is aligned along the Z-axis and with the edge of the face touching BLC in the Z-direction. All measurements have a precision of ± 0.2 cm.

The detectors were connected through a junction box in Cave 02 to the CAEN Model V1730 DAQ and CAEN 4 channel programmable high voltage (HV) power supply. The DAQ and HV supply were housed in CAEN NV8020 nuclear instrumentation module (NIM) crate powered by a CAEN N8315 power supply and connected to a workstation using a CAEN Model V1718 bridge. The connection ports and bias settings are described in Table 8.2.

In PAT mode, the CAEN Digital Pulse Processing for Pulse Shape Discrimination (DPP-PSD) software was used to perform pile-up rejection (PUR) and PSD. The PUR algorithm looks for a peak-valley-peak condition that exceeds a user-specified PUR-GAP, as shown in Figure 8.3. The PSD algorithm uses the tail-to-total method described in Subsection 7.3.1.

For these experiments, the trigger threshold was set to 50 LSB with a charge sensitivity of 20 fC/LSB corresponding to a minimum pulse amplitude of 1pC. The PUR-GAP was set to 30 LSB. The DPP-DSP software was set to record 992 ns traces with a pre-trigger of 240

Table 8.2: Connection ports and bias settings for the EJ-309 cabling.

Detector	PMT Data Out	Junction Data	Junction HV	HV Ch #	Bias [V]	DAQ Ch #
Det0	A1	30	50 (HV1)	0	1235	0
Det45	A1	31	51 (HV2)	1	1250	2
Det90	A1	32	52 (HV3)	2	1250	4

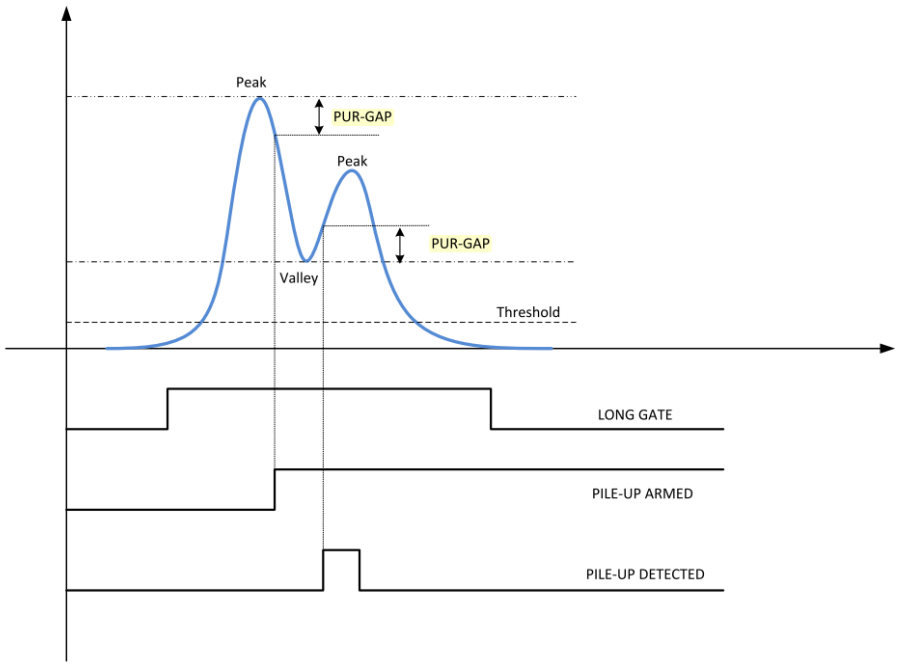

Figure 8.3: PUR algorithm implemented in the DPP-PSD software [29]. For the PAT data sets, a threshold of 50 LSB and a PUR-GAP of 30 LSB was used [29].

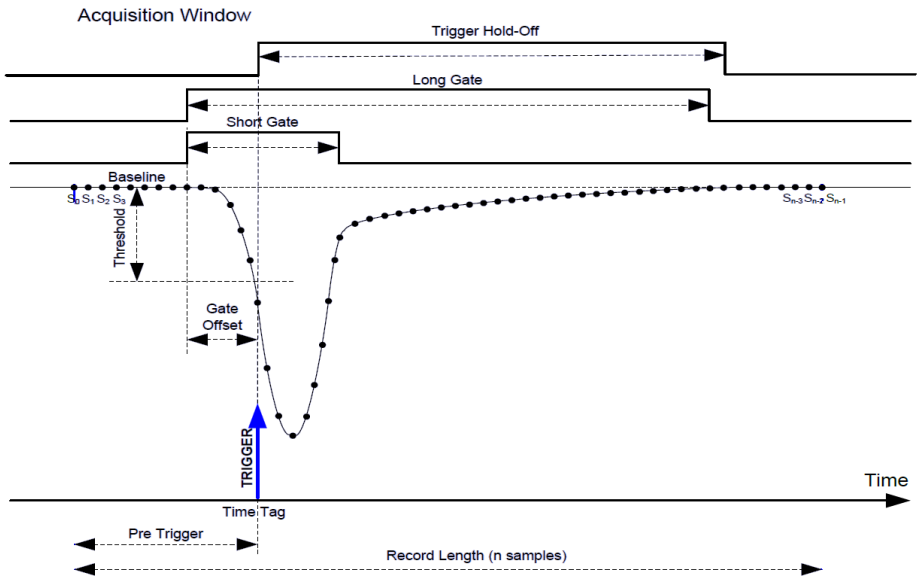

Figure 8.4: Diagram relating the DPP-PSD parameters [29].

ns. The PSD parameters were set to have a short gate of 36 ns and a long gate of 300 ns with a gate offset of 12 ns. The DC offset was set to -47 to ensure a full dynamic range of 2 V peak-to-peak. The baseline was calculated using a moving average over a 2048 ns window. The relationships between these signal processing parameters are illustrated in Figure 8.4.

Calibrations were performed using the 4.439 MeV AmBe (from the ^{9}Be(α,n) reaction), 1173 and 1332 keV ^{60}Co, and 661 keV ^{137}Cs lines. Additionally, background data was taken with each of the three calibration data sets described in Table 8.3. The first calibration data set was taken during beam tuning and had bias settings of 1190, 1220, and 1220 V for Det0, Det 45, and Det90, respectively. Once the beam was tuned, the 33 MeV deuteron breakup on Ta source was used to adjust the bias to ensure the largest signals observed covered the full dynamic range without clipping. The adjusted gain settings are shown in Table 8.2, and a second calibration data set was taken prior to the series of PHS measurements. After the series of PHS measurements, a third calibration data set was taken. The second and third calibration data sets can be used to test for gain drift during the experiment.

After the second calibration data set, a series of PAT measurements was taken, as described in Table 8.4. Each of these measurements was 15-20 minutes, with total event rates of ∼50-60 kHz between all three detectors and ≤1% pile-up in each. The first source run without the ETA (33MeVTa_001_ls_[ch#].dat) was done with an unstable beam. The beam would fail after ∼45 sec due to a current limit on the inflector. This issue was fixed for the remaining data sets. The first run with tungsten (ETA_W_001_ls_[ch#].dat) was done with Valve 0 in place, and the second run (ETA_W_002_ls_[ch#].dat) was done without resetting the current integrator. None of these data sets should not be used for analysis.

Table 8.3: Calibration data sets taken during the 29-31 March PHS experiments. [src] is the name of the source (i.e. Co60) and [ch#] is the channel number from Table 8.2.

Cal #	Collection Time	File Names	Note
1	30 min	[src]_001_ls_[ch#].dat	Pre-beam
2	5 min	[src]_002_ls_[ch#].dat	Gains modified; pre-experiment
3	5 min	[src]_003_ls_[ch#].dat	Post-experiment

Table 8.4: Description of the experimental data sets for the 29-31 March PHS measurements of the beam and ETA modified spectra.

Measurement	Run Time	Beam Current	Integrated Current	File Names
Source w/o ETA	15m 18s	∼140 nA	115.0 μC	33MeVTa_002_ls_[ch#].dat
+ ETA case	19m 55s	∼150 nA	166.2 μC	ETA_Case_001_ls_[ch#].dat
+ Tungsten	12m 16s	∼550 nA	373.2 μC	ETA_W_003_ls_[ch#].dat
+ Bismuth	14m 43s	∼1.8 μA	1442 μC	ETA_Bi_001_ls_[ch#].dat
+ Praseodymium	16m 33s	∼1.8 μA	1572 μC	ETA_Pr_001_ls_[ch#].dat
+ Boron Carbide	14m 52s	∼3.5 μA	2976 μC	ETA_B4C_001_ls_[ch#].dat
+ Silicon	17m 42s	∼4.0 μA	3828 μC	ETA_Si_001_ls_[ch#].dat

8.3.2 25-27 April, 2017 Waveform Data

During 25-27 April run, data were taken in full WF mode using the CAEN V1730 DAQ and EJ-309 organic liquid scintillators. The 2-inch RCC EJ-309 detectors with Hamamatsu H1949-50 PMTs were placed at BLC, ∼45°, and 90°. The locations of the three detectors and the ETA for this experiment are listed in Table 8.5. The ETA and detectors were placed using lasers aligned to BLC, and the measurements were made relative to the Cave 02 side of the Cave 01/02 wall and BLC. This side of the wall is 540 cm from the breakup target located in the vault as shown in Figure 8.1. For the detectors, the distance measured is to the center of the face. Det0 is aligned along the Z-axis and with the edge of the face 2.2 cm from BLC in the Z-direction due to a misalignment. All measurements have a precision of $\pm$0.2 cm.

The detectors were connected through a junction box in Cave 02 to the CAEN Model V1730 DAQ and CAEN 4 channel programmable HV power supply. The DAQ and HV supply were housed in CAEN NV8020 NIM crate powered by a CAEN N8315 power supply and connected to a workstation using a CAEN Model V1718 bridge. The connection ports

Table 8.5: Locations of the EJ-309 detectors and ETA for the 25-27 April PHS experiments. All measurements are relative to BLC in the Y and Z directions and the Cave 02 side of the Cave 01/02 wall (540 cm from the Ta breakup target) in the X direction.

	X [cm]	**Y [cm]**	**Z [cm]**
ETA	44.0	0	0
Det0	81.0	0	2.2
Det45	73.4	34.7	0
Det90	52.4	91.4	0

Table 8.6: Connection ports and bias settings for the 25-27 April PHS experiments.

Detector	**PMT Data Out**	**Junction Data**	**Junction HV**	**HV Ch #**	**Bias [V]**	**DAQ Ch #**
Det0	A1	30	50 (HV1)	0	1235	0
Det45	A1	31	51 (HV2)	1	1250	2
Det90	A1	32	52 (HV3)	2	1250	4
Beam RF	N/A	39	N/A	N/A	N/A	14

and bias settings are described in Table 8.6.

In WF mode, the CAEN Digital Pulse Processing for Pulse Shape Discrimination (DPP-PSD) firmware was used only to trigger the DAQ and record the WF. The trigger threshold was set to 50 LSB with a charge sensitivity of 20 fC/LSB corresponding to a minimum pulse amplitude of 1pC. The DPP-DSP software was set to record 496 ns traces with a gate offset of 40 ns. The DC offset was set to -47 to ensure a full dynamic range of 2 V peak-to-peak.

Calibrations were performed using the 4.439 MeV AmBe (from the ^{9}Be(α,n) reaction), 1173 and 1332 keV ^{60}Co, and 661 keV ^{137}Cs lines. Additionally, background data was taken with each of the three calibration data sets described in Table 8.7. The first calibration data set was taken with a gate offset of 12 ns, which was too short for proper baseline estimation. A second calibration data set was taken prior to the series of PHS measurements using a 40 ns gate offset. Once the beam was tuned, the 33 MeV deuteron breakup on Ta source was used to ensure the largest signals observed covered the full dynamic range without clipping. After the series of PHS measurements, a third calibration data set was taken. The second and third calibration data sets can be used to test for gain drift during the experiment.

After the second calibration data set, a series of WF measurements were taken as described in Table 8.8. Each of these measurements was $\sim$30 minutes long, with total transfer rates of $\sim$20 MB/s between all three detectors and $\leq$1% pile-up in each. A second source

Table 8.7: Calibration data sets taken during the WF PHS experiments conducted 25-27 April, 2017. [src] is the name of the source (i.e. Co60), [f#] is the auto-incriminating file number, and [ch#] is the channel numbers from Table 8.6.

Cal #	Collection Time	File Names	Note
1	5-15 min	[src]_001.[f#].[ch#].root	Pre-beam
2	5-15 min	[src]_002.[f#].[ch#].root	Gate off modified; pre-experiment
3	5-10 min	[src]_003.[f#].[ch#].root	Post-experiment

Table 8.8: Description of the 25-27 April, 2017 experiments run for the WF PHS data measurements of the beam and ETA modified spectra.

Measurement	Run Time	Beam Current	Integrated Current	File Names
Source w/o ETA	29m 43s	∼50 nA	79.98 μC	CleanBeam_001.[f#].[ch#].root
+ ETA case	31m 53s	∼50 nA	90.66 μC	Case_001.[f#].[ch#].root
+ Tungsten	28m 26s	∼150 nA	232.6 μC	W_001.[f#].[ch#].root
+ Bismuth	33m 29s	∼650 nA	1212 μC	Bi_001.[f#].[ch#].root
+ Silicon	45m 27s	∼800 nA	1970 μC	Si_001.[f#].[ch#].root
+ Praseodymium	26m 23s	∼1.0 μA	1522 μC	Pr_001.[f#].[ch#].root
+ Boron Carbide	30m 56s	∼2.0 μA	3530 μC	B4C_001.[f#].[ch#].root
Source w/o ETA	29m 39s	∼100 nA	156.6 μC	CleanBeam_002.[f#].[ch#].root

measurement was taken due to the high background rates at the beginning of the WF PHS run from the previous normalization activation foil run (see Section 8.4).

PAT Data

Two PAT data sets were taken during the 25-27 April experiments to allow the WF data from this experiment to be related to the previous 29-31 March data set. These were taken with the same setup and settings described in Subsection 8.3.1, with the exception that the detectors were arranged as shown in Table 8.5. The calibration data sets for these measurements are shown in Table 8.9, and the data sets are shown in Table 8.10.

Table 8.9: Calibration data sets taken during the PAT PHS experiments conducted from 25-27 April, 2017. [src] is the name of the source (i.e. Co60) and [ch#] is the channel numbers from Table 8.2.

Cal #	Collection Time	File Names	Note
1	5-10 min	[src]_001_ls_[ch#].dat	Pre-experiment
3	5-10 min	[src]_003_ls_[ch#].dat	Post-experiment

Table 8.10: Description of the 25-27 April experiments run for the PAT PHS measurements of the beam and ETA modified spectra.

Measurement	Run Time	Beam Current	Integrated Current	File Names
Source w/o ETA	26m 17s	∼100 nA	145.8 μC	CleanBeam_002_ls_[ch#].dat
Full ETA	27m 03s	∼2.0 μA	2970 μC	ETA_001_ls_[ch#].dat

8.4 Neutron Activation Experiments

Neutron activation data were taken during the 25-27 April, 2017 88-Inch Cyclotron experiments to measure both the source and the ETA modified spectra. The general experimental set-up is the same as described in Section 8.2, and the specific foil locations for each irradiation are described in Subsection 8.4.1, Subsection 8.4.2, and Subsection 8.4.3 for each of the activation experiments.

Counting of the foils was conducted using the 88-Inch Cyclotron counting lab's Ortec HPGe GMX-50220-S detector (Det02) with GammaVision spectroscopy software. Efficiency calibration data were taken at positions 1 cm, 5 cm, 10 cm, and 18 cm from the detector surface using the following sources and lines: ^{137}Cs (661.657 keV), ^{60}Co (1173.23 and 1332.49 keV), ^{241}Am (59.54 keV), ^{133}Ba (80.998, 276.40, 302.45, and 356.01 keV), and ^{152}Eu (121.70, 244.70, 344.29, 778.90, 964.06, 1085.837, 1112.08, and 1408.01 keV). The calibration source data are listed in Table 8.11. Additionally, ^{88}Y (392.87 and 1836.063 keV) and ^{88}Zr (898.042 keV) were used for energy-only calibration lines.

Three sets of activation foils were irradiated during this experiment. The first set, described in Subsection 8.4.1, was irradiated to provide geometry and coincidence summing correction factors. The second foil set, described in Subsection 8.4.2, was irradiated to measure the source spectrum. The third foil set, described in Subsection 8.4.3, was irradiated in the ETA sample cavity to measure the ETA modified spectrum. The open-source location of the calibrations, data, and BCM files are described in Appendix B. For post-irradiation decay purposes, it should be noted that the BCM time stamp is 71 $\pm$ 2 seconds ahead of the GammaVision time stamps.

Table 8.11: Calibration sources used for the efficiency and energy calibrations.

Source	**Initial Activity [μCi]**	**Relative Uncertainty [%]**	**Initial Date**	**Half-life [s]**
^{241}Am	10.3	1.165	01Jan1970	1.3644E+10
^{152}Eu	1.062	1.165	01Jan2009	4.2633E+8
^{60}Co	1.007	1.165	01Jan2009	1.6634E+8
^{137}Cs	1.0042	1.165	01Jan2009	9.4872E+8
^{133}Ba	1.078	1.165	01Jan2009	3.3274E+8

For the source and ETA foils, several of the activation products will have contributions from channels other than the primary channel of interest indicated in Subsection 8.4.2 and Subsection 8.4.3. The contributions from other channels are due to the broad nature of the 33 MeV deuteron breakup source that extends to ~38 MeV. These cross-channel contributions can be problematic as nuclear data generally do not exist to deconvolve the results. The activation products affected are:

1. **^{57}Ni Product:** In addition to the desired ^{58}Ni(n,2n) channel, there will be contributions from the ^{60}Ni(n,4n), threshold 33.15 MeV, channel.

2. **^{58}Co Product:** In addition to the desired ^{58}Ni(n,p) channel, there will be contributions from the ^{60}Ni(n,2np), threshold 20.32 MeV, and ^{61}Ni(n,3np), threshold 28.27 MeV, channels.

3. **^{89}Zr Product:** In addition to the desired ^{90}Zr(n,2n) channel, there will be contributions from the ^{91}Zr(n,3n), threshold 19.38 MeV, and ^{92}Zr(n,4n), threshold 28.80 MeV, channels.

8.4.1 Normalization Foils

To correct for geometry and coincident summing, a normalization foil pack was used to generate data for the double ratio method described in Section 7.2. The foil pack was irradiated for 16 min at ~8 μA in the Cave 01 beam line using a beryllium target plunged into the Cave 01 beam box. The foil pack was attached directly to the face of the beam box at BLC. Since the double ratio method is independent of the measured spectrum, this approach allowed for a quick, uniform irradiation with a high foil activity. However, this approach also activated Cave 01 and 02, causing later issues for the PHS measurements.

Each foil used in the measurement of the source or ETA spectra had an analog to correct for both geometry and coincidence summing. When possible, foils of the same elemental composition and size were used, but this was not possible for the HEU and gold (Au)

Table 8.12: Normalization foil characteristics.

Foil	Diameter [cm]	Uncertainty [cm]	Thickness [mm]	Uncertainty [mm]	Weight [g]	Uncertainty [g]	Density [g cm^{-3}]	Elemental Purity
Zr1	49.95	0.05	1.000	0.002	13.217	0.002	6.74	0.9885
Ni1	49.95	0.05	1.040	0.005	17.335	0.002	8.51	0.9898
In1	49.8	0.2	1.050	0.025	14.461	0.002	7.07	0.99999
Au1	-	-	0.028	0.002	0.278	0.002	-	-
Du1	-	-	0.487	0.010	1.559	0.002	-	-
Al1a	50.05	0.10	1.020	0.005	5.324	0.002	2.65	0.99999
Al1b	13.5	0.2	1.13	0.01	0.363	0.002	2.24	-

foils. Foil Al1b (shop aluminum of unknown purity) was used to provide the geometry correction for the HEU foil. A depleted uranium (DU) foil was used for the HEU coincidence summing corrections. The 336 keV line from the In1 foil can be used to determine the Au geometry correction factor, and the Au1 foil can be used to determine the coincidence summing correction factors. The foil characteristics are described in Table 8.12. Au1 and Du1 were both irregularly shaped and of unknown purity. Each foil was counted at 1 cm, 5 cm, and 18 cm from the detector surface.

8.4.2 Source Spectrum Foils

A second foil pack was used to measure the source spectrum through activation analysis and unfolding, as described in Section 7.1 and Section 7.2, respectively. The foil pack was irradiated for 2 hr 11 min 1 sec at $\sim$8.5 μA for a total integrated current of 64.32 mC. The foils were suspended by fishing line in a small pastic bag in Cave 02 at the same location that they would be inside the ETA. This corresponded to a coordinate location of (58.6 cm, 0 cm, 0 cm) measured from the Cave 02 side of the Cave 01/02 wall in the X direction and BLC for the Y and Z directions.

The foil characteristics are described in Table 8.13. The reaction channels considered for this experiment were described in Table 7.1. Each foil was counted at 1 cm until 10,000 counts were achieved in the peaks associated with each reaction channel. For post-irradiation decay purposes, it should be noted that the BCM time stamp is 71 $\pm$ 2 seconds ahead of the GammaVision time stamps.

8.4.3 ETA Spectrum Foils

A third foil pack was used to measure the ETA modified spectrum through activation analysis and unfolding, as described in Section 7.1 and Section 7.2, respectively. The foil pack was irradiated for 19 hr 30 min at $\sim$12.0 μA for a total integrated current of 760.34 mC. The foils were placed in the sample irradiation cavity located in the ETA irradiation drawer shown in

Table 8.13: Source spectrum foil characteristics.

Foil	Diameter [cm]	Uncertainty [cm]	Thickness [mm]	Uncertainty [mm]	Weight [g]	Uncertainty [g]	Density [g cm^{-3}]	Elemental Purity
Zr2	49.90	0.05	1.036	0.002	13.189	0.002	6.51	0.9885
In2	50.15	0.10	1.021	0.005	14.326	0.002	7.10	0.99999
Ni2	49.50	0.10	1.000	0.003	16.934	0.002	8.80	0.9898
Au2	49.35	0.10	0.094	0.003	3.298	0.002	18.34	0.999
Al2	50.00	0.10	1.013	0.003	5.306	0.002	2.67	0.99999

Table 8.14: ETA spectrum foil characteristics.

Foil	Diameter [cm]	Uncertainty [cm]	Thickness [mm]	Uncertainty [mm]	Weight [g]	Uncertainty [g]	Density [g cm^{-3}]	Elemental Purity
Zr3	49.93	0.05	1.037	0.002	13.152	0.002	6.48	0.9885
In3	50.05	0.10	1.026	0.010	14.47	0.002	7.17	0.99999
Ni3	49.85	0.10	1.003	0.003	17.267	0.002	8.82	0.9898
Au3	49.35	0.10	0.100	0.003	3.542	0.002	18.52	0.999
Al3	49.96	0.10	1.010	0.005	5.284	0.002	2.67	0.99999
HEU	12.70	0.05	0.49	0.02	1.167	0.004	18.70	0.9315

Figure 6.15. This corresponded to a coordinate location of (58.6 cm, 0 cm, 0 cm) measured from the Cave 02 side of the Cave 01/02 wall in the X direction and BLC for the Y and Z directions.

The foil characteristics are described in Table 8.14. The reaction channels considered for this experiment were described in Table 7.1. Each foil was counted at 1 cm until 10,000 counts were achieved in the peaks associated with each reaction channel. The HEU foil pack was counted at 1 and 5 cm over the course of two weeks in count increments ranging from 6-24 hours. For post-irradiation decay purposes, it should be noted that the BCM time stamp is 71 $\pm$ 2 sec ahead of the GammaVision time stamps.

8.5 Simulated Results

MCNP simulations of the experimental setup were performed for experiment planning purposes. In future analyses of the experimental data, these modeled results will be used to interpret the data. These models closely represent the final, as-built ETA and experimental configuration. A horizontal slice of the model through BLC is shown in Figure 8.2, and a vertical slice though BLC is shown in Figure 8.5. Both models depict the setup for the PHS measurements. A separate model, without the three EJ-309 detectors, was used for the activation measurements. The full models, including all inputs and outputs, for each set-up are available as described in Appendix B.

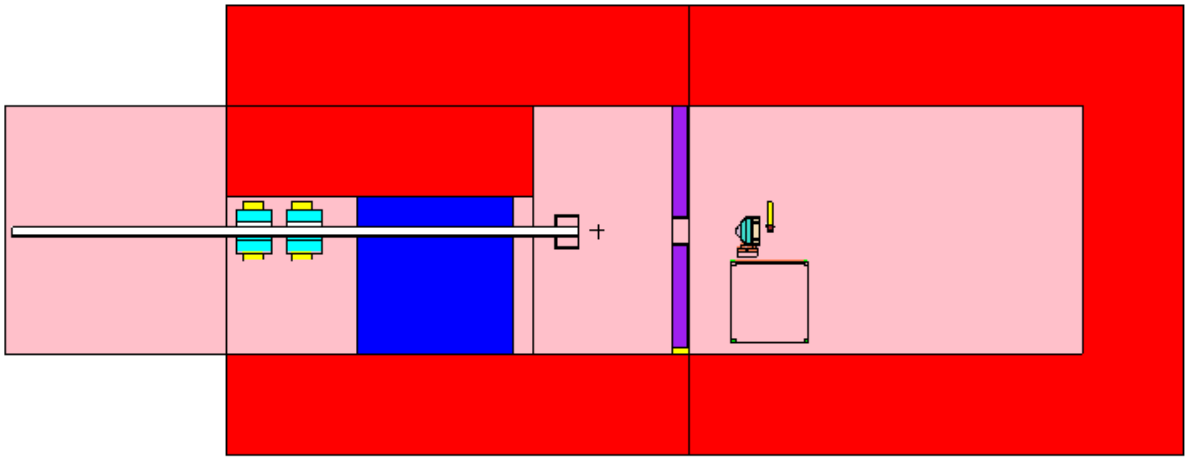

Figure 8.5: Experimental configuration for the PHS measurements. In the figure, concrete walls are red, sandbags are blue, lead walls are purple, and the air is pink.

Given that the ETA was designed for the NIF source spectrum, the ETA modified spectrum using the 88-Inch Cyclotron is not expected to reproduce the TN+PFNS spectrum. The ETA shaped spectrum using the 88-Inch Cyclotron 33 MeV deuteron breakup on Ta source is shown in comparison with the source spectrum in Figure 8.6. While the ETA modified result differs from the desired TN+PFNS, it does exhibit some similarities in that it has a Watt-like portion and a peak near 10 MeV. The thermalization is higher due to the increase in "room return" neutrons.

The activation model was used to determine the activation rates to develop experimental run times and count plans. The simulated results are listed in Table 8.15 for the source spectrum measurements and Table 8.16 for the ETA modified spectrum measurements. The (n,γ) results for the source foil are artificially depressed due to the use of the Meulders spectrum, which does not measure below 2 MeV, as the starting source for the model. The activation rates in Table 8.15 and Table 8.16 do not capture the contributes from other channels to the ^{57}Ni, ^{58}Co, and ^{89}Zr activation products. The results of the HEU foil irradiation with the ETA modified spectrum are shown in Table 8.17. The decreased fluence delivered and lack of radio-chemistry will make it difficult to measure non-peak products with any reasonable statistics.

The modeled source spectrum for the results presented was determined through transport of the Meulders 33 MeV deuteron breakup on Ta spectrum through the Cave 0 geometry shown in Figure 8.2 [141]. The model captures the first five degrees of the source from BLC, and simulations showed that neutrons emitted at angles greater than five degrees from BLC

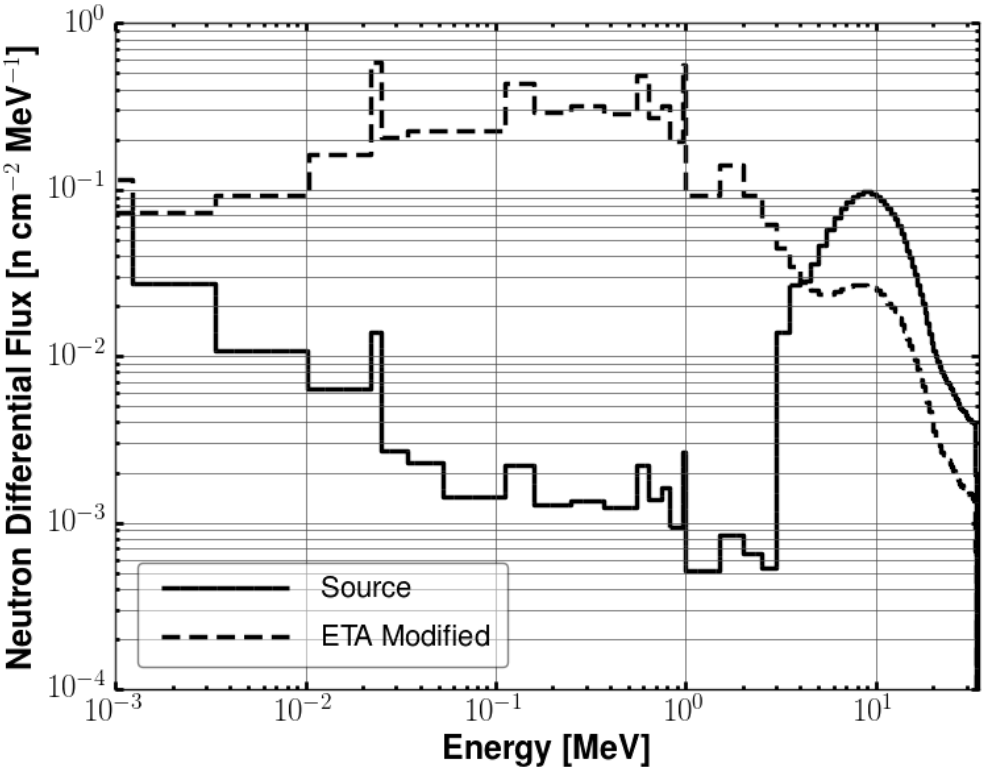

Figure 8.6: Comparison of the initial 33 MeV deuteron breakup on Ta source and the ETA modified spectrum.

Table 8.15: Predicted reactions product yields from foils exposed to 33 MeV deutron breakup on Ta source spectrum with 64.32 mC of integrated current.

Foil	**Reaction**	A_0 **[Bq]**
Aluminum	^{27}Al(n,α)^{27}Mg	261.5 ± 2.5
	^{27}Al(n,p)^{27}Mg	1359.8 ± 11.7
Nickel	^{58}Ni(n,2n)^{57}Ni	22.2 ± 0.3
	^{58}Ni(n,p)^{58}Co	20.1 ± 0.2
Zirconium	^{90}Zr(n,2n)^{89}Zr	76.2 ± 1.1
Indium	^{115}In(n,n')^{115m}In	815.5 ± 6.7
	^{115}In(n,γ)^{116m}In	366.8 ± 4.4
Gold	^{197}Au(n,2n)^{196}Au	31.4 ± 0.3
	^{197}Au(n,γ)^{198}Au	1.5 ± 0.1

Table 8.16: Predicted reactions product yields from foils exposed to the ETA modified 33 MeV deutron breakup on Ta source spectrum with 760.34 mC of integrated current.

Foil	**Reaction**	$\boldsymbol{A_0}$ **[Bq]**
Aluminum	^{27}Al(n,α)^{27}Mg	360.4 ± 1.3
	^{27}Al(n,p)^{27}Mg	311.9 ± 0.9
Nickel	^{58}Ni(n,2n)^{57}Ni	43.7 ± 0.2
	^{58}Ni(n,p)^{58}Co	46.7 ± 0.1
Zirconium	^{90}Zr(n,2n)^{89}Zr	162.0 ± 0.8
Indium	^{115}In(n,n')^{115m}In	1131.2 ± 2.4
	^{115}In(n,γ)^{116m}In	1765.6 ± 3.4
Gold	^{197}Au(n,2n)^{196}Au	62.0 ± 0.2
	^{197}Au(n,γ)^{198}Au	47.6 ± 0.1

Table 8.17: Predicted fission product activity from a 93.15% ^{235}U HEU foil exposed to the ETA modified 33 MeV deutron breakup on Ta source spectrum with 760.34 mC of integrated current.

FP	$\boldsymbol{A_0}$ **[Bq]**
$^{95}_{40}$Zr	0.37 ± 0.01
$^{97}_{40}$Zr	24.32 ± 0.24
$^{111}_{47}$Ag	0.015 ± 0.001
$^{115}_{48}$Cd	0.012 ± 0.001
$^{133}_{53}$I	23.71 ± 0.24
$^{140}_{56}$Ba	0.73 ± 0.01
$^{147}_{60}$Nd	0.36 ± 0.01
$^{151}_{61}$Pm	0.39 ± 0.01
$^{153}_{62}$Sm	0.14 ± 0.01

are negligible given the small solid angle subtended by the ETA. The model assumes no extrapolation of the Meulders spectrum to zero at high or low energies. Finally, the model does not include transport through the target geometry.

The Meulders source spectrum is sufficient for the simulations for experimental planning purposes, but it will be insufficient for comparison with experimental results for several reasons. First, Meulders' measurement does not have error bars. Comparison of other measured deuteron breakup spectra have shown Meulders to be consistently high in the tail of the distribution. Without error bars, it is difficult to quantify experimental and model correlation if Meulders is used as the starting source. Second, Meulders has a minimum measured energy of 2 MeV, thereby producing an artificially depressed flux below 2 MeV in the models. Since the measured PHS data goes down to ∼1 MeV and the activation data to thermal, the 2 MeV source neutron cutoff is insufficient to model these results. Finally, Meulders experimental set-up and target is different than the set-up and target used for these experiments [1] [141].

Alternatively, the Meulders spectra can be used to gain confidence in the PHS and activation measurements of the source spectrum. Once measured, these can be incorporated into the model as the source term and transported through the ETA PHS and activation models to update the ETA results. This effort is underway, but is not complete as of the time of this writing.

[1] The experimental differences could be "reverse-engineered" to modify the spectrum to match this experiment and target if required, but all of the other issues would remain.

Chapter 9

NIF Design of Experiment

No amount of experimentation can ever prove me right; a single experiment can prove me wrong.

- Albert Einstein

This research proposed to address the TNF synthetic debris gap through the development of an experimental ETA platform at NIF. While no NIF experiment was conducted during the course of this research, an experimental plan was developed, coordinated with LLNL, and proposed to the NIF National Security Applications (NSA) call for proposals. This chapter describes the NIF facility and its unique capabilities with respect to this experiment, the proposed experiment configuration, and the modeled results expected from the ETA design developed by Coeus.

9.1 Facility Overview

The bulk of the NIF facility is dedicated to amplifying the seed pulses from a nJ up to a few MJ by the time they reach the NIF target chamber (TC). All 192 beams arriving at the TC are frequency shifted 3ω from infrared to ultraviolet light before arriving at target chamber center (TCC) [123]. The 192 laser beams with a pulse width ranging from $\sim$2 - $\sim$20 nsec are delivered to the $\sim$2 mm target capsule housed inside of a 9.425 x 5.75 mm, high-Z (often gold) hohlraum held cryogenically at 18-20 K located at TCC. The laser drive strikes the hohlraum walls, creating x-rays that compress the target to densities greater than 1000 g cm^{-3} and temperatures approaching 100 million K [96, 123]. This causes the D-T fuel in the target to fuse[1], resulting in the release of 10^{14}-10^{16} neutrons in a pulse that is only tens of picoseconds wide [123]. This intense pulse of neutrons is necessary for time-dependent nuclear effects and reaction histories.

[1]Target compositions and design vary significantly, but the fuel is generally a combination of deuterium and tritium.

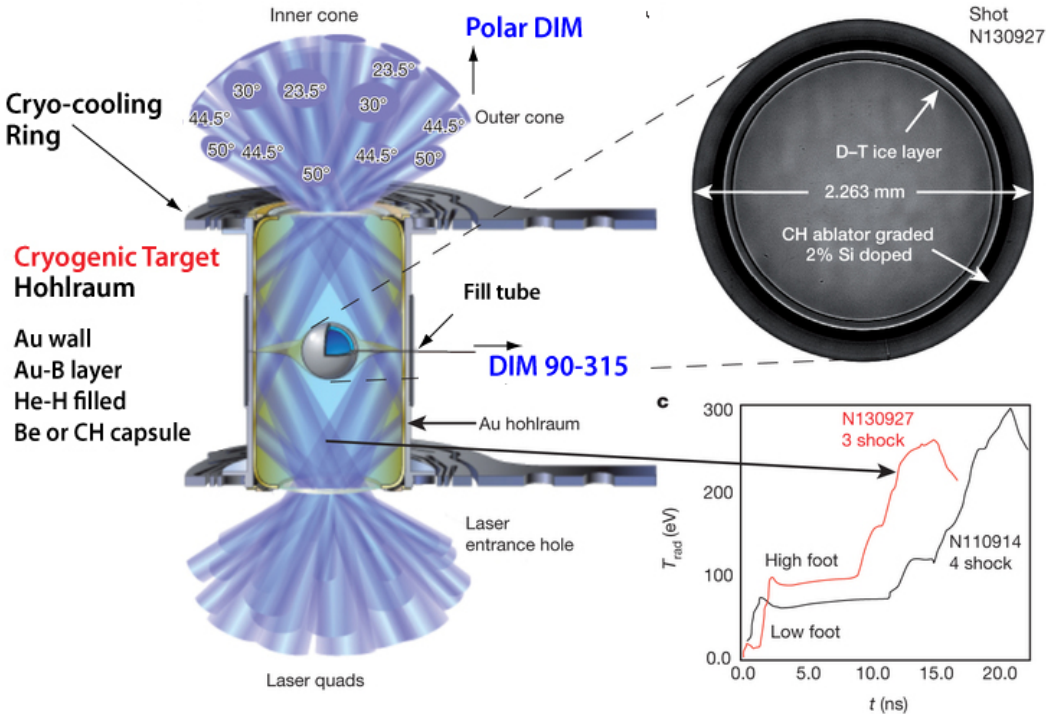

Figure 9.1: NIF holhraum configuration for shot N130927 [96, 123].

Figure 9.1 shows the experimental configuration for NIF shot 130927, one of the shots used to derive the NIF source term for this research. Shown in Figure 9.1 is the hohlraum configuration with the laser entrance holes, the NIF target capsule configuration, comparison of the drive for the high-yield "high foot" campaign vs the previous "low foot" series of shots, and the location of two of the diagnostic instrument manipulators (DIMs) that could be utilized to field the ETA.

While there are several permutations of experimental configurations on NIF, only the representative details of the high yield shots relevant to this research were presented. The highest yield shots as of 2017 were from the the high-foot campaign. Of these, NIF shots 130927 and 140520 were selected as the basis for the NIF spectrum used in this research. Shot 140520 was shown in Figure 2.7 and compared with the desired final TN+PFNS. This figure is repeated in Figure 9.2 for clarity.

For many TN+PFNS applications, including the generation of synthetic debris and FPs, reaction rates and/or products generated in a neutron irradiated sample are dependent on the temporal (for second order reactions or reaction products with short half-lives) as well as the spectral distributions of the source neutrons. For these applications, NIF provides a unique starting source for spectral modification because of the significant fluence of neutrons, $\sim 10^{16}$, delivered in $\sim$200 picoseconds with the hard D-T fusion spectrum shown in Figure 9.2 [96, 123].

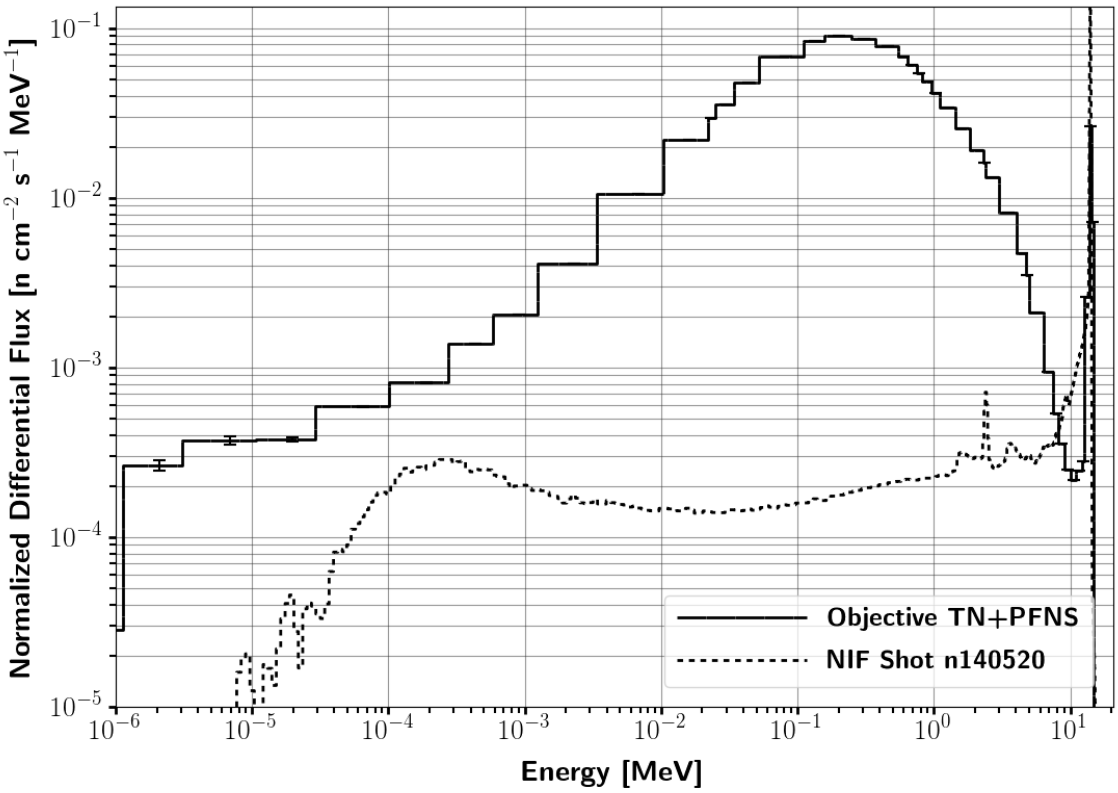

Figure 9.2: Comparison of the normalized NIF Shot 140520 vs the objective TN+PFNS [35].

Other sources with similar spectral characteristics, such as OMEGA, are at least two orders of magnitude lower in total neutron output [33, 73]. Using a source like OMEGA would result in a corresponding ∼two order of magnitude increase in the fissionable foil mass needed to achieve the number of fissions required for radio-chemistry. This mass increase alone would make the experiment un-executable.

Additionally, the D-T fusion end-point energy matches the end-point energy characteristic of the TN+PFNS, thereby allowing for spectral modification techniques to be pursued. This characteristic end-point can also be achieved using other D-T fusion sources, but the down-scatter associated with NIF is significantly lower than comparable sources due to the low mass of the target and hohlraum. The neutrons leaving the hohlraum then encounter a 10 m diameter evacuated TC with 10 cm thick aluminum walls surrounded by 0.3 m of borated concrete, which minimize additional thermalization and "room return" neutrons [123]. Having lower down-scatter and "room return" results in a minimized thermal and epi-thermal background, which allows for spectral shaping and moderation without exceeding the TN+PFNS at the thermal and epi-thermal energies. The D-T fusion end-point energy also eliminates any higher energy neutron component of the spectrum. White neutron sources, such as deuteron breakup at the 88-Inch Cyclotron, will have higher energy components that

can be extremely difficult to remove.

Further, it is not possible to replicate NIF's timescale for the neutron output in combination with the level of neutron fluence at other facilities. For the purposes of the proposed experiment, the NIF source is essentially instantaneous with respect to the creation of fission and/or reaction products. In one pulse, NIF can deliver the number of neutrons required to create enough fission and reaction products for radio-chemistry and to achieve statistically-significant results. For the few pulsed facilities that exist with a spectrum and timing characteristics similar to NIF, such as the OMEGA laser, they lack the required fluence by at least two orders of magnitude. Other continuous or semi-continuous sources, such as cyclotrons, lack a suitable starting neutron spectrum and have a significantly lower flux. Therefore, they require longer irradiations, resulting in competing and alternate in-growth and decay channels.

A final motivation for using NIF is access to world-class radio-chemistry facilities at the same site. This provides a great benefit over other comparable facilities in that the samples can be transported and analyzed in hours instead of days. The short time frame preserves a greater fraction of the fission and reaction products created for analysis, which greatly expands the applications and measurements that can be made for short-lived fission and reaction products.

9.2 Experimental Configuration

This experiment is designed to be executed using existing NIF capabilities and proven shot configurations. In general, the primary facility configuration considerations are related to maximizing the neutron fluence (10^{15} neutrons in 4π minimum) seen by the energy tuning assembly (ETA). The high neutron output is necessary to account for geometric attenuation, out-scattering, and parasitic absorption that will occur in the target chamber (TC), diagnostics instrument manipulator (DIM), and ETA. Lower neutron outputs risk: a) not meeting the minimum number of reactions required for the radio-chemical separations and/or gamma spectroscopy measurements or b) increasing the uncertainty in the fission yields, reaction products, and neutron spectrum measurements, thereby limiting the quality of the data gathered.

Two proposed configurations are described in the following sections. Both are existing NIF capabilities. For simplicity and consistency, the same configuration used in shot Fa_Diag_CSym_HDC_S01 N160831-003 is reffered to as C1. The configuration that is similar to the N160717-001 I_Stag_SymCDT_BigFoot_S02a shot is referred to as C2.

While the ETA experiment could be fielded as a "ride-along", practical considerations make this unlikely for several reasons. First, the experiment requires complete use of the 90-78 DIM as described in Subsection 9.2.3. DIM 90-78 is typically used to field an x-ray imager and pinholes for a separate, higher-fidelity x-ray imager for implosion diagnostics. Substitution of the ETA as a "ride-along" would remove the primary method used to measure the quality of the implosion, a necessary diagnostic for many high yield shots. Second, a

dedicated shot enables priority access to the irradiated foils, something that may conflict with other objectives on a "ride-along" shot. Third, other experiments that contribute additional mass to the chamber or target can result in additional undesirable moderation of the spectrum or a lower fluence of neutrons seen by the ETA. Finally, there is concern about interference on other diagnostics due to the location and size of the ETA (described further in Subsection 9.2.3 and Section 9.3) [99].

9.2.1 Laser Configuration

C1 uses a drive of 192 lasers with a 6.5 ns high density carbon (HDC) subscale symcap pulse shape, 30 kJ/inner beam, 27 kJ/outer beam, and 408 TW total peak power. It uses standard phase plates, and no backlighter beams are required.

C2 uses a drive of 192 lasers with a 6.0-6.5 ns Bigfoot subscale symcap pulse shape, 22.1 kJ/beam, and 6.24 TW peakpower/beam. It uses standard phase plates, and no backlighter beams are required.

9.2.2 Target

C1 uses a gold hohlraum with a 5.75 mm diameter, 10.13 mm length, and a 3.37 mm light entry hole (LEH) diameter. The capsule is a D-T filled, undoped HDC with a 80 μm ablator thickness.

C2 uses a gold hohlraum with a 5.40 mm diameter, 10.13 mm length, and a 3.45 mm light entry hole (LEH) diameter. The capsule is a D-T filled, Tungsten-doped HDC with a 64 μm ablator thickness.

9.2.3 Primary Diagnostics

ETA is designed to be fielded as a snout replacement for a diagnostic load package (DLP) mounted on the 90-78 DIM. The 90-78 DIM is required as it provides the closest possible approach to target chamber center (TCC) while maintaining the beam and TARPOS/CRYO-TARPOS clearances. A close approach to TCC is necessary to maximize the neutron fluence seen by the experiment and reduce the capsule neutron output required[2]. Initial calculations show that the tip of the ETA can be placed at $\sim$ 75 mm from TCC [99]. The remaining requirements and experimental design are based on this assumption coupled with a 10^{15} neutron output.

The ETA is a passive standalone package and requires no power or modifications to existing diagnostic capabilities at NIF. However, the experiment will need the full neutron time of flight (nTOF) suite, Nuclear Activation Diagnostic System (NADS), Neutron Imaging System (NIS), and Magnetic Recoil Spectrometer (MRS) to measure the source term seen

[2]Refer to Subsection 2.3.1 for the full analysis of the DIMs and the competing factors.

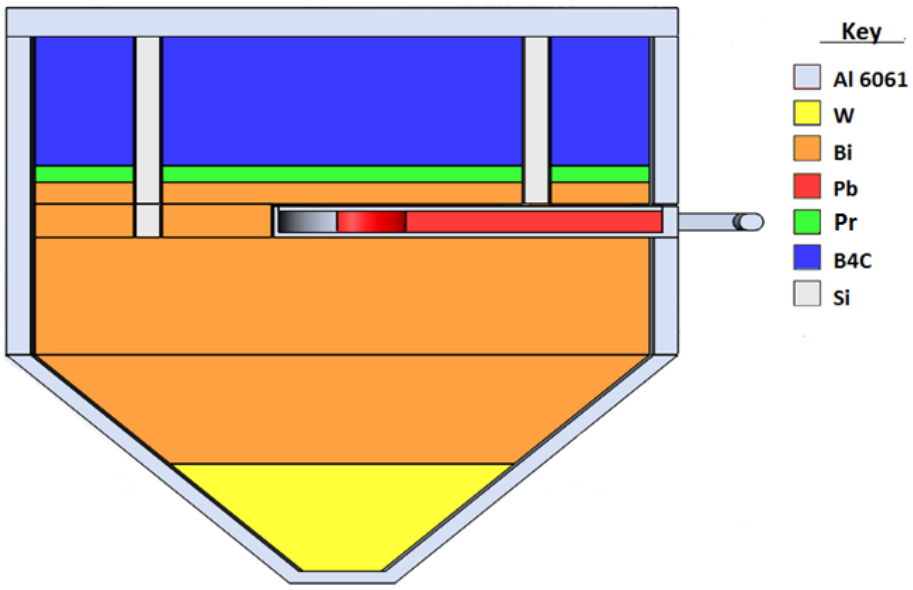

Figure 9.3: NIF ETA design.

by the ETA. Verification of the source term is required to calibrate the expected ETA output as this will vary based on the input spectrum.

No on-line DIM diagnostics are required for this experiment, but the experiment will require use of the radio-chemistry and gamma spectroscopy facilities for post-shot analysis. The facilities will be used to measure the neutron spectrum obtained in the ETA through fission and reaction product analysis. Access to the removable foil pack is required within a few hours to measure short-lived fission and reaction products.

9.3 Expected Results

The goal of the ETA is to reproduce the TN+PFNS across the volume of a set of test foils. The irradiated foils will serve as an indirect measurement of the spectrum obtained by analyzing the fission and reaction products generated. While the analysis of the foils is crucial to establishing the spectral shaping performance, it also establishes a capability of interest to multiple national security communities.

The calculated neutron spectrum achieved across the set of foils for the ETA design and a comparison with the objective TN+PFNS are presented in Section 6.3, and they are reproduced in Figure 9.3 and Figure 9.4 for clarity. All uncertainties in Figure 9.4 and Table 6.8 are 1σ statistical uncertainties.

Post irradiation, the 1.2 g highly-enriched uranium (HEU) foil will be used to study the fission products generated from exposure to the TN+PFNS. From MCNP simulations, the ETA design achieves 1.6×10^9 fissions in the HEU foil assuming 10^{15} source neutrons. The

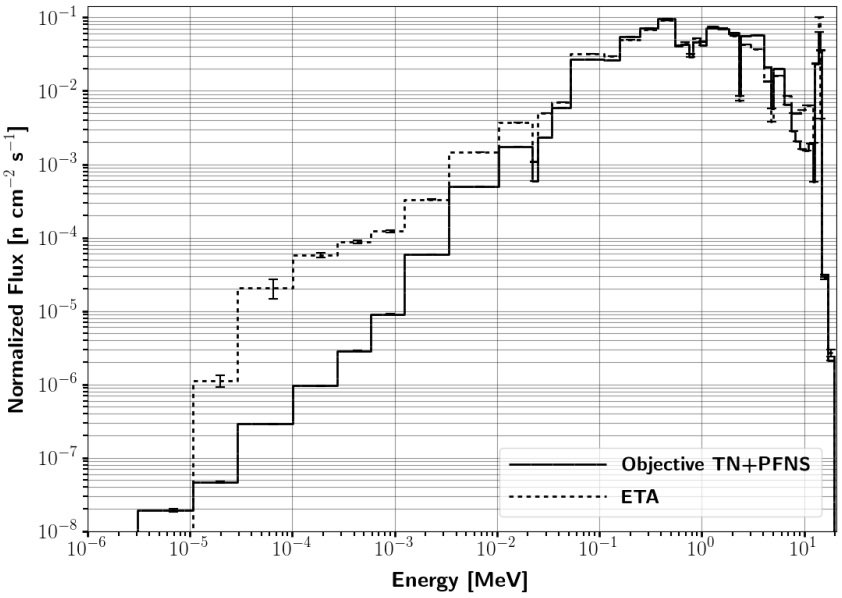

Figure 9.4: Comparison of the ETA-produced spectrum as modeled in MCNP and the objective TN+PFNS.

number of fissions in the foil scales 1:1 with any changes in the source neutrons, and scales ∼1:1 for moderate changes in the fissile mass. The fission products considered, along with *a priori* GEF and Nagy calculations for the expected experimental results, are displayed in Table 9.1. The experimentally measured fission product yields of the isotopes shown in Table 9.1, and the four or six factor fission splits generated from this data, can be compared to the modeled predictions to determine the neutron spectrum seen by the HEU foil [155, 185].

Additionally, the foils shown in Table 9.2 can be used to measure the experimental neutron spectrum through forward fits and neutron spectrum unfolding using STAYSL [85]. Table 9.2 shows the modeled reaction rates, and Figure 9.5 shows the STAYSL spectrum unfold in comparison to the ETA modeled TN+PFNS. In Figure 9.5 the ETA MCNP modeled spectrum is directly underneath the STAYSL unfold.

While the results presented here are all modeled, they demonstrate that sufficient information can be obtained from the experiment to measure the ETA produced TN+PFNS. The modeled results give confidence in the likelihood for success of this proposed experimental technique, but they are not an explicit guarantee of success. Finally, it is important to note that none of these measurements provide unique solutions, and it is only in the combination of multiple independent techniques that confidence in the spectrum and concept validation can be achieved.

Table 9.1: Nagy and GEF based fission product cumulative yield ($f_{cum}(A, Z)$) estimates of select FPs from a 93.15% ^{235}U HEU foil exposed to the TN+PFNS achieved by the ETA [155, 185].

FP	**Nagy**	**GEF**
$^{95}_{40}$Zr	6.15 ± 0.09	6.47 ± 0.30
$^{97}_{40}$Zr	5.74 ± 0.09	6.46 ± 0.28
$^{111}_{47}$Ag	0.26 ± 0.01	0.22 ± 0.12
$^{115}_{48}$Cd	0.26 ± 0.01	0.26 ± 0.16
$^{133}_{53}$I	6.38 ± 0.14	6.01 ± 0.37
$^{140}_{56}$Ba	5.68 ± 0.07	5.41 ± 0.28
$^{147}_{60}$Nd	2.11 ± 0.03	1.99 ± 0.23
$^{151}_{61}$Pm	0.47 ± 0.02	0.46 ± 0.10
$^{153}_{62}$Sm	0.18 ± 0.01	0.17 ± 0.05

Table 9.2: Predicted reactions product activities from foils exposed to ETA generated TN+PFNS.

Foil	**Reaction**	A_0 **[Bq]**
Zirconium	^{90}Zr(n,2n)^{89}Zr	1724
Nickel	^{58}Ni(n,2n)^{57}Ni	398
	^{58}Ni(n,p)^{58}Co	330
Indium	^{115}In(n,n')^{115m}In	6.97E4
	^{115}In(n,g)^{116m}In	6.18E+5
Gold	^{197}Au(n,2n)^{196}Au	3547
	^{197}Au(n,g)^{198}Au	578
Aluminum	^{27}Al(n,α)^{27}Mg	4224
	^{27}Al(n,p)^{196}Au	31.3

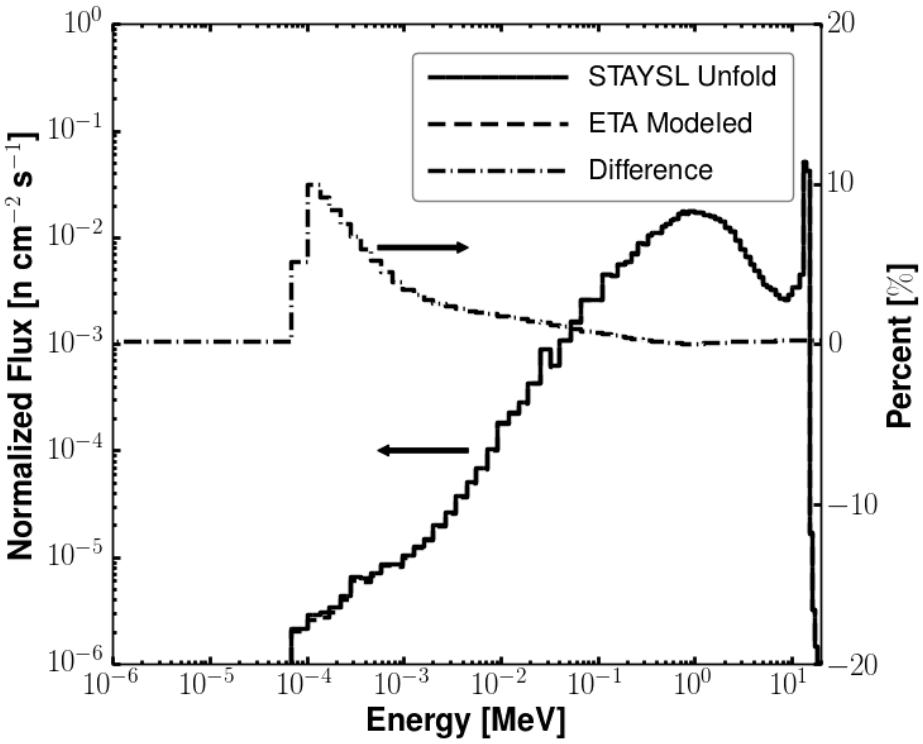

Figure 9.5: Comparison of the unfolded ETA-produced spectrum using STAYSL and the MCNP modeled objective TN+PFNS. The STAYSL unfolded spectrum is mostly beneath and indistinguishable from the ETA Modeled spectrum.

9.4 NIF Feasibility Scoping Study

A scoping study was performed by LLNL to assess the feasibility of fielding the ETA on NIF. The scoping study had the following key findings [99]:

1. The dimensions (280 mm outer diameter), shape, and weight ($\sim$ 71 kg) for the design shown in Figure 9.3 have been determined to be compatible with current laser and TARPOS/Cryo-TARPOS stay-out requirements and DLP load limits.

2. Activation of the ETA was found to produce a exposure rate of $<$ 5 mR/hr at 1 ft after 1 hour from a 10^{15} shot, which is within NIF guidelines.

3. The use of the TOAD and 1.2 g HEU foil accelerates the FP inventory approval process given that it is similar to previous experiments.

4. The materials and machining processes are expected to pass NIF cleanliness standards.

5. No insurmountable hazardous material issues are foreseen; lead may have to be encapsulated.

6. The cost should be ∼$230k to field the ETA experiment. Approximately $100k is needed for the radio-chemistry, ∼$130k is needed for engineering analysis, deployment, and commissioning. The ETA, ∼$60k, has already been procured.

The study found that the proposed ETA design and overall experiment were "low risk," have "no show stoppers," and have a "reasonable cost" [99]. If necessary, further refinements of this design, primarily the mechanical components and mounting interface of the case, would be performed to fully adapt the design for mounting on a DLP.

Chapter 10

Summary

If you optimize everything you will always be unhappy.

- Donald Ervin Knuth

The goal of this research was to develop a platform that will enable neutron irradiation with modified neutron spectra. Specifically, the research targeted the development of a thermonuclear plus prompt fission neutron spectrum (TN+PFNS) that mimics sources of interest to national security applications, including the production of synthetic debris and fission products (FPs) for technical nuclear forensics (TNF) applications. A customized energy tuning assembly (ETA) was designed and constructed to spectrally shape the National Ignition Facility (NIF) neutron spectrum to match a TN+PFNS. Initial validation tests of the ETA design were conducted at the Lawrence Berkeley National Laboratory (LBNL) 88-Inch Cyclotron.

To modify the NIF characteristic neutron spectrum to the objective TN+PFNS, neutron spectral shaping techniques were used. Most previous research utilizing spectral shaping targeted large, gross changes to a spectrum such as cuts using neutron filters or thermalization using low-Z moderators. This research leveraged and expanded on the concept of beam shaping assemblies (BSAs) which used layered combinations of materials to develop nearly mono-energetic 10 keV neutrons for boron neutron capture therapy (BNCT).

The primary limitation with BSA design was the typical labor intensive, parametric approach that dominated the literature. Similar to the BNCT application, many different combinations of source and objective spectra could be imagined for TNF or other national security applications. Therefore, to maximize the utility of this research, a parametric point design approach was discarded in favor of formal optimization techniques.

However, the ETA design problem is complex, and no directly applicable open-source optimization algorithm was found[1]. To this end, the Gnowee algorithm was developed for rapid convergence to nearly globally optimum solutions for complex, constrained engineering

[1]There may be commercial solutions that exist behind pay-walls. However, even those would require some level of modification, which may not be possible, to work with radiation transport codes.

problems with mixed-integer and combinatorial design vectors and high-cost, noisy, discontinuous, black box objective function evaluations. Gnowee uses a hybrid metaheuristic framework based on a set of diverse, robust heuristics that appropriately balance diversification and intensification strategies across a wide range of optimization problems. Comparisons between Gnowee and several well-established metaheuristic algorithms are made for a set of continuous, mixed-integer, and combinatorial benchmarks. These results demonstrated Gnoweee to have superior flexibility and convergence characteristics over a wide range of design spaces.

Gnowee provided the optimization engine that drives the ETA assembly design code, Coeus. Coeus builds and performs radiation transport on ETA designs based on Gnowee permutations of design space variables to evaluate ETA design performance against the TN+PFNS objective spectrum. The radiation transport is conducted with a hybrid approach that uses ADVANTG to perform adjoint Denovo deterministic transport calculations to develop weight windows for speeding up stochastic MCNP transport calculations. Coeus implements two levels of parallelization by taking advantage of the "embarrassingly parallel" nature of metaheuristic optimization and Monte-Carlo methods. Coeus has been implemented on Savio, UC-Berkeley's HPC cluster.

Coeus was then used to generate an ETA design for the TNF synthetic debris application. This design was modified to reduce cost and improve ease of manufacturing, resulting in a 3.9% reduction in overall performance. This process was aided by the numerous alternative designs considered and carried forward by the Coeus population based optimization process. The finalized deign was able to closely match both the objective TN+PFNS and the objective FP distributions as modeled using the GEF and Nagy models while also meeting all of the design constraints. This design was built by American Elements and delivered March of 2017.

Experimental validation tests of the NIF TNF ETA design were carried out at the 88-Inch Cyclotron. While the starting source spectrum precludes the generation of a TN+PFNS spectrum using this ETA design at the 88-Inch Cyclotron, experimental and process validation could be performed to pave the way for a future integral test on NIF. The 88-Inch Cyclotron experiments took two full sets of pulse-amplitude-time and full waveform pulse height spectroscopy data to measure the source spectrum, the ETA modified field, and the ETA modified field as the ETA was assembled component-by-component. Additionally, foil activation data were taken to measure the source spectrum and full ETA modified spectrum. This data was not fully analyzed as of the time of this writing.

Finally, an experimental plan and anticipated results for a future NIF shot were presented. The proposed experimental plan and ETA design have undergone a scoping study at Lawrence Livermore National Laboratory to assess the feasibility and cost of running the experiment at NIF. The study found that the proposed ETA design and overall experiment were "low risk," have "no show stoppers," and have a "reasonable cost."

The capabilities developed in this research are unique on many levels. From an applications perspective, the ETA design proposed represents a massive improvement in the state-of-the-art for synthetic fission product generation. Coupled with research into develop-

ing synthetic debris matrices, the ETA would be able to generate synthetic debris that can be customized to the weapon design and employment scenario. At the minimum, this would allow "stress testing" of the TNF system and training of a new generation of TNF experts. At the other extreme, the ETA concept could enable development of new TNF markers and techniques, improve nuclear weapon effects certification processes while lowering testing and systems procurement costs, and aid in science-based stockpile stewardship.

While out-of-sight and out-of-mind for the general public, each of these areas play fundamental roles that underpin U.S. national security and other tools of statecraft. In the 2010 Nuclear Posture Review, President Obama concluded that nuclear terrorism was the top objective for U.S. nuclear weapon policies and posture, and it is unlikely that President Trump will come to significantly different conclusions. TNF and post-detonation attribution are key components to counter-proliferation efforts, especially with respect to state-sponsored nuclear terrorism. Similarly, nuclear weapon effects hardness requirements and science-based stockpile stewardship are means to enhance the credibility of the effectiveness of the nuclear deterrent. Capabilities, such as the ETA, which enhance credibility and post-detonation forensics strengthen deterrence and counter-proliferation efforts, even if the effects cannot be measured directly.

However, the larger potential lies within the methods used to generate the ETA design, Gnowee and Coeus. Gnowee and, in principal, Coeus are not limited to the narrow scope of application pursued in this research. Gnowee is fully implemented as a general purpose optimization algorithm and can be applied to any problem whose objective function can be assessed analytically. Coeus, by design, could also be applied to any nuclear engineering optimization problem, but the implementation is currently limited by geometry. Removing the ETA specific constructs[2] would allow Coeus to consider optimized design for BNCT BSAs, radiation shielding design, radiation converters, medical isotope production targets, fusion blankets, detector networks, detector imaging masks, reactor design, and more. As discussed further in Appendix A, efforts are underway to remove these limitations to expand the applicability of Coeus to other applications within the nuclear engineering community.

[2]Some problems, such as BNCT or medical isotope production targets, could be considered even with current limitations.

Appendix A

Future Work

Always leave them wanting more.

- P. T. Barnum

Much future work was highlighted throughout this dissertation. This appendix is an attempt to consolidate these items in a semi-coherent fashion and expound upon them where necessary. This is by no means an all-inclusive list, and it is primarily only focused on immediate research efforts for Gnowee and Coeus, and the validation experiments are discussed in detail.

A.1 Gnowee

If anything that was done in this research could be considered "complete," Gnowee is probably that item. The code base and documentation are in a documented and usable condition, and the interfaces allow for adoption into other frameworks. However, there are several items that could be done to improve the methodology[1].

One of the issues in developing metaheuristic algorithms identified by Sorensen is the need for a framework to optimize the selection of different heuristics[2]. While the full implementation of Sorensen's vision is an ambitious undertaking, a basic implementation within the construct of Gnowee and the methods used for parameter selection is easily within reach. To accomplish this, a module needs to be added to track the efficacy of each heuristic. This can enhance Gnowee's flexibility and performance by providing feedback suggesting alterations to Gnowee's parameters for a given problem.

[1]These, along with a few extra, are included on the issues tab of the code GitHub repo at `https://github.com/SlaybaughLab/Gnowee/issues/5`.

[2]See Section 5.4 for more details and a full listing of areas of growth for metaheuristic algorithm development.

When Gnowee does not perform well[3], the primary reason is a loss of diversity in the population. Currently, Gnowee starts with a diverse initial population through latin-hypercube or nearly orthogonal latin-hypercube sampling. An attempt to maintain this diversity is inherent in the heuristics chosen and their implementation into Gnowee's operators. However, Gnowee does not employ methods to track or enforce diversity. Implementing an "affirmative action" algorithm would improve Gnowee's performance in the cases where diversity loss is prevalent due to the structural confines of the problem.

Gnowee itself runs very quickly, but it was developed with the intention of integration into frameworks to solve optimization problems containing computationally expensive objective and/or constraint function evaluations. Since computers crash and engineers make mistakes, it would be beneficial to have a restart capability whereby a future run could utilize information from a previous one. This could take many forms, but the most straightforward is to save the population state for pre-defined checkpoint intervals and the current population. A module could be added to Gnowee to save the checkpoints and initialize a seed population for a new run based on a previous checkpoint and user specifications.

Gnowee currently has a "once in, once out" interface. This requires the bulk of the main program code to be duplicated when incorporating Gnowee into another framework, such as Coeus. Development of a "in-n-out" interface would streamline the integration of Gnowee into other optimization and design frameworks. Each Gnowee operator is its own function within the GnoweeHeuristics class, so the basic structure exists to implement this interface.

Finally, Gnowee is a single-objective optimization code. Modification of Gnowee to a multi-objective function algorithm would benefit many applications.

A.2 Coeus

Unlike Gnowee, Coeus has many items that could be updated to improve its usability and applicability to problems outside of ETA design (or problems with similar geometries). The list of improvement tasks for Coeus is, as of this writing, hosted on Asana but will be moved to the GitHub repo in the near future. For the purposes of this Appendix, only the major changes are highlighted.

Currently, a new user input method is being developed. The proposed method uses a modified MCNP input deck as the primary user input definition for Coeus. In principal, this approach could be expanded to other transport codes to allow for their adoption into Coeus. It also improves usability by mimicking input formats familiar to a large segment of potential users. More importantly, this approach solves several of the primary issues with the current version of Coeus.

First, this approach allows the geometry to be made more general. Currently, the geometry has flexibility in terms of dimensions, but the user inputs limit the choice to a conical and cylindrical geometry that was used for the NIF ETA. Fundamentally, there is no reason

[3]See Subsection 6.1.5 for a full description of the benchmark problems and comparisons with other well-established metaheuristic algorithms.

for this to be necessary, and allowing for full definition of any geometry within the confines of the radiation transport code itself is a smart way to go. Second, Coeus currently uses PyNE to process material definitions and provide a basic material library. This is a cumbersome dependency for this limited benefit. By allowing user specification within the transport code input, supplemented by a library of basic materials provided with Coeus, this dependency can be removed. Finally, the tally specifications and corresponding tie to the objective and constraint functions are limited. The use of the radiation transport input allows for full tally specification for any possible design constraints and objective functions.

Further, a new class of constraint and objective functions is being developed that allows for incorporation of user defined functions and methods. The class for each allows the definition of one or more tallies to be associated with each constraint and objective function. The updated constraint and objective classes inherent from the Gnowee classes that perform the same basic functions, and benefit from the tally flexibility allowed by the proposed modified MCNP deck user input method.

In keeping with the same design philosophy, the user input file for ADVANTG should be migrated to an ADVANTG-style format. This will allow for a wider range of ADVANTG options to be selected while streamlining the user input process. Similar to the MCNP inputs, modifications to the standard format will need to be made to define variables used to adaptively modify the mesh used to discretize the geometry for the deterministic transport.

Additionally, the efficiency of the ADVANTG-generated weight windows can be improved by the addition of a module that tracks the suitability of the weight windows to the generated designs. This would enable the calculation of ADVANTG weight windows to automatically change from once-per-generation to once-per-evaluation for very dynamic problems where the weight windows rapidly become non-ideal. In the cases of dynamic changes, the once-per-generation approach can result in low fitness solutions being assessed as high fitness due to poor statistics. Unless this happens many times, Coeus will still develop valid solutions, but it will also result in many wasted function evaluations while Coeus attempts to improve upon an artificially inflated solution.

Initial development included a test suite that covered every function in the code that was used to perform this research. However, subsequent development has both failed to include tests and neglected to update the test suite. The current test functions need to be revisited in the context of the Coeus algorithm changes, and new functions need to be added where appropriate.

Finally, Coeus could benefit from the addition of a make file. While not overly complicated, Coeus currently depends on other non-standard packages. Adding a make file would make it easier and more repeatable to use the software by building the dependencies and adding the appropriate environment variables.

A.3 Validation Experiments

Two sets of validation experiments were proposed for the 88-Inch Cyclotron and NIF. The 88-Inch Cyclotron experiments were successfully completed as of this writing. However, very little of the data has been analyzed, and none of it has been analyzed fully. This represents a fantastic research opportunity as there are several complete sets of foil activation, PHS, and HEU activation data.

The analyzed data can be compared with simulated results to determine the ability to model ETA performance. The initial models have been developed, but updates need to be made to fully propagate nuclear data uncertainties. This can be done within the current MCNP models, but a better approach is to use Mercury and the LLNL tools that have been developed to do so. Since partial ETA data sets were collected, the models can be used to gain insight into nuclear data issues where the model diverges from ETA performance.

Analysis of the 88-Inch Cyclotron experiment data is also crucial as a development step for a NIF integral test and the generation of synthetic fission products. The propagation of nuclear data uncertainties into the modeled NIF results would also be beneficial and worthwhile.

Appendix B

A Nod to Reproducible Research

> *The success and credibility of science are anchored in the willingness of scientists to independent testing and replication by other scientists. This requires the complete and open exchange of data, procedures, and materials.*
>
> - American Physical Society

Reproducible, open-source science is a worthwhile endeavor, and this appendix documents the steps taken along that path for this research. While not perfect, these principles provided a strong foundation for a bulk of the data, code, and analysis performed in this research. Links are provided to the location for each of the repositories, and a brief description is provided:

- **Gnowee:** All of the Gnowee source code, documentation, examples, benchmark results, and ongoing development can be found at: `https://github.com/SlaybaughLab/Gnowee`. Gnowee version 1.1 is the release that is current as of the writing of this dissertation.
- **Coeus:** All of the Coeus code, inputs, and documentation can be found at: `https://github.com/SlaybaughLab/Coeus`. This repository does not currently contain a list of ongoing and future work but will in the future once migrated from Asana. Coeus version 0.1 is the release that was used to design the ETA described in this dissertation. Coeus version 1.0 is the release that is current as of the writing of this dissertation.
- **ETA Design:** All of the information pertaining to the final ETA design is located at: `https://github.com/SlaybaughLab/Gnowee`. This repository contains the Coeus inputs and outputs for the optimization run and the series of modifications made for cost and manufacturability. It also contains the as-contructed purchase information, elemental analysis, CAD models, MCNP models, and pictures of final product.

- **88-Inch Cyclotron Experimental Data:** Most of the data for the 88-Inch Cyclotron experiments is located at: `https://github.com/SlaybaughLab/88_Data`. This repository is broken into experimental data and simulations of each experiment. The simulations and experiment directory are further divided into the activation and pulse height data. All of the activation data are stored in the repository, but the raw data files from the PHS experiments are not due to their size, and only the synthesized results and ancillary data files are available.
- **NIF Experiment Data:** The ETA scoping study results and NIF related simulations are located at: `https://github.com/jamesbevins/NIF_ETA_Experiment`.
- **Python Support Scripts:** A library of python support scripts used to perform various aspects of the analyses conducted in this research are located at: `https://github.com/jamesbevins/PyScripts`.

Bibliography

[1] 111th Congress. *Nuclear Forensics and Attribution Act*. 2010.

[2] Petter Abrahamsen and Fred Espen Benth. "Kriging with Inequality Constraints". In: 33.6 (2001), pp. 719–744.

[3] M. Adib and M. Kilany. "On the use of Bismuth as a Neutron Filter". In: *Radiation Physics and Chemistry* 66.2 (2003), pp. 81–88.

[4] Shamim Akhtar, Kang Tai, and Tapabrata Ray. "A Socio-Behavioural Simulation Model for Engineering Design Optimization". In: *Engineering Optimization* 34.4 (2002), pp. 341–354.

[5] American Society for Testing and Materials International. "Standard Guide for Application of Neutron Spectrum Adjustment Methods in Reactor Surveillance". In: *ASTM E944-08* (2008).

[6] M Asnal, T Liamsuwan, and T Onjun. "An Evaluation on the Design of Beam Shaping Assembly Based on the D-T reaction for BNCT". In: *Journal of Physics: Conference Series* 611 (2015).

[7] M. D. Aspinall et al. "Verification of the Digital Discrimination of Neutrons and Gamma Rays using Pulse Gradient Analysis by Digital Measurement of Time of Flight". In: *Nuclear Instruments and Methods in Physics Research, Section A* 583.2-3 (2007), pp. 432–438.

[8] M. Avrigeanu and A. M. Moro. "Improved Deuteron Elastic Breakup Energy Dependence via the Continuum-Discretized Coupled-channels Method". In: *Physical Review C - Nuclear Physics* 82.3 (2010), pp. 1–4.

[9] M Aziz et al. "Improved Formula for Prompt Fision Neutron Spectrum". In: *Journal of Nuclear and Radiation Physics* 6.1 (2011), pp. 31–41.

[10] Thomas Bäck and Hans-Paul Schwefel. "An Overview of Evolutionary Algorithms for Parameter Optimization". In: *Evolutionary Computation* 1.1 (1993), pp. 1–23.

[11] D. E. Bartine et al. "Production and Testing of the DNA Few-Group Coupled Neutron Gamma Cross-Section Library". In: *ORNL/TM-4840* (1977).

[12] E. Bavarnegin, Y. Kasesaz, and F. M. Wagner. "Neutron Beams Implemented at Nuclear Research Reactors for BNCT". In: *Journal of Instrumentation* 12.05 (2017).

[13] Pietro Belotti et al. “Mixed-Integer Nonlinear Optimization”. In: *Acta Numerica* 22 (2013), pp. 1–131.

[14] Lee Bernstein et al. *Nuclear Data Needs and Capabilities for Applications*. 2016.

[15] Abigail A. Bickley et al. “Design and testing of a boron carbide based neutron spectrometer for homeland security applications”. In: *Abstracts Of Papers Of The American Chemical Society*. Washington, DC: American Chemical Society, 2011.

[16] J. B. Birks. *The Theory and Practice of Scintillation Counting*. Oxford: Pergamon Press, 1964.

[17] D L Bleuel. “Determination and Production of an Optical Neutron Energy Spectrum for Boron Neutron Capture Therapy”. PhD thesis. University of California Berkeley, 2003.

[18] D L Bleuel et al. “Designing Accelerator-Based Epithermal Neutron Beams for Boron Neutron Capture Therapy.” In: *Medical Physics* 25.9 (1998), pp. 1725–1734.

[19] Darren Bleuel. “Neutron Sources”. In: *Workshop on Nuclear Data Needs and Capabilities for Applications*. Berkeley, CA, 2015.

[20] Niels Bohr and John Archibald Wheeler. “Mechanism of Nuclear Fission”. In: *Physical Review* 56 (1939), pp. 426–450.

[21] Pierre Bonami, Mustafa Kilinç, and Jeff Linderoth. “Algorithms and Software for Convex Mixed Integer Nonlinear Programs”. In: *Mixed Integer Nonlinear Programming*. Ed. by J. Lee and S. Leyffer. New York: Springer, 2012, pp. 1–39.

[22] T. W. Bonner and L. M. Mott-Smith. “The Energy Spectra of the Neutrons from the Disintegration of Flourine, Boron, and Beryllium by Alpha-Particles”. In: *Physical* 46 (1934), pp. 258–268.

[23] Andrew J. Booker et al. “A Rigorous Framework for Optimization of Expensive Functions by Surrogates”. In: *Structural and Multidisciplinary Optimization* 17.1 (1998).

[24] J S Brenizer et al. “Development of a New Electronic Neutron Imaging System”. In: *Nuclear Instruments and Methods in Physics Research A* 424 (1999), pp. 9–14.

[25] E. Browne and J. K. Tuli. “Nuclear Data Sheets for A = 137”. In: *Nuclear Data Sheets* 108.10 (2007), pp. 2173–2318.

[26] Samuel Burer and Adam N. Letchford. “Non-Convex Mixed-Integer Nonlinear Pogramming: A Survey”. In: *Surveys in Operations Research and Management Science* 17.2 (2012), pp. 97–106.

[27] A. A. Burlon et al. “Optimization of a Neutron Production Target and a Beam Shaping Assembly Based on the 7Li(p,n)7Be Reaction for BNCT”. In: *Nuclear Instruments and Methods in Physics Research, Section B: Beam Interactions with Materials and Atoms* 229.1 (2005), pp. 144–156.

[28] S Cabral et al. “Neutron Production from the Deuteron Breakup Reaction on Deuterium”. In: *Nuclear Science and Engineering* 106 (1990), pp. 308–317.

[29] CAEN. *DPP-DSP User Manual EM2580 rev8*. 2016. DOI: 10.1049/esn.1986.0048. URL: http://link.aip.org/link/ESNWDY/v1986/i2/p32/s1%7B%5C&%7DAgg=doi.

[30] Leticia C. Cagnina, Susana C. Esquivel, and Carlos A. Coello Coello. “Solving Engineering Optimization Problems with the Simple Constrained Particle Swarm Optimizer”. In: *Informatica (Ljubljana)* 32.3 (2008), pp. 319–326.

[31] M. E. Capoulat, D. M. Minsky, and A. J. Kreiner. “Computational Assessment of Deep-Seated Tumor Treatment Capability of the 9Be(d,n)10B Reaction for Accelerator-Based Boron Neutron Capture Therapy (AB-BNCT)”. In: *Physica Medica* 30.2 (2014), pp. 133–146.

[32] B. V. Carlson, R. Capote, and M. Sin. “Elastic and Inelastic Breakup of Deuterons with Energy Below 100 MeV”. In: 163.1 (2015), pp. 163–169.

[33] D T Casey et al. “Measuring the Absolute Deuterium-Tritium Neutron Yield Using the Magnetic Recoil Spectrometer at OMEGA and the NIF.” In: *The Review of Scientific Instruments* 83.10 (2012), p. 10D912. ISSN: 1089-7623. DOI: 10.1063/1.4738657. URL: http://www.ncbi.nlm.nih.gov/pubmed/23126915.

[34] M Cavazzuti. *Optimization Methods: From Theory to Design*. Berlin: Springer, 2013.

[35] Charlie Cerjan. “NIF Shot 120405”. In: *Personal Correspondence 29 April* (2015).

[36] J. Chadwick. “The Existence of a Neutron”. In: *Proceedings of the Royal Society of London, Series A* 136.830 (1932), pp. 692–708.

[37] J Chadwick and M Goldhaber. “Disintegration by Slow Neutrons”. In: *Mathematical Proceedings of the Cambridge Philosophical Society* 31.4 (1935), pp. 612–616.

[38] M B Chadwick et al. “ENDF/B-VII.1 Nuclear Data for Science and Technology: Cross Sections, Covariances , Fission Product Yield”. In: 112.12 (2011), pp. 2887–2996.

[39] Pramoth Chandrikamohan and Timothy A Devol. “Comparison of Pulse Shape Discrimination Methods for Phoswich and CsI:Tl Detectors”. In: *IEEE Transactions on Nuclear Science* 54.2 (2007), pp. 398–403.

[40] T. C. Chapman et al. “Fission Product Yields from 6-9 MeV Neutron-Induced Fission of U235 and U238”. In: *Physical Review C* 17.3 (1978), pp. 1089–1097.

[41] YongHao Chen et al. “Unfolding the Fast Neutron Spectra of a BC501A Liquid Scintillation Detector using GRAVEL Method”. In: *Science China: Physics, Mechanics and Astronomy* 57.10 (2014), pp. 1885–1890.

[42] N Chrysanthopoulou et al. “Compilation of Existing Neutron Screen Technology”. In: *Science and Technology of Nuclear Installations* (2014).

[43] M Cinausero et al. “A Proton Recoil Telescope for Neutron Spectroscopy”. In: *Journal of Physics: Conference Series* 41 (2006), pp. 219–224.

[44] Thomas M Cioppa and Thomas W Lucas. "Efficient Nearly Orthogonal and Space-Filling Latin Hypercubes". In: *Technometrics* 49.1 (2007), pp. 45–55.

[45] Pinar Civicioglu and Erkan Besdok. "A Conceptual Comparison of the Cuckoo-Search, Particle Swarm Optimization, Differential Evolution and Artificial Bee Colony Algorithms". In: *Artificial Intelligence Review* (2011).

[46] Matthew T. Cook et al. "A Comparison of Gamma Spectra from Trinitite Versus Irradiated Synthetic Nuclear Melt Glass". In: *Journal of Radioanalytical and Nuclear Chemistry* 307.1 (2016), pp. 259–267.

[47] John R. D. Copley and Terrence J Udovic. "Neutron Time-of-Flight Spectroscopy". In: *Journal of Research of the National Institute of Standards and Technology* 98.1 (1993), pp. 71–87.

[48] J. G. Cuninghame, J. A. B. Goodall, and H. H. Harris. "Absolute Yields in the Fission of 235U By Mono-Energetic Neutrons of Energy 130-1700 keV". In: *Journal of Inorganic Nuclear Chemistry* 36 (1974), pp. 1453–1457.

[49] Eddie Davis and Marianthi Ierapetritou. "A Kriging Based Method for the Solution of Mixed-Integer Nonlinear Programs Containing Black-Box Functions". In: *Journal of Global Optimization* 43.2-3 (2009), pp. 191–205.

[50] Klaus Debertin and Ulrich Schotzig. "Coincident Summing Corrections in Ge(Li)-Spectrometry at Low Source-to-Detector Distances". In: *Nuclear Instruments and Methods* 158 (1978), pp. 471–477.

[51] Defense Science Board. "Nuclear Weapon Effects Test, Evaluation, and Simulation". In: (2005).

[52] Department of Defense. *Alternative Source for Neutron Generation*. 2012.

[53] Department of Defense. "Nuclear Posture Review Report". In: (2010).

[54] Department of Defense. "Nuclear Weapons Technology". In: *Military Critical Technologies List*. 1998.

[55] Jean-Michel Do et al. "Use of Meta-Heuristics for Design of Fuel Loading Pattern in Light Water Reactors Comprising Some Radial and Axial Heterogeneities". In: *2011 IEEE International Parallel and Distributed Processing Symposium*. 2011, pp. 374–380.

[56] Wang Dong and H E Bin. "Application of Genetic Algorithm in Neutron Spectrum Unfolding". In: 21 (2010), pp. 3–7.

[57] Marco Dorigo. "Optimization, Learning and Natural Algorithms". Ph.D. Thesis. Politecnico di Milano, Italy, 1992.

[58] J. R. Dunning et al. "Interaction of Low Energy Neutrons with Atomic Nuclei". In: *Physical Review* 47 (1935), pp. 416–417.

[59] Jose A. Egea, Rafael Marti, and Julio R. Banga. "An Evolutionary Method for Complex Process Optimization". In: *Computers & Operations Research* 37.1 (2010), pp. 315–324.

[60] Jose A Egea et al. "MEIGO: An Open-Source Software Suite Based on Metaheuristics for Global Optimization in Systems Biology and Bioinformatics". In: *BMC Bioinformatics* 15 (2014), p. 136. ISSN: 1471-2105.

[61] P. A. Egelstaff and R. S. Pease. "The Design of Cold Neutron Filters". In: *Journal of Scientific Instruments* (1954), pp. 207–212.

[62] Emad Elbeltagi, Tarek Hegazy, and Donald Grierson. "Comparison among Five Evolutionary-Based Optimization Algorithms". In: *Advanced Engineering Informatics* 19.1 (2005), pp. 43–53. ISSN: 14740346. DOI: 10.1016/j.aei.2005.01.004.

[63] Mark Ellis et al. "The Effect of Detector Geometry on EJ-309 Pulse Shape Discrimination Performance". In: *IEEE Nuclear Science Symposium Conference Record* (2013).

[64] T. R. England and B. F. Rider. *Evaluation and Compilation of Fission Product Yields 1993*. 1994.

[65] Andreas Enqvist et al. "Neutron Light Output Response and Resolution Functions in EJ-309 Liquid Scintillation Detectors". In: *Nuclear Instruments and Methods in Physics Research, Section A: Accelerators, Spectrometers, Detectors and Associated Equipment* 715 (2013), pp. 79–86.

[66] Andreas Enqvist et al. "Neutron-induced 235U Fission Spectrum Measurements Using Liquid Organic Scintillation Detectors". In: *Physical Review C - Nuclear Physics* 86.6 (2012), pp. 1–10.

[67] Jutta E. Escher et al. "Compound-Nuclear Reaction Cross Sections from Surrogate Measurements". In: *Reviews of Modern Physics* 84.1 (2012), pp. 353–397.

[68] Oliver Exler et al. "A Tabu Search-based Algorithm for Mixed-integer Nonlinear Problems and its Application to Integrated Process and Control System Design". In: *Computers & Chemical Engineering* 32.8 (2008), pp. 1877–1891.

[69] Iztok Jr. Fister, Dusan Fister, and Iztok Fister. "A Comprehensive Review of CS". In: *International Journal of Mathermatical Modeling and Numerical Optimization* 4.4 (2013), pp. 387–409.

[70] I. Fister et al. "Cuckoo Search: A Brief Literature Review". In: *Studies in Computational Intelligence* (2014).

[71] C. A. Floudas and C. E. Gounaris. "A Review of Recent Advances in Global Optimization". In: *Journal of Global Optimization* 45.1 (2009), pp. 3–38.

[72] G. P. Ford and R. B. Leachman. "Fission Mass Yield Dependence on Angular Momentum". In: *Physical Review* 137.4 B (1965).

[73] J A Frenje et al. “First Measurements of the Absolute Neutron Spectrum Using the Magnetic Recoil Spectrometer at OMEGA”. In: *The Review of Scientific Instruments* 79.10 (2008), 10E502. ISSN: 1089-7623. DOI: 10.1063/1.2956837. URL: http://link.aip.org/link/?RSI/79/10E502/1%7B%%7D5Cnhttp://www.ncbi.nlm.nih.gov/pubmed/19044488.

[74] Narek Gharibyan et al. “Development of Fission-Proxy Method for the Measurement of 14-MeV Neutron Fission Yields at CAMS”. In: *Lawrence Livermore National Labs LDRD* (2015).

[75] Narek Gharibyan et al. “First Fission Yield Measurements at the National Ignition Facility: 14-MeV Neutron Fission of 238U”. In: *Journal of Radioanalytical and Nuclear Chemistry* 303.2 (2015), pp. 1335–1338.

[76] Alexander Glaser. “On the Proliferation Potential of Uranium Fuel for Research Reactors at Various Enrichment Levels”. In: *Science & Global Security* 14.1 (2006), pp. 1–24.

[77] Samuel Glasstone and Philip J. Dolan. *The Effects of Nuclear Weapons*. 3rd Ed. Washington D.C.: United State Department of Defense, 1977.

[78] V. Yu Glebov et al. “The National Ignition Facility Neutron Time-of-flight System and its Initial Performance”. In: *Review of Scientific Instruments* 81.10 (2010).

[79] L.E. Glendenin et al. “Mass Distributions for Monoenergetic-Neutron-Induced Fission of 235U”. In: *Physical Review C* 24.6 (1981), pp. 2600–2605.

[80] Fred Glover. “Paths for Integer Programming”. In: *Computers and Operations Research* 13.5 (1986), pp. 533–549.

[81] William H. Goldstein. “Lawrence Livermore National Laboratory’s Role and Contributions to the Nuclear Security Enterprise”. In: *Hearing of the Subcommittee on Strategic Forces Committee on Armed Services U.S Senate* (2014).

[82] Matthew Edgell Gooden. “Energy Dependence of Fission Product Yields from 235U, 238U, and 239Pu for Incident Neutron Energies Between 0.5 and 14.8 MeV”. PhD thesis. North Caroline State University, 2014.

[83] E. Greenspan, W. G. Price, and H. Fishman. “SWAN: A Code for the Analysis and Optimization of Fusion Reactor Nucleonic Characteristics”. In: *Princeton Plasma Physics Laboratory, MATT-1008* (1973).

[84] E Greenspan et al. “SWANS: A Prototypic SCALE Criticality Sequence for Automated Optimization Using the SWAN Methodology”. In: *ORNL/TM-1999/274* (1999).

[85] Lawrence R. Greenwood and Christian D. Johnson. “User Guide for the STAYSL PNNL Suite of Software Tools”. In: *PNNL-22253* (2013).

[86] Patrick J. Griffin. “White Sands Missile Range Fast Burst Reactor Spectrum”. In: *Personal Correspondence 23rd July, 2015* (2015).

[87] Patrick Griffin et al. "Neutron Reference Benchmark Field Specification: SPR-III Central Cavity". In: *SAND2015-4719* (2015).

[88] O. Guler. *Foundations of Optimization*. Ed. by S. Axler and K. A. Ribet. New York: Springer, 2010.

[89] J. T. Harvey et al. "Distribution of Fission Yields in the 3.0 MeV Neutron-Induced Fission of 238U". In: *Journal of Inorganic and Nuclear Chemistry* 37.2 (1975), pp. 2243–2246.

[90] W. K. Hastings. "Monte Carlo Sampling Methods Using Markov Chains and Their Applications". In: *Biometrika* 57.1 (1970), pp. 97–109.

[91] Thomas Hemker. "Derivative Free Surrogate Optimization for Mixed-Integer Nonlinear Black Box Problems in Engineering". PhD thesis. Informatik der Technischen Universitat Darmstadt, 2008.

[92] D. Hilscher and H. Rosner. "Dynamics of Fission". In: *Annales de Physique* 17.3 (1992), pp. 471–552.

[93] John H. Holland. *Adaptation in Natural and Artificial Systems: An Introductory Analysis with Applications to Biology, Control and Artificial Intelligence*. Cambridge, MA: MIT Press, 1992.

[94] R. J. Howerton, R. E. Dye, and S. T. Perkins. "The Lawrence Livermore Laboratory Evaluated Nuclear Data Library (ENDL): Evaluation Techniques, Reaction Index, and Description of Individual Evaluations". In: *UCRL-50400* 15, Part A (1975).

[95] Huasi Hu and Qunshu Wang. "Study on Composit Material for Shielding Mixed Neutron and Gama Rays". In: *IEEE transactions on science* 55.4 (2008), pp. 2376–2384.

[96] O A Hurricane et al. "Fuel Gain Exceeding Unity in an Inertially Confined Fusion Implosion". In: *Nature* 506.7488 (2014), pp. 343–348. URL: `http://www.ncbi.nlm.nih.gov/pubmed/24522535`.

[97] International Atomic Energy Agency. *International Reactor Dosimetry and Fusion File IRDFF v 1.05*. Vienna, Austria, 2014.

[98] M.F. James, R.W. Mills, and D.R. Weaver. "A New Evaluation of Fission Product Yields and the Production of a New Library (UKFY2) of Independent and Cumulative Yields". In: *Progress in Nuclear Energy* 26.1 (1991), pp. 1–29.

[99] Don Jedlovec et al. *ETA Scoping Study*. 2016.

[100] Joint Defense Science Board/Threat Reduction Advisory Comittee Task Force. *The Nuclear Weapons Effects National Enterprise*. Tech. rep. Washington, DC: Office of the Under Secretary of Defense for Acquisition, Technology, and Logistics, 2010.

[101] Joint Nuclear Forensics Working Group of the American Physical Society and the American Association for the Advancement of Science. *Nuclear Forensics: Role, State of the Art, and Program Needs*. Tech. rep. 2013.

[102] Beatriz Jurado. "The Surrogate-Reaction Method: Status and Perspectives". In: *2nd ERINDA Progress Meeting and Scientific Workshop*. 2013.

[103] A. C. Kaplan et al. "EJ-309 Pulse Shape Discrimination Performance with a High Gamma-ray-to-neutron Ratio and Low Threshold". In: *Nuclear Instruments and Methods in Physics Research, Section A* 729 (2013), pp. 463–468.

[104] John G. Kelly, Patrick J. Griffin, and Wesley C. Fan. "Benchmarking the Sandia Pulsed Reactor III Cavity Neutron Spectrum for Electronic Parts Calibration and Testing". In: *IEEE Transactions on Nuclear Science* 40.6 (1993), pp. 1418–1425.

[105] J Kennedy and R Eberhart. "Particle Swarm Optimization". In: *IEEE International Conference on Neural Networks*. Vol. 4. 1995, pp. 1942–1948.

[106] Hak-Sung Kim et al. "Design of a Neutron Screen for 6-Inch Neutron Transmutation Doping in Hanaro". In: *Nuclear Engineering and Technology* 38.7 (2006), pp. 675–680.

[107] V. G. Kiptilyi et al. "Investigation of the Parameters of Neutron Filters". In: *Technical Physics* 43.4 (1998), pp. 471–472.

[108] H. H. Knitter, U. Brosa, and C. Budzt-Jorgensen. "The Nuclear Fission Process". In: ed. by C. Wagemans. CRC, 1991.

[109] Glenn F. Knoll. *Radiation Detection and Measurement*. 3rd Ed. Ann Arbor: John Wiley & Sons, 2000.

[110] Kenneth S. Krane. *Introductory Nuclear Physics*. New York: John Wiley and Sons, 1988.

[111] Jouni Lampinen and Ivan Zelinka. "Mixed Integer-Discrete-Continuous Optimization by Differential Evolution". In: *MENDEL'99*. Brno, 1999.

[112] T. J. Langford et al. "Fast Neutron Detection with a Segmented Spectrometer". In: *Nuclear Instruments and Methods in Physics Research, Section A: Accelerators, Spectrometers, Detectors and Associated Equipment* 771 (2015), pp. 78–87.

[113] T. A. Laplace et al. "Low Energy Light Yield of Organic Scintillators". In: *National Nuclear Security Administration University Program Review*. 2017. Walnut Creek, CA, 2017.

[114] Christopher C Lawrence. "Neutron Spectrum Unfolding with Organic Scintillators for Arms-control Verification". PhD thesis. The University of Michigan, 2014.

[115] D. S. Lee et al. "Efficient Hybrid-game Strategies Coupled to Evolutionary Algorithms for Robust Multidisciplinary Design Optimization in Aerospace Engineering". In: *IEEE Transactions on Evolutionary Computation* 15.2 (2011), pp. 133–150.

[116] Jean François Lemaître et al. "New Statistical Scission-Point Model to Predict Fission Fragment Observables". In: *Physical Review C* 92.3 (2015), pp. 1–12.

[117] M. C. Lépy et al. "Intercomparison of Methods for Coincidence Summing Corrections in Gamma-ray Spectrometry". In: *Applied Radiation and Isotopes* 68 (2010), pp. 1407–1412.

[118] Marie Christine Lépy. "Total Efficiency Calibration for Coincidence-Summing Corrections". In: *Nuclear Instruments and Methods in Physics Research A* 579.1 (2007), pp. 284–287.

[119] Marie Christine Lépy et al. "Experimental Validation of Coincidence Summing Corrections Computed by the ETNA Software". In: *Applied Radiation and Isotopes* 64.10-11 (2006), pp. 1340–1345.

[120] Sven Leyffer et al. "Applications and Algorithms for Mixed Integer Nonlinear Programming". In: *Journal of Physics: Conference Series* 180 (2009), p. 012014.

[121] By Ze Li et al. "Fission Product Yields from 11.3 MeV Neutron-Induced Fission of 238 U". In: 7 (1994), pp. 95–98.

[122] S. Lin and W. Kernighan. "An Effective Heurisic Algorithm for the Traveling-Salesman Problem". In: *Operations Research* 21.2 (1973), pp. 498–516.

[123] LLNL. *National Ignition Facility and Photon Science*. URL: `https://lasers.llnl.gov/` (visited on 08/16/2015).

[124] M. A. Lone et al. "Thick Target Neutron Yields and Spectral Distributions from the 7Li(d,n) and 9Be(d,n) Reactions". In: *Nuclear Instrumentd and Methods* 143 (1977), pp. 331–344.

[125] Michael A. Lones. "Metaheuristics in Nature-Inspired Algorithms". In: *Proceedings of the 2014 Conference on Genetic and Evolutionary Computation*. 2014, pp. 1419–1422.

[126] Nicholas Patrick Luciano. "A High-Energy Neutron Flux Spectra Measurement Method for the Spallation Neutron Source". PhD thesis. University of Tennessee, 2012.

[127] Rosari Nunzio Mantegna. "Fast, Accurate Algorithm for Numerical Simulation of Levy Stable Stochastic Processes". In: *Physical Review E* 49.5 (1994).

[128] Rosario N. Mantegna and H. Eugene Stanley. "Stochastic Process with Ultraslow Convergence to a Gaussian: The Truncated Levy Flight". In: *Physical Review Letters* 73.22 (1994), pp. 2946–2949.

[129] Marsh J. W., Thomas D. J., and Burke M. "High Resolution Measurements of Neutron Energy Spectra from Am-Be and Am-B Neutron Sources". In: *Nuclear Instruments and Methods in Physics Research A* 366.95 (1995), pp. 340–348.

[130] S G Mashnik et al. "7Li(p,n) Nuclear Data Library for Incident Proton Energies to 150 MeV". In: *2000 ANS/ENS International Meeting, Nuclear Applications of Accelerator Technology*. LA-UR-00-5524, 2008.

[131] Mathworks. "MatLab: Global Optimization Toolbox User's Guide R2015b". In: (2015).

[132] A Mattera et al. "Measurement of the Energy Spectrum from the Neutron Source Planned for IGISOL". In: *European Research Infrastructures for Nuclear Data Applications (ERINDA) worksho*. Geneva, Switzerland, 2013.

[133] M. Matzke. "Propagation of Uncertainties in Unfolding Procedures". In: *Nuclear Instruments and Methods in Physics Research, Section A: Accelerators, Spectrometers, Detectors and Associated Equipment* 476.1-2 (2002), pp. 230–241.

[134] Manfred Matzke. "The HEPROW Program System". In: (2003).

[135] Manfred Matzke. *Unfolding Methods*. Tech. rep. 2003.

[136] Manfred Matzke. "Unfolding of Particle Spectra". In: *Proc. SPIE 2867, International Conference Neutrons in Research and Industry*. Vol. 568. 1997, pp. 598–607.

[137] Manfred Matzke. "Unfolding of Pulse Height Spectra: The HEPRO Program". In: *Physikalisch Technicshce Bundesanstalt* 19 (1994).

[138] M. A. McMahan et al. "Neutron Beams from Deuteron Breakup at the 88-Inch Cyclotron at Lawrence Berkeley National Laboratory". In: *Science And Technology* April 2016 (2008), pp. 3–6.

[139] James W Meadows and Donald L Smith. "Neutron Source Investigations in Support of the Cross Section Program at the Argonne Fast-Neutron Generator". In: *ANL/NDM-53* (1980).

[140] Lise Meitner and O. R. Frisch. "Disintegrations of Uranium by Neutrons: A New Type of Nuclear Reaction". In: *Nature* 143 (1939), pp. 239–240.

[141] J.P. Meulders et al. "Fast Neutron Yields and Spectra from Targets of Varying Atomic Number Bombarded with Deuterons from 16 to 50 MeV (for Radiobiology and Radiotherapy)". In: *Physics in Medicine and Biology* 20.2 (1975), pp. 235–243. ISSN: 0031-9155. URL: `http://www.ncbi.nlm.nih.gov/pubmed/1153513`.

[142] D. M. Minsky, A. J. Kreiner, and A. A. Valda. "AB-BNCT Beam Shaping Assembly Based on 7Li(p,n)7Be Reaction Optimization". In: *Applied Radiation and Isotopes* 69.12 (2011), pp. 1668–1671.

[143] Joshua James Molgaard. "Production of Nuclear Debris Surrogates for Forensic Methods Development". PhD thesis. Univeristy of Tennessee, 2014.

[144] Joshua J. Molgaard et al. "Development of Synthetic Nuclear Melt Glass for Forensic Analysis". In: *Journal of Radioanalytical and Nuclear Chemistry* 304.3 (2015), pp. 1293–1301.

[145] P. Möller and A. J. Sierk. "80 Years of the Liquid Drop-50 Years of the Macroscopic-Microscopic Model". In: *International Journal of Mass Spectrometry* 349-350.1 (2013), pp. 19–25.

[146] P Möller et al. "Nuclear Fission Modes and Fragment Mass Asymmetries in a Five-dimensional Deformation Space." In: *Nature* 409.6822 (2001), pp. 785–790.

[147] Mateusz Monterial et al. "Application of Bayes Theorem for Pulse Shape Discrimination". In: *Nuclear Instruments and Methods in Physics Research Section A* 795 (2015), pp. 318–324.

[148] Edward Morse. "RTNS-II Neutron Energy Spectrum". In: *Personal Correspondence 27July* (2015).

[149] S. W. Mosher et al. "ADVANTG: An Automated Variance Reduction Parameter Generator". In: *ORNL/TM-2013/416 Rev 1* (2015).

[150] Bhaskar Mukherjee. "ANDI-03: A Genetic Algorithm Tool for the Analysis of Activation Detector Data to Unfold High-energy Neutron Spectra". In: *Radiation Protection Dosimetry* 110.1-4 (2004), pp. 249–254.

[151] Juliane Müller, Christine A. Shoemaker, and Robert Piché. "SO-MI: A Surrogate Model Algorithm for Computationally Expensive Nonlinear Mixed-Integer Black-Box Global Optimization Problems". In: *Computers and Operations Research* 40.5 (2013), pp. 1383–1400.

[152] M. Mullner and H. Jex. "Converter-Thickness for Optimum Intensity in Neutron-Radiography". In: *Nuclear Instruments and Methods* 103 (1972), pp. 229–233.

[153] A.V. Murzin et al. "Neutron Filters Based on V, Mn, S, and the Stable Isotopes 52Cr, 56Fe, 58Ni, and 60Ni". In: *Atomnaya Energiya* 67.3 (1989), pp. 216–218.

[154] S. M. Myers. "The Science of QASPR (Qualification Alternatives to the Sandia Pulsed Reactor) in Sandia' s Physical , Chemical , and Nano Sciences Center (PCNSC)". In: (2008).

[155] S. Nagy et al. "Mass Distributions in Monoenergetic-Neutron-Induced Fission of U238". In: *Physical Review C* 17.1 (1978), pp. 163–171.

[156] M. Nakhostin. "Recursive Algorithms for Digital Implementation of Neutron/Gamma Discrimination in Liquid Scintillation Detectors". In: *Nuclear Instruments and Methods in Physics Research, Section A* 672 (2012), pp. 1–5. URL: http://dx.doi.org/10.1016/j.nima.2011.12.113.

[157] D. R. Nethaway and G.W. Barton. "A Compilation of Fission Product Yields in use at the Lawrence Livermore Labratory". In: *UCRL-51458* (1973).

[158] Mark A. Norsworthy et al. "Evaluation of Neutron Light Output Response Functions in EJ-309 Organic Scintillators". In: *Nuclear Instruments and Methods in Physics Research, Section A* 842.June 2016 (2017), pp. 20–27.

[159] NTNFC. "National Technical Nuclear Forensics (NTNF) Overview". In: (2015).

[160] Nuclear Energy Agency. "Intercomparison of Calculations for Godiva and Jezebel". In: *JEFF Report 16* (1999).

[161] *Nuclear Fission*. URL: http://www.nuclear-power.net/nuclear-power/fission/ (visited on 07/19/2017).

[162] *Optimization Taxonomy*. URL: https://neos-guide.org/content/optimization-taxonomy (visited on 05/25/2017).

[163] C. A. Oster. "Review of Unfolding Methods Used in the U.S. and Their Standardization for Doismetry". In: *Second ASTM-EURATOM Symposium on Reactor Dosimetry*. Palo Alto, 1977, pp. 1689–1699.

[164] Xinxin Ouyang et al. "A Novel Discrete Cuckoo Search Algorithm for Spherical Traveling Salesman Problem". In: *Applied Mathematics and Information Sciences* 7.2 (2013), pp. 777–784.

[165] E. Pantaleo, P. Facchi, and S. Pascazio. "Simulations of Lévy flights". In: *Physica Scripta* T135 (2009).

[166] Edward J. Parma et al. "Radiation Characterization Summary: ACRR Central Cavity Free-Field Environment with the 32-Inch Pedestal at the Core Centerline (ACRR-FF-CC-32-cl)". In: *SAND2015-6483* (2015).

[167] I. A. Pawełczak et al. "Studies of Neutron-Gamma Pulse Shape Discrimination in EJ-309 Liquid Scintillator Using Charge Integration Method". In: *Nuclear Instruments and Methods in Physics Research, Section A* 711 (2013), pp. 21–26.

[168] H.C. Paxton. "Los Alamos Critical-Mass Data". In: *LAMS-3067* (1964).

[169] H.C. Paxton and N. L. Pruvost. "Critical Dimensions of Systems Containing 235U, 239Pu, and 233U". In: *LA-10860-MS* (1987).

[170] Larry Phair. "Surrogate Reactions and their Applications". In: *The John Cramer Symposium*. Seattle, 2009.

[171] J. Praena, P. F. Mastinu, and G. Martín Hernández. "A Method to Obtain a Maxwell–Boltzmann Neutron Spectrum at kT = 30 keV for Nuclear Astrophysics Studies". In: *Publications of the Astronomical Society of Australia* 26.3 (2009), p. 225.

[172] Radiation Effects Research Foundation. *Reassessment of the Atomic Bomb Radiation Dosimetry for Hiroshima and Nagasaki*. Hiroshima, 2005.

[173] Faezeh Rahmani and Majid Shahriari. "Beam Shaping Assembly Optimization of Linac Based BNCT and In-Phantom Depth Dose Distribution Analysis of Brain Tumors for Verification of a Beam Model". In: *Annals of Nuclear Energy* 38.2-3 (2011), pp. 404–409.

[174] François-Michel D. Rainville et al. "Evolutionary Optimization of Low-Discrepancy Sequences". In: *ACM Transactions on Modeling and Computer Simulation* 22 (2012), pp. 1–25.

[175] Jorgen Randrup and Ramona Vogt. "Calculation of Fission Observables Through Event-by-event Simulation". In: *Physical Review C - Nuclear Physics* 80.2 (2009), pp. 1–11.

[176] Marcel Reginatto and Paul Goldhagen. *MAXED, A Computer Code for the Deconvolution of Mutilsphere Neutron Spectrometer Data Using the Maximum Entropy Method*. Tech. rep. New York: Environments Measurement Laboratory, 1998.

[177] Marcel Reginatto, Paul Goldhagen, and Sonja Neumann. "Spectrum Unfolding, Sensitivity Analysis and Propagation of Uncertainties with the Maximum Entropy Deconvolution Code MAXED". In: *Nuclear Instruments and Methods in Physics Research A* 47 (2002), pp. 242–246.

[178] H Edwin Romeijn and Fabio Schoen. "Handbook of Global Optimization". In: *Optimization* 62 (2002), pp. 515–569.

[179] F. Rossitto, M. Terrani, and S. Terrani. "Choice of Neutron Filters in Activation Analysis". In: *Nuclear Instruments and Methods* (1972), pp. 77–83.

[180] Steven J. Sampson. "Advancing Qualification Alternatives to the Sandia Pulsed Reactor Activities". In: *Stockpile Stewardship Quarterly* 3.4 (2013).

[181] Jorma Sandberg. "Determination of Particle Flux Spectra with Multireaction Activation Detectors". In: *Acta Polytechnica Scandinavica* 146 (1984).

[182] Sandia National Laboratories. *Survivor: Sandia ensures US Nuclear Weapons Deterrent can remain Effective, Credible*. Albuquerque, July 2014.

[183] Joseph L Sapir, Russell Kidman, and R W Brewer. "235U (94 %) Sheres Surrounded by Natural-Uranium Reflectors". In: *LA-UR-98-1664* (1998).

[184] P. Schillebeeckx et al. "Comparative Study of the Fragments' Mass and Energy Characteristics in the Spontaneous Fission of 238Pu, 240Pu, and 242Pu and in the Thermal-Neutron-Induced Fission of 239Pu*". In: *Nuclear Physics A* 545 (1992), pp. 623–645.

[185] Karl-Heinz Schmidt and Beatriz Jurado. "General Description of Fission Observables". In: *JEFF Report 24* (2014).

[186] T. R. Schmidt, B. F. Estes, and J.A. Reuscher. "Recent Operational History of the New Sandia Pulsed Reactor III". In: *SAND-77-1116C* (1977).

[187] Thomas M Semkow, Pravin P Parekh, and Mark Virgil. "Coincidence Summing in Gamma-Ray Spectroscopy". In: 290 (1990), pp. 437–444.

[188] Sujoy Sen et al. "Determination of Neutron Energy Spectrum at KAMINI Shielding Experiment Location". In: *Applied Radiation and Isotopes* 115 (2016), pp. 165–171.

[189] Robert Serber. *The Los Alamos Primer*. Berkeley: University of California Press, 1992.

[190] D Shaughnessy et al. "Radiochemical Measurements of Neutron Reaction Products at the National Ignition Facility". In: *248th ACS National Meeting*. San Francisco, 2014.

[191] Fiona Simpson. "The U.S. Stockpile Stewardship Program: Domestic Perspectives and International Implications". In: *International Commission on Nuclear Non-proliferation and Disarmament* (2009).

[192] Solid Radiochemistry Nuclear Diagnostic Group. "Fission Yield Measurements at NIF". In: *LLNL-PRES-667181*. 2015.

[193] Kenneth Sorensen, Marc Sevaux, and Fred Glover. "A History of Metaheuristics". In: *Handbook of Heuristics*. Springer, 2016.

[194] Timothy Starkweather et al. "A Comparison of Genetic Sequencing Operators". In: *Proceedings of the fourth International Conference on Genetic Algorithms*. 1991, pp. 69–76.

[195] Rainer Storn and K Price. "Differential Evolution - A Simple and Efficient Heuristic for Global Optimization over Continuous Spaces". In: *Journal of Global Optimization* 11 (1997), pp. 341–359.

[196] IE. A. Straker et al. "Simulataneous Determination of Fast-Neutron Spectra by Time-of-Flight and Pulse-Height Unfolding Techniques". In: *Nuclear Instruments* 97 (1971), pp. 275–285.

[197] S Adam Stratz et al. "Modern Advancements in Post-Detonation Nuclear Forensic Analysis". In: *International Journal of Nuclear Security International Journal of Nuclear Security International Journal of Nuclear Security* 2.3 (2016).

[198] Guo Tao and Zbigniew Michalewicz. "Iver-over Operator for the TSP". In: *Parallel Problem Solving from Nature - PPSN V, 5th International Conference*. Amsterdam, 1998.

[199] Bruce Tarter. "Annual Certification Takes a Snapshop of Stockpile's Health". In: *Science & Technology Review* (2001), pp. 4–10.

[200] X-5 Monte Carlo Team. "MCNP - A General Monte Carlo N-Particle Transport Code, Version 5". In: *LA-UR-03-1987* (2008).

[201] D J Thomas and A V Alevra. "Bonner Sphere Spectrometers - a Critical Review". In: *Nuclear Instruments and Methods in Physics Research A* 476 (2002), pp. 12–20.

[202] Fredrik Tovesson. "Nuclear Science Research at the LANSCE-WNR Facility". In: (2013).

[203] Truyen Tran, Trung Thanh Nguyen, and Hoang Linh Nguyen. "Global Optimization using Levy Flights". In: *Second National Symposium on Research, Development and Application of Information and Communication Technology*. Hanoi, 2004.

[204] S. P. Tripathy et al. "Activation Foils Unfolding for Neutron Spectrometry: Comparison of Different Deconvolution Methods". In: *Nuclear Instruments and Methods in Physics Research, Section A: Accelerators, Spectrometers, Detectors and Associated Equipment* 583.2-3 (2007), pp. 421–425.

[205] US Department of Energy. "United States Nuclear Tests: July 1945 through September 1992". In: *DOE/NV–209-Rev 15* (2000).

[206] Hector Rene Vega Carrillo. "Geometrical Ffficiency for a Parallel Disk Source and Detector". In: *Nuclear Instruments and Methods in Physics Research, Section A* 371.3 (1996), pp. 535–537.

[207] Richard M Vega et al. "Neutron Reference Benchmark Field Specification: ACRR Free-Field Environment (ACRR-FF-CC-32-CL)". In: *SAND2015-5360* (2015).

[208] J. M. Verbeke. "Development of High-Intensity D-D and D-T Neutron Sources and Neutron Filters for Medical and Industrial Applications". PhD thesis. University of California - Berkeley, 2000.

[209] J M Verbeke, J Randrup, and R Vogt. "Fission Reaction Event Yield Algorithm FREYA". In: *LLNL-TM-654899* (2014).

[210] J. M. Verbeke et al. "Designing an Epithermal Neutron Beam for Boron Neutron Capture Therapy for the Fusion Reactions 2H(d,n)3He and 3H(d,n)4He". In: *eScholarship* (1998).

[211] V. V. Verbinski et al. "Calibration of an Organic Scintillator for Neutron Spectrometry". In: *Nuclear Instruments and Methods* 65 (1968), pp. 8–25.

[212] Felipe A C Viana. "Things You Wanted to Know About the Latin Hypercube Design and Were Afraid to Ask". In: *10th World Congress on Structural and Multidisciplinary Optimization*. Orlando, 2013, pp. 1–9.

[213] R. Vogt and J. Randrup. "Event-by-event study of photon observables in spontaneous and thermal fission". In: *Physical Review C - Nuclear Physics* 87.4 (2013), pp. 1–14.

[214] R. Vogt et al. "Event-by-event evaluation of the prompt fission neutron spectrum from 239Pu(n,f)". In: *Physical Review C - Nuclear Physics* 85.2 (2012), pp. 1–20.

[215] J. Vujic et al. "Optimal Neutron Source & Beam Shaping Assembly for Boron Neutron Capture Therapy". In: *UCBNE-4239* (2003).

[216] A. C. Wahl. "Mass and Charge Distribution in Low-Energy Fission". In: *Physics and Chemistry of Fission*. Salzburg, 1965, pp. 317–331.

[217] A C Wahl. *Systematics of Fission-Product Yields*. Los Alamos, 2002.

[218] R. L. Walsh. "Spin-Dependent Calculation of Fission Neutron Spectra and Fission Spectrum Integrals for Six Fissioning Systems". In: *Nuclear Science and Engineering1* 102.2 (1989), pp. 119–133.

[219] S. Walton et al. "Modified Cuckoo Search: A New Gradient Free Optimisation Algorithm". In: *Chaos, Solitons and Fractals* 44.9 (2011), pp. 710–718.

[220] Yukinobu Watanabe, Tao Ye, and Kazuyyki Ogata. "Analysis of Deuteron Breakup Reactions for Energies up to 100 MeV". In: *EPJ Web of Conferences* 2 (2010).

[221] Keith Allen Weaver. "Neutrons from Deuteron Bombardment of Light Nuclei". In: *UCRL-51310* (1972).

[222] M. J. Weber, ed. *Selected Papers on Phospors, LEDs, and Scintillators*. Bellingham, Washington: SPIE Optical Engineering Press, 1998.

[223] K. Weise and M. Matzke. "A Priori Distributions from the Principle of Maximum Entropy for the Monte Carlo Unfolding of Particle Energy Spectra". In: *Nuclear Instruments and Methods in Physics Research* 280 (1989), pp. 103–112.

[224] B. D. Wilkins, E. P. Steinberg, and R. R. Chasman. "Scission-Point Model of Nuclear Fission Based on Deformed-Shell Effects". In: *Physical Review C* 14.5 (1976), pp. 1832–1863.

[225] Thomas F Wimett. "Fast Burst Reactors in the U.S.A." In: *LA-DC-6786* (1965).

[226] Stephan Winkler and Stefan Wagner. "Evolutionary System Identification: New Algorithmic Concepts and Applications". In: *Advances in Evolutionary Algorithms*. Ed. by Witold Kosiński. Vienna, Austria, 2008. ISBN: 9789537619114.

[227] Alexandra Witze. *Sharks Use Math to Hunt*. 2010. URL: `https://www.sciencenews.org/article/sharks-use-math-hunt` (visited on 02/12/2015).

[228] David H. Wolpert and William G. Macready. "No Free Lunch Theorems for Optimization". In: *IEEE Transactions on Evolutionary Computation* 1.1 (1997), pp. 67–82.

[229] Harold L. Wright, John L. Meason, and James T. Harvey. "Neutron Spectrum Measurements at the White Sands Missile Range Fast Burst Reactor (FBR)". In: (1976).

[230] Xin-She Yang. *Engineering Optimization*. Hoboken: John Wiley & Sons, 2010.

[231] Xin-She Yang. *Nature-Inspired Optimization Algorithms*. 1st. London: Elsevier, 2014.

[232] Xin-She Yang and Suash Deb. "Cuckoo Search via Levy Flights". In: *Nature & Biologically Inspired Computing*. 2009, pp. 210–214.

[233] Tao Ye, Yukinobu Watanabe, and Kazuyuki Ogata. "Analysis of Deuteron Breakup Reactions on Li7 for Energies up to 100 MeV". In: *Physical Review C - Nuclear Physics* 80.1 (2009), pp. 1–8. ISSN: 05562813. DOI: `10.1103/PhysRevC.80.014604`.

[234] Luo Yiqing, Yuan Xigang, and Liu Yongjian. "An Improved PSO Algorithm for Solving Non-convex NLP/MINLP Problems with Equality Constraints". In: *Computers and Chemical Engineering* 31.3 (2007), pp. 153–162.

[235] Walid Younes. *NE290A Lecture Notes*. 2016.

[236] S. Yousefi, L. Lucchese, and M. D. Aspinall. "Digital Discrimination of Neutrons and Gamma-rays in Liquid Scintillators Using Wavelets". In: *Nuclear Instruments and Methods in Physics Research, Section A* 598.2 (2009), pp. 551–555.

[237] Kun Zhao et al. "Optimal Levy-Flight Foraging in a Finite Landscape". In: *Journal of the Royal Society Interface* 12 (2015).

[238] Yongquan Zhou, Xinxin Ouyang, and Jian Xie. "A Discrete Cuckoo Search Algorithm for Travelling Salesman Problem". In: *International Journal of Collaborative Intelligence* 1.1 (2014), pp. 68–84.